Creating and shaping light at single photon level

by

Supratik Sarkar

A thesis
presented to the University of Waterloo
in fulfillment of the
thesis requirement for the degree of
Master of Applied Science
in
Electrical and Computer Engineering
(Quantum Information)

Waterloo, Ontario, Canada, 2021

Author's declaration

I hereby declare that I am the sole author of this thesis. This is a true copy of the thesis, including any required final revisions, as accepted by my examiners.

I understand that my thesis may be made electronically available to the public.

Abstract

The ability to control light at the single photon level is essential for fully harnessing the power of quantum information theory, and precision measurements. In this thesis, we study two phenomena which can help us to create, and shape light at the smallest scale. In the first part of the thesis, we explore deterministic single photon subtraction based upon single photon Raman interaction of a single three-level Λ-type quantum emitter in a bimodal cavity or coupled with a chiral waveguide. We study the effect of photon subtraction from different types of optical inputs - continuous-wave or pulsed coherent states and Fock states, and dependence of the fidelity of subtraction upon key system parameters. We also discuss the suitability and prospects of using different emitter-waveguide systems reported in literature to successfully extract a single photon from an optical input. We find that a quantum dot coupled with a photonic crystal waveguide with high group index could subtract photons with fidelity close to unity. Moreover, we explore how such a SPRINT-based single photon subtraction process can be used to create non-Gaussian states with negative values of Wigner distribution, and negative conditional entropies. Such states can be used as quantum resources in various fields of quantum information theory. Finally, as an interesting example, we also discuss how this mechanism can also be used to create non-classical Fock states of arbitrary photon number.

In the second part of this thesis, we study how to shape the emission from a single solid-state quantum emitter, in particular an NV^- center in diamond, using two dimensional patterns with sub-wavelength features. We propose a pattern etched on the surface of a diamond sample that enhances the NV's emission in a particular direction, and maximizes coupling with a waveguide substantially far away from the diamond-air interface. Our proposed structure was designed using the adjoint optimization technique, which significantly reduces the amount of computational resources compared to brute-force methods to design an optical element with desired properties. Our structure exhibits a higher directionality of emission compared to other nanophotonic structures reported in the literature – solid immersion lenses, nanopillars, and bull's eye structures. Finally, we also discuss in details the steps pertaining to setting up a confocal microscope in our laboratory for imaging NV centers, and characterizing our proposed device.

Acknowledgements

During my Master's in Waterloo I have come across many wonderful and knowledgeable people, who have taught me a lot, not only about science, but also life in general. I feel extremely lucky to have crossed paths with all of them. First, I would like to thank my advisor Michal Bajcsy for the wonderful opportunity of pursuing my Master's at Institute for Quantum Computing, which led me to great amounts of personal and professional growth. I absolutely enjoyed the multi-disciplinary aspect of IQC, where people working on AMO, circuit QED, ion traps, solid state, algorithms, complexity theory, cryptography and security could all learn from each other during regular seminars/talks, and specially over charcuterie and drinks during monthly gatherings. I started as a theorist with little knowledge about experimental physics. In the last couple of years, I have learnt to enjoy both the experimental and theoretical aspects of AMO and nanophotonics, which I find to be invaluable.

In addition, I would like to thank my fellow group members in somewhat chronological order. First and foremost, I would like to express my gratitude to Vinodh Raj with whom I have made many cherished memories during my Master's. He has been a great friend, providing mental support and encouragement through thick and thin. I cannot emphasize enough, how much his presence made my experience at IQC easier and cherishable. Our trip to DC definitely has to be one of the highlights of the past two years. I will miss our conversations over French vanillas, and watching Game of Thrones in conference rooms. Next, I would like to thank Zhenghao Ding (Andy) and Sheng-Xiang Lin (Sean) for all their support and encouragement. Even though I knew them for only 4 months, they became one of the closest friends I made in Waterloo. The two of them are truly inspirational, and helped me navigate my ways around the field and Waterloo during my initial days. Sean is one of the most humble people I have met, and has been a great office mate. And Andy is still only a knock-on-the-door away whenever I need any help or suggestions. Next, I would like to convey my sincere thanks to Behrooz Semnani. I have learnt so much from our discussions, and he has been a very supportive mentor to me throughout my time in Waterloo. I always enjoyed our conversations at the IQC kitchen, which used to range from science to world politics and philosophy. I am grateful to Rubayet Al Maruf for all his help and support while setting up the experiment. Thank you for taking the time to teach me the basics of optical alignment and working in the nanofab. Next, I would like to thank Sema Kuru and Pritam Priyadarshi for being good friends throughout the journey. I am also thankful to Jinjin Du, Wenfang Li, Divya Bharadwaj, Jeremy Flannery, Paul Anderson, Pablo Palacios Avila, Sreesh Venuturumilli, and Jiawei Qiu (Jackson) for their support throughout the past couple of years.

Outside my group, I was lucky to have fantastic friends like Lane Gunderman, Soumik Ghosh, Sayan Gangopadhyay, and Sam Winnick. Lane is undoubtedly one of the smartest people I have ever met. His breadth of knowledge on topics like pure maths, algorithms, QECC, theoretical physics, and chemistry (and also random spices from around the world) is truly inspiring. But what is more inspirational is probably his humility and simplicity. In Soumik, I found a piece of Jadavpur at IQC, and I had a really great time discussing culture, movies, society, politics, and everything in between with him during our time in Waterloo. I will miss going out on random walks on weekends, watching movies, and hanging out with Sayan to overcome the stress of applying to grad schools during a pandemic. I deeply cherished all the scientific and sociopolitical conversations, the road trips, the hikes, and the innumerable dinner parties at Sam and Yamin's place. Sam's knowledge of mathematics is pretty astounding, and I have learnt so much from our conversations. I am certain all of them will be stalwarts in their respective fields, and I can't wait to bump into them at future conferences.

Apart from that, I would like to thank Jérémy Béjanin for being a great office mate. Outside IQC, I would like to thank Susmita Bose for hosting me, and treating me to her superior culinary skills often. I will also like to thank Sayan Nag for his friendship, and giving me a tour of Toronto and introducing me to one of the best sushi restaurants in GTA!

I feel indebted to all the friends since high school, and my teachers who fanned my curiosity and made me interested in pursuing scientific research. Finally, I must express my gratitude to my parents and my family (particularly my grandma) who taught me to ask questions and think freely. They worked hard, and made so many personal sacrifices to give me all the necessary resources throughout my life. I wouldn't be here without their unflinching support, and unconditional love.

Dedication

I dedicate this thesis to my parents, my grandma, my friends, my teachers, and to every well-wisher who has loved me, nurtured me, supported me, tolerated me, and helped in moulding me. I am grateful for all of you!

Table of Contents

List of Tables

List of Figures

Chapter 1

Introduction

In the end of the nineteenth century, it seemed that physicists were pretty confident that most of physics had been already figured out. After all, classical mechanics, Maxwell's equations, and thermodynamics seemed to explain most of the natural phenomena. However, at the turn of the century, in 1900, Max Planck laid the foundation stone for a quantum theory of electromagnetic waves with his work on black-body radiation [1]. It might seem that his work to quantize the emission/absorption of electromagnetic energy into discrete quantities was an act of desperation to match the experimentally observed black-body radiation spectrum. But within half a decade, in 1905, Einstein in his landmark work on photoelectric effect proposed the concept of a photon – the fundamental unit of electromagnetic radiation [2]. However, in 1927, it was Paul Dirac who finally put the pieces of Maxwell and Einstein's theory together by treating light as a collection of harmonic oscillators, and started the field of quantum electrodynamics [3]. That led to the understanding of phenomena like the spontaneous emission, the Lamb shift, and Casimir forces. Finally, in 1963, Roy Glauber in his seminal paper laid the groundwork for the current understanding of light by studying photon statistics, and showing the difference between a coherent laser and other sources of light [4].

Once we had quite an advanced understanding of light, and how it interacts with matter, we started exploring how to use the various degree of freedoms of a photon as quanta of information. But to fully realize the promise quantum optics holds in quantum information theory, we need to have proper control over the light at single photon level. In this thesis, we explore two ways we can engineer the behavior of light at the single photon level. First, we explore how to deterministically subtract a single photon from an arbitrary beam of light. Second, we shall investigate how we can shape photon emission from an NV center using custom made nanophotonic structures.

1.1 Deterministic single photon subtraction

In the first half of the thesis, we shall study deterministic single photon subtraction from an arbitrary state of light using single photon Raman interaction with a single three-level Λ-type quantum emitter. Single photon subtraction has been used to study fundamental principles of quantum mechanics, and has been shown to be an useful tool to create non-classical resource states for use in quantum information theory [5–7]. However, most of the photon subtraction based on heralding techniques rely upon a beamsplitter type operation, which lead to very low rates of successful subtraction. Moreover, they are non-deterministic in nature, rely upon the heralded detection of a single subtracted photon, and the fidelity depends upon the intensity of the incident beam. Thus, deterministic photon subtraction which can provide improved success rates, and can subtract a single photon irrespective of the strength of the input beam is a topic of great interest.

In Chapter 2, we begin by providing a brief background to the problem of single photon subtraction, and cavity quantum electrodynamics. Next, we investigate how to perform deterministic single photon subtraction in a bi-modal cavity. We also study the temporal dynamics of the single photon Raman interaction, and study three different situations. First, we look at the system's response with a continuous-wave (CW) coherent input. Then, we investigate what would happen if the cavity mode is initialized with a pulsed coherent state or a Fock state. In Chapter 3, first, we start by providing a brief background to waveguide quantum electrodynamics. Later, we propose and investigate the feasibility of deterministic single photon subtraction using a three-level emitter coupled to a chiral waveguide instead of a bi-modal cavity. Moreover, we explore how the mechanism works for three different types of input – a continuous-wave (CW) coherent state, a coherent Gaussian pulse, and a Fock state input. We study the important system parameters that need to be considered for experimental design, and predict how recently reported emitter-waveguide systems might perform. Later, in Chapter 4, we ask the question if this kind of deterministic single photon subtraction mechanism can be employed to generate entanglement, and non-classical states. We show that SPRINT-based single photon subtraction can be used to create non-Gaussian quantum states with negative Wigner functions, and negative conditional entropies. Such states can be used as quantum resources in quantum computing, quantum information theory, and quantum cryptography. Finally, as an interesting example, we show how this mechanism can also be used to create Fock states of arbitrary photon number. We conclude with a brief discussion about the future directions of the ongoing project.

1.2 Inverse design of nanophotonic structures for directional emission from NV centers

NV centers have been one of the most prospective solid state emitters for quantum technologies, with applications to quantum sensing in particular. It provides multiple advantages over other quantum emitters, one of the most important one being easy initialization and long coherence times for room temperature operations [8–10]. Efficiently coupling emission from the emitter to a waveguide in the far-field is a challenging problem. In this thesis, we have tried to address that problem with tailor-made nanophotonic structures designed with the help of optimization algorithms.

In the second half of the thesis, we will study how we can use nanophotonic structures to control the emission properties of an NV center in a diamond substrate for efficient coupling with a waveguide. Such nanophotonic structures can be modeled as an antenna, and the NV center can be treated as a classical dipole. In Chapter 5, we provide a background on the classical and quantum theory of dipole radiation to understand why we can study such problems under the umbrella of classical antenna theory. In Chapter 6, we introduce the working principles of adjoint optimization based solutions to inverse design problems in electromagnetic theory. We discuss the adjoint optimization algorithm in sufficient detail, and show how it helps in reducing the amount of computational resources. Moreover, we also introduce the two ways in which we can perform adjoint optimization, namely geometry and topology optimization. We also briefly discuss how we can design nanophotonic devices by employing the level set method to impose fabrication dependent optimization constraints. Finally, in Chapter 7, we propose our device designed with the help of adjoint optimization. The proposed device helps in directional emission of radiation from NV centers, and enhances free space coupling of the emitter with a nanofiber, without the presence of separate optical arrangements for the purpose of efficient coupling. For comparison, we also study the performance of other nanophotonic structures proposed in the literature to enhance the emission properties of solid state emitters. Then, we discuss the confocal microscopy setup we built in our laboratory to image the NV centers in diamonds. We conclude with a brief discussion about the future directions of the project, which mainly consists of fabricating and characterizing our proposed device.

The computer programs used for numerical simulations has been provided in the Appendix section of this thesis.

Part I

Deterministic single photon subtraction

Chapter 2

Deterministic single photon subtraction with a three-level emitter in a bi-modal cavity

2.1 Motivation

Subtraction of a single photon from a light pulse has been an interesting problem in the recent times, as it can be used to probe the fundamental nature of quantum mechanics [5, 11]. It can be an effective tool in generating non-classical exotic states of light. Non-classical states are an essential resource for quantum computation and communication [6, 12, 13], and lie at the heart of harnessing quantum supremacy. Single photon subtraction has been experimentally used for enhancing entanglement via entanglement distillation, and for creation of hybrid entangled states [6, 14–16]. Moreover, it can be used to investigate the quantum commutation rules, which form the very basis of quantum optics [5]. Heralded single photon subtraction using a low reflectance beamsplitter as shown in Fig. 2.1a has been used to generate various non-Gaussian states of light like Fock states [17], and Schrödinger's cat states with a negative Wigner function [6, 18–22]. In this simplistic approach, the detection of a single photon by the photo-detector in the mode with the subtracted photons projects the output to state [23, 24]

$$\hat{\rho}_{out} = \frac{1}{N} \sum_{n} \hat{a}_n \hat{\rho} \hat{a}_n^{\dagger},$$

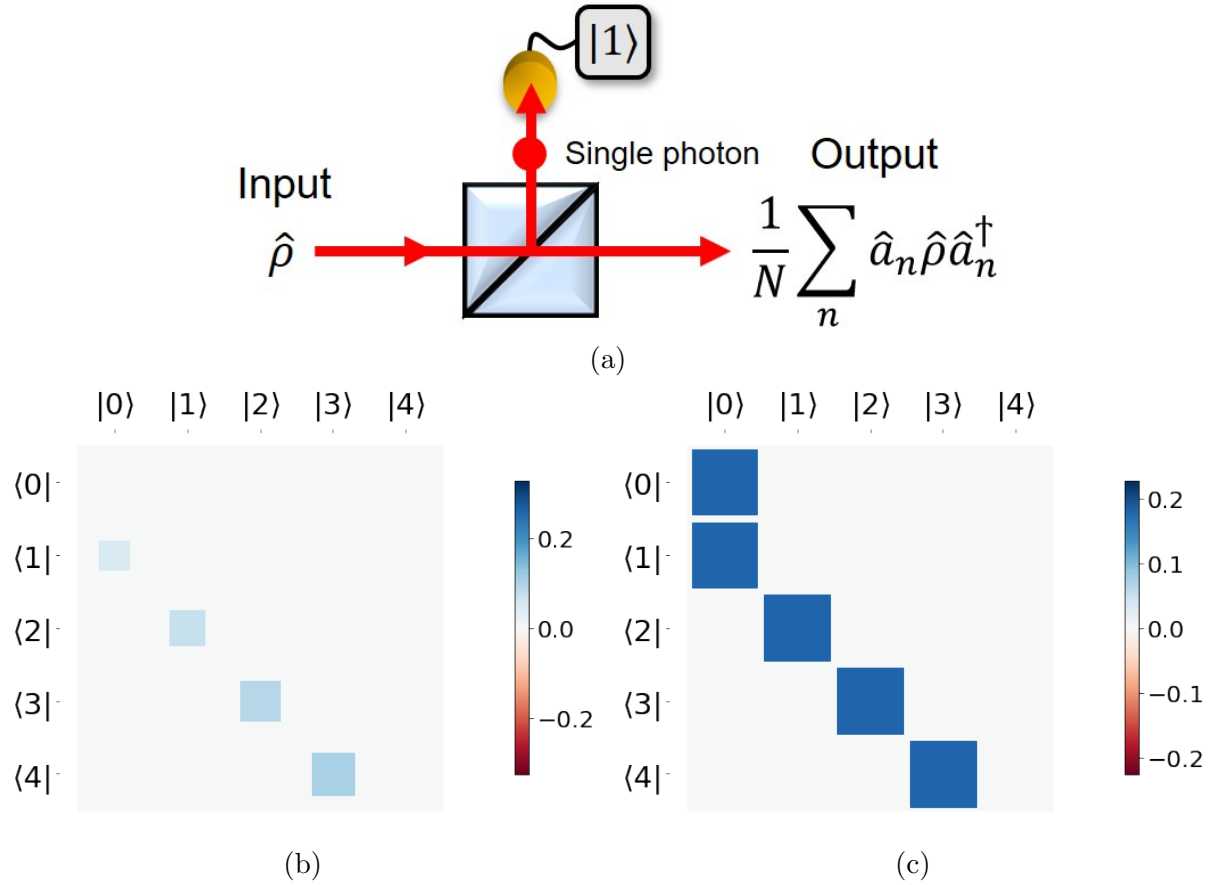

Figure 2.1: (a) The mechanism of heralded single photon subtraction with a beamsplitter. The detection of a single photon by the photo-detector in the reflected mode heralds a single photon subtraction in the transmitting mode. (b) The Hinton diagram of the annihilation operator. (c) The Hinton diagram of the deterministic subtraction operator. The coefficients of $|n-1\rangle\langle n|$ in the annihilation operator scale as $\sqrt{n}$, whereas it is independent of n for the deterministic subtraction operator.

where $\hat{a}_n$ is the annihilation operator of mode n (in a more generalized scenario it could also be a linear combination of the annihilation operators of the different modes with individual weights [23]), $\hat{\rho}$ is the input state, and N is the total number of modes. For a single mode input, the output is simply $\hat{a}\hat{\rho}\hat{a}^\dagger$. However, this kind of non-deterministic/ probabilistic single photon subtraction has a disadvantage because of its low success rates. The low success probability can be attributed to the probabilities associated with the subtraction of greater than one photon. Even for a weak optical input, there are non-zero probabilities

that greater than one photon will be subtracted. Also, in this type of heralded single photon subtraction mechanism, the probability of successful subtraction is dependent upon the intensity of the input optical signal, as $\hat{a} = \sum_n \sqrt{n} \left|n-1\right\rangle \left\langle n\right|$. Thus, more photons will be subtracted if the input light field has more photons. Also, this type of photon subtraction is highly incoherent leading to a mixed state of purity of $1/N$ [23]. Apart from using low-reflectance beamsplitters, single photon subtraction has also been demonstrated by heralding measurement of the output of a non-linear optical process [23, 25]. In Ref. [23], the input beam was incident on a $\chi^{(2)}$ BiBO crystal along with a strong gate beam to create an up-converted photon by sum frequency generation as shown in Fig. 2.2a. The detection of the up-converted photon heralds photon subtraction from the input. Even though it can provide superior mode selectivity over using a simple beamsplitter, it is still a non-deterministic process.

However, unlike the probabilistic photon subtraction mechanism discussed above, an ideal deterministic photon subtraction operator should be $\hat{S} = \left|0\right\rangle \left\langle 0\right| + \sum_n \left|n-1\right\rangle \left\langle n\right|$, where the probability of subtraction is independent of the input number state. The Hinton diagrams of the operators are shown in Figs. 2.1b, and 2.1c. The size and the colour of the matrix elements are proportional to the value. Unlike, the annihilation operator, the deterministic subtraction operator has identical coefficients for the $\left|n-1\right\rangle \left\langle n\right|$ matrix elements, and is independent of n.

In 2011, Honer *et al.* in their seminal work proposed deterministic single photon subtraction using Rydberg blockade phenomenon as shown in Fig. 2.2c [26]. A strong laser of Rabi frequency Ω_c couples the excited Rydberg state with a very high principal quantum number $\left|e\right\rangle_i$ to an intermediary state $\left|p\right\rangle_i$ such that detuning $\Delta_c \gg \Omega_c$. The $\left|g\right\rangle_i \leftrightarrow \left|p\right\rangle_i$ atomic transition is driven by a probe field of frequency Ω_p. When an atom absorbs a photon and ends up in the excited Rydberg state, the rest of the atoms within the Rydberg blockade radius r_B experience a shift in their electronic levels due to strong interaction with the excited atom. Thus, the subtracted photon resides as a coherent superposition of a single excitation in atoms within the Rydberg blockade radius. The ensemble has the following two bright states: the ground state $\left|G\right\rangle = \left|g_1, g_2, \ldots, g_N\right\rangle$ and the excited state $\left|E\right\rangle = \left(1/\sqrt{N}\right) \sum_i \left|g_1, \ldots, e_i, \ldots, g_N\right\rangle$ for N atoms in the blockade radius. The collective Rabi frequency for the $\left|G\right\rangle \leftrightarrow \left|E\right\rangle$ transition is $\Omega = \sqrt{N}\frac{\Omega_c \Omega_p}{4\Delta_c}$. The ensemble superatom also has $N-1$ dark states given by $\left|D_i\right\rangle$. Inhomogenous dephasing couples the excited state to the dark states. As a result, the single photon excitation inhabits within the N levels of the superatom. Once a single photon has been extracted from the probe, the ensemble becomes transparent for subsequent photons. Using a Rydberg atom ensemble has certain advantages. It results in greater coupling, which translates to a higher co-operativity, since the coupling strength scales as $\sqrt{N}$. Moreover, the fidelity of a successful subtraction using

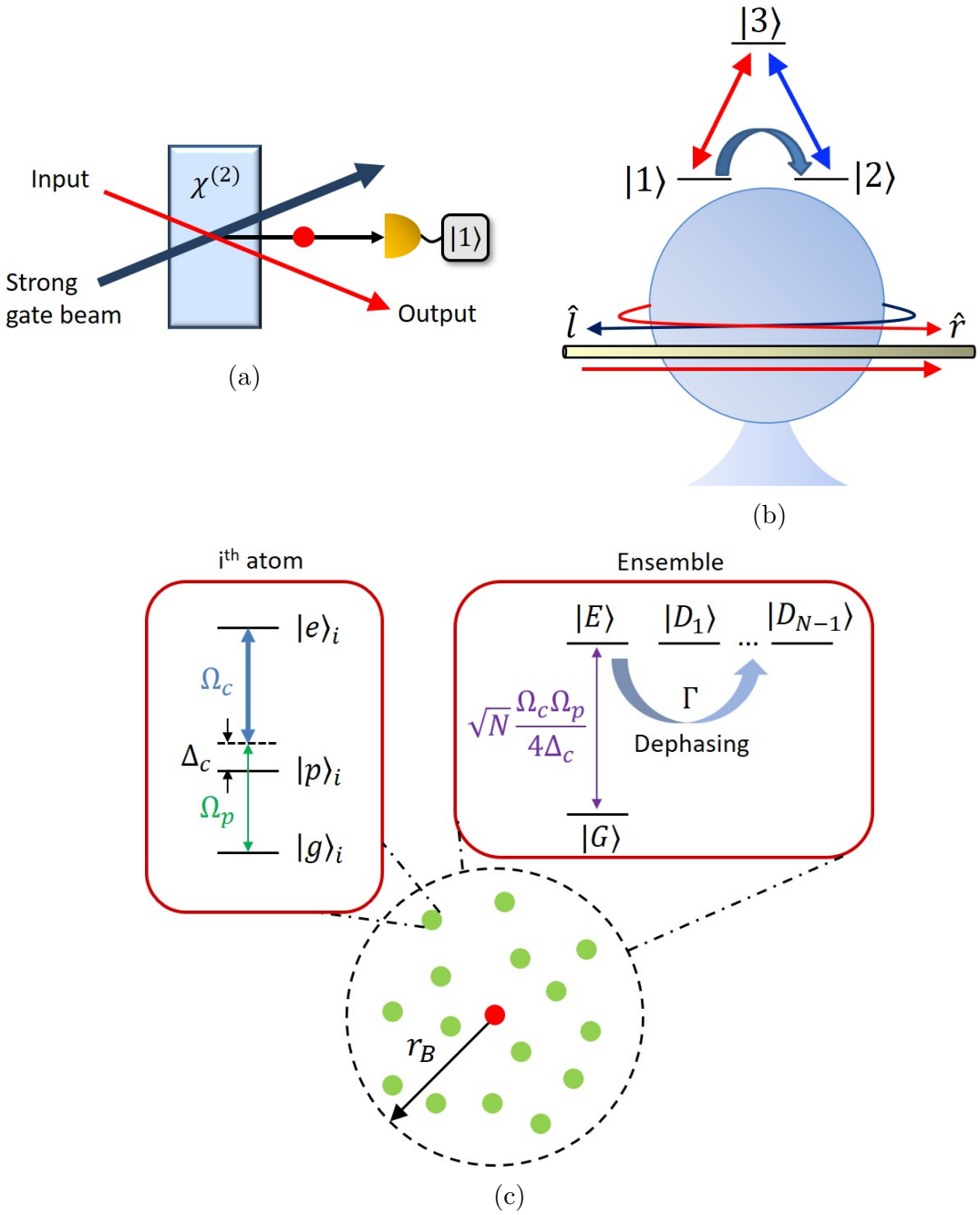

Figure 2.2: (a) Single photon subtraction via sum-frequency generation using a $\chi^{(2)}$ non-linear crystal [23]. The input signal interacts with a strong gate beam in the non-linear material. The detection of a single up-converted photon heralds a single photon subtraction in the input. (b) Single photon subtraction based upon single photon Raman interaction using a three-level quantum emitter coupled to opposite directions in a waveguide via a micro-resonator of high quality factor [27]. At the end of the subtraction process, the emitter has switched from $|1\rangle \rightarrow |2\rangle$, and becomes transparent to the incident field. (c) Single photon subtraction using an ensemble of Rydberg atoms as proposed by [26]. The single subtracted photon resides as a coherent superposition of a single excitation in atoms within the Rydberg blockade radius r_B.

the Rydberg atoms scales as $N/(N+1)$. Later, in 2016, Tresp *et al.* implemented single photon subtraction using a Rydberg ensemble of ^{87}Rb atoms [28].

Later in 2015, Rosenblum *et al.* experimentally extracted a single photon from an optical pulse using a single laser cooled ^{87}Rb atom, with a three-level Λ energy scheme, coupled with a micro-resonator with a high quality factor as shown in Fig. 2.2b [27]. Exploiting the single photon Raman interaction or SPRINT mechanism [29–31], they successfully subtracted a single photon from the red mode travelling to the right, and transferred it to the blue mode going to the left with pretty high efficiency. Unlike using a beamsplitter or a non-linear crystal, Rydberg blockade and SPRINT are self-terminating processes, i.e., the medium becomes transparent to the input signal after a photon has been subtracted. So, it is not possible to subtract more than a single photon. In subsequent sections, we shall discuss how such a SPRINT based photon subtraction works in detail.

Though it is possible to subtract single photons using cold atomic systems, the main obstacle in these technologies lie in the cumbersome nature of the physical system, and difficulties associated with loading and efficient coupling between these laser cooled atoms with the mode of the waveguide. On the contrary, solid-state emitters offer the promise of an on-chip platform, and can be a viable candidate for miniaturized quantum technologies [32]. Some of the solid state emitter platforms that can be considered for such applications are nitrogen-vacancy (NV) [33], or silicon-vacancy (SiV) centers in diamonds [34], defect centers in silicon carbide (SiC) [35], zinc oxide (ZnO) [36], rare-earth ion impurities in yttrium aluminium garnet (YAG) [37], and yttrium orthosilicate (YOS) crystals [32, 37]. Other potential lower dimension solid state emitters and platforms are defects in 2D hexagonal boron nitrides (hBN) [38], 1D carbon nanotubes (CNT) [39], and 0D quantum dots (QD) [32, 40]. In particular, QDs coupled with photonic crystal waveguides (PCWs) are a very promising platform since a very small mode volume, and low group velocity is achievable with PCWs, which lead to high coupling efficiencies.

In this chapter, we investigate deterministic single photon subtraction using SPRINT in a three-level quantum emitter coupled to a bi-modal cavity. Similar to Ref. [27, 41], our proposal relies on the SPRINT mechanism [29–31]. We discuss the temporal dynamics of the SPRINT mechanism inside the cavity for different types of optical input. First, we look at the case of single photon subtraction from a continuous-wave (CW) coherent input by driving the system using a coherent CW source. Second, we shall study what happens if a coherent state with a specified mean photon number is injected into the cavity, and the system is left to evolve. Third, we shall also study the dynamics of the photon subtraction process with an input Fock state. Finally, we investigate the second order auto-correlation function of the photon-subtracted mode to look for signatures of non-classical light.

I will like to thank Dr. Jinjin Du, and Prof. Michal Bajcsy for helpful discussions

regarding the work reported in this chapter. All the Python programs used for simulations in this chapter are available in Appendix C.

2.2 A quantum emitter in a cavity

2.2.1 A quantum emitter coupled with a single cavity mode

The proposed system for deterministic single photon subtraction consists of a single three-level Λ-type quantum emitter coupled with a bi-modal cavity. But before diving into that, first we look at the interaction of a two-level system coupled with a cavity mode as shown in Fig. 2.3. Solving the Maxwell's wave equations under the boundary conditions set by the geometry of the cavity gives rise to a discrete spectrum of field solutions called modes characterized by its wavevector $\mathbf{k}$. Each mode is associated with a certain spacio-temporal distribution of electric and magnetic fields in the cavity, much like the standing waves in a string held at both ends. Mathematically, the mode of the electromagnetic field is a vector field $\mathbf{f_k}(\mathbf{r}, t)$, which is a normalized solution of the Maxwell's equations and satisfies the following relationships [42]:

$$\left(\nabla^2 - \frac{1}{c^2}\frac{\partial^2}{\partial t^2}\right)\mathbf{f_k}(\mathbf{r}, t) = 0, \tag{2.1a}$$

$$\nabla \cdot \mathbf{f_k}(\mathbf{r}, t) = 0, \tag{2.1b}$$

$$\frac{1}{V}\iiint_V |\mathbf{f_k}(\mathbf{r}, t)|^2 d^3r = 1. \tag{2.1c}$$

Here V is a fairly large volume where the system is confined, and the fields are normalized over. One can construct an orthonormal mode basis $\{\mathbf{f_{k_1}}(\mathbf{r}, t), \mathbf{f_{k_2}}(\mathbf{r}, t), \ldots, \mathbf{f_{k_N}}(\mathbf{r}, t)\}$, such that all solutions of the Maxwell's equations can be expressed as a linear superposition in that basis. The positive frequency component of the complex electric field could be expressed as $\mathbf{E}^{(+)}(\mathbf{r}, t) = \sum_{\mathbf{k}_i} \mathcal{E}_i \mathbf{f_{k_i}}(\mathbf{r}, t)$. The field has a discrete spectrum owing to confining it in a finite volume V. Also, the modes satisfy the orthogonality condition

$$\frac{1}{V}\iiint_V \mathbf{f}^*_{\mathbf{k}_i}(\mathbf{r}, t)\mathbf{f}_{\mathbf{k}_j}(\mathbf{r}, t) d^3r = \delta_{ij}. \tag{2.2}$$

For simplicity, let us consider that the two-level atom interact with only one cavity mode. We can make this assumption if the atom is on resonance or close to resonance with

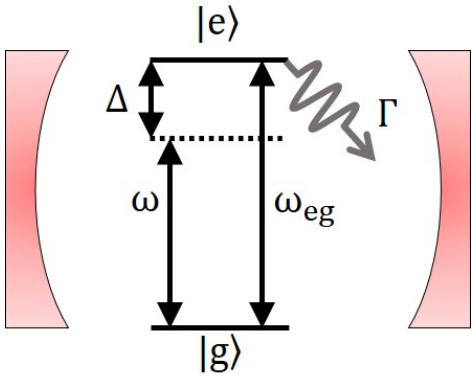

Figure 2.3: A two-level emitter interacting with the field inside a cavity with a single mode. The frequency of the cavity mode is ω, whereas the transition frequency is ω_{eg}. The frequency detuning is given by $\Delta = \omega - \omega_{eg}$.

the fundamental cavity mode frequency. The ground state $|g\rangle$ and the excited state $|e\rangle$ have a transition frequency ω_{eg}, whereas ω is the resonance frequency of the cavity mode under consideration (see Fig. 2.3). The detuning of the cavity mode from the atomic transition is given by $\Delta = \omega - \omega_{eg}$.

The total Hamiltonian of the system, H, is the sum of the atomic Hamiltonian H_A, the Hamiltonian of the cavity field mode H_F, and the interaction Hamiltonian H_{AF}. It is given by $H = H_A + H_F + H_{AF}$ where

$$H_A = \hbar\omega_{eg}\sigma^\dagger\sigma, \tag{2.3a}$$

$$H_F = \hbar\omega a^\dagger a \tag{2.3b}$$

$$H_{AF} = \hbar g(\sigma a^\dagger + \sigma^\dagger a). \tag{2.3c}$$

In these equations, $\sigma = |g\rangle\langle e|$ is the atomic lowering operator, a is the annihilation operator of the cavity mode, and g is the coupling constant giving the strength of interaction between

the cavity modes and the emitter given by

$$g = -\hat{e} \cdot \mathbf{d}_{ge} \sqrt{\frac{\omega}{2\hbar\epsilon_0 V_m}}. \tag{2.4}$$

Here, $\hat{e}$ is the unit polarization vector of the cavity mode at the position of the two-level emitter, $\mathbf{d}_{ge} = \langle g| \mathbf{d} |e\rangle$ is a dipole matrix element of the emitter with dipole operator $\mathbf{d}$, and V_m is the mode volume. This is the well-known Jaynes-Cummings Hamiltonian for an atom interacting with a single cavity mode near resonance under rotating wave approximation. It also assumes the dipole approximation can be used, i.e., the atom is considered to be much smaller than the wavelength.

The total quantum state of the system is expressed as $|\psi_A, \psi_F\rangle$, where ψ_A is the atomic state and ψ_F is the cavity field state. To solve this system, we can use the ansatz wavefunction

$$|\psi(t)\rangle = \sum_{n=0}^{\infty} \left(c_{g,n}(t) |g, n\rangle + c_{e,n}(t) |e, n\rangle \right), \tag{2.5}$$

where $|g(e), n\rangle$ means that the atom is in state $|g\rangle$ ($|e\rangle$), and there are n photons in the cavity. Plugging the ansatz in the Schrödinger's equation

$$\frac{\mathrm{d}}{\mathrm{d}t} |\psi(t)\rangle = -\frac{i}{\hbar} H |\psi(t)\rangle, \tag{2.6}$$

gives us the coupled differential equations

$$\dot{c}_{g,n+1}(t) = -i(n+1)\omega c_{g,n+1}(t) - ig\sqrt{n+1} c_{e,n}(t), \tag{2.7a}$$

$$\dot{c}_{e,n}(t) = -ig\sqrt{n+1} c_{g,n+1}(t) - i(\omega_{eg} + n\omega) c_{e,n}(t). \tag{2.7b}$$

For initial conditions defined by $c_{g,n+1}(0) = 1$, i.e., the atom is in the ground state and there are $n+1$ photons in the cavity, at resonance (i.e. $\Delta = 0$), we get the following solution

$$c_{g,n+1}(t) = \cos\left(g\sqrt{n+1}t\right), \tag{2.8a}$$

$$c_{e,n}(t) = -i \sin\left(g\sqrt{n+1}t\right). \tag{2.8b}$$

The population in the two states oscillate as

$$P_{g,n+1}(t) = |c_{g,n+1}(t)|^2 = \frac{1}{2}\left[1 + \cos\left(2g\sqrt{n+1}t\right)\right], \tag{2.9a}$$

$$P_{e,n}(t) = |c_{e,n}(t)|^2 = \frac{1}{2}\left[1 - \cos\left(2g\sqrt{n+1}t\right)\right]. \tag{2.9b}$$

Thus, the system oscillates between the states $|g, n+1\rangle$ and $|e, n\rangle$ with a Rabi oscillation frequency of $2g\sqrt{n+1}$.

2.2.2 Introducing dissipation

Now, we can introduce dissipation in the system. We consider the spontaneous emission rate Γ, and the cavity decay rate κ. Then, for the density matrix ρ, we can write down the Liouville-von Neumann equation of motion as

$$\frac{\mathrm{d}\rho(t)}{\mathrm{d}t} = -\frac{i}{\hbar}\left[H, \rho(t)\right] + \Gamma\mathcal{L}[\sigma]\rho(t) + \kappa\mathcal{L}[a]\rho(t), \tag{2.10}$$

where the Lindblad superoperator acting on the density matrix takes care of the dissipation, and is explicitly defined as

$$\mathcal{L}[o]\rho(t) = o\rho(t)o^\dagger - \frac{1}{2}\left[\rho(t)o^\dagger o + o^\dagger o\rho(t)\right], \tag{2.11}$$

for operator o coupling the system with the environmental bath modes. Now, one can introduce the following two collapse operators $C_1 = \sqrt{\Gamma}\sigma$, and $C_2 = \sqrt{\kappa}a$. That allows us to write the master equation as

$$\frac{\mathrm{d}\rho(t)}{\mathrm{d}t} = -\frac{i}{\hbar}\left[H, \rho(t)\right] + \sum_k \frac{1}{2}\left[2C_k\rho(t)C_k^\dagger - \rho(t)C_k^\dagger C_k - C_k^\dagger C_k\rho(t)\right] \tag{2.12}$$

This can be re-arranged in the following fashion:

$$\frac{\mathrm{d}\rho(t)}{\mathrm{d}t} = -\frac{i}{\hbar}\left[H_{\text{eff}}\rho(t) - \rho(t)H_{\text{eff}}^\dagger\right] + \sum_k C_k\rho(t)C_k^\dagger, \tag{2.13}$$

where the effective non-Hermitian Hamiltonian is given by

$$H_{\text{eff}} = H - \frac{i\hbar}{2}\sum_k C_k^\dagger C_k. \tag{2.14}$$

It must be noted that the effective Hamiltonian is non-Hermitian, and has imaginary eigenvalues. One can use this Hamiltonian to solve quantum trajectories satisfying the non-unitary Schrödinger's equation [43]

$$\frac{\mathrm{d}}{\mathrm{d}t}\left|\psi(t)\right\rangle = -\frac{i}{\hbar}H_{\text{eff}}\left|\psi(t)\right\rangle. \tag{2.15}$$

We will be solving the open quantum system master equations numerically in Python using QuTiP [44, 45]. One can use the vanilla Lindblad master equation solver (*mesolve*) in QuTiP for simple simulations. For an N-dimensional Hilbert space, the master equation evolves density matrix of size $N\times N$, with N^2 terms. This can be computationally expensive for large values of N. However, the stochastic quantum Monte Carlo solver (*mesolve*) can be useful for simulations in such situations, i.e., when N is large. The following digression gives a brief look into the inner mechanisms of the quantum Monte Carlo method.

Quantum Monte Carlo simulations

In the Monte Carlo algorithm, we use the non-Hermitian Hamiltonian in Eq. 2.14 to evolve the wavefunction which is an N-dimensional vector instead of an $N\times N$ matrix. This helps in reducing the computational complexity of solving the transient response of the quantum system. For a sufficiently small time interval Δt, the wavefunction at time $t+\Delta t$ can be calculated from the wavefunction at time t using the relationship

$$\left|\psi'(t+\Delta t)\right\rangle = e^{-iH_{\text{eff}}\Delta t/\hbar}\left|\psi(t)\right\rangle \approx \left(1 - \frac{iH_{\text{eff}}\Delta t}{\hbar}\right)\left|\psi(t)\right\rangle. \tag{2.16}$$

The new wavefunction is not normalized because of the action of the non-Hermitian Hamiltonian. Thus, we get

$$\begin{aligned}\langle\psi'(t+\Delta t)|\psi'(t+\Delta t)\rangle &= 1-\Delta t\frac{i}{\hbar}\langle\psi(t)|\, H_{\text{eff}}-H_{\text{eff}}^{\dagger}\,|\psi(t)\rangle\\ &= 1-\Delta t\sum_k \langle\psi(t)|\, C_k^{\dagger}C_k\,|\psi(t)\rangle\\ &= 1-\sum_k p_k\\ &= 1-p. \end{aligned} \tag{2.17}$$

The time should be discretized such that, $p \ll 1$. Thus, $1-p$ is the probability amplitude of the state $\psi'(t+\Delta t)$ at time $t+\Delta t$. This means, the probability of a quantum jump happening in the time range $(t+\Delta t]$ is p.

Now, we pick a random number r uniformly distributed within the range $[0,1]$. If the random number is greater than p, i.e., for $r > p$, no quantum jump takes place, and we set the new normalized wavefunction at time $t+\Delta t$ as

$$|\psi(t+\Delta t)\rangle\Big|_{\text{No jump}} = \frac{|\psi'(t+\Delta t)\rangle}{\sqrt{1-p}}. \tag{2.18}$$

Most of the time $r > p$, as $p \ll 1$. However, when $p > r$, a quantum jump takes place. The quantum state collapses to the wavefunction

$$|\psi(t+\Delta t)\rangle\Big|_{\text{Jump } C_k} = \frac{C_k\,|\psi(t)\rangle}{\sqrt{\langle\psi(t)|\, C_k^{\dagger}C_k\,|\psi(t)\rangle}} = \frac{C_k\,|\psi(t)\rangle}{\sqrt{p_k/\Delta t}} \tag{2.19}$$

with probability p_k/p, where $p_k = \Delta t\,\langle\psi(t)|\, C_k^{\dagger}C_k\,|\psi(t)\rangle$. Using the new normalized state at $t+\Delta t$, we calculate the state at $t+2\Delta t$ using the same procedure. We continue this process until the end of the simulation time. This stochastic process of simulation is repeated multiple times, each giving a slightly different 'trajectory' of the quantum state in the Hilbert space. Finally, the state of the quantum system at any time τ is the result of the average of all the simulated quantum trajectories.

Thus, the average density matrix at time $t+\Delta t$ is given by [46]

$$\overline{\rho(t+\Delta t)} = (1-p)\frac{|\psi'(t+\Delta t)\rangle}{\sqrt{1-p}}\frac{\langle\psi'(t+\Delta t)|}{\sqrt{1-p}} + p\sum_k \frac{p_k}{p}\frac{C_k\,|\psi(t)\rangle}{\sqrt{p_k/\Delta t}}\frac{C_k\,\langle\psi(t)|}{\sqrt{p_k/\Delta t}}. \tag{2.20}$$

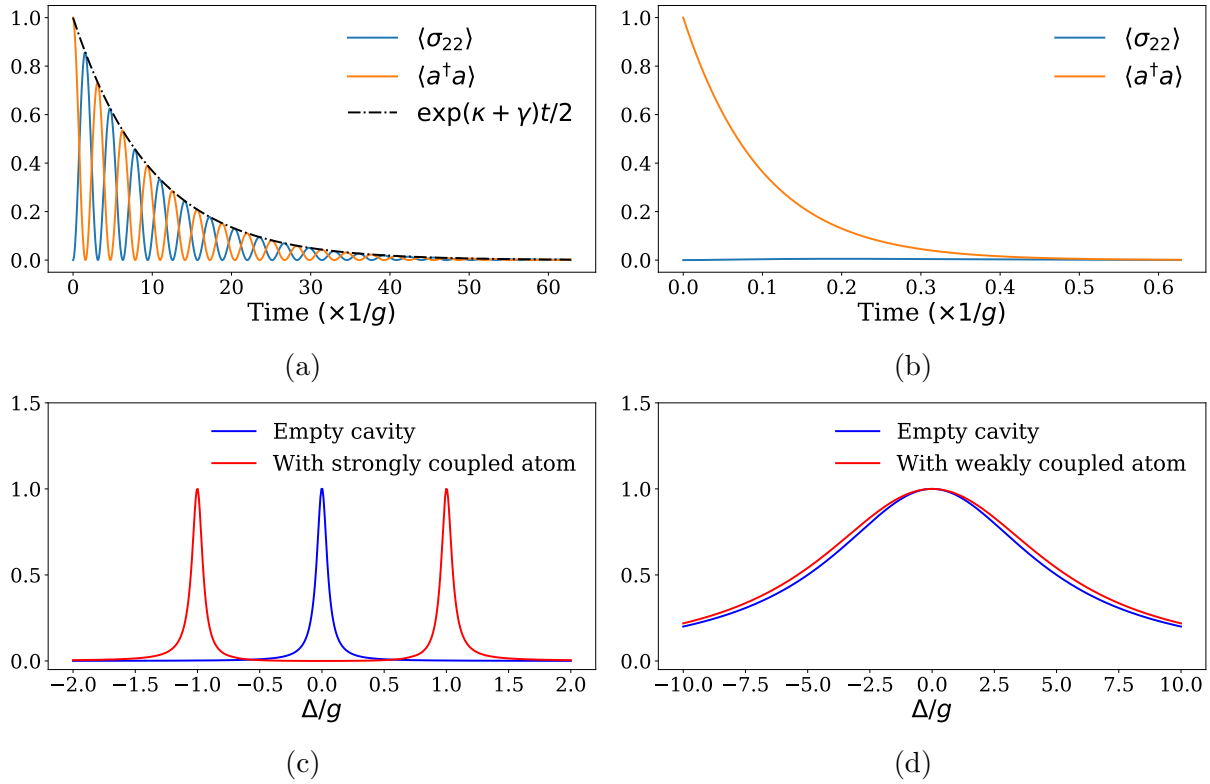

Figure 2.4: Transient response and transmission of a two-level emitter coupled with a cavity in the (a, c) strong coupling regime with $\Gamma = \kappa = g/10$, and (b, d) weak coupling regime with $\Gamma = \kappa = 10g$. In both the scenarios, the coupling strength is $g = 2\pi \times 10$ GHz.

Doing some algebra, we arrive at the following relationship:

$$\overline{\rho(t + \Delta t)} = \rho(t) - \frac{i\Delta t}{\hbar}[H, \rho(t)] + \Delta t \Gamma \mathcal{L}[\sigma]\rho(t) + \Delta t \kappa \mathcal{L}[a]\rho(t), \tag{2.21}$$

which gives the master equation

$$\frac{\mathrm{d}\overline{\rho(t)}}{\mathrm{d}t} = -\frac{i}{\hbar}[H, \rho(t)] + \Gamma \mathcal{L}[\sigma]\rho(t) + \kappa \mathcal{L}[a]\rho(t). \tag{2.22}$$

This shows, that for a large number of trajectories, the Monte Carlo simulation is equivalent to solving the master equation. Moreover, it is computationally favourable for simulating quantum systems with a large Hilbert space. Thus, we shall be using QuTiP's master

equation solver or the Monte Carlo solver while simulating the systems in this chapter based upon computational power required.

We numerically solve the dynamics of the interaction between the two-level emitter and the single cavity mode in QuTiP for two different cavity regimes as shown in Fig. 2.4. First, we consider the strong coupling regime with the coupling strength $g = 2\pi \times 10$ GHz, and the dissipation rates are $\Gamma = \kappa = g/10$. In this case, we can see the damped Rabi oscillations, before the excitation is lost to the radiative bath modes. Next, we also look at the system dynamics for $\Gamma = \kappa = 10g$ in the weak coupling regime. Here, the atom and the mode is very feebly coupled and the Rabi oscillations are no longer visible. The cavity mode simply decays exponentially.

Next, we drive the cavity with a weak coherent drive given by the Hamiltonian $H_{in} = \Omega_d \left(ae^{-i\omega_d t} + r^\dagger e^{i\omega_d t}\right)$ where $\Omega_d = 0.01g$. The drive must be weak, so that we can truncate the Hilbert space at only one excitation or the first manifold. For $g >> \kappa/2$ in the strong coupling regime (see Fig. 2.4c), we observe that the transmission spectrum splits by $2g$, because of the creation of dressed states. Using a stronger drive would create additional peaks corresponding to dressed states in the higher manifolds. However, in the weak coupling regime, no splitting is observed, and the transmission peaks at resonance. However, the transmission peak with the weakly coupled atom is slightly wider compared to the completely empty cavity due to the inclusion of a new channel in the system, through the spontaneous emission rate of the emitter.

2.3 Photon subtraction in a bi-modal cavity

The proposed system for deterministic single photon subtraction consists of a single three-level Λ-type quantum emitter, initialized in the ground state $|1\rangle$, which is coupled to a bi-modal cavity as shown in Fig. 2.5. In the ideal case, the red mode with the annihilation operator r has right-hand circularly polarized (RHCP) photons, while the blue mode with the annihilation operator l has left-hand circularly polarized (LHCP) photons. Each of the two transitions of the emitter is coupled to one of the cavity modes. Specifically, the emitter is coupled to the bi-modal cavity such that, $|1\rangle \rightarrow |3\rangle$ transition requires an RHCP photon and $|2\rangle \rightarrow |3\rangle$ transition requires an LHCP photon. The basic principle behind the SPRINT mechanism can be described as follows. When photons in the red cavity interact with the Λ-type emitter, the emitter gets excited to $|3\rangle$. When the incoming light has a greater pulsewidth compared to the decay time of $|3\rangle$, there cannot be subsequent emission from the $|3\rangle \rightarrow |1\rangle$ transition, because of the destructive interference of subsequent re-emission with the incoming field [27]. Thus, the emitter can only de-excite via the $|3\rangle \rightarrow |2\rangle$

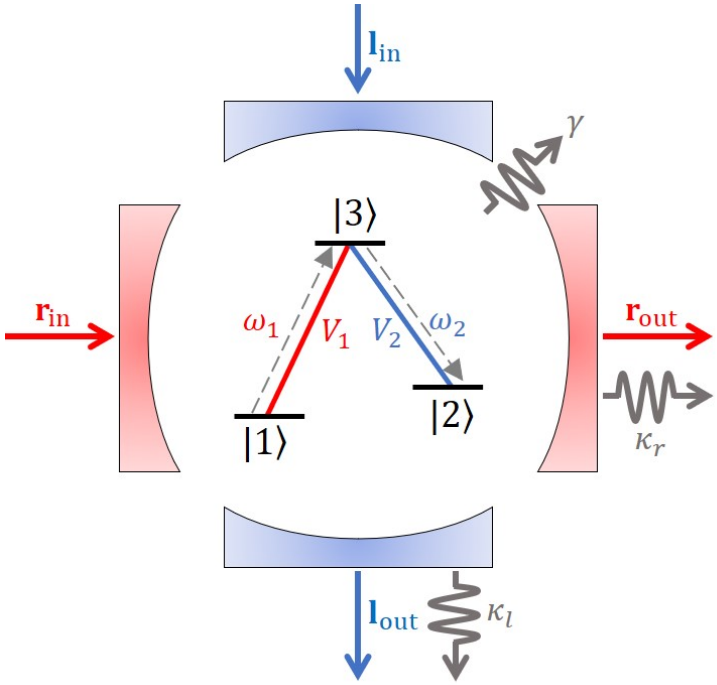

Figure 2.5: The schematic of a three-level quantum emitter coupled with a bi-modal cavity.

transition, thereby emitting a single photon into the blue l mode. Once in state $|2\rangle$, the emitter stops interacting with the red r mode.

We can use three different approaches to study the atom-light interaction in the cavity. First, we can use a classical drive to get photons into the cavity mode. This is a quasi-semi-classical approach, in the sense that we do not track the state of the classical driving field. We follow only the states in the cavity mode, and the state of the three-level emitter. This is similar to the semi-classical model of light-matter interactions that describe Rabi oscillations, where we only follow the state of the quantum emitter, and not the classical field. This approach leads to a coherent state of the field in the cavity in the steady-state limit. Experimentally, this corresponds to shining a laser beam onto the cavity.

Secondly, we can initialize the cavity to a particular state of the field, and then let it evolve. In this chapter, we shall see the dynamics of the system when the cavity is initialized with a coherent state, and a Fock state. This is similar to introducing a coherent or Fock state pulse into the cavity.

Third, one can use a feeder cavity or a waveguide to introduce the optical signal into the bi-modal cavity as in Ref. [41]. This approach allows us to track the state of the input

field, and control the interaction properties of the external input field and the system. We will briefly discuss how we can model the feeder cavity system. However, we shall only be exploring the first two cases in details in this thesis.

2.4 Continuous-wave coherent drive input

First, we will consider subtracting a single photon from an incoming continuous-wave (CW) coherent state. Let us consider we have a three-level Λ-type quantum emitter, initialized in its ground state $|1\rangle$, in a bi-modal cavity as shown in Fig. 2.5. A CW coherent laser beam is sent as an input to the red mode with the mode operator r. This mode interacts with the $|1\rangle \leftrightarrow |3\rangle$ atomic transition, and their coupling strength is given by g_1. The Hamiltonian of the system is given by

$$H = H_0 + H_{int} + H_{in} \tag{2.23}$$

such that

$$H_0/\hbar = \omega_r r^\dagger r + \omega_l l^\dagger l + \omega_1 \sigma_{33} + (\omega_1 - \omega_2)\sigma_{22}, \tag{2.24a}$$

$$H_{int}/\hbar = g_1(r\sigma_{31} + r^\dagger \sigma_{13}) + g_2(l\sigma_{32} + l^\dagger \sigma_{23}), \tag{2.24b}$$

$$H_{in}/\hbar = \Omega_d(re^{-i\omega_d t} + r^\dagger e^{i\omega_d t}), \tag{2.24c}$$

In these equations, ω_r (ω_l) is the frequency of the $|1\rangle \leftrightarrow |3\rangle$ ($|2\rangle \leftrightarrow |3\rangle$) atomic transition, g_1 (g_2) is the coupling strength of the $|1\rangle \leftrightarrow |3\rangle$ ($|2\rangle \leftrightarrow |3\rangle$) transition with the r (l) mode, ω_d is the frequency of the input coherent drive, and Ω_d is the drive strength. The CW coherent laser drive strength is given by $\Omega_d = \sqrt{\kappa_r P/\hbar\omega_d}$, where P is the power of the input laser beam.

To eliminate the time harmonic components in the coherent drive field, we go to a frame rotating with the frequency ω_d using the unitary transformation given by

$$U = \exp\left[-it\omega_d\left(r^\dagger r + l^\dagger l + \sigma_{33}\right)\right]. \tag{2.25}$$

The Hamiltonian in the rotating frame is given by

$$H_{rot} = U^{\dagger} H U + i \frac{\partial U^{\dagger}}{\partial t} U. \tag{2.26}$$

In the rotating frame, the Hermitian Hamiltonian gets modified to

$$\tilde{H}_0/\hbar = (\omega_r - \omega_d) r^{\dagger} r + (\omega_l - \omega_d) l^{\dagger} l + (\omega_1 - \omega_d)\sigma_{33} + (\omega_1 - \omega_2)\sigma_{22}, \tag{2.27a}$$

$$\tilde{H}_{int}/\hbar = g_1(r\sigma_{31} + r^{\dagger}\sigma_{13}) + g_2(l\sigma_{32} + l^{\dagger}\sigma_{23}), \tag{2.27b}$$

$$\tilde{H}_{in}/\hbar = \Omega_d(r + r^{\dagger}). \tag{2.27c}$$

The non-Hermitian effective Hamiltonian of the system can be expressed as

$$\tilde{H}_{eff} = \tilde{H}_0 + \tilde{H}_{int} + \tilde{H}_{in} - \frac{i\hbar}{2} \sum_k C_k^{\dagger} C_k, \tag{2.28}$$

where,

$$C_1 = r_{out} = \sqrt{\kappa_r} r, \quad C_2 = l_{out} = \sqrt{\kappa_l} l, \tag{2.29a}$$

$$C_3 = \sqrt{\gamma_{coh}}\sigma_{33}, \quad C_4 = \sqrt{\gamma_1}\sigma_{13}, \quad C_5 = \sqrt{\gamma_2}\sigma_{23}. \tag{2.29b}$$

In these equations, C_k's are the different collapse operators corresponding to different quantum jumps, κ_r (κ_l) is the transmission loss of the red (blue) cavity corresponding to the mode r (l), γ_1 (γ_2) is the spontaneous emission rate from the $|3\rangle \rightarrow |1\rangle$ ($|3\rangle \rightarrow |2\rangle$) transition, and γ_{coh} is the pure coherence decay/ dephasing rate beyond the coherence decay rate resulting from spontaneous emission, such that the total coherence decay rate is given by $\gamma_{\perp} = \frac{\gamma_1}{2} + \frac{\gamma_2}{2} + \gamma_{coh}$. For simplicity, here we shall consider the co-operativity to be high. We ignore the collapse operators C_4 and C_5 corresponding to radiative spontaneous emission leading to population decay. Moreover, we also consider that the cavity is driven resonantly, i.e., $\omega_r = \omega_d$. First, we shall start with the simplest cases, and run a few diagnostics to check that the simulation model is working properly.

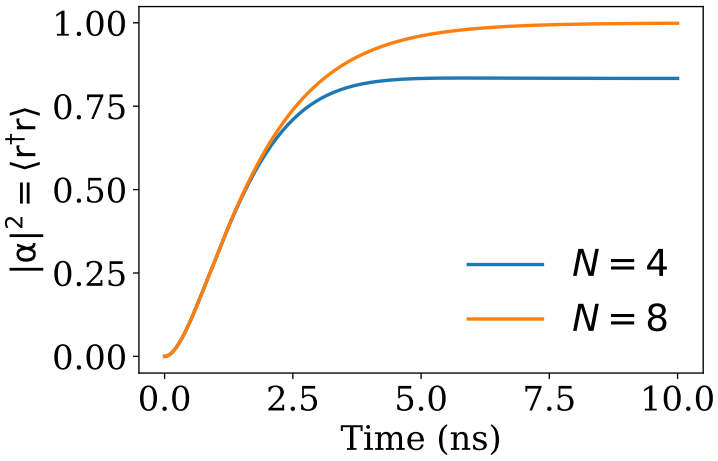

Figure 2.6: The time evolution of mean photon number in the cavity for Hilbert space of dimension $N = 4, 8$. For $N = 8$, the mean photon number in the cavity saturates at unity as expected. However, for $N = 4$, the saturation point is truncated to ~ 0.8.

I. Drive an empty cavity resonantly

If there is no atom in the cavity, and the cavity is driven resonantly, $H_0 = H_{int} = 0$. The equation of motion for the expectation value of any operator $\mathcal{O}$ is given by

$$\frac{\mathrm{d}\langle \mathcal{O} \rangle}{\mathrm{d}t} = \mathrm{Tr}\left[\mathcal{O}\frac{\mathrm{d}\rho}{\mathrm{d}t}\right]. \tag{2.30}$$

Using that, we can write down the equation of motion for the mode r as

$$\frac{\mathrm{d}\langle r \rangle}{\mathrm{d}t} = -i\Omega_d - \frac{\kappa_r}{2}\langle r \rangle. \tag{2.31}$$

The steady state solution of the differential equation gives

$$\alpha = \langle r\,(t \to \infty) \rangle = -\frac{2i\Omega_d}{\kappa_r}. \tag{2.32}$$

Thus, in steady state the average photon number in the cavity is $\bar{n} = \langle r^\dagger r \rangle = |\alpha|^2 = 4\Omega_d^2/\kappa_r^2$.

For our simulations, we set $\omega_d = \omega_r = 2\pi \times 200$ THz, $\kappa_r = 2\pi \times 0.25$ GHz, $P = 52$ pW. That gives $\bar{n} = 1$. The non-Hermitian master equation is solved in Python using

QuTiP, and the solution matches our expectations, as seen in Fig. 2.6. However, one has to be cautious about the size of the Hilbert space while solving the system of equations on QuTiP. The cavity mode has an infinitely large Hilbert space, unlike the two-level emitter. We can keep on populating higher number states with a stronger drive. However, for our simulations we need to truncate the Hilbert space to a low dimension to speed up our computation. But truncating the Hilbert space too aggressively produces incorrect results, since we start ignoring the higher order state occupations. For this simulation, a Hilbert space with dimension $N \geq 7$ gives the correct answer. However, using $N = 5$ truncates $\bar{n}$ to ~ 0.9. Fig. 2.6 shows the dependence of the time evolution of the mean number of photons in the cavity with size of Hilbert space (for $N = 4$, 8). The proper choice of N depends strongly on the driving strength, as that determines the probability of higher order excitation states, and hence the level at which the Hilbert space could be truncated.

II. Drive an empty cavity resonantly with $N = 2$

Now, for educational purposes, we set the size of the Hilbert space to $N = 2$. That makes the situation similar to externally driving a two-level system (TLS). Thus simulating the same system with $N = 2$ gives the dynamics of a driven dipole oscillator. We simulate the system for $\kappa_r = 0, 2\pi \times 25$ MHz corresponding to an undamped, and a moderately damped condition. The power is set to 13.25 nW, which corresponds to a strong drive in this scenario. We observe the system oscillating at it's 'Rabi frequency', just like an externally driven TLS oscillator. Fig. 2.7 shows the mean cavity photon number for $\kappa_r = 0$, $2\pi \times 25$ MHz.

III. Complete model

Now, finally we add a 3 level Λ-type atomic system in the cavity so that the two modes, r and l, can talk with each other via the emitter. The system is characterized by the parameters: $\omega_d = \omega_r = \omega_1 = 2\pi \times 200$ THz, $\omega_2 = \omega_l$, $\omega_r - \omega_l = 2\pi \times 0.5$ GHz, $g_1 = g_2 = 2\pi \times 10$ GHz, $\kappa_r = \kappa_l = \gamma_{coh} = 2\pi \times 0.25$ GHz, $\gamma_1 = \gamma_2 = 0$, $P = 52$ pW. This corresponds to a steady state mean photon number of unity in the r mode of the cavity. The coupling strength of $2\pi \times 10$ GHz was chosen according to reported values in the literature for quantum dots coupled with photonic crystal cavities [41, 47, 48]. Typically, the coupling strengths for such systems lie in the range $\sim 1 - 40$ GHz [41]. The coupling strength is directly related to the spatial confinement of the field in the cavity, and thus the mode volume. Here we considered $\gamma_1, \gamma_2 << g_1, g_2, \kappa_r, \kappa_l$, as in the case of a nano-cavity and set $\gamma_1 = \gamma_2 \approx 0$ for simplicity.

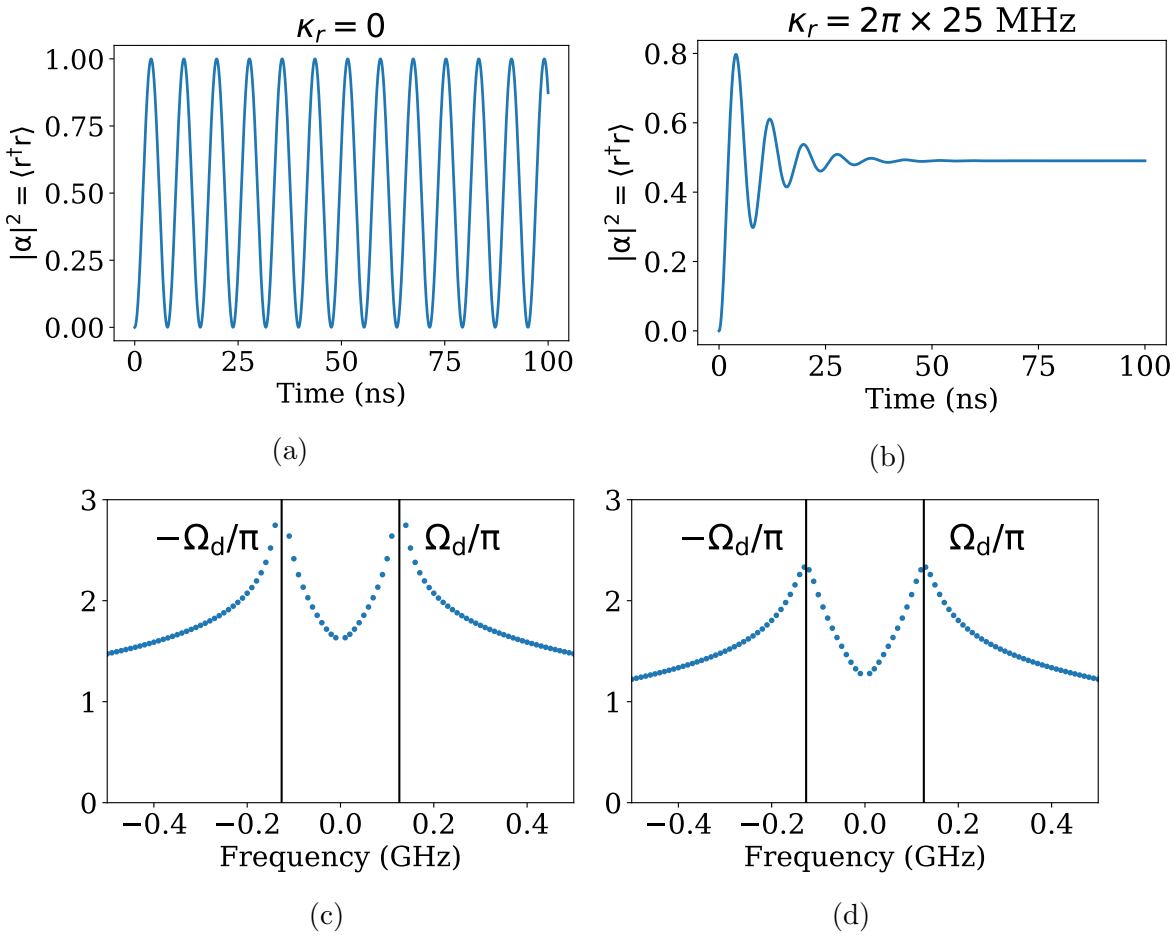

Figure 2.7: Plots of average photon number in r mode, i.e., $\langle r^\dagger r \rangle$ for κ_r = (a) 0, (b) $2\pi \times 25$ MHz. FFT of the oscillations in average photon number with κ_r = (c) 0, (d) $2\pi \times 25$ MHz. The frequency of oscillation is twice the drive strength Ω_d, reminiscent of the fact that the Rabi frequency is twice the coupling strength.

Fig. 2.8 shows the transient dynamics of the system, and the steady state in the r mode of the cavity. As expected, the atom which was initialized in $|1\rangle$, eventually ends up in $|2\rangle$, whereby the atom becomes transparent to the incoming laser. The state in the r mode of the cavity saturates to a coherent state with average photon number unity. Also, a single photon has been successfully extracted from the incoming drive field, and released into the left mode, as verified from the fact that the time integral of $\langle l_{out}^\dagger l_{out} \rangle$ saturates to unity. Accordingly, we can also define the probability of a single photon subtraction at

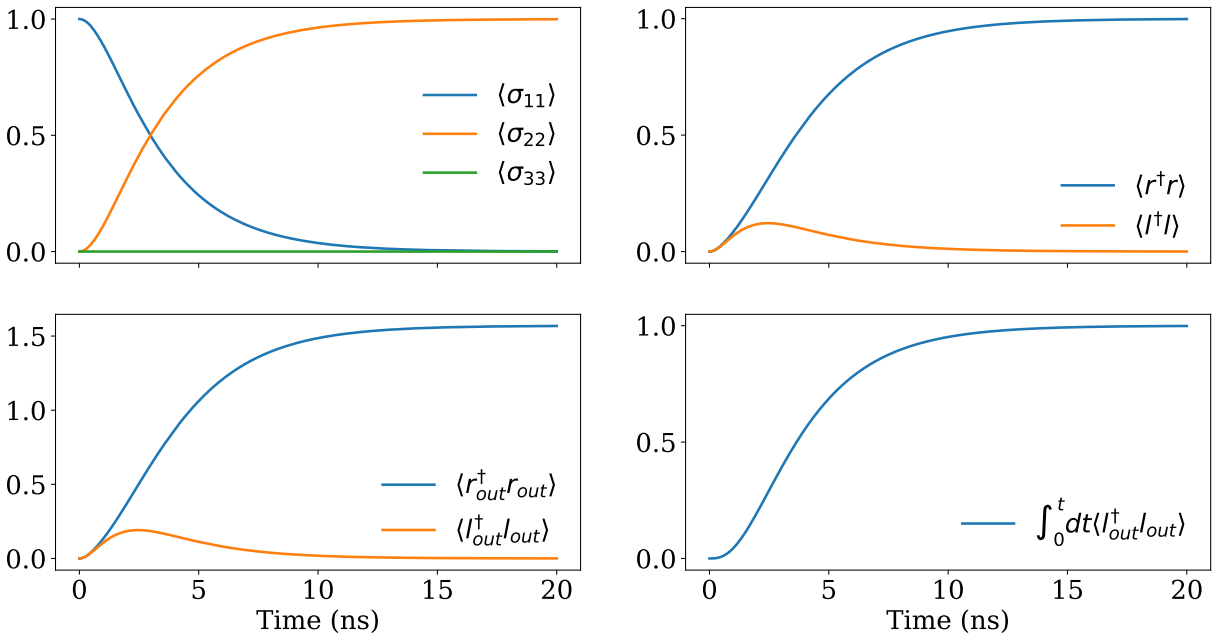

(a)

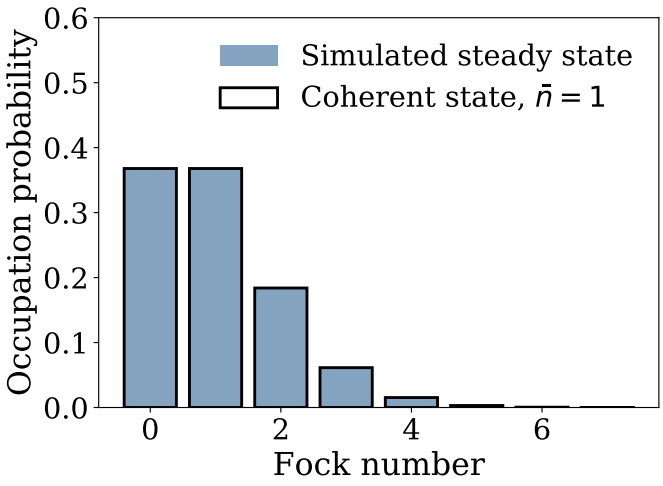

(b)

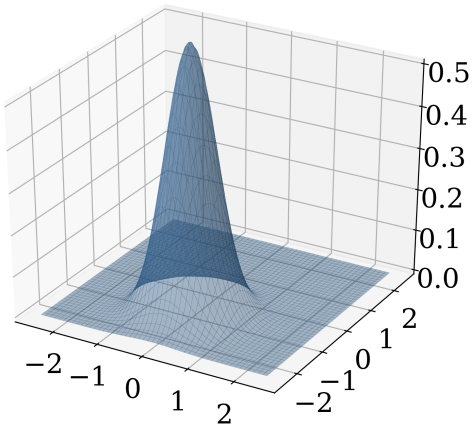

(c)

Figure 2.8: (a) The transient dynamics of the atomic levels, the cavity modes, and the input-output modes of the cavity with a coherent laser drive. The units of $\langle r^\dagger_{out} r_{out}\rangle$ and $\langle l^\dagger_{out} l_{out}\rangle$ are in GHz. (b) The photon statistics of the r mode in the cavity in steady state condition. (c) The Wigner function of the r mode in the cavity in steady state condition. (For a more formal introduction to Wigner functions please refer to Chap. 4.)

time t as

$$P = \int_0^t \langle l_{out}^\dagger l_{out} \rangle dt. \tag{2.33}$$

This is the probability of observing a single LHCP photon at the output of the blue cavity in time t. However, the number of photons actually subtracted from the incoming filed could be more. That is because photons can also escape the red cavity because of non-zero κ_r, even before SPRINT takes place.

2.5 Pre-specified initial state

2.5.1 Coherent state input

In this section, we consider the situation where a coherent state with a specified average input photon number ($\bar{n} = 1$ in our case) is in the r mode of the cavity. Then, we shall evolve the state of the system to study the dynamics of the atom, and the relevant modes. First, we write down the effective non-Hermitian Hamiltonian as

$$H_{\text{eff}} = H_0 + H_{int} - \frac{i\hbar}{2} \sum_k C_k^\dagger C_k, \tag{2.34}$$

where H_0, H_{int}, and C_k's are the same as in Eq. 2.24. However, this time we do not have the classical input drive. We set the initial condition to $|\psi(0)\rangle = |\alpha, 0, 1\rangle$, which refers to the presence of a coherent state α in the r mode, vacuum in the l mode, and the emitter in the ground state $|1\rangle$. We use the Hamiltonian to evolve this initial condition in Python using QuTiP's master equation solver.

Once again, we start with the simple case of a cavity with no atoms in it. We simulate it for $\kappa_r = 2\pi \times 0.25$ GHz, and get the transient dynamics as seen in Fig. 2.9. As expected, the mean number photons in the r mode exponentially decays with time, and the entire photon is collected at the output as the time integral of $\langle r_{out}^\dagger r_{out} \rangle$ saturates to unity.

Next, we put an atom in the cavity so that the two modes start interacting via the atomic transitions. The system is characterized by the same set of parameters as earlier: $\omega_d = \omega_r = \omega_1 = 2\pi \times 200$ THz, $\omega_2 = \omega_l$, $\omega_r - \omega_l = 2\pi \times 0.5$ GHz, $g_1 = g_2 = g = 2\pi \times 10$ GHz, $\kappa_r = \kappa_l = \gamma_{coh} = 2\pi \times 0.25$ GHz, $\gamma_1 = \gamma_2 = 0$. The transient dynamics of the system with these system parameters is shown in Fig. 2.10a. We observe that the probability of

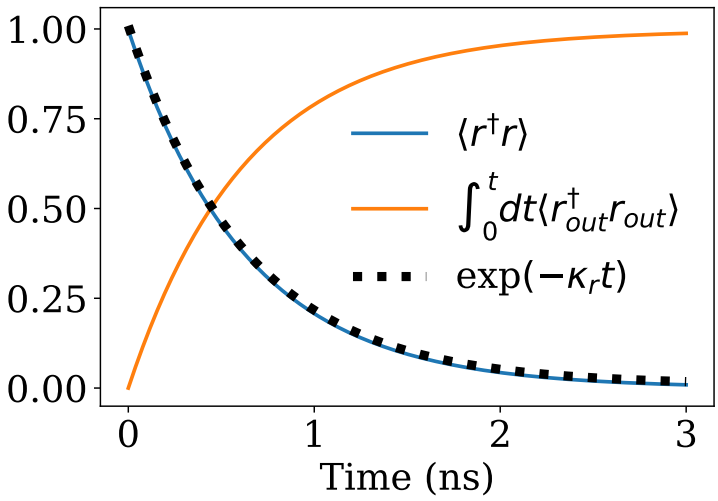

Figure 2.9: The transient dynamics of the cavity (with no atom) when the r cavity mode is initialized with a coherent state of average photon number one.

photon subtraction (given by the time integral of $\langle l_{out}^\dagger l_{out} \rangle$) from the r mode is quite low, and about ~ 0.3, which is similar to $\langle \sigma_{22} \rangle$, or the probability of the atom ending up in state $|2\rangle$ in the steady state in magnitude.

From the transient response of the system Fig. 2.10a, we notice that there are some fast oscillations in the system. We perform FFT of $\langle l_{out}^\dagger l_{out} \rangle$ to analyse the oscillation frequencies. From the results shown in Fig. 2.11, we see that the oscillation frequencies are $n \times \sqrt{2}g/2\pi$, and $n \times \sqrt{3}g/2\pi$ corresponding to two-photon, and three-photon processes respectively where $n \in \{1, 2\}$. We can also observe, higher-order manifolds, but their contributions are small. Also, the oscillations in the r and l modes are π out of phase with each other.

However, ideally we do not want such many-photon Rabi oscillations in the l mode. We want the single photon emitted in the l mode to be ejected from the cavity quickly, so that it does not get re-absorbed by the atom. Ideally, that should also increase the speed of single photon subtraction. We can achieve that by having a lossy cavity for the l mode. Thus, we set $\kappa_r = 2\pi \times 0.25$ GHz, and $\kappa_l = 2\pi \times 25$ GHz; and simulate the system. The other parameters of the system have been kept unchanged. The transient dynamics of the system with higher κ_l is shown in Fig. 2.10b. This shows that increasing κ_l dampens the oscillations, speeds up the process of photon subtraction, and more importantly increases the probability of a single photon being subtracted from the r mode to ~ 0.6. However, the probability still does not go up to one. This is primarily due to the large vacuum

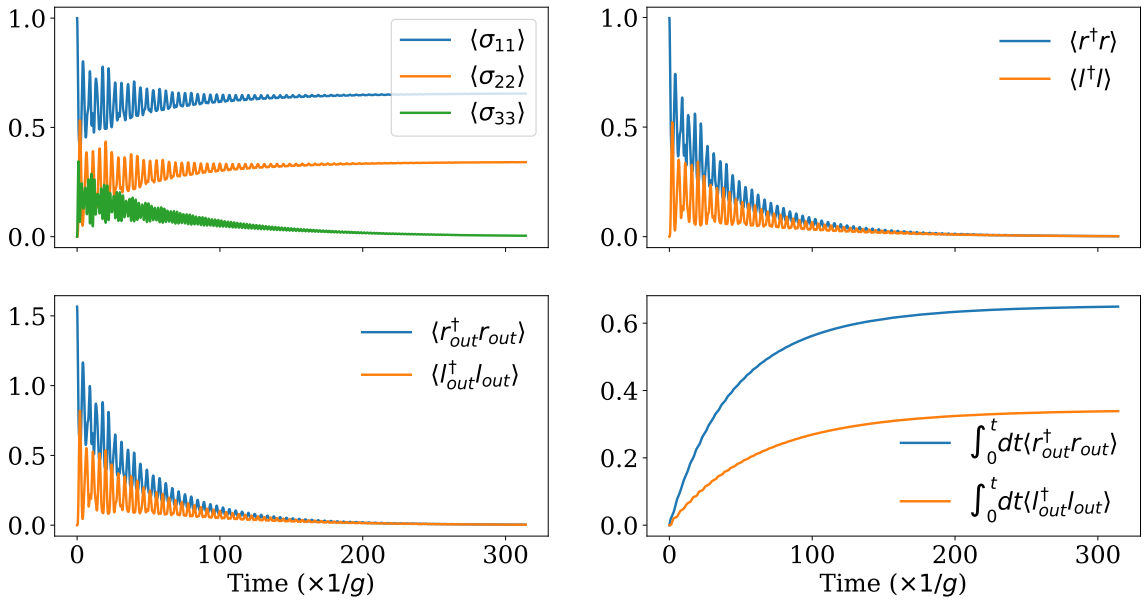

(a)

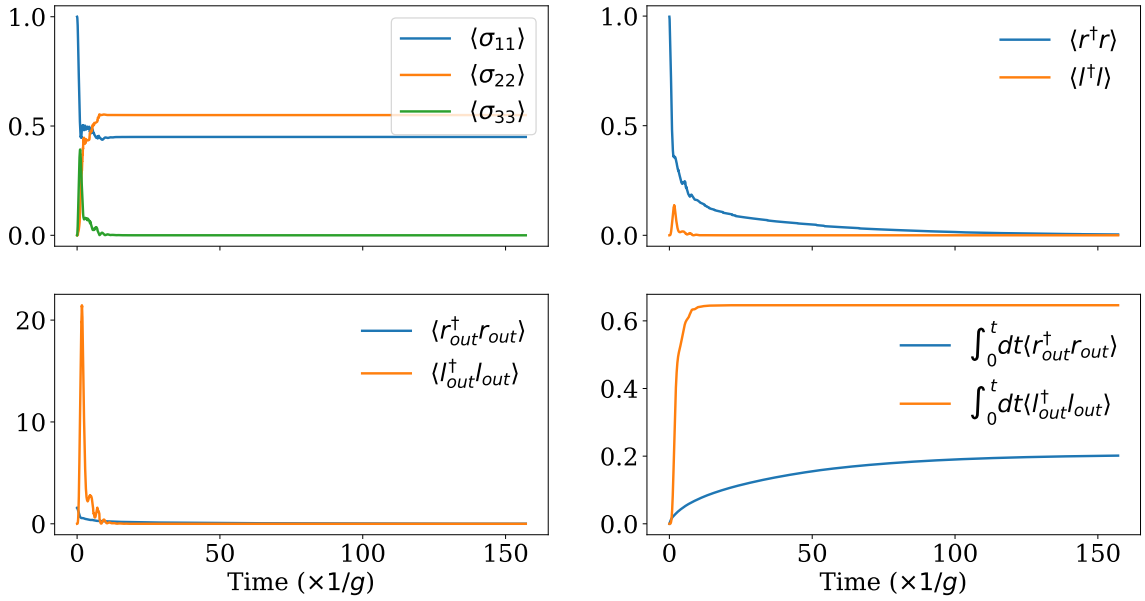

(b)

Figure 2.10: The transient dynamics of the atomic levels, the cavity modes, and the input-output modes of the cavity when the r mode is initialized with a coherent state with $\bar{n} = 1$, for (a) $\kappa_r = \kappa_l = 2\pi \times 0.25$ GHz, and (b) $\kappa_r = 2\pi \times 0.25$ GHz, and $\kappa_l = 2\pi \times 25$ GHz. The units of $\langle r^\dagger_{out} r_{out}\rangle$ and $\langle l^\dagger_{out} l_{out}\rangle$ are in GHz.

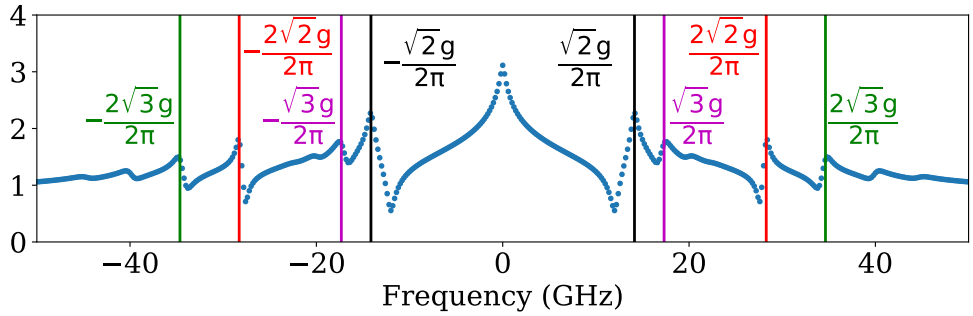

Figure 2.11: The FFT of $\langle l_{out}^{\dagger} l_{out} \rangle$ showing two-photon and three-photon Rabi-oscillations in the system.

component present in weak coherent pulses – for example the probability of zero photons present in a coherent pulse with average photon number of 1, 2, and 3 is approximately 0.37, 0.13, and 0.05, respectively.

2.5.2 Fock state input

In this subsection, we consider that the r mode in the cavity is initialized with a Fock state (the two photon Fock state $|2\rangle$ for our simulations), instead of a coherent state. The transient dynamics of the system is shown in Fig, 2.12. Once again, we find that having a higher κ_l increases the chance of a proper single photon subtraction from the r mode. Also, the process of subtraction is much faster, and as a result energy lost through decay channels is also less when $100\kappa_r = \kappa_l = 2\pi \times 25$ GHz. For a leaky mode l, we see that we can achieve a perfect single photon subtraction with the Fock state even with low levels of excitation. We simulated our system with the same system parameters for a single photon Fock state $|1\rangle$ input, and still got a perfect single photon subtraction from the r mode, as shown in Fig. 2.13.

Parameter considerations

Now, we try to consider the role of different cavity parameters, like the coupling strength and the cavity decay in determining the probability of successful single photon subtraction from mode r. As expected, we find that the probability of successful subtraction is maximum for $g_1 = g_2$ for any given value of cavity decay rate. Fig. 2.14a shows the contour plot of the probability of single photon subtraction from a single photon Fock state $|1\rangle$

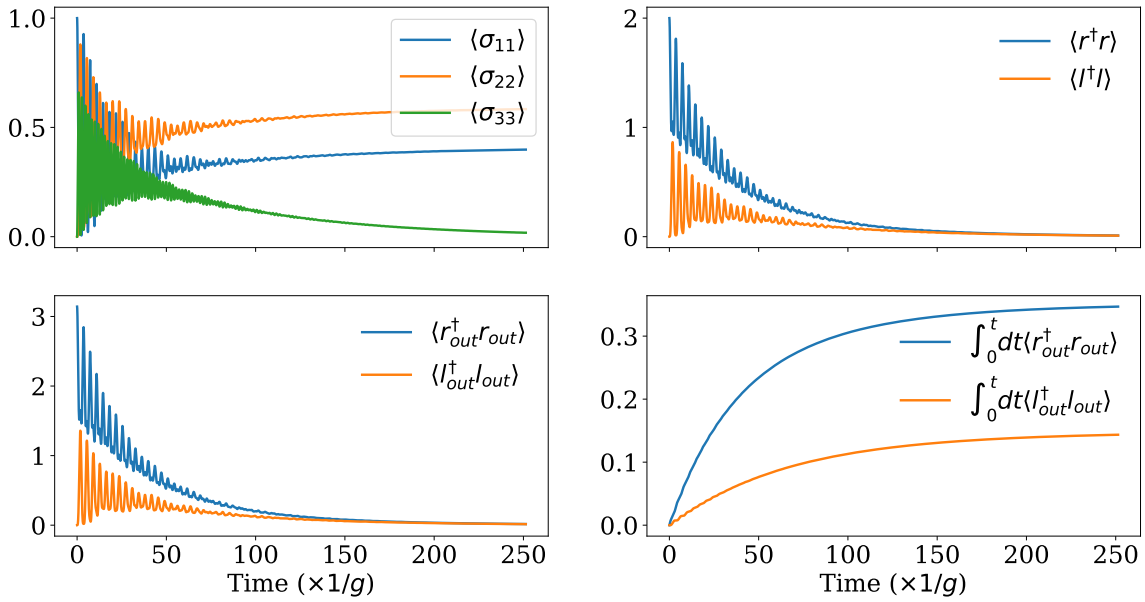

(a)

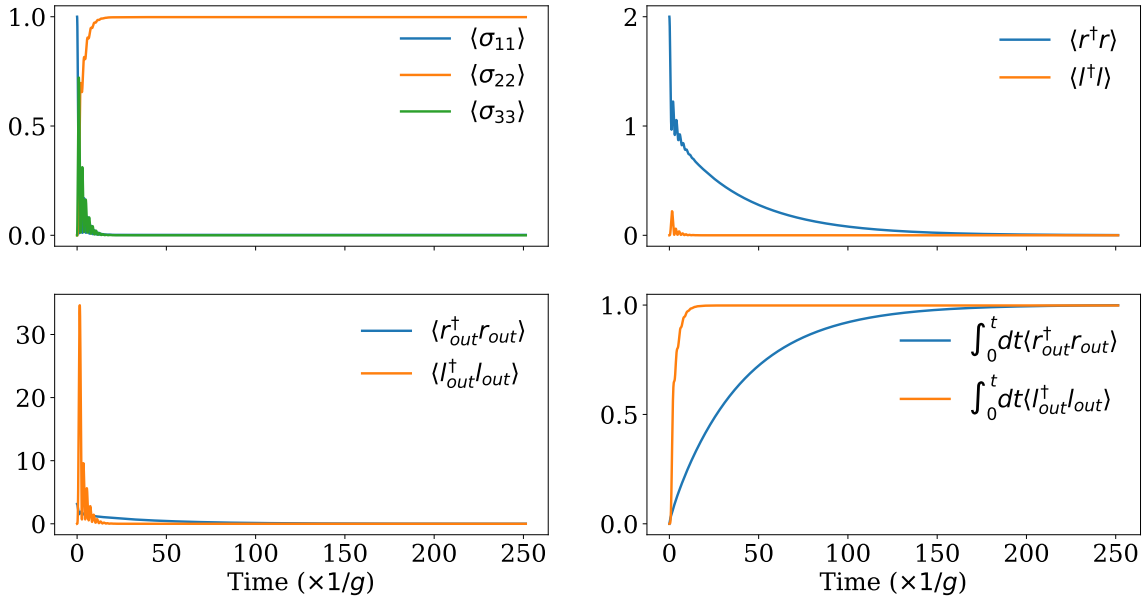

(b)

Figure 2.12: The transient dynamics of the atomic levels, the cavity modes, and the input-output modes of the cavity when the r mode is initialized with the Fock state $|2\rangle$, for (a) $\kappa_r = \kappa_l = 2\pi \times 0.25$ GHz, and (b) $\kappa_r = 2\pi \times 0.25$ GHz, and $\kappa_l = 2\pi \times 25$ GHz. The units of $\langle r^\dagger_{out} r_{out}\rangle$ and $\langle l^\dagger_{out} l_{out}\rangle$ are in GHz.

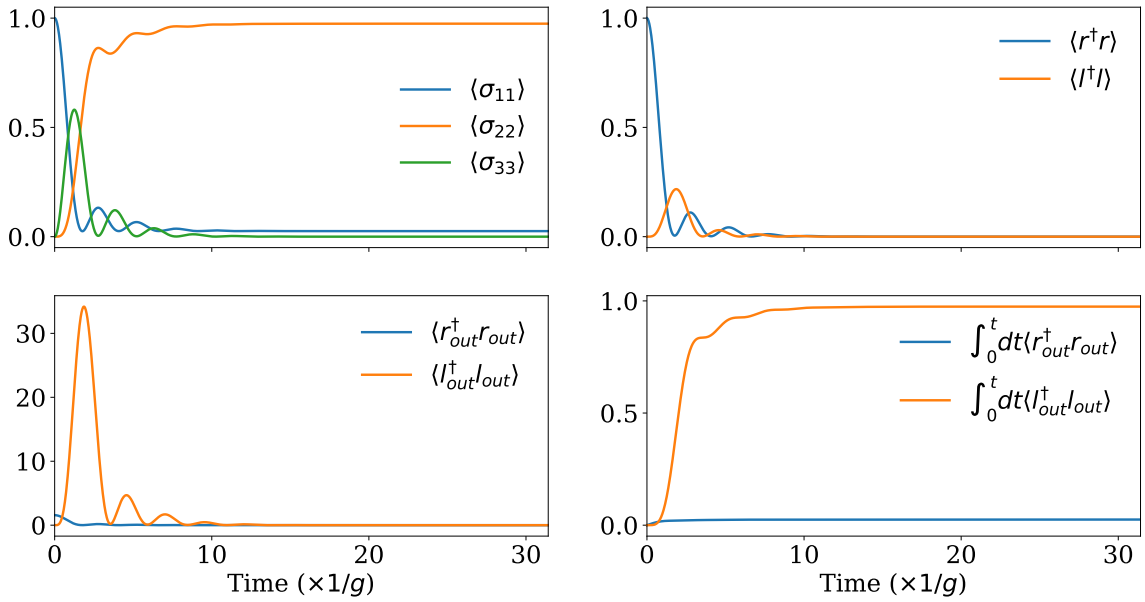

Figure 2.13: The transient dynamics of the atomic levels, the cavity modes, and the input-output modes of the cavity when the r mode is initialized with the Fock state $|1\rangle$, for $\kappa_r = 2\pi \times 0.25$ GHz, and $\kappa_l = 2\pi \times 25$ GHz. The units of $\langle r^\dagger_{out} r_{out}\rangle$ and $\langle l^\dagger_{out} l_{out}\rangle$ are in GHz.

as a function of the coupling strengths g_1 and g_2 for $\kappa_r = \kappa_l = 2\pi \times 0.25$ GHz. As we can see, the probability is highest around $g_1 \approx g_2$. However, it is much less that one. We noticed this previously when we chose the cavity decay rates to be equal. Choosing $\kappa_r = 2\pi \times 0.25$ GHz and $\kappa_l = 2\pi \times 25$ GHz solves this issue, and we can have perfect single photon subtraction along $g_1 \approx g_2$ as shown in Fig. 2.14b. We also notice that the coupling strengths do not need to be strictly equal, and one can get unit probability of subtraction even with a small mismatch in the coupling strengths.

Thus, we find that it is important to note the range of permissible cavity decay rates that still allow us to have perfect single photon subtraction. For that we fix our coupling rate at $g_1 = g_2 = g = 2\pi \times 10$ GHz, and sweep over the two cavity decay rates κ_r and κ_l as shown in Fig. 2.14c. As we can see from the figure, κ_r should be lower than a threshold value. If the cavity for r mode is too leaky, the photon might be lost from the cavity even before it interacts with the emitter. On the contrary, there are stricter bounds on the values of κ_l we can choose. If κ_l is too low, the subtracted photon in the l mode can get re-absorbed. Thus ideally, $\kappa_l \geq g$. But, κ_l cannot be too high, and has a turn-around point around $\kappa_l \sim 100g$. However, till now we ignored the population decay rates and used

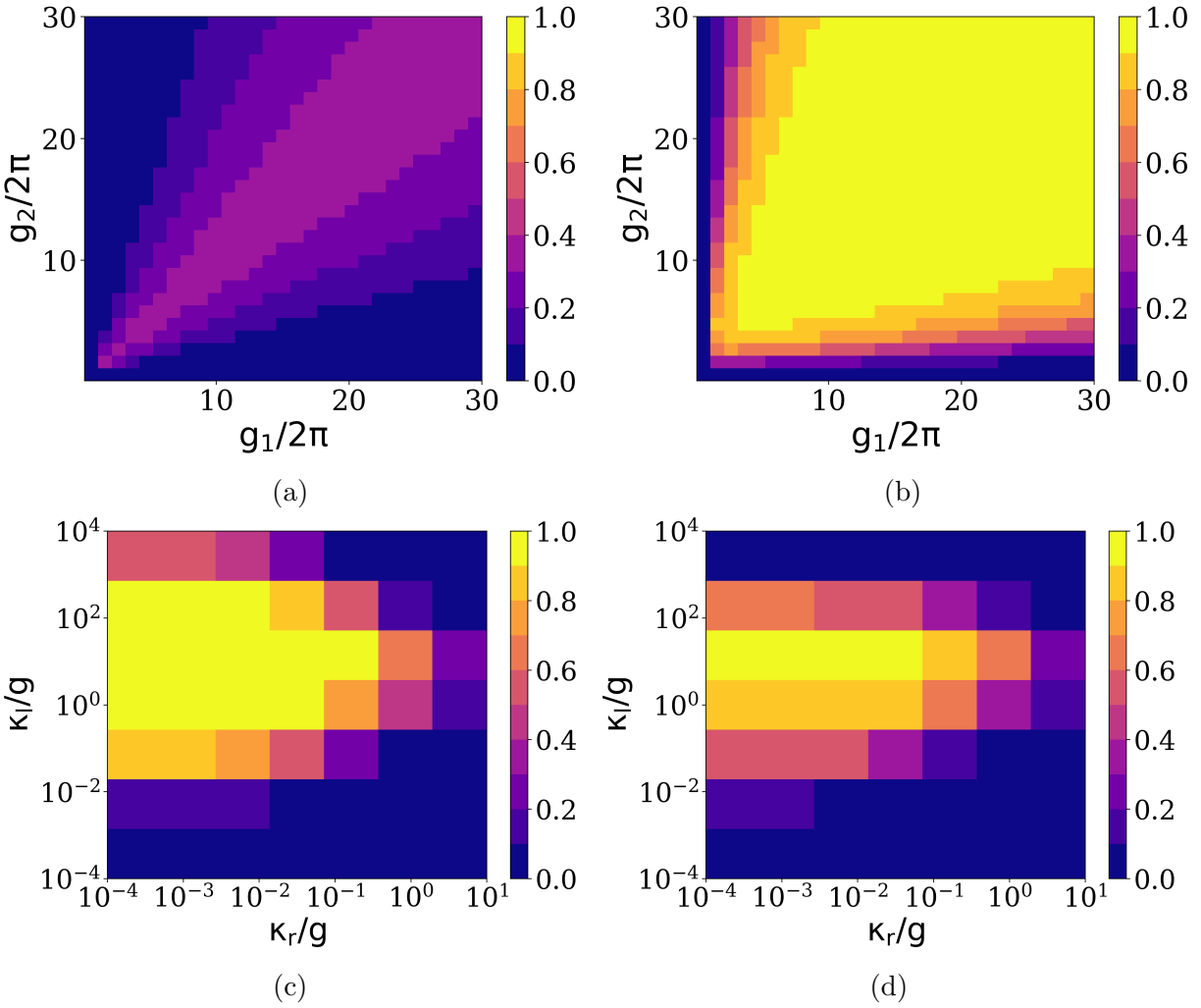

Figure 2.14: The single photon subtraction probability from a single photon Fock state $|1\rangle$ as a function of the coupling strengths g_1 (in GHz) and g_2 (in GHz) for (a) $\kappa_r = \kappa_l = 2\pi \times 0.25$ GHz, and for (b) $100\kappa_r = \kappa_l = 2\pi \times 25$ GHz. For (a,b) $\gamma_{coh} = 2\pi \times 0.25$ GHz, $\gamma_1 = \gamma_2 = 0$ was used. (c,d) The dependence of single photon subtraction probability from a single photon Fock state $|1\rangle$ on cavity decay rates κ_r and κ_l for $g_1 = g_2 = g = 2\pi \times 10$ GHz with (c) $\gamma_{coh} = 2\pi \times 0.25$ GHz, $\gamma_1 = \gamma_2 = 0$, and (d) $\gamma_{coh} = \gamma_1 = \gamma_2 = 2\pi \times 0.25$ GHz.

$\gamma_1 = \gamma_2 \approx 0$. However, if we consider the atomic linewidth into our calculations, we end up having stronger bounds on the permissible values of the cavity decay rates as seen in Fig. 2.14d. Here we picked the atomic spontaneous decay rates to be $\gamma_1 = \gamma_2 = 2\pi \times 0.25$ GHz, which is a reasonable value for quantum dot systems. We notice that having non-zero $gamma_1$ and γ_2 restricts the values of κ_l, and ideally $\kappa_l \sim 10g$ to achieve close to unit probability of deterministic single photon subtraction.

2.6 Using a cascaded feeder/ source cavity

Another way we can introduce photons into the system is by using a feeder/ source cavity or a waveguide to send the input pulse. In particularly, we will briefly see how it can be done with a cavity using a system as shown in Fig. 2.15. A single-sided feeder cavity can be used to create a properly designed pulse. That pulse can be sent over to the bi-modal cavity using some kind of waveguide system. Preferably, it should be a chiral waveguide allowing uni-directional flow of photons from the feeder to the bi-modal cavity. That stops photons from the red mode in the target cavity flow back into the feeder cavity.

The single photon subtraction from the pulse takes place in the target cavity that houses the three-level emitter as we discussed in the previous sections. This model, has certain advantages over using CW coherent laser beam or initializing the cavity mode with a coherent or a Fock state. It helps us track the input state unlike our previous models. In this model, the Hamiltonian of the system gets modified to

$$H = H_0 + H_{int} + H_s, \tag{2.35}$$

where H_0 and H_{int} are the same as before. H_s is the source Hamiltonian given by $H_s = \hbar\omega_s r_s^\dagger r_s$, where r_s is the annihilation operator, and ω_s is the resonant frequency of the feeder cavity mode. The source cavity mode collapse operator C_1 gets modified to

$$C_1 = r_{out} = \sqrt{\kappa_s} r_s + \sqrt{\kappa_r} r, \tag{2.36}$$

where κ_s is the decay rate of the source cavity, while the other collapse operators remain unchanged. The interaction of the cavity modes, and the emitter is governed by the non-Hermitian effective Hamiltonian

$$H_{\text{eff}} = H_0 + H_{int} + H_s - \frac{i\hbar}{2} \sum_k C_k^\dagger C_k. \tag{2.37}$$

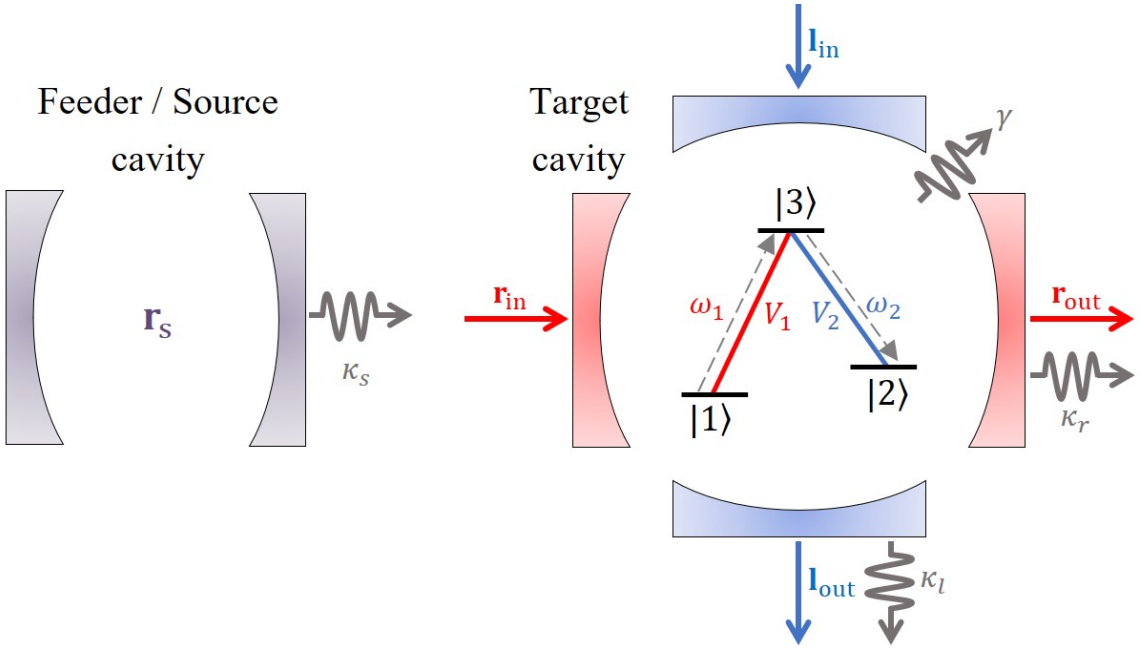

Figure 2.15: Schematic of using a cascaded feeder cavity to create a well-defined input pulse, from which a single photon is deterministically subtracted in the target cavity.

The target cavity is initialized as $|\psi_t\rangle = |0, 0, 1\rangle$, i.e., both the modes have vacuum, and the emitter is in state $|1\rangle$. Next, we can initialize the r_s mode of the source cavity accordingly, and observe the dynamics of the system as it evolves according to the non-Hermitian Hamiltonian using QuTiP's Monte Carlo master equation solver. But in this thesis we will not be explicitly solving this model.

However, we must note that the cavity parameters required for single photon subtraction to happen in this model can be expected to differ from the cavity parameters needed for the case when the cavity is initialized with a coherent or a Fock state. The reason being, for efficient photon subtraction, it is important to get the input pulse into the target cavity. The decay rate of the red cavity mode κ_r cannot be too low, since that would make it difficult to inject the input pulse into the cavity. That would put a lower limit in the range of permissible κ_r's. However, κ_r cannot be too high, since that would result in the photons leaking from the red cavity easily, and that would in turn decrease the probability of subtraction. Moreover, the choice of κ_r will also hinge upon the choice of κ_s, since the impedances of the two cavities must be matched to efficiently get the pulse from the source to the target cavity.

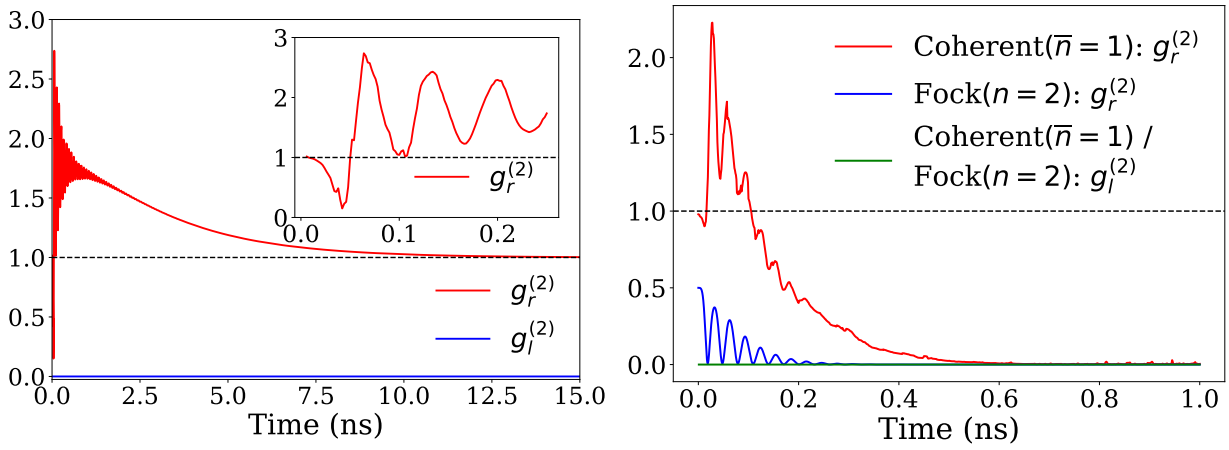

(a) (b)

Figure 2.16: The second order auto-correlation function for both modes r and l for: (a) CW coherent laser input (inset shows that the value of $g^{(2)}$ for mode r goes below one, thereby showing sub-Poissonian photon statistics), and (b) when the r mode in the cavity is initialized with coherent state with average photon number one, and Fock state with two photons with $\kappa_r = 2\pi \times 0.25$ GHz, and $\kappa_l = 2\pi \times 25$ GHz.

2.7 Second order auto-correlation function

In this section, we shall look at the second order auto-correlation function $g^{(2)}(\tau)$ of the photon subtracted fields to look for non-classical signatures generated as a result of SPRINT. The second order auto-correlation function for a mode m with annihilation operator a_m can be mathematically defined as:

$$g^{(2)}(\tau) = \frac{\langle a_m^\dagger a_m^\dagger a_m a_m \rangle}{\langle a_m^\dagger a_m \rangle^2}. \tag{2.38}$$

First, we shall consider the case, where a CW coherent beam of laser is sent into mode r, as discussed in Sec. 2.4. Initially, both the modes are in the vacuum state. A classical Gaussian CW coherent laser is sent into the r mode. The second order auto-correlation function of the coherent state is 1. However, we observe $g^{(2)} < 1$ in the photon subtracted mode, as shown in the inset of Fig. 2.16a. This indicates that the process of photon subtraction leads to introduction of non-classicality/ sub-Poissonian photon statistics into the otherwise classical r mode.

Next, we revisit the case from Sec. 2.5, where we initialized with a coherent state in the r mode. Once again, we observe a second order auto-correlation less than unity, as shown in Fig. 2.16b, even though it is a coherent state. That is followed by a super-bunching event whereby $g^{(2)} > 1$. With time $g^{(2)}$ decays to zero, as all the photons eventually leak out of the cavity.

For a Fock state with n photons, $g^{(2)} = 1 - 1/n$. So, for the two Fock state input $|2\rangle$ as discussed in Sec. 2.5.2, the second order auto-correlation starts at 0.5 at $t = 0$. Then, it decays gradually until all the photons have leaked out of the cavity, and eventually becomes zero.

Chapter 3

Deterministic single photon subtraction with a three-level emitter coupled to a chiral waveguide

3.1 Motivation

In this chapter, we propose and investigate the feasibility of deterministic single photon subtraction using a single three-level quantum emitter coupled to a chiral waveguide instead of a bi-modal optical cavity [41]. Using a waveguide instead of a cavity offers several advantages – such as the removal of the need to spatially couple, and temporally match the input light into a cavity, as well as relaxed requirement on spatial positioning of the emitter. Additionally, there would be no need to worry about controlling a cavity-emitter detuning, and cascading of multiple photon subtraction stages should be significantly simplified.

In Sec. 3.2, we start by introducing the theoretical formulations for a single two-level quantum emitter coupled to a one-dimensional (1D) single mode waveguide. Next, we discuss how to use a single quantum emitter coupled with a waveguide for single photon subtraction. In Sec. 3.3.1, we introduce the theoretical formulations for a perfectly chiral waveguide. We use the input-output formalism proposed by Gardiner *et al.* in Ref. [49] to get the relevant input-output relations, and the coupled differential equations of motion for the relevant operators. In Sec. 3.3.2, we describe how realistic waveguides with chirality less than unity can be studied under the same framework. Furthermore, in Section 3.4 we numerically simulate the probability of a single photon subtraction for different optical inputs – continuous-wave coherent state, coherent Gaussian pulse, and Fock states. Finally,

we discuss a variety of recently reported three-level emitter and waveguide systems in terms of their potential to subtract a single photon from an optical pulse, and find that photonic crystal waveguides have the potential to become a platform in which the probability of successful single photon subtraction can approach unity.

The work reported in this chapter is a continuation of the work done by previous graduate student Golam Bappi [50]. I will like to thank Dr. Jinjin Du, and Prof. Michal Bajcsy for helpful discussions regarding the work reported in this chapter. The Python programs used for simulations in this chapter are available in Appendix C.

3.2 A quantum emitter coupled with a waveguide

At the inception, we will consider a two-level quantum emitter coupled with a 1D waveguide. The extension of the problem to a three-level quantum coupled to a 1D waveguide with two chiral modes is pretty straightforward.

First, for simplicity let us consider the Hamiltonian for a 1D optical cavity of length L, parallel to the direction of propagation of light. For a planewave propagating in such a cavity, the modes are separated by $\Delta k = 2\pi/L$ under periodic boundary conditions. The total energy of the modes in the cavity is sum of the energies of the individual modes, and is given by

$$H/\hbar = \sum_k \omega_k \hat{a}_k^\dagger \hat{a}_k, \tag{3.1}$$

where $\hat{a}_k$ ($\hat{a}_k^\dagger$) is the annihilation (creation) operator of the mode with wavevector k in this discrete picture, and obey the commutation relationship $\left[\hat{a}_k, \hat{a}_{k'}^\dagger\right] = \delta_{k,k'}$. In the limit $L \to \infty$, we jump from the discrete mode picture to continuous mode formalism in an infinitely long waveguide by using the conversion relationship

$$\sum_k \to \frac{1}{\Delta k} \int_{-\infty}^{\infty} dk.$$

The new continuous mode operator $\tilde{a}_k$ is related to the discrete mode operator by the relationship

$$\hat{a}_k \to \sqrt{\Delta k}\tilde{a}_k. \tag{3.2}$$

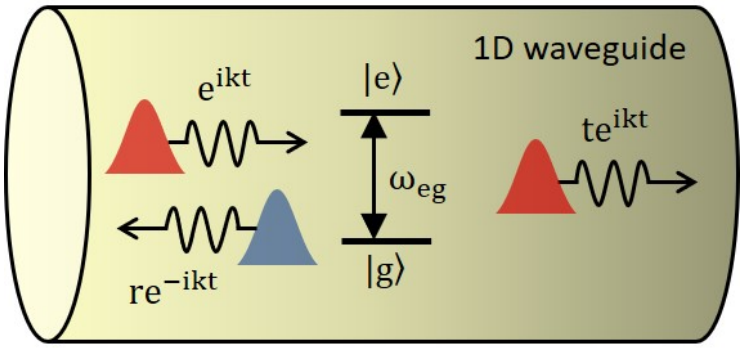

Figure 3.1: A simplified model of a two-level emitter coupled with a 1D waveguide when a single photon is sent into the waveguide from the left.

Also, the continuous mode operators follow the commutation relationship $\left[\tilde{a}_k, \tilde{a}^\dagger_{k'}\right] = \delta(k - k')$. The discrete Kronecker delta is connected to the Dirac delta function by the transformation

$$\delta_{k,k'} \to \Delta k \delta(k - k'). \tag{3.3}$$

Thus, the Hamiltonian for the guided mode can be expressed in the continuum limit as

$$H/\hbar = \int_{-\infty}^{\infty} dk \omega_k \tilde{a}^\dagger_k \tilde{a}_k. \tag{3.4}$$

The limit of the integration can be justified as we will be only considering near resonant interactions between the emitter and the waveguide, and we can ignore far detuned interactions, Henceforth, we will be working in the continuum limit, and will be dropping the tilde on the operators for notational convenience.

Now, we return to the case of the two-level emitter coupled with a 1D waveguide. The Hamiltonian for such a simplified system, as shown in Fig. 3.1, is given by the sum of the Hamiltonian corresponding to the waveguide H_{wg}, the atomic Hamiltonian H_a, and the interaction Hamiltonian H_{int}, such that, $H = H_{wg} + H_a + H_{int}$, where

$$H_{wg}/\hbar = \sum_k \omega_k a^\dagger_k a_k, \quad H_a/\hbar = \omega_{eg} \sigma_{ee}, \tag{3.5a}$$

$$H_{int}/\hbar = \sum_k V(k)\left(a_k\sigma_+ + a_k^\dagger\sigma_-\right). \tag{3.5b}$$

Here, ω_{eg} is the frequency of the $|g\rangle \leftrightarrow |e\rangle$ transition, $\sigma_{-(+)}$ is the lowering (raising) operator for the emitter, a_k ($a_k^\dagger$) is the annihilation (creation) operator for incoming photons in the wavevector mode basis, and the projection operator $\sigma_{ee} = |e\rangle\langle e|$. $V(k)$ is the coupling constant between the waveguide mode k and the emitter, and is given by

$$V(k) = d\sqrt{\frac{\omega_k}{2\hbar\epsilon_0 V_m}}, \tag{3.6}$$

where d is the atomic dipole matrix element, and $V_m = \pi R^2 L$ is the effective mode volume for a waveguide of radius R. In the continuous mode limit we can reformulate this Hamiltonian as:

$$H/\hbar = \omega_{eg}\sigma_{ee} + \int_{-\infty}^{\infty} a_k^\dagger a_k \omega_k dk + \int_{-\infty}^{\infty} V(k)\sqrt{\frac{L}{2\pi}}\left(a_k\sigma_+ + a_k^\dagger\sigma_-\right)dk, \tag{3.7}$$

We can study the response of this system in multiple ways. We shall briefly explore the situation when a single photon is incident from the left using two separate formalisms – first, the real space approach, and second, the input-output formalism and scattering matrix based approach.

Method I: Real space approach

Assuming that the dispersion relationship of the waveguide can be linearized around the transition frequency ω_{eg}, i.e., $\omega_k = v_g|k|$; the coupling constant is frequency independent, i.e., $V(k) = \mathcal{V}$; and there are two independent left and right-propagating modes, the continuous k-space Hamiltonian can be expressed in the position space as [51]

$$\begin{aligned} H/\hbar = \omega_{eg}\sigma_{ee} - iv_g\int_{-\infty}^{\infty} dx\left[r^\dagger(x)\frac{\partial}{\partial x}r(x) - l^\dagger(x)\frac{\partial}{\partial x}l(x)\right] \\ + \int_{-\infty}^{\infty} dx V\delta(x)\left(r^\dagger(x)\sigma_- + r(x)\sigma_+ + l^\dagger(x)\sigma_- + l(x)\sigma_+\right), \end{aligned} \tag{3.8}$$

where $V = \sqrt{L}\mathcal{V}$, v_g is the group velocity of guided mode, and $l(x)$ ($r(x)$) is the destruction operator for left (right) travelling photons at x in the waveguide. A derivation of this Hamiltonian is provided in Appendix A

The eigenstate of the Hamiltonian in Eq. 3.7 for a photon incident from the left with group velocity v_g and wavevector k is

$$|\Psi_k\rangle = \int_{-\infty}^{\infty} dx \left(u_R(x)r^\dagger(x) + u_L(x)l^\dagger(x)\right)|0,g\rangle + e_k\,|0,e\rangle\,, \tag{3.9}$$

where e_k is the probability that the emitter is excited, $u_R(x)$ and $u_L(x)$ are mode functions of photons travelling in the left and right directions respectively. If only one photon is sent from the left, the mode functions take the following form

$$u_R(x) = \begin{cases} e^{ikx} & \text{for } x < 0 \\ te^{ikx} & \text{for } x > 0 \end{cases} \tag{3.10a}$$

$$u_L(x) = re^{-ikx} \text{ for } x < 0, \tag{3.10b}$$

where t and r are the transmission and reflection coefficients, and the emitter is located at $x = 0$. Furthermore, we can check the value of the mode functions at the input and output of the waveguide. In the limits of $x \to -\infty$ (at input) and $x \to \infty$ (at output) we get the relationships:

$$\lim_{x\to\infty} u_R(x) = t,\ \lim_{x\to-\infty} u_R(x) = 1,\ \lim_{x\to\infty} u_L(x) = 0,\ \lim_{x\to-\infty} u_L(x) = r. \tag{3.11}$$

We solve the eigenvalue equation $H\,|\Psi_k\rangle = E_k\,|\Psi_k\rangle$ for the transmission and reflection coefficients t and r respectively, under the assumption of a slowly varying field, to arrive at the following solution:

$$t = e^{ib}\cos b, \quad r = ie^{ib}\sin b, \quad e_k = -\frac{v_g}{V}e^{ib}\sin b, \tag{3.12}$$

where the phase shift is given by $b = \tan^{-1}(V^2/v_g\Delta_k)$, where detuning between the incident field and the atomic transition is $\Delta_k = \omega_{eg} - E_k/\hbar$. For sanity check, we can verify that $|r|^2 + |t|^2 = 1$ is satisfied. We define $J = V^2/v_g$. It is an important parameter of the system with units of frequency. The reflectivity is a Lorentzian with a width proportional to J. The transmittance has been plotted in Fig. 3.2 for different values of J. We observe that on resonance the photon is completely reflected, and higher emitter-waveguide coupling results in a wider spectral window for reflection.

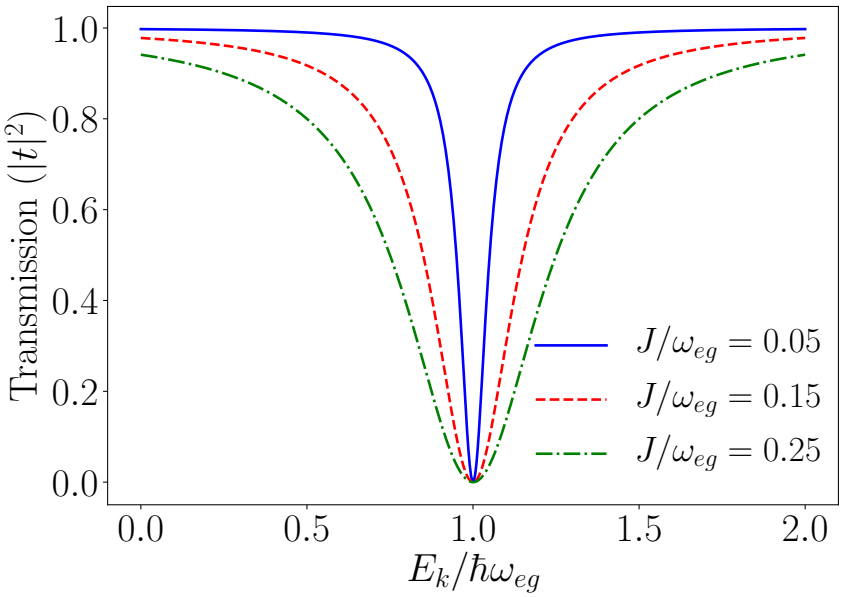

Figure 3.2: The single photon transmittance $|t|^2$ for different values of J/ω_{eg}. The light is completely reflected at resonance.

Method II: Input-output formalism and scattering matrix approach

We can also study the system using input-output formalism. Since this method is more involved, first, we shall consider the simple Hamiltonian of a two-level emitter coupled with a waveguide supporting wave-propagation in only one direction as follows (this time we express the Hamiltonian in frequency mode basis):

$$H/\hbar = \omega_{ge}\sigma_{ee} + \int a_\omega^\dagger a_\omega \omega d\omega + \frac{V}{\sqrt{v_g}} \int \left(\sigma_+ a_\omega + \sigma_- a_\omega^\dagger\right) d\omega. \tag{3.13}$$

It is important to note that this Hamiltonian is normalized by group velocity, and the annihilation operator a_ω is defined as $a_{\omega(k)} = a_k/\sqrt{v_g}$ for the mode labeled by frequency ω in the frequency mode basis. The input and the output mode operators can be defined as [49]

$$a_{in}(t) = \frac{1}{\sqrt{2\pi}} \int d\omega a_\omega(t_0)\, e^{-i\omega(t-t_0)}, \tag{3.14a}$$

$$a_{out}(t) = \frac{1}{\sqrt{2\pi}} \int d\omega a_\omega(t_1)\, e^{-i\omega(t-t_1)}, \tag{3.14b}$$

where t_0 is a time long before, and t_1 is a time long after the interaction between the emitter and the input signal. They follow the commutation relationship $[a_{in}(t), a_{out}(t')] = \delta(t - t')$. By solving the Heisenberg equations of motion we arrive at the following input-output relationship [49, 52]

$$a_{out}(t) = a_{in}(t) - i\sqrt{\frac{2}{\tau}}\sigma_-(t). \tag{3.15}$$

for spontaneous emission rate into guided mode $\gamma_g = 2/\tau = 2\pi V^2/v_g$. For now, we shall consider that the emitter only couples with the waveguide modes, and ignore its coupling to any dissipative baths. The input-output formalism is very useful for few photon transport problems, since the dynamics of the emitter with the modes gives us about the field's properties at the input and the output of the coupled systems. In later sections we shall see in more details how to reach the input-output relationship as shown in Eq. 3.15.

The input-output formalism can be directly associated with the well known scattering matrix approach. The scattering matrix is mathematically defined in terms of the time evolution operator $U_{int}(t_0, t_1) = \mathcal{T}\exp\left[-i\int_{t_0}^{t_1} dt H_{int}(t)\right]$ in the interaction picture as [53]

$$\begin{aligned} S &= \lim_{\substack{t_0\to-\infty \\ t_1\to\infty}} U_{int}(t_1, t_0) && (3.16)\\ &= \lim_{t_1\to\infty} U_{int}(t_1, 0) \times \lim_{t_0\to-\infty} U_{int}(0, t_0) && (3.17)\\ &= \Omega_-^\dagger \Omega_+, && (3.18) \end{aligned}$$

where $\Omega_\pm$ are the Møller wave operators. $\mathcal{T}$ is known as the Dyson chronological operator, and it properly orders the time discretized evolution operators as its name suggests. The Møller wave operators are given by $\Omega_+ = \lim_{t_0\to-\infty} U_{int}(0, t_0)$, and $\Omega_- = \lim_{t_1\to\infty} U_{int}(0, t_1)$. If $|i_1, i_2\rangle$ and $|o_1, o_2\rangle$ are the two particle input and output states corresponding to photons of frequency i_n and o_n respectively $\forall n \in \{1, 2\}$, the scattering matrix elements are given by

$$S_{o_1,o_2;i_1,i_2} = \langle o_1, o_2|S|i_1, i_2\rangle. \tag{3.19}$$

This formalism easily allows us to scale up to n-body scattering problems. The scattering eigenstates $\left|i_1, i_2^\pm\right\rangle$ are the states that the input will evolve to at $t_1 \to \infty$, and the state at

$t_0 \to -\infty$ from which we arrived at the current input in the interaction picture. They are related to the current input through the Møller wave operators as

$$\left|i_1, i_2^+\right\rangle = \lim_{t_0 \to -\infty} U_{int}(0, t_0) \left|i_1, i_2\right\rangle = \Omega_+ \left|i_1, i_2\right\rangle, \tag{3.20a}$$

$$\left|i_1, i_2^-\right\rangle = \lim_{t_1 \to \infty} U_{int}(0, t_1) \left|i_1, i_2\right\rangle = \Omega_- \left|i_1, i_2\right\rangle. \tag{3.20b}$$

This implies that the scattering matrix element can be expressed as

$$\langle o_1, o_2|S|i_1, i_2\rangle = \langle o_1, o_2|\Omega_-^\dagger \Omega_+|i_1, i_2\rangle = \langle o_1, o_2^-|i_1, i_2^+\rangle.$$

The scattering matrix elements can be expressed in terms of the input-output operators as

$$\langle o_1, o_2^-|i_1, i_2^+\rangle = \langle 0|a_{out}(o_1)a_{out}(o_2)a_{in}^\dagger(i_1)a_{in}^\dagger(i_2)|0\rangle, \tag{3.21}$$

where $a_{in(out)}(i_n) = \Omega_{+(-)} a_{i_n} \Omega_{+(-)}^\dagger$, $\left[a_{in(out)}(i_n), a_{in(out)}^\dagger(o_n)\right] = \delta(i_n - o_n)$, and they create the input-output scattering eigenstates $a_{in}^\dagger(i_n)\left|0\right\rangle = \left|i_n^+\right\rangle$ and $a_{out}^\dagger(o_n)\left|0\right\rangle = \left|o_n^-\right\rangle$. A simple Fourier relationship relates the operators $a_{in(out)}(t)$ and $a_{in(out)}(k)$ in time and k-space as

$$a_{in(out)}(t) = \frac{1}{\sqrt{2\pi}} \int a_{in(out)}(k) e^{-ikt} dk. \tag{3.22}$$

Ref. [53, 54] provide a more detailed discussion of the scattering matrix approach in waveguide quantum electrodynamics (QED). Here we have only introduced concepts necessary to understand the next steps of our calculation.

Using the aforementioned formulation of scattering matrices, we get the S matrix for a single input photon to be

$$\langle o_1|S|i_1\rangle = \langle 0|a_{out}(o_1)a_{in}^\dagger(i_1)|0\rangle = \frac{1}{\sqrt{2\pi}} \int \langle 0|a_{out}(t)|i_1^+\rangle e^{io_1 t} dt. \tag{3.23}$$

On solving the Heisenberg equations of motion for σ_{ee} and σ_- with the given Hamiltonian, and using the definition of the input-output operators, we get

$$\frac{\mathrm{d}\sigma_{ee}}{\mathrm{d}t} = -i\sqrt{\frac{2}{\tau}} \left(\sigma_+(t)a_{in}(t) - a_{in}^\dagger(t)\sigma_-(t)\right) - \frac{2}{\tau}\left[\sigma_{ee}(t) + \frac{1}{2}\right], \tag{3.24a}$$

$$\frac{\mathrm{d}\sigma_-}{\mathrm{d}t} = i2\sqrt{\frac{2}{\tau}}\sigma_{ee}a_{in} - i\left(\omega_{eg} - i\frac{1}{\tau}\right)\sigma_- = i2\sqrt{\gamma_g}\sigma_{ee}a_{in} - i\left(\omega_{eg} - i\frac{\gamma_g}{2}\right)\sigma_-. \tag{3.24b}$$

Now, using the input-output relationship of the waveguide mode from Eq. 3.15 we get:

$$\begin{aligned}\langle 0|a_{out}|i_1^+\rangle =& \langle 0|a_{in}|i_1^+\rangle - i\sqrt{\frac{2}{\tau}}\langle 0|\sigma_-|i_1^+\rangle \\ =& \langle 0|a_{in}a_{in}^\dagger(i_1)|0\rangle - i\sqrt{\frac{2}{\tau}}\langle 0|\sigma_-|i_1^+\rangle \\ =& \frac{e^{ii_1t}}{\sqrt{2\pi}} - i\sqrt{\frac{2}{\tau}}\langle 0|\sigma_-|i_1^+\rangle.\end{aligned} \tag{3.25}$$

We solve Eq. 3.24b, and use Eq. 3.25 to arrive at the following relationships:

$$\langle 0|\sigma_-|i_1^+\rangle = \frac{1}{\sqrt{2\pi}}e^{-ii_1t}\frac{\sqrt{2/\tau}}{(i_1-\omega_{eg})+i/\tau}, \tag{3.26a}$$

$$\langle 0|a_{out}|i_1^+\rangle = \frac{1}{\sqrt{2\pi}}e^{-ii_1t}\frac{(i_1-\omega_{eg})-i/\tau}{(i_1-\omega_{eg})+i/\tau}. \tag{3.26b}$$

From there we get the S matrix to be

$$\langle o_1|S|i_1\rangle = \frac{1}{\sqrt{2\pi}}\int\langle 0|a_{out}(t)|i_1^+\rangle e^{io_1t}dt = \frac{(i_1-\omega_{eg})-i/\tau}{(i_1-\omega_{eg})+i/\tau}\delta(i_1-o_1). \tag{3.27}$$

Thus, the transmission coefficient is

$$t_{\text{1-way}} = \frac{(E_k/\hbar-\omega_{eg})-i/\tau}{(E_k/\hbar-\omega_{eg})+i/\tau}, \tag{3.28}$$

for input frequency $i_1 = E_k/\hbar$. Since there is only one mode, the transmittance $|t|^2$ is one. Similarly, the excitation amplitude is given by

$$e_k = \frac{\sqrt{2/\tau}}{(E_k/\hbar-\omega_{eg})+i/\tau}. \tag{3.29}$$

Now that we have studied the one-way propagation model, it can be extrapolated to the two-way propagation situation by introducing left and right propagating modes. We can define the Hamiltonian as

$$H/\hbar = \omega_{ge}\sigma_{ee} + \int \left(r_\omega^\dagger r_\omega - l_\omega^\dagger l_\omega\right)\omega d\omega + \frac{V}{\sqrt{v_g}}\int \left[\sigma_+\left(r_\omega + l_\omega\right) + \sigma_-\left(r_\omega^\dagger + l_\omega^\dagger\right)\right] d\omega, \quad (3.30)$$

where r_ω (l_ω) is the annihilation operator of the photons traveling right (left). In a similar fashion, we can establish the input-output relationships for the two chiral modes, and calculate the S matrix for a single photon input using the method in Ref. [52]. Upon doing that, we get

$$\langle 0|r_{out}(o_1)r_{in}^\dagger(i_1)|0\rangle = \frac{1}{2}\left(t_{\text{1-way}} + 1\right)\delta(o_1 - i_1) = t\delta(o_1 - i_1). \quad (3.31)$$

Thus, the transmission coefficient is

$$t = \frac{E_k/\hbar - \omega_{eg}}{(E_k/\hbar - \omega_{eg}) + i/\tau} = \frac{E_k/\hbar - \omega_{eg}}{(E_k/\hbar - \omega_{eg}) + i\frac{\gamma_g}{2}}, \quad (3.32)$$

which is same as the one derived using the real-space Hamiltonian approach in method I. The transfer matrix relating the input and output of the waveguide coupled to the two-level emitter is given by

$$\begin{bmatrix} L_+ \\ \\ L_- \end{bmatrix} = \begin{bmatrix} 1 - i\dfrac{J}{\Delta_k} & -i\dfrac{J}{\Delta_k} \\ \\ i\dfrac{J}{\Delta_k} & 1 + i\dfrac{J}{\Delta_k} \end{bmatrix} \begin{bmatrix} R_+ \\ \\ R_- \end{bmatrix}, \quad (3.33)$$

where $L_\pm$ ($R_\pm$) are the field amplitudes with positive and negative k-vectors on the left (right) of the two-level system.

Introducing dissipation

Until now, we have only considered that the emitter can radiate into the guided mode mode only. However, we can take system dissipation into account by considering coupling of the system with a reservoir/ bath mode with mode operators b_ω and $b_\omega^\dagger$ as shown in Fig.

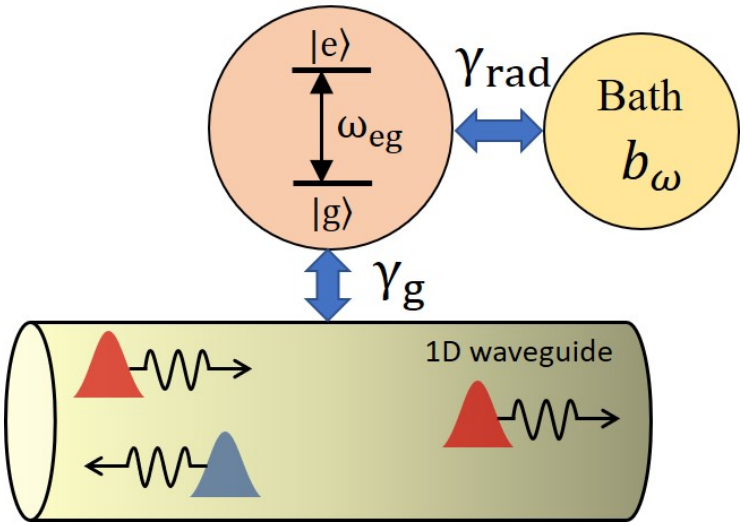

Figure 3.3: Figure showing coupling of the two-level emitter to the waveguide modes and the bath mode. The rates of emission onto the guided modes and the bath are γ_g and γ_{rad} respectively.

3.3. First, for simplicity we consider the case of uni-directional propagation. Including the new bath mode modifies the Hamiltonian in Eq. 3.13 to

$$H/\hbar = \omega_{ge}\sigma_{ee} + \int a_\omega^\dagger a_\omega \omega d\omega + \int b_\omega^\dagger b_\omega \omega d\omega + \sqrt{\frac{\gamma_g}{2\pi}} \int \left(\sigma_+ a_\omega + \sigma_- a_\omega^\dagger\right) d\omega + \sqrt{\frac{\gamma_{rad}}{2\pi}} \int \left(\sigma_+ b_\omega + \sigma_- b_\omega^\dagger\right) d\omega \quad (3.34)$$

where γ_{rad} is the decay rate into the bath mode. Using this Hamiltonian modifies Eq. 3.24b to

$$\frac{\mathrm{d}\sigma_-}{\mathrm{d}t} = i2\sqrt{\gamma_g}\sigma_{ee}a_{in} + i2\sqrt{\gamma_{rad}}\sigma_{ee}b_{in} - i\left(\omega_{eg} - i\frac{\gamma_g}{2} - i\frac{\gamma_{rad}}{2}\right)\sigma_-. \quad (3.35)$$

On solving the scattering matrix for a radiative spontaneous emission rate γ_{rad}, we find that the transmission and reflection coefficients can be readily derived by using the simple transformation $\omega_{eg} \to \omega_{eg} - i\frac{\gamma_{rad}}{2}$ [55]. In general, for n loss channels with different rates

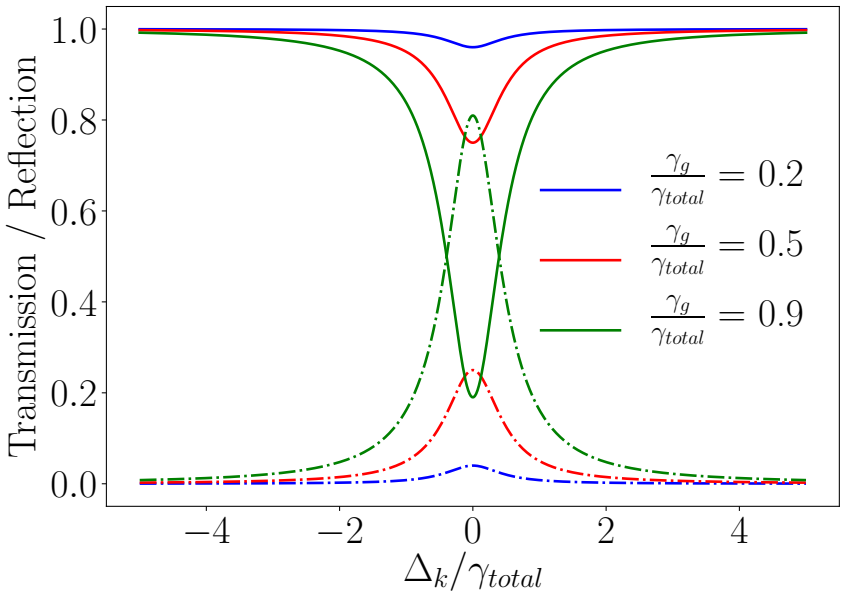

Figure 3.4: The single photon transmittance (solid line) and reflectance (dash-dotted line) for different values of γ_g/γ_{total}, where $\gamma_{total} = \gamma_g + \gamma_{rad}$, and detuning $\Delta_k = E_k/\hbar - \omega_{eg}$.

of dissipation, we can use the transformation $\omega_{eg} \to \omega_{eg} - i\sum_n \frac{\gamma_n}{2}$. We can extend this to case of the waveguide with the counter-propagating modes. Doing so, we find that the transmission coefficient is

$$t = \frac{(E_k/\hbar - \omega_{eg}) + i\frac{\gamma_{rad}}{2}}{(E_k/\hbar - \omega_{eg}) + i\left(\frac{\gamma_g}{2} + \frac{\gamma_{rad}}{2}\right)}. \tag{3.36}$$

The effect of the radiative loss is shown in Fig. 3.4. The reflectance at resonance ($\Delta_k = E_k/\hbar - \omega_{eg} = 0$) decreases as photons couple more with the radiative modes with increasing γ_{rad}. Moreover, the maximum reflectance is calculated to be $R_{max} = (\gamma_g/\gamma_{total})^2$ at resonance, as reflected in Fig. 3.4.

3.3 Photon subtraction in a waveguide

Having introduced the basics of waveguide QED, in this section we are in a position to discuss deterministic single photon using a three-level quantum emitter coupled with a waveguide.

3.3.1 Perfectly chiral waveguide

The proposed system for deterministic single photon subtraction consists of a single three-level Λ-type quantum emitter, initialized in the ground state $|1\rangle$, which is coupled to a 1D chiral waveguide. In the chiral waveguide, the light is confined at a wavelength or sub-wavelength scale. That results in significant interaction between the light's spin and orbital angular momentum. Under this kind of tight confinement, the polarization of light is no longer transverse to the direction of propagation. There is also a non-zero longitudinal component of polarization along the direction of propagation. The electric field at position r follows the time-reversal symmetry relationship $E_{-k}(r) = E_k^*(r)$ for wave-vectors k and $-k$. That implies, for a mode with transverse circular polarized light, the counter-propagating mode has circular polarization of opposite polarity [56]. Thus, the two modes can now co-exist in the chiral waveguide because of broken symmetry along the longitudinal direction of propagation.

In the ideal case with a perfectly chiral waveguide, the right-hand circularly polarized (RHCP) photons can only propagate from left to right, while the left-hand circularly polarized (LHCP) photons can only propagate from right to left. Each of the two transitions of the emitter is coupled with equal co-operativity that is much greater than unity to one of the chiral modes. Specifically, the emitter is coupled to the waveguide such that, $|1\rangle \rightarrow |3\rangle$ transition requires an RHCP photon and $|2\rangle \rightarrow |3\rangle$ transition requires an LHCP photon. The basic principle behind the SPRINT mechanism in the waveguide is similar to the case of the bi-modal cavity, and can be described as follows. When photons traveling in the waveguide from left to right interact with the Λ-type emitter, the emitter gets excited to $|3\rangle$. When the incoming light has a greater pulsewidth compared to the decay time of $|3\rangle$, there cannot be subsequent emission from the $|3\rangle \rightarrow |1\rangle$ transition, because of the destructive interference of subsequent re-emission with the incoming field [27]. Thus, the emitter can only de-excite via the $|3\rangle \rightarrow |2\rangle$ transition, thereby emitting a single photon that travels to the left. Once in state $|2\rangle$, the emitter stops interacting with the left to right propagating light.

The Hamiltonian for such a system is given by the sum of the Hamiltonian corresponding to the waveguide H_{wg}, the atomic Hamiltonian H_a, and the interaction Hamiltonian H_{int}, such that, $H = H_{wg} + H_a + H_{int}$, where,

$$H_{wg}/\hbar = \int_{-\infty}^{\infty} \left(r_\omega^\dagger r_\omega - l_\omega^\dagger l_\omega\right) \omega d\omega, \tag{3.37a}$$

$$H_a/\hbar = \omega_1 \sigma_{33} + (\omega_1 - \omega_2)\, \sigma_{22}, \tag{3.37b}$$

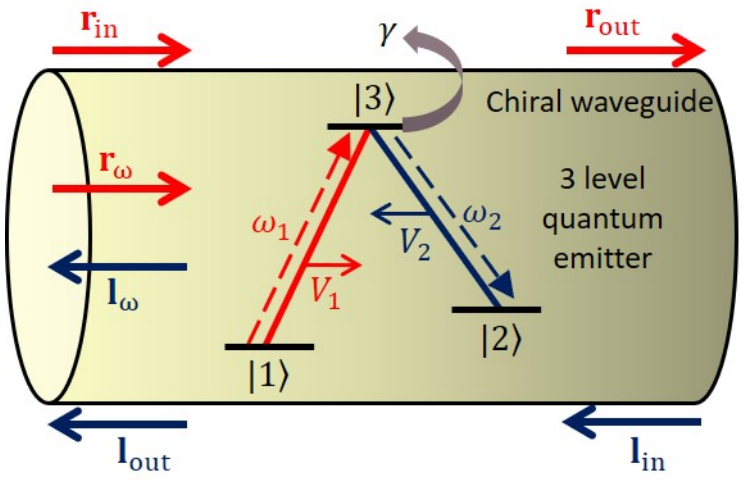

Figure 3.5: The schematic of a three-level Λ-type quantum emitter coupled with a perfectly chiral 1D waveguide.

$$H_{int}/\hbar = V_1 \int_{-\infty}^{\infty} \left(r_\omega \sigma_{31} + r_\omega^\dagger \sigma_{13}\right) d\omega + V_2 \int_{-\infty}^{\infty} \left(l_\omega \sigma_{32} + l_\omega^\dagger \sigma_{23}\right) d\omega. \tag{3.37c}$$

Here, ω_1 is the frequency of $|1\rangle \leftrightarrow |3\rangle$ transition, ω_2 is the frequency of $|2\rangle \leftrightarrow |3\rangle$ transition, and $\sigma_{ab} = |a\rangle\langle b|$ are the atomic transition operators from state $|b\rangle$ to state $|a\rangle$, $\forall\{a,b\} \in \{1,2,3\}$. r_ω and $r_\omega^\dagger$ are the bosonic creation and annihilation operators associated with the mode traveling to right, l_ω and $l_\omega^\dagger$ are the bosonic creation and annihilation operators associated with the mode traveling to left. The bosonic mode operators follow the commutation relationship $\left[l_\omega(t), l_\omega^\dagger(t')\right] = \left[r_\omega(t), r_\omega^\dagger(t')\right] = \delta(t-t')$. We consider that the modes are monochromatic circularly polarized plane waves. Our Hamiltonian is normalized by group velocity, and the annihilation operator a_ω is defined as $a_{\omega(k)} = a_k/\sqrt{v_g}$, $\forall a \in \{l, r\}$, where k is the wavevector and v_g is the group velocity of the waveguide mode. The coupling constants V_1 and V_2 with the relevant waveguide modes can be expressed as $V_1 = \sqrt{\gamma_r^{(1)}/2\pi}$ and $V_2 = \sqrt{\gamma_l^{(2)}/2\pi}$ [52, 57], with $\gamma_{r(l)}^{(i)}$ representing the spontaneous emission rate from the $|3\rangle \to |i\rangle$ transition into the right-(left-) propagating modes of the waveguide [58]:

$$\gamma_{r(l)}^{(i)} = \frac{n_{g_{r(l)}}\, \sigma_0^{(i)} \gamma_0^{(i)}}{2\, A_{mode_{r(l)}}(\vec{r})}. \tag{3.38}$$

Here, $\gamma_0^{(i)}$ is the spontaneous emission rate of the $|3\rangle \rightarrow |i\rangle$ transition in free space and $\sigma_0^{(i)}$ is resonant scattering cross section, $n_{g_{r(l)}}$ is the group index of the right- (left-) propagating mode, and $A_{m_{r(l)}}(\vec{r})$ is the effective area of the right-(left-) propagating mode for the emitter located at position $\vec{r}$. The effective area of a mode i, $A_{mode_i}(\vec{r})$, for the emitter located at position $\vec{r}$ is defined as [58]

$$A_{mode_i}(\vec{r}) = \frac{\int \epsilon(\vec{r'})|E(\vec{r'})|^2 d^3r'}{a\epsilon(\vec{r})|E(\vec{r})|^2}, \tag{3.39}$$

where a is the lattice constant of the waveguide, $E(\vec{r})$ and $\epsilon(\vec{r})$ are the electric field and the dielectric constant at position $\vec{r}$, and the integration runs over the space occupied by a unit cell of the waveguide. In our model we considered monochromatic circularly polarized plane waves propagating in the waveguide. The exact spatial field profile in the waveguide can be determined by solving the wave-guiding equations under boundary conditions determined by the particular geometry of the waveguide. But in this chapter, we will mainly focus on the photon statistics at the input and output ports of the waveguide, and will not consider the propagation of the modes inside the waveguide into account.

Since the coupling constants V_1 and V_2 only describe the interaction of the emitter with the waveguide modes, we also define the coupling efficiency of each $|3\rangle \rightarrow |i\rangle$ transition of the emitter to the two waveguide modes to account for the other decay channels as [59, 60]

$$\beta^{(i)} = \frac{\gamma_r^{(i)} + \gamma_l^{(i)}}{\gamma_r^{(i)} + \gamma_l^{(i)} + \gamma_{rad}^{(i)} + \gamma_{nr}^{(i)}}, \tag{3.40}$$

where $\gamma_{rad}^{(i)}$ is the rate of decay into non-guided radiation modes, $\gamma_{nr}^{(i)}$ is intrinsic non-radiation decay rate, and $\gamma_l^{(1)} = \gamma_r^{(2)} = 0$ in a perfectly chiral waveguide considered at the moment.

In this scenario, the single emitter co-operativity for the $|3\rangle \leftrightarrow |i\rangle$ transition is given by [58, 59]

$$C^{(i)} = \frac{\beta^{(i)}}{1 - \beta^{(i)}} = \frac{\gamma_g^{(i)}}{\gamma_{rad}^{(i)} + \gamma_{nr}^{(i)}}, \tag{3.41}$$

where $\gamma_g^{(i)}$ is the rate of spontaneous emission into the guided mode. Thus, for a perfectly chiral waveguide, $\gamma_g^{(1)} = \gamma_r^{(1)}$ and $\gamma_g^{(2)} = \gamma_l^{(2)}$. For SPRINT in the coupled emitter-waveguide system, both the modes should be symmetric and have similar co-operativity. Thus, for

simplicity we will drop the superscripts, and consider $\beta^{(1)} = \beta^{(2)} = \beta$. Also, the cooperativity can be simplified as

$$C = \frac{\beta}{1-\beta} = \frac{\sigma_0}{A_{mode}} n_{eff}, \tag{3.42}$$

where σ_0 is the dipole cross-sectional area, A_{mode} is the mode area, and $n_{eff} = c/v_g$ is the effective refractive index. Thus, we can also express the coupling efficiency as

$$\beta = \frac{\sigma_0}{\sigma_0 + A_{mode}\left(v_g/c\right)}. \tag{3.43}$$

We obtain the Heisenberg equations of motion for the mode operators r_ω and l_ω as

$$\dot{r}_\omega = -i\left[r_\omega, H\right] = -i\omega r_\omega - iV_1\sigma_{13}, \tag{3.44a}$$

$$\dot{l}_\omega = -i\left[l_\omega, H\right] = i\omega l_\omega - iV_2\sigma_{23}. \tag{3.44b}$$

The input and output mode operators can be defined as

$$r_{in}\left(t\right) = \frac{1}{\sqrt{2\pi}} \int d\omega r_\omega\left(t_0\right) e^{-i\omega\left(t-t_0\right)}, \tag{3.45a}$$

$$l_{in}\left(t\right) = \frac{1}{\sqrt{2\pi}} \int d\omega l_\omega\left(t_0\right) e^{i\omega\left(t-t_0\right)}, \tag{3.45b}$$

$$r_{out}\left(t\right) = \frac{1}{\sqrt{2\pi}} \int d\omega r_\omega\left(t_1\right) e^{-i\omega\left(t-t_1\right)}, \tag{3.45c}$$

$$l_{out}\left(t\right) = \frac{1}{\sqrt{2\pi}} \int d\omega l_\omega\left(t_1\right) e^{i\omega\left(t-t_1\right)}, \tag{3.45d}$$

where t_0 is a time long before, and t_1 is a time long after the interaction between the emitter and the pulse. These are essentially the Fourier counterparts of the frequency domain operators, and follow the commutation relationships $\left[l_{in}\left(t\right), l_{out}\left(t'\right)\right] = \left[r_{in}\left(t\right), r_{out}\left(t'\right)\right] =$

$\delta(t-t')$. Following the derivation for the input-output formalism in Ref. [49], one can arrive at the following relationships:

$$\begin{aligned}\frac{1}{\sqrt{2\pi}}\int d\omega r_\omega &= r_{in} - i\sqrt{\frac{\pi}{2}}V_1\sigma_{13} \\ &= r_{out} + i\sqrt{\frac{\pi}{2}}V_1\sigma_{13},\end{aligned} \tag{3.46a}$$

$$\begin{aligned}\frac{1}{\sqrt{2\pi}}\int d\omega l_\omega &= l_{in} - i\sqrt{\frac{\pi}{2}}V_2\sigma_{23} \\ &= l_{out} + i\sqrt{\frac{\pi}{2}}V_2\sigma_{23}.\end{aligned} \tag{3.46b}$$

From this, we can derive the input output relationship of the modes as [49]

$$r_{out} = r_{in} - i\sqrt{2\pi}V_1\sigma_{13}, \tag{3.47a}$$

$$l_{out} = l_{in} - i\sqrt{2\pi}V_2\sigma_{23}. \tag{3.47b}$$

Now, we can also write down the Master equation for the density operator ρ by plugging in the Lindbladians as

$$\begin{aligned}\dot{\rho} &= -i\left[H,\rho\right] + 2\gamma_1\mathcal{L}\left(\sigma_{13}\right)\rho + 2\gamma_2\mathcal{L}\left(\sigma_{23}\right)\rho \\ &= -i\left[H,\rho\right] + 2\gamma_1\sigma_{13}\rho\sigma_{31} + 2\gamma_2\sigma_{23}\rho\sigma_{32} \\ &\quad - \left(\gamma_1+\gamma_2\right)\left(\sigma_{33}\rho + \rho\sigma_{33}\right),\end{aligned} \tag{3.48}$$

where the Lindblad superoperator are given by $\mathcal{L}(a)\rho = a\rho a^\dagger - \frac{1}{2}\left\{a^\dagger a,\rho\right\}$, where $\{\cdot,\cdot\}$ is the anti-commutator operation. From Eq. 3.48, we arrive at the set of Optical Bloch Equations (OBEs) corresponding to the various transitions:

$$\dot{\sigma}_{11} = i\sqrt{2\pi}V_1\left(\sigma_{31}r_{in} - \sigma_{13}r_{in}^\dagger\right) + 2\left(\pi V_1^2 + \gamma_1\right)\sigma_{33}, \tag{3.49a}$$

$$\dot{\sigma}_{22} = i\sqrt{2\pi}V_2\left(\sigma_{32}l_{in} - \sigma_{23}l_{in}^\dagger\right) + 2\left(\pi V_2^2 + \gamma_2\right)\sigma_{33}, \tag{3.49b}$$

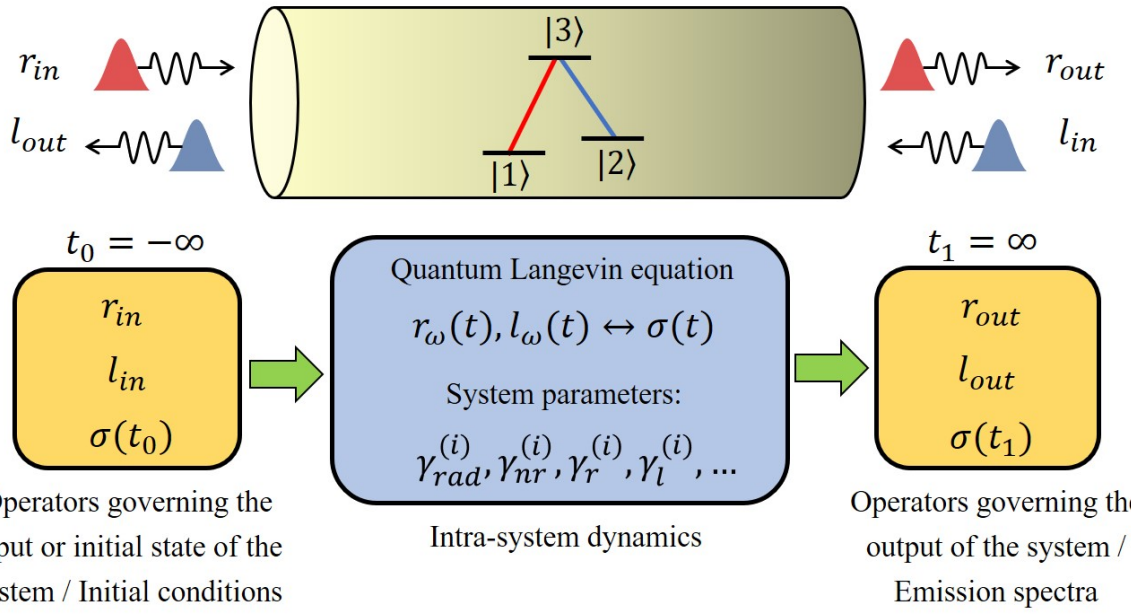

Figure 3.6: Figure illustrating the principle behind the input-output formalism for a chiral waveguide coupled with a three-level atom. Figure adapted from Ref. [61].

$$\dot{\sigma}_{33} = -i\sqrt{2\pi}V_1\left(\sigma_{31}r_{in} - \sigma_{13}r_{in}^\dagger\right) - i\sqrt{2\pi}V_2\left(\sigma_{32}l_{in} - \sigma_{23}l_{in}^\dagger\right) - 2\left[\pi\left(V_1^2 + V_2^2\right) + \gamma_1 + \gamma_2\right]\sigma_{33}, \tag{3.49c}$$

$$\dot{\sigma}_{12} = i\sqrt{2\pi}V_1\sigma_{32}r_{in} - i\sqrt{2\pi}V_2\sigma_{13}l_{in}^\dagger - i\left(\omega_1 - \omega_2\right)\sigma_{12}, \tag{3.49d}$$

$$\dot{\sigma}_{13} = i\sqrt{2\pi}V_1\left(\sigma_{33} - \sigma_{11}\right)r_{in} - i\sqrt{2\pi}V_2\sigma_{12}l_{in} - \left[\pi\left(V_1^2 + V_2^2\right) + \gamma_1 + \gamma_2 + i\omega_1\right]\sigma_{13}, \tag{3.49e}$$

$$\dot{\sigma}_{23} = i\sqrt{2\pi}V_2\left(\sigma_{33} - \sigma_{22}\right)l_{in} - i\sqrt{2\pi}V_1\sigma_{21}r_{in} - \left[\pi\left(V_1^2 + V_2^2\right) + \gamma_1 + \gamma_2 + i\omega_2\right]\sigma_{23}. \tag{3.49f}$$

The OBEs for σ_{21}, σ_{31}, and σ_{32} can be calculated easily by taking the complex conjugates of OBEs for σ_{12}, σ_{13}, and σ_{23} respectively. Here it must be noted that the system is

composed of the emitter and the waveguide, and thus, the spontaneous emission rates, $2\gamma_1$ $(= \gamma_{rad}^{(1)} + \gamma_{nr}^{(1)})$ and $2\gamma_2$ $(= \gamma_{rad}^{(2)} + \gamma_{nr}^{(2)})$, in the OBEs are the spontaneous emission rates into the radiative and non-radiative modes that are not coupled with the waveguide. This set of coupled differential equations dictate the entire dynamics of the photon subtraction process.

Fig. 3.6 illustrates the core principle behind the input-output formalism for a chiral waveguide coupled with a three-level atom. The initial condition of the mode operators and the atom (which is treated as a bath here) at $t = t_0 = -\infty$ is the *input* of the system. The dynamics of the system is governed by the quantum Langevin equations, which take into account the contributions from different system parameters. The *output* of the system is given by the the state of the system operators at $t = t_1 = \infty$. The quantities t_0 and t_1 have been defined in Eq. 3.45. The output of the system gives access to the emission spectrum, and experimentally observed quantities like transmitance, reflectance, state of the emitter, etc.

3.3.2 Imperfectly chiral waveguide

The previous formulation is true only in the ideal limit. The schematic of a three-level Λ system coupled with an imperfectly chiral waveguide is shown in Fig. 3.7. This effectively modifies our Hamiltonian to $H = H_{wg} + H_a + H_{int}$, where

$$H_{wg}/\hbar = \int_{-\infty}^{\infty} \left(r_{\omega 1}^{\dagger} r_{\omega 1} + r_{\omega 2}^{\dagger} r_{\omega 2} - l_{\omega 1}^{\dagger} l_{\omega 1} - l_{\omega 2}^{\dagger} l_{\omega 2} \right) \omega d\omega, \tag{3.50a}$$

$$H_a/\hbar = \omega_1 \sigma_{33} + (\omega_1 - \omega_2)\, \sigma_{22}, \tag{3.50b}$$

$$\begin{aligned} H_{int}/\hbar = {} & V_{1R} \int_{-\infty}^{\infty} \left(r_{\omega 1} \sigma_{31} + r_{\omega 1}^{\dagger} \sigma_{13} \right) d\omega + V_{2L} \int_{-\infty}^{\infty} \left(l_{\omega 2} \sigma_{32} + l_{\omega 2}^{\dagger} \sigma_{23} \right) d\omega \\ & + V_{1L} \int_{-\infty}^{\infty} \left(l_{\omega 1} \sigma_{31} + l_{\omega 1}^{\dagger} \sigma_{13} \right) d\omega + V_{2R} \int_{-\infty}^{\infty} \left(r_{\omega 2} \sigma_{32} + r_{\omega 2}^{\dagger} \sigma_{23} \right) d\omega. \end{aligned} \tag{3.50c}$$

The coupling constants are defined in a way that is similar to the ideal case, i.e., $V_{1R} = \sqrt{\gamma_r^{(1)}/2\pi}$, $V_{1L} = \sqrt{\gamma_l^{(1)}/2\pi}$, etc.

To include the anticipated non-idealities associated with an imperfectly directional waveguide into our model, we define the quantitative chirality of a waveguide as

$$\xi = \frac{V_{1R}^2}{V_{1R}^2 + V_{1L}^2} = \frac{V_{2L}^2}{V_{2R}^2 + V_{2L}^2}. \tag{3.51}$$

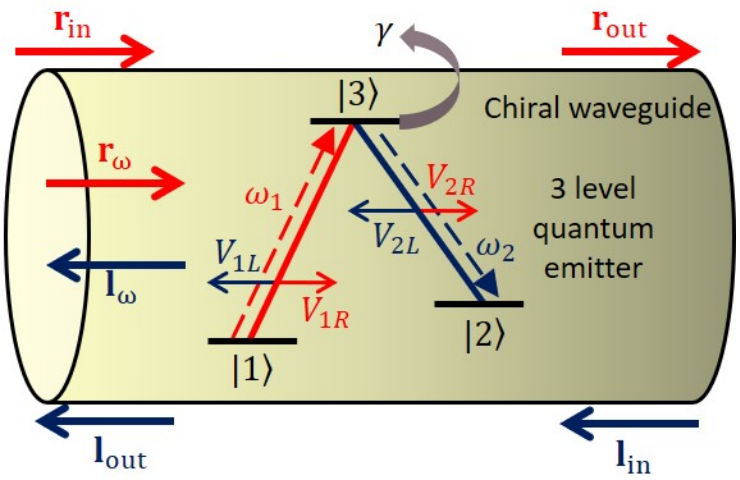

Figure 3.7: The schematic of a three-level Λ-type quantum emitter coupled with an imperfectly chiral waveguide.

If we define $\mathscr{V}_1^2 = V_{1R}^2 + V_{1L}^2$, and $\mathscr{V}_2^2 = V_{2R}^2 + V_{2L}^2$, the coupling strength of the $|1\rangle \leftrightarrow |3\rangle$ transition with the right propagating mode is then given by $V_{1R} = \sqrt{\xi}\mathscr{V}_1$, and the coupling strength with the left propagating mode is $V_{1L} = \sqrt{1-\xi}\mathscr{V}_1$. Similarly, we can define $V_{2L} = \sqrt{\xi}\mathscr{V}_2$, and $V_{2R} = \sqrt{1-\xi}\mathscr{V}_2$ for the $|2\rangle \leftrightarrow |3\rangle$ transition.

The modified Hamiltonian gives us the modified Heisenberg equations of motion for r_ω and l_ω,

$$\dot{r}_\omega = -i\omega r_\omega - i\left(V_{1R}\sigma_{13} + V_{2R}\sigma_{23}\right), \tag{3.52a}$$

$$\dot{l}_\omega = i\omega l_\omega - i\left(V_{2L}\sigma_{23} + V_{1L}\sigma_{13}\right), \tag{3.52b}$$

and the modified input-output relations,

$$r_{out} = r_{in} - i\sqrt{2\pi}\left(V_{1L}\sigma_{13} + V_{2R}\sigma_{23}\right), \tag{3.53a}$$

$$l_{out} = l_{in} - i\sqrt{2\pi}\left(V_{2L}\sigma_{23} + V_{1L}\sigma_{13}\right). \tag{3.53b}$$

Similarly, the OBEs will be replaced by a new set of coupled differential equations and solving that would give us the transition rates and occupation probabilities of the emitter.

3.3.3 Probability of single photon subtraction

I. Perfectly chiral waveguide

We define a successful deterministic subtraction as an event where a single photon is subtracted from the input optical pulse, and sent to the left-propagating output, while the emitter ends in state $|2\rangle$ and stops interacting with the right-propagating input field . The probability of such event in time τ can be expressed as the integral of the expectation value of the number operator for that mode over time τ. Thus, the probability of a successful deterministic subtraction for a perfectly chiral waveguide is given by

$$\begin{aligned} P &= \int_0^\tau \langle l_{out}^\dagger l_{out} \rangle dt \\ &= \int_0^\tau 2\pi V_2^2 \langle \sigma_{33} \rangle dt. \end{aligned} \tag{3.54}$$

Once in state $|2\rangle$, the emitter no longer interacts with the incoming field. Detecting a single photon in the left-propagating mode, or detecting the atom in $|2\rangle$ can act as experimental heralding signals to confirm the subtraction of a single photon. Since we assumed high co-operativity of the guided modes to ensure success of SPRINT, we can expect the subtracted photon to go into a guided mode, rather than into some radiation mode with high probability. In the limits of ideal chirality and for large co-operativity, calculating the expression given in Eq. 3.54 is essentially similar to calculating the probability of the atom ending up in state $|2\rangle$, mathematically expressed by $\langle \sigma_{22}(\tau) \rangle$.

Here, it must also be noted that in the low co-operativity regime, the emission of a single photon into the radiation mode also counts as an event of photon subtraction from the input mode. In that scenario, one cannot detect the subtracted photon in the left-propagating mode to ensure that subtraction has indeed taken place. If the emitter makes $|3\rangle \rightarrow |2\rangle$ transition while radiating to the bath, detecting the emitter in state $|2\rangle$ might be a stronger heralding/ post-selective measurement to experimentally ensure photon subtraction has happened. However, unfortunately, for low co-operativity, the emitter might also undergo the $|3\rangle \rightarrow |1\rangle$ transition, and emit a photon into the radiation mode. That re-initializes the emitter to $|1\rangle$, and it can undergo another SPRINT interaction, thereby subtracting more than one photon before finally ending up in $|2\rangle$. However, for weak input signals, the chances of that happening is low.

II. Imperfectly chiral waveguide

Following the previous definition of the probability of single photon subtraction in a chiral waveguide, we can define the probability of subtraction in an imperfectly chiral waveguide as

$$\begin{aligned} P &= \int_0^\tau \langle l_{out}^{(2)\dagger} l_{out}^{(2)} \rangle dt \\ &= \int_0^\tau 2\pi V_{2L}^2 \langle \sigma_{33} \rangle dt \\ &= \int_0^\tau 2\pi \xi \mathscr{V}_2^2 \langle \sigma_{33} \rangle dt, \end{aligned} \tag{3.55}$$

where $l_{out}^{(2)} = l_{in} - i\sqrt{2\pi} V_{2L} \sigma_{23}$. This corresponds to the probability of collecting a single photon in the left output while the emitter relaxes to state $|2\rangle$, thereby signalling a successful single photon subtraction, and can also be expressed as $\sim \xi \langle \sigma_{22}(\tau) \rangle$ in the high co-operativity regime.

It is important to note that even if the emitter ends up in $|2\rangle$, but the emitted photon couples to the right-travelling mode since $\xi \neq 1$, the emitter will become transparent to the incoming field. However, it cannot be considered to be a successful event of photon subtraction. Thus, experimentally one can ensure that a successful subtraction has taken place only if the atom is detected in $|2\rangle$, and there is a single photon detected in the left-propagating mode. Eq. 3.55 essentially gives the probability of such an event occurring.

However, the mean number of photons from the input mode might slightly differ from P, since a photon lost to the radiative mode also constitutes an event of successful subtraction. The emitter might radiate to the bath while making either $|3\rangle \to |1\rangle$ or $|3\rangle \to |2\rangle$ transition. If it makes the $|3\rangle \to |1\rangle$ transition, the number of photons subtracted from the input field can be greater than one as discussed earlier. But unfortunately, it is difficult to experimentally verify that a successful event of subtraction has happened in that case. We can safely ignore such rogue events if we can satisfy the criteria of high co-operativity.

III. Alternative benchmark for photon subtraction

Another alternative benchmark for photon subtraction that could be used is the difference in the total number of photons going into the waveguide, and the total number of photons

detected at the output on the waveguide on the right. Mathematically, it can be expressed as

$$N_{sub} = \int_0^\tau \left(\langle r_{in}^\dagger r_{in} \rangle - \langle r_{out}^\dagger r_{out} \rangle \right) dt. \tag{3.56}$$

In the limits of perfect coupling and chirality and high co-operativity, it is essentially the same as the definition of probability given in Eq. 3.54, and saturates at unity. However, as discussed earlier, for low co-operativity there can be situations where more than one photon is subtracted from the incoming field.

3.4 Numerical simulations and results

In the previous section we have seen how we can derive the OBEs using the input-output relationships. For a given type of input optical signal $|\psi_{in}\rangle$, we calculate the expectation values $\langle \dot{\sigma}_{ab} \rangle = \langle \psi_{in} | \dot{\sigma}_{ab} | \psi_{in} \rangle$ for all a's and b's from Eq. 3.48. This gives us a set of differential equations for each kind of optical input which is solved using Python under the constraint that $\langle \sigma_{11}(0) \rangle = 1$, i.e., the emitter is in state $|1\rangle$ initially. Solving them gives us the expectation values of the atomic operators, from which we can calculate the probability of a successful single photon subtraction using Eq. 3.55.

3.4.1 Different optical inputs

For our simulations, we consider three different kinds of input optical signals to the waveguide. First, we consider a continuous-wave coherent input state. Then we consider the case of a coherent Gaussian input pulse, and pulsed Fock state inputs for calculating the photon subtraction probabilities.

For continuous-wave coherent input $|\alpha\rangle$ in the r_{in} mode, such that

$$r_{in} |\alpha\rangle = \frac{\alpha}{\sqrt{2\pi}} \exp(-i\omega t) |\alpha\rangle, \tag{3.57}$$

we can directly calculate the expectation values of $\langle \dot{\sigma}_{11} \rangle$, $\langle \dot{\sigma}_{33} \rangle$ and $\langle \dot{\sigma}_{13} \rangle$ in the rotating frame from Eqs. 3.49a, 3.49c and 3.49e respectively.

$$\langle \dot{\sigma}_{11} \rangle = iV_1 \left(\langle \sigma_{31} \rangle \alpha - \langle \sigma_{13} \rangle \alpha^* \right) + 2 \left(\pi V_1^2 + \gamma_1 \right) \langle \sigma_{33} \rangle, \tag{3.58a}$$

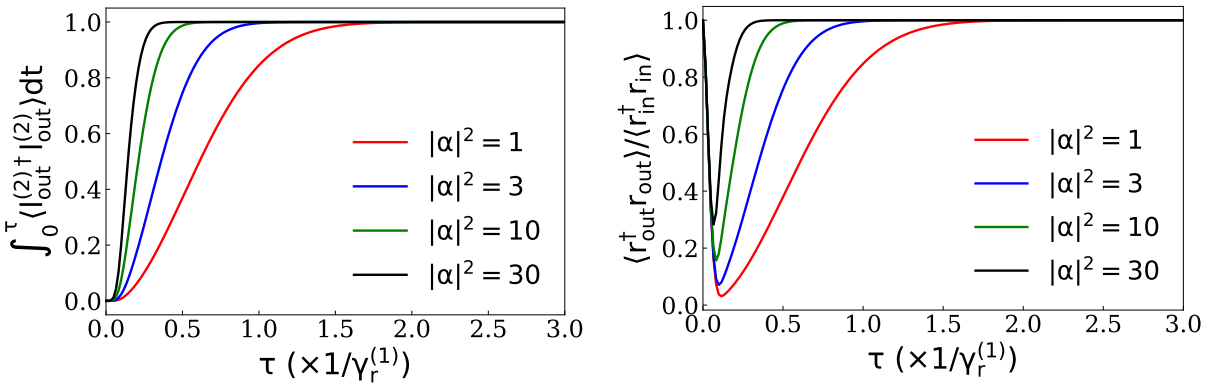

(a) (b)

Figure 3.8: (a) The probability of a successful single photon subtraction and, (b) instantaneous transmission as a function of time for a continuous-wave coherent source of light as input for the case of a perfectly chiral waveguide with ideal coupling efficiency ($\xi = \beta = 1$), and assuming $\gamma_r^{(1)} = \gamma_l^{(2)}$, which means $V_1 = V_2$. The chances of single photon subtraction at an earlier time increases with an increase in $|\alpha|^2$, which is the rate of the average number of photons arriving into the system in MHz.

$$\langle \dot{\sigma}_{33} \rangle = -iV_1 \left(\langle \sigma_{31} \rangle \alpha - \langle \sigma_{13} \rangle \alpha^* \right) - 2 \left[\pi \left(V_1^2 + V_2^2 \right) + \gamma_1 + \gamma_2 \right] \langle \sigma_{33} \rangle, \tag{3.58b}$$

$$\langle \dot{\sigma}_{13} \rangle = iV_1 \left(\langle \sigma_{33} \rangle - \langle \sigma_{11} \rangle \right) \alpha - \left[\pi \left(V_1^2 + V_2^2 \right) + \gamma_1 + \gamma_2 + i \left(\omega_1 - \omega \right) \right] \langle \sigma_{13} \rangle. \tag{3.58c}$$

Next, using the identity for the Laplace transform of a derivative, $\mathscr{L}\left[\langle \dot{\sigma}_{33} \rangle\right] = s\mathscr{L}\left[\langle \sigma_{33} \rangle\right] - \langle \sigma_{33}(0) \rangle$, we get three simultaneous equations for $\langle \sigma_{11}(s) \rangle$, $\langle \sigma_{33}(s) \rangle$, and $\langle \sigma_{13}(s) \rangle$. On solving the set of equations under the constraint that the emitter is initialised in state $|1\rangle$, i.e., $\langle \sigma_{11}(s) \rangle = 1$, we get

$$\langle \sigma_{33}(s) \rangle = \frac{2V_1^2 |\alpha|^2 \{ s + \pi (V_1^2 + V_2^2) + \gamma_1 + \gamma_2 \}}{\left[\begin{array}{l} 4V_1^2 |\alpha|^2 (s + \pi V_2^2 + \gamma_2) \{ s + \pi (V_1^2 + V_2^2) + \gamma_1 + \gamma_2 \} \\ \quad + s[s + 2\{\pi (V_1^2 + V_2^2) + \gamma_1 + \gamma_2\}][\{ s + \pi (V_1^2 + V_2^2) + \gamma_1 + \gamma_2)^2 + (\omega_1 - \omega)^2 \} \end{array} \right]}. \tag{3.59}$$

Thus, for a waveguide with chirality ξ, the probability of observing a photon in the left-propagating mode coming from the $|3\rangle \rightarrow |2\rangle$ transition is

$$
\begin{aligned}
P &= \int_0^\infty 2\pi V_{2L}^2 \langle \sigma_{33} \rangle dt \\
&= 2\pi V_{2L}^2 \lim_{s\to 0} s \frac{\mathscr{L}\left[\langle \sigma_{33} \rangle\right]}{s} = \frac{\pi \xi \mathscr{V}_2^2}{\pi \mathscr{V}_2^2 + \gamma_2} \\
&= \frac{\xi}{1 + (2\gamma_2/\pi \mathscr{V}_2^2)} = \frac{\xi}{1 + 2\gamma_2/\gamma_g} = \xi\beta.
\end{aligned} \tag{3.60}
$$

In the limit of strong coupling ($\beta \sim 1$), such that $\gamma_g^{(2)} \gg 2\gamma_2$, and $V_2 \gg \sqrt{\gamma_2/\pi}$, we always get unity probability of the event of successful single photon subtraction for arbitrary strength of the input field, and a perfectly chiral waveguide ($\xi = 1$). As can be seen from Fig. 3.8, the time at which unit probability is reached, and the emitter becomes transparent to the incoming field decreases as we increase the average photon number arriving into the system per unit time, since the emitter can be more easily excited if the input has larger number of photons. Also, the transmission doesn't quite drop off to zero for higher rate of photon input, since the rate of atomic decay can only absorb one photon. Also, the emission from $|3\rangle \to |1\rangle$ transition cannot destructively interfere with the high rate of incident photons. For the simulations we used $\gamma_0 = 2\pi \times 5.2227$ MHz corresponding to D2 transition in Cesium (Cs) atoms.

However, for practical purposes, the performance of the photon subtraction scheme is more intriguing when the input into the system is a pulsed state of light. When a Gaussian pulsed coherent state defined by [62]

$$
\alpha(t) = \frac{\sqrt{2\bar{n}}}{\sqrt[4]{\pi\tau^2}} \exp\left\{\left(2t^2/\tau^2\right)\right\}, \tag{3.61}
$$

and satisfying the property $r_{in}(t)|\alpha\rangle = \alpha(t)|\alpha\rangle$, is sent into the system, the controllable parameters are the pulsewidth τ, and the average photon number $\langle n \rangle$. Using the methodology shown previously, one can calculate the equations for $\langle \dot{\sigma}_{ab} \rangle$, and solve them numerically. After solving them numerically we observe, for a constant average photon number, the probability of a single photon subtraction increases with increase in pulsewidth, until it saturates to a constant value, as shown in Fig. 3.9a.

It is important to notice that the probability of a successful single photon subtraction is less than unity for small values of average input photon number, even in the ideal limit of chirality and coupling efficiency being set to one. This is similar to the results we observed in Chapter 2, where we found that the probability of single photon subtraction is less than

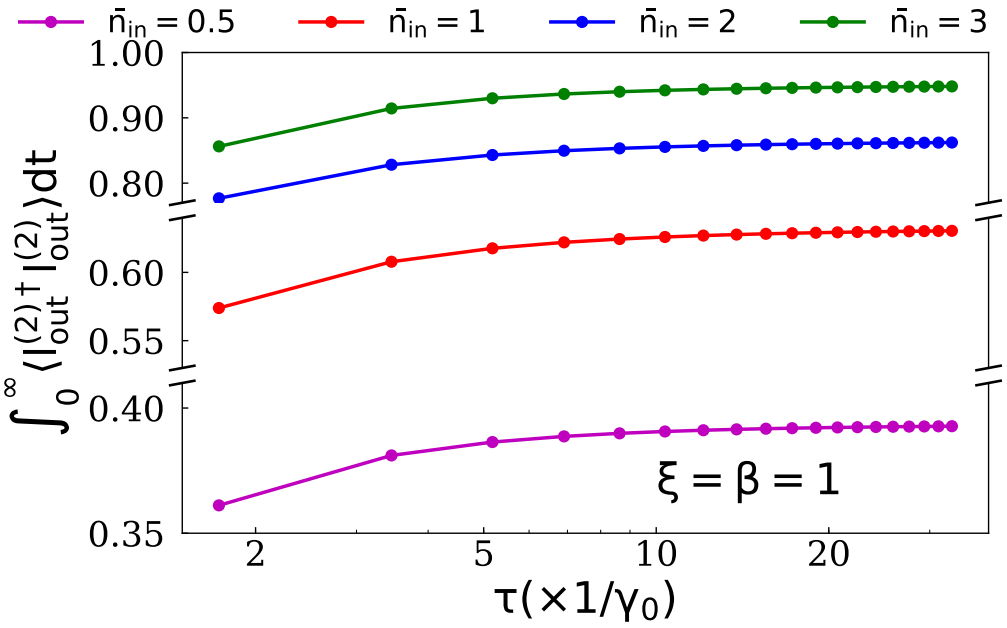

(a)

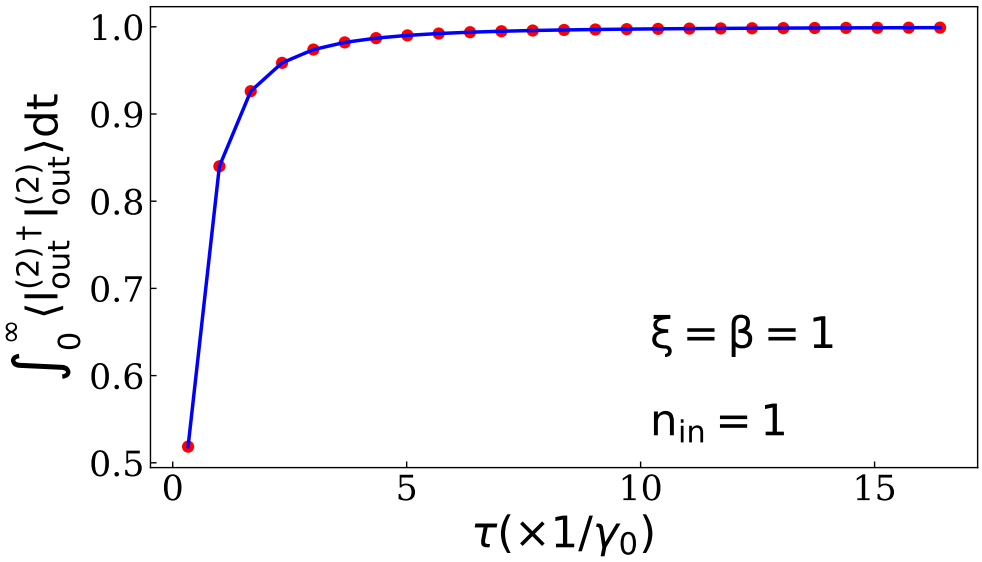

(b)

Figure 3.9: The probability of the event of a successful single photon subtraction as a function of the pulsewidth for (a) pulsed coherent input ($\bar{n}_{in} = 0.5, 1, 2, 3$) and (b) Fock state input ($n_{in} = 1$) with perfect chirality and coupling efficiency. For both of them, an increase in the probability P is observed with an increase in the pulsewidth τ.

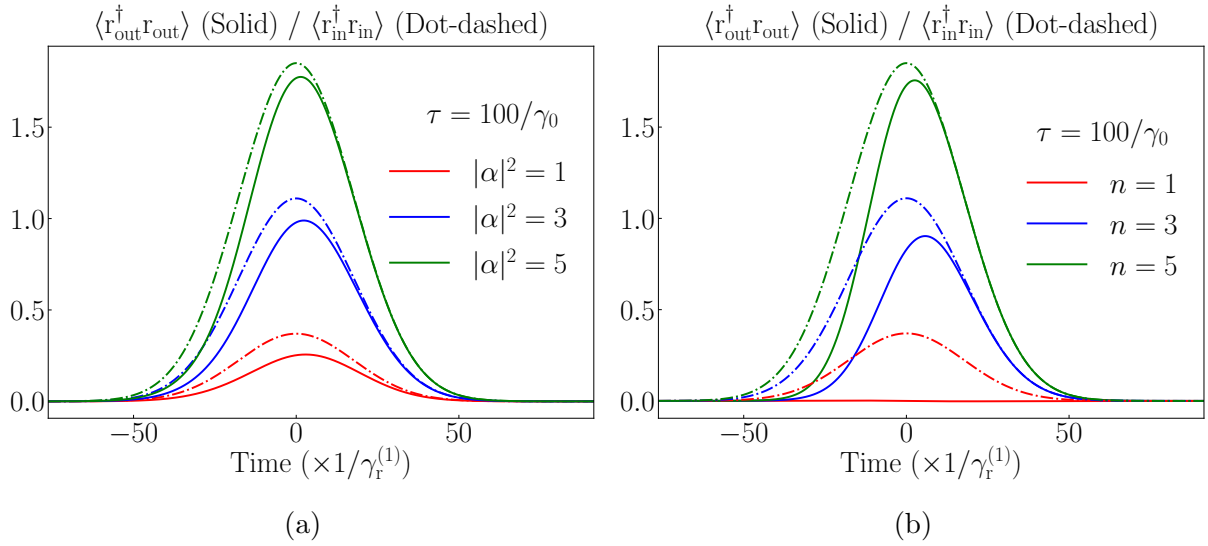

Figure 3.10: The right-propagating input (dot-dashed) and the output (solid) pulse shape for (a) pulsed coherent input ($\bar{n}_{in} = 1, 3, 5$) and (b) Fock state input ($n_{in} = 1, 3, 5$) of pulsewidth $\tau = 100/\gamma_0$. For this simulation perfect chirality and coupling efficiency was considered.

one when the cavity was initialized in a coherent state. The average number of photons subtracted increases with an increase in $\bar{n}_{in}$, and $\bar{n}_{out}$ converges to $\bar{n}_{in} - 1$ for $\bar{n}_{in} \sim 4$ (in our simulation with $\tau = 100/\gamma_0$), as shown in Fig. 3.11a. This is similar to the results recently reported from our group for numerical simulation of photon subtraction with a charged QD coupled to a bi-modal cavity [41]. Fig. 3.10a shows the number of photons in the right-propagating input pulse, and the right-propagating output of the waveguide. The difference in the area of the curves gives the expectation value of the number of subtracted photons.

Next, we consider the case of a pulsed Fock state input. The N photon Fock state with N independent single photon wave packets defined by their Gaussian amplitude profile $\alpha(t)$ is defined as [62]

$$|N\rangle = \frac{\left(r^\dagger_{in,\alpha}\right)^N}{\sqrt{N!}} |0\rangle \,, \tag{3.62}$$

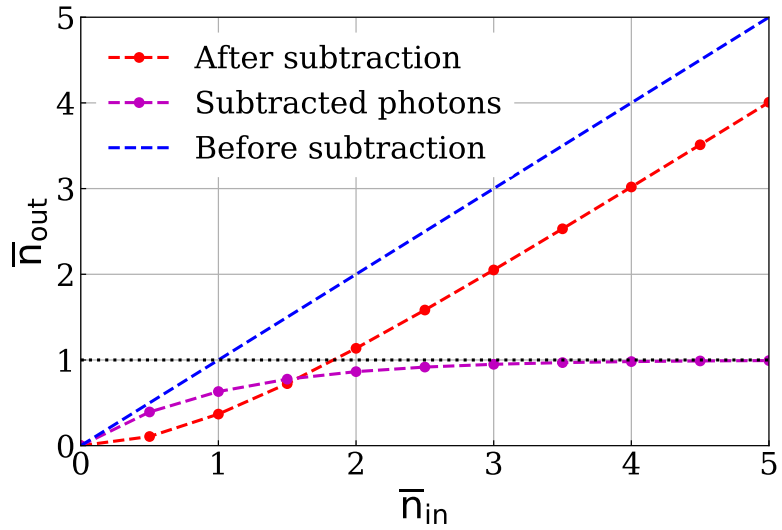

(a)

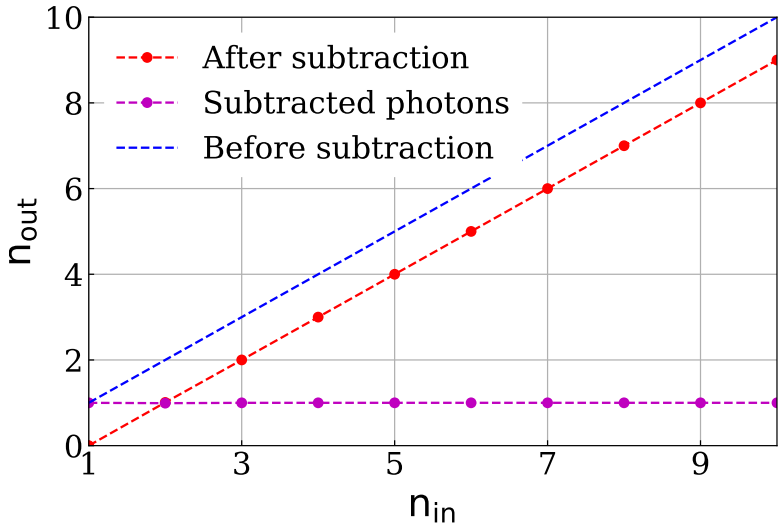

(b)

Figure 3.11: The variation in the number of subtracted photons for different input photon numbers for (a) pulsed coherent input, and (b) Fock state input with perfect chirality and coupling efficiency. For both the simulations $\tau = 100/\gamma_0$, and $\xi = \beta = 1$.

where $r^{\dagger}_{in,\alpha}$ is the photon wave-packet creation operator given by

$$r^{\dagger}_{in,\alpha}(t) = \int dt\alpha(t)r^{\dagger}_{in}(t) = \int d\omega\alpha(\omega)r^{\dagger}_{in}(\omega), \tag{3.63}$$

where $\int |\alpha(t)|^2 dt = \int |\alpha(\omega)|^2 d\omega = 1$. We can again write down the expectation values of the rate of change of the time derivative of the density matrix elements to numerically calculate the probability of a successful single photon subtraction.

Once again, just like in the case of a pulsed coherent state input, we observe that the probability of photon subtraction increases with an increase in pulsewidth τ, as shown in Fig. 3.9b. However, unlike the case of coherent pulses, for Fock state input the probability of single photon subtraction reaches unity even for values of input photon number as low as one, in the ideal limit of perfect chirality, and coupling efficiency. Once again, this corroborates our simulations in Chap. 2, where we observed a photon subtraction probability of unity even with photon numbers as low as one, for a Fock state input. The variation in the number of subtracted photons with input photon number is shown in Fig. 3.11b, and displays a similar trend to what was recently predicted for the bi-modal cavity platform from our group [41]. Fig. 3.10b shows the number of photons in the right-propagating input pulse, and the right-propagating output of the waveguide. We can see, that for a single photon Fock state input, the entire photon has been reflected back, and the expectation value of the number of right-propagating photons at the output is zero.

It thus appears that, in the ideal limit, chiral waveguides are essentially equivalent to bi-modal cavities in SPRINT-based photon subtraction. The primary difference is that is that there is no frequency selectivity provided by the presence of a cavity mode, and the desired photon emission by the $|3\rangle \rightarrow |2\rangle$ transition relies only on a proper combination of selection rules, and the chirality of the waveguide. As a result, realizing photon subtraction with a chiral waveguide, and an emitter with a more complicated level structure, such as found in alkali atoms, will require a proper selection of the states forming the Λ-system.

3.4.2 Experimental feasibility

(I) Parameterization

In Section 3.3.1 we assumed our systems to be perfectly chiral, namely $\xi = 1$. We also assumed that the coupling efficiency between the atomic transition modes and the waveguide modes are unity, i.e., $\beta = 1$. Now, the dependence of the probability of single photon subtraction on the coupling constant of the transitions, the chirality of the waveguide and

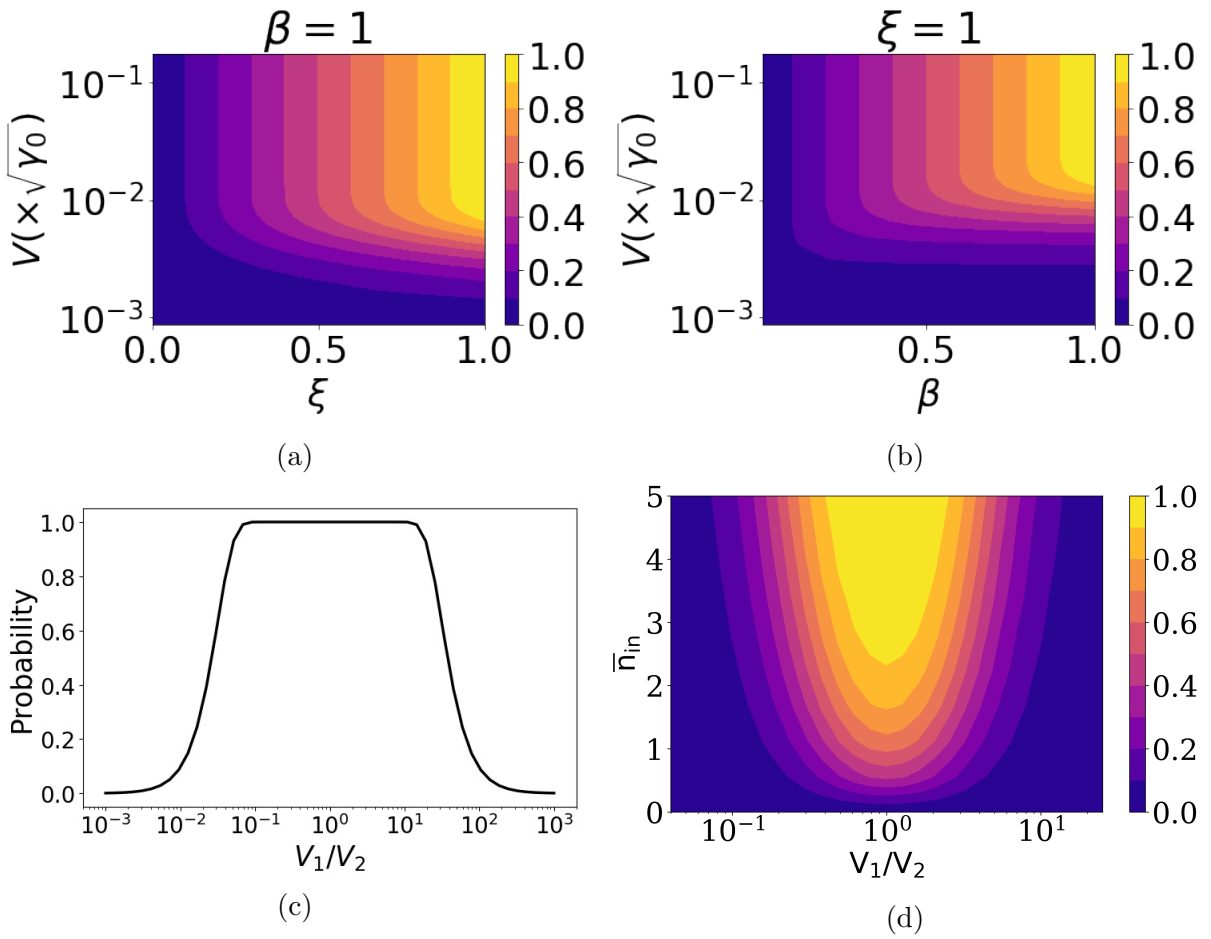

Figure 3.12: Contour plots showing the dependence of (a) the coupling strength V and the chirality ξ (with $\beta = 1$), and (b) the coupling strength V and the coupling efficiency β (with $\xi = 1$) on the probability of photon subtraction. From the plots we observe that the probability of a successful single photon subtraction is not a strong function of the coupling strength, but instead is a function of the chirality ξ, and the coupling efficiency β of the system, as long as the coupling strength is not too small. (c) The variation of probability of single photon subtraction from a continuous-wave coherent input as a function of ratio of coupling strengths. (d) Average number of photons subtracted from a coherent pulse of width $\tau = 100/\gamma_0$ as a function of the mean photon number of the input pulse, and the ratio of coupling strengths. Once again $\xi = \beta = 1$ was considered.

the coupling efficiency are considered. Fig. 3.12a and 3.12b shows that the probability is not explicitly dependent upon the coupling strength (as long as it is not too small), but is a function of the chirality of the waveguide and the coupling efficiency. Thus, given the chirality of a waveguide, and the coupling efficiency of the emitter's transitions to the modes of the waveguide, we should be able to predict the performance of the emitter-waveguide system as a potential candidate for single photon subtraction.

The success of SPRINT relies upon the symmetry of the emitter system. The parameters related to the two emitter transitions corresponding to the two modes must be ideally equal. Thus, we check the probability of a successful single photon subtraction from a continuous-wave coherent input with $|\alpha|^2 = 1$ by varying the ratio of coupling constants. For simplicity, $\xi = \beta = 1$ was considered for the simulation and the coupling strength V_1 was fixed (while V_2 was varied). Fig. 3.12c shows that ideally the coupling strengths should be as similar as possible, with a maximum permissible difference of an order of magnitude.

We also plot the number of photons subtracted as a function of the average photon number of a pulsed coherent input, and the ratio of the two coupling strengths, as shown in Fig. 3.12d. Once again, the probability of single photon subtraction is symmetric around the peak at $V_1 = V_2$, and also increases with increasing $\bar{n}_{in}$. Thus, once can compensate for a little mismatch in symmetry of the coupling strengths by increasing the intensity of the input, as long as the asymmetry isn't too high.

(II) Different emitter-waveguide systems

Finally, we plot the probability of a single photon subtraction as a function of the waveguide's chirality and coupling efficiency for a continuous-wave coherent optical input in Fig. 3.13 to predict the upper limit of single photon subtraction probabilities for some of the recently reported experimental emitter-waveguide platforms, with the effects of the waveguide mode area and group index shown in the inset.

A laser-cooled Cesium atom coupled with a chiral nanofiber (NF) [63, 64] is one of the most extensively studied emitter-waveguide systems. Though the nanofiber shows a fairly high chirality ($\xi = 0.92$) [56], the coupling efficiency β is not very high. For example, it can reach $\sim 0.2 - 0.28$ depending on the specific selected transition in the D_2–line of Cs atom (it goes up to a maximum of $\beta \sim 0.28$ for the $M_e = \pm 5$ sublevel) in the hypothetical scenario when the atom is located directly on the surface of the nanofiber with a radius of $a = 200$nm [63, 65]. Practically though, it is not possible to put the atom directly on the surface of the nanofiber, and the coupling efficiency decays exponentially as a function of distance from the nanowire. Fig. 3.13 shows the predicted probability of single photon subtraction for the Cesium atom on the surface of the nanofiber ($r/a = 1$), and in a

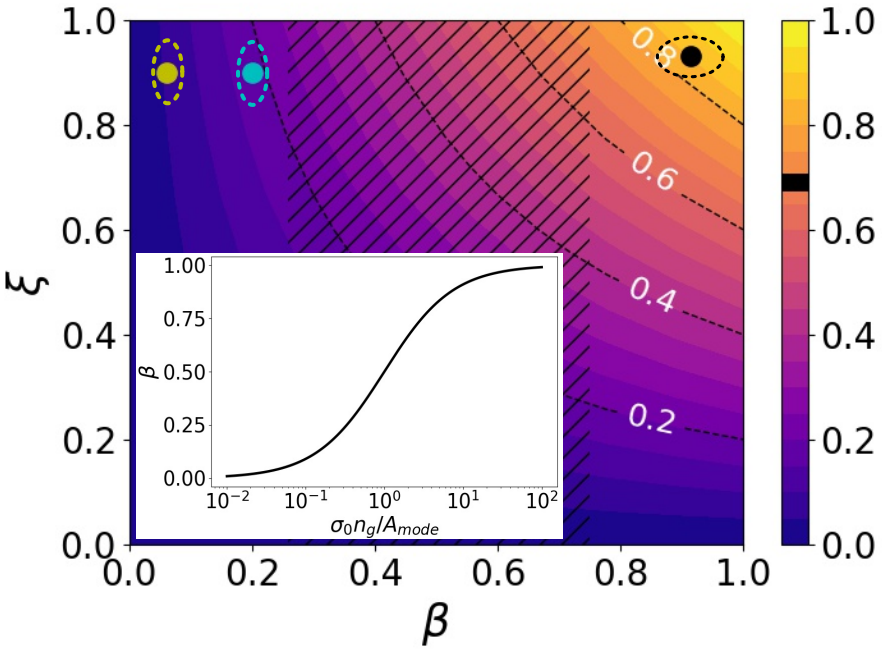

Figure 3.13: Contour plot showing the photon subtraction probabilities for (i) cold Cs atoms on the surface of a nanofiber ($r/a = 1$) (cyan dot), and (ii) 215nm away from the surface of a nanofiber ($r/a = 2$) of radius $a = 215$nm (yellow dot), (iii, iv) cold Cs atoms and APCW for guided modes with group index n_g between 2 and 10 (hatched region), (v) charged QDs and PCW (black dot), and (vi) for a Rb-microresonator system (black bar) as reported in Ref. [27] for a continuous-wave coherent input. Inset shows the dependence of coupling efficiency on $\sigma_0 n_g/A_{mode}$.

more realistic case, if the atom is trapped 215nm away from the surface ($r/a = 2$) of a nanofiber with $\beta \sim 0.06 - 0.08$ [66]. We see that an atom coupled to a nanofiber is not an ideal system to be used for deterministic photon subtraction. This is not particularly surprising as the coupling efficiency is less than 0.5, implying a co-operativity of $C < 1$. For SPRINT to be successful in photon subtraction, the emitter should interact predominantly with the guided mode, compared to other parasitic radiation and non-radiation modes, i.e., the co-operativity should be greater than unity. At the same time, this platform offers some interesting advantages. Compared to probabilistic single photon subtraction implemented with a beamsplitter and photon detector, this system may provide a more robust heralding mechanism that does not have to rely on a single-shot measurement of a photon, since a successful subtraction can be confirmed by measuring the final state of the atom. Additionally, although the tapered nanofiber cannot compete in terms of coupling

efficiency with photonic crystal waveguides that we will discuss shortly, the positioning requirement is significantly relaxed in this platform as the nanofiber chirality is independent of the location of the atom along the fiber [60].

The use of photonic crystal waveguides (PCWs) instead of a plain nanofiber opens the possibilities to increase both the chirality and the coupling efficiency, e.g., through group velocity engineering. In particular, the effects of group velocity on the emitter's coupling efficiency to the mode of the waveguide can be illustrated well in the regime when the non-radiative decay can be neglected. In this regime, the co-operativity of the emitter with respect to a specific waveguide mode, can be written as $C = \gamma_{mode}/\gamma_{rad} \approx \gamma_{mode}/\gamma_0$. The relationship $\gamma_{rad} \approx \gamma_0$ offers a good approximation for waveguides based on 1D photonic crystals, while 2D and 3D photonic crystal waveguides can result in $\gamma_{rad} < \gamma_0$.

For example, Goban *et al.* achieved $\beta \sim 0.26$ for Cesium atoms coupled to alligator photonic crystal waveguide (APCW) [58]. The reported device operated in a region of group index $n_g \sim 2$ to improve the interaction between the optical signal and the emitter. Further improvement can be achieved by fabricating the waveguide so that the wavelength of the atomic transition is closer to the waveguide's bandgap, although one would also need to tweak the design to make the structure chiral. For example, with $n_g \sim 10$ one can expect a co-operativity of ~ 3.2, and a coupling efficiency of ~ 0.75. Using a PCW with even higher group index would allow for high coupling efficiencies even when the atom is trapped further away from the waveguide resulting in a larger effective A_{mode} (Fig. 3.13, inset). This would, in turn, reduce the experimental challenges that arise in trapping cold atoms at sub-wavelength distances from surfaces, and for example, open the possibility to trap the atoms using an optical tweezer reflected from the surface of the waveguide [67]. While achieving large group index in PCWs can be challenging as disorder from fabrication imperfections can create localized, cavity-like modes, observations of $n_g \sim 58$ have been reported [59].

At the same time, solid state emitters can achieve an extremely large coupling efficiency, such as the coupling efficiency of $\beta \sim 0.98$ reported by Arcari *et al.* for a charged quantum dot (QD) coupled with a PCW with high n_g. Unlike laser-cooled atoms, solid state emitters can be relatively easily embedded in a PCW, which leads to a significant reduction in the effective A_{mode} even before group index engineering is considered. The high coupling efficiencies reported for the QD-PCW system, combined with superior directional properties available with a PCW [70, 71], can result in probability of deterministic single photon subtraction reaching almost unity. However, the potential drawbacks of solid-state emitters compared to laser-cooled atoms include the need to apply high magnetic field to form a Λ-system for some emitters, such as QDs, and challenges to realization of cascaded photon subtraction as finding multiple emitters with identical $|1\rangle \rightarrow |3\rangle$ transition energy

Table 3.1: Values of coupling efficiency, chirality, mode area, and group velocities for various emitter-waveguide systems reported in the literature.

Emitter	Waveguide	ξ	β	A_{mode}	v_g
Cs	NF ($a = 200$nm)	-	0.2 ($r/a \sim 1$) [63, 65]	-	-
Cs	NF ($a = 200$nm)	-	0.06 ($r/a \sim 2$) [63, 65]	-	-
Cs	NF ($a = 215$nm)	-	0.06 ($r/a \sim 2$) [66]	1.8μm^2 [66]	$\sim c$
Cs	NF ($a = 250$nm)	0.92 [56]	-	-	-
Cs	APCW	-	0.26 [58]	0.2μm^2[58]	$c/2$[58]
QD	PCW	-	0.98 [59]	0.4μm^2 [59]	$c/58$ [59]
QD	PCW	$0.90 - 0.98$ [68]	$0.90 - 1$ [68]	-	$c/10$ [68]
QD	PCW	-	0.85 [69]	-	-
QD	PCW	-	0.90 [70]	1.1μm^2 [70]	$c/70$ [70]

can be difficult.

Finally, we present Table 3.1 which provides an overview of experimental emitter-waveguide systems reported recently in the literature, including the parameters relevant to their potential use for photon subtraction.

Chapter 4

Non-classical state generation using deterministic single photon subtraction

4.1 Motivation

In this chapter, we investigate how deterministic single photon subtraction can be used to generate non-classical states, like Fock states. First, we give a brief introduction to the Wigner function and Gaussian state formalisms, and why non-Gaussian states are important in quantum information theory. Then, we study how the SPRINT-based single photon subtraction process can be used to create non-Gaussian quantum states with negative conditional entropies. Next, we shall see how this process can be used to create arbitrary Fock states, and finally conclude with future outlook.

4.2 Wigner function formalism

The quantum state can be expressed in an infinite dimensional Hilbert space with the help of observables with continuous eigenspectra, somewhat analogous to the phase space representation of classical mechanics. The quadrature operators for a bosonic mode in the phase space can be represented as linear combination of creation, and annihilation

operators, as shown

$$q = \frac{1}{\sqrt{2}}\left(a + a^\dagger\right), \quad p = \frac{i}{\sqrt{2}}\left(a^\dagger - a\right). \tag{4.1}$$

They are often expressed in a vectorial representation as $X = (q_1, p_1, \ldots, q_N, p_N)^T$ for N bosonic modes where T denotes the transposition operation of the row vector of length $2N$. Unlike canonical variables in classical mechanics, these quadrature operators do not commute. The commutation relationship is given by $[q, p] = i$, or, more generally $[X_i, X_j] = i\Omega_{ij}$ where Ω_{ij} is the element of a $2N \times 2N$ symplectic matrix:

$$\Omega = \bigoplus_{k=1}^{N} \omega, \quad \omega = \begin{pmatrix} 0 & 1 \\ -1 & 0 \end{pmatrix}. \tag{4.2}$$

The $2N \times 2N$ symplectic matrix is an N-time direct sum ($\bigoplus$) of the simplest 2×2 symplectic matrix ω. Also, from CCR (canonical commutation relations) algebra, for two operators A, and B [72]:

$$\Delta A \cdot \Delta B \geq \frac{1}{2}|\langle [A, B] \rangle|^2. \tag{4.3}$$

This directly leads to the widely know uncertainty relationship $\Delta q \Delta p \geq 1/2$. The quadrature operators are observables with continuous eigenspectra, and obey the following eigenvalue equations:

$$q\,|q\rangle = q\,|q\rangle\,, p\,|p\rangle = p\,|p\rangle\,, \tag{4.4}$$

The eigenvectors $|q\rangle$, and $|p\rangle$ form an orthogonal basis, and are related by Fourier transform:

$$|p\rangle = \frac{1}{\sqrt{2\pi}} \int_{-\infty}^{\infty} e^{ipq}\,|q\rangle\,dq, \quad |q\rangle = \frac{1}{\sqrt{2\pi}} \int_{-\infty}^{\infty} e^{-ipq}\,|p\rangle\,dp. \tag{4.5}$$

For any given density matrix ρ, the Wigner characteristic function is given by the expectation value of the Weyl displacement operator $D(\Lambda)$ as:

$$\chi[\rho](\Lambda) = \mathrm{Tr}\left[\rho D(\Lambda)\right] = \mathrm{Tr}\left[\rho \exp\left\{iX^T \Omega \Lambda\right\}\right], \tag{4.6}$$

where the vector Λ belongs to the $2N$ dimensional phase space. The Weyl displacement operator $D(\Lambda)$ results in a displacement in the symplectic phase space. It acts on the mode operators as:

$$D^{\dagger}(\Lambda) X D(\Lambda) = X + \Lambda. \tag{4.7}$$

The quasi-probabilistic Wigner function is given by the Fourier transform of the Wigner characteristic function:

$$W[\rho](X) = \frac{1}{(2\pi^2)^N} \int_{\mathbb{R}^{2N}} d^{2N}\Lambda \exp\left\{-iX^T \Omega \Lambda\right\} \chi[\rho](\Lambda). \tag{4.8}$$

For a single mode density matrix ρ, the Wigner function can also be expressed in terms of the phase space co-ordinate (q, p) as

$$W(q,p) = \frac{1}{2\pi} \int_{-\infty}^{\infty} e^{ipx} \langle q - \frac{x}{2} | \rho | q + \frac{x}{2} \rangle dx. \tag{4.9}$$

In terms of the field operator, the Wigner function takes the following form:

$$W(\alpha) = \frac{1}{\pi^2} \int_{-\infty}^{\infty} e^{\lambda^* \alpha - \lambda \alpha^*} \operatorname{Tr}\left[\rho e^{\lambda a^{\dagger} - \lambda^* a}\right] d^2\lambda, \tag{4.10}$$

where $\operatorname{Tr}\left[\rho e^{\lambda a^{\dagger} - \lambda^* a}\right] = \operatorname{Tr}\left[\rho D(\lambda)\right]$ is the Wigner characteristic function is terms of the field operator, and $\alpha = (q + ip)/\sqrt{2}$ where q and p are the field quadratures and not operators. The Wigner function is directly related to the histograms of the quadrature measurements by a homodyne measurement setup. The probability distribution of quadrature q after applying a phase shift of θ to the state is given by the Radon transform

$$\Pr(q, \theta) = \int_{-\infty}^{\infty} W(q\cos\theta - p\sin\theta, q\sin\theta + p\cos\theta) dp. \tag{4.11}$$

Fig. 4.1 shows how the quasi-probabilistic Wigner function is related to the probability distribution of the quadrature measurements in a homodyne detection experiment. This probability distribution is a form of marginal of the Wigner function as it is the integral projection of the Wigner distribution onto the plane perpendicular to the phase-space, and positioned at an angle θ with respect to the q quadrature. The angle θ is controlled by the phase of the local oscillator in the homodyne measurement setup.

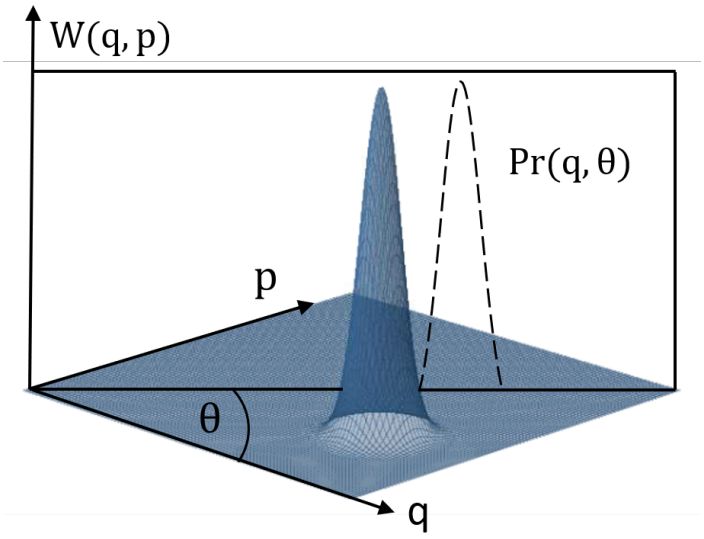

Figure 4.1: The integral projection of the Wigner function onto the plane oriented at an angle θ to the q quadrature gives $\Pr(q, \theta)$, which is the probability distribution of quadrature measurements from a homodyne measurement setup. The figure has been adapted from Ref. [73].

The Wigner function of a density matrix can be expressed in terms of moments of various orders. The first moment is defined by the expectation value $\bar{X} = \langle X \rangle = \mathrm{Tr}(\rho X)$. The second moment is the covariance matrix σ, whose elements are given by $\sigma_{ij} = \frac{1}{2}\langle\{\Delta X_i, \Delta X_j\}\rangle$, where the curly bracket $\{,\}$ is the anti-commutator operation. More importantly, the uncertainty theorem can be expressed in terms of the covariance matrix as $\sigma + i\Omega/2 \geq 0$ [74], which highlights the fundamental statistical importance of the second moment in particular.

Gaussian states

Gaussian states are a special class of quantum states that have a Gaussian Wigner function. These states can be completely characterized by their first two moments, as the higher order moments go to zero. The Wigner function of a Gaussian state with covariance matrix σ is given by [75]:

$$W(X) = \frac{\exp\left[-\frac{1}{2}(X - \bar{X})^T \sigma^{-1} (X - \bar{X})\right]}{\pi^N \sqrt{\mathrm{Det}(\sigma)}}. \tag{4.12}$$

Similarly, the class of quantum operations (channels) that transform any arbitrary Gaussian state to another Gaussian state is a Gaussian operation. Any Gaussian unitary operation can be characterized by the map:

$$(S, d) : X \to SX + d, \tag{4.13}$$

where S is a $2N \times 2N$ real matrix and $d \in \mathbb{R}^{2N}$. It is an affine map consisting of a linear transformation $X \to SX$, where S is symplectic, or in other words $S\Omega S^T = \Omega$; and a phase space displacement $X \to X + d$. The Gaussian unitary operation can be completely characterized by its action on the first two moments [76]:

$$\bar{X} \to S\bar{X} + d, \quad V \to SVS^T. \tag{4.14}$$

4.2.1 Why do we care about non-Gaussian quantum states?

Extended Gottesman-Knill theorem in phase space

First, let us define the Pauli group, and the Clifford group. Any element of the Pauli group can be defined by $P_n = \{\pm 1, \pm i\} \times \{I, X, Y, Z\}^{\otimes n}$, where I is the identity matrix, and X, Y, Z are the Pauli X, Y and Z matrices respectively. An element of the Clifford group is defined by $C_n = \left\{U : UP_nU^\dagger = P_n\right\}$. In other words, the Clifford group normalizes the Pauli group. Examples of some popularly used Clifford gates are the Hadamard gate, the CNOT gate, and the phase gate.

The Gottesman-Knill (GK) theorem proves that all Clifford group operations can be efficiently simulated in polynomial time on a probabilistic classical computer, and we need a non-Clifford operation for universal quantum computing [77]. An example of such a non-Clifford gate is the T ($\pi/8$) gate. The GK theorem can be extended to the continuous variable phase space. The Gaussian operations in continuous variable regime are analogous to the Clifford operations in the discrete variable formulation. These operations are quadratic functions of quadratures, and it has been shown that they are not sufficient for universal computing. We need non-Gaussian (non-Clifford) operations which are at least cubic functions of quadratures, for example something like $\exp[itq^m p^n]$ where $m + n \geq 3$.

Non-Gaussianity and negative Wigner functions can be studied under the resource theoretic framework, and it has been shown that such features can be used as *quantum resources* that contribute towards computational speed-up. They can also be used for

other applications like entanglement distillation[1] [79], and non-deterministic noiseless linear amplification [80–82]. Heralded single photon subtraction has been used as a non-Clifford operation for creating non-Gaussian states with negative Wigner functions [23], and thus it can be used as a tool to harness this *resource*. But the low success rate of such heralded processes proves to be a serious bottleneck for such applications. Thus, a more deterministic photon subtraction can play a key role in improving the performance of such protocols.

4.3 Entanglement entropy

The von Neumann entropy of a quantum state given by the density matrix ρ is a measure of the minimum amount of quantum resources required to encode the state [83]. Formally it is defined as [84]:

$$S(\rho) = -\operatorname{Tr}(\rho \log_2 \rho) \tag{4.15}$$

If λ_i are the eigenvalues of the density matrix, then the von Neumann entropy can be expressed as $S(\rho) = -\sum_i \lambda_i \log_2 \lambda_i$. We can clearly see from the definition that the entropy is non-negative since $\sum_i \lambda_i = 1$, and thus $\lambda_i \leq 1$. The entropy is zero for a pure state when only one of the eigenvalues is 1, and the rest are 0. The maximum possible value of the entropy is $\log_2 d$ for a completely mixed state in a d-dimensional Hilbert space.

The Shannon conditional entropy is defined for any two random variables X and Y as $H(X|Y) = H(X,Y) - H(Y)$, where $H(X,Y)$ is the joint Shannon entropy. It gives the entropy of X, given that we know Y. For a bipartite quantum system AB, we can similarly define the conditional entropy as $S(A|B) = S(A,B) - S(B)$. For classical systems, the joint Shannon entropy is always greater than or equal to the entropy of any of the subsystems, i.e., $H(X,Y) \geq H(X), H(Y)$. This always makes the conditional Shannon entropy non-negative, i.e., $H(X|Y) \geq 0$. However, that is not true for von Neumann entropies. If the subsystems are entangled, the joint entropy can be smaller than the entropy of the individual subsystems. A simple example for that is any of the Bell states. The Bell states are pure states, and thus have joint von Neumann entropy of zero. This makes the von Neumann conditional entropy $S(A|B)$ negative. It has been proved that non-negative conditional entropies, and satisfying Bell's inequalities are equivalent as a necessary condition for separability [85]. Also, the negative conditional entropy is sufficient to show non-separability of any quantum state. We will use this fact later in the chapter to show the creation of entanglement by deterministic single photon subtraction.

[1] In fact, there exists a no-go theorem that proves that Gaussian operations cannot achieve entanglement distillation from Gaussian input states [78].

4.4 Creating non-classical states from Gaussian states

Once again, in this section we shall revisit the problem with a three level emitter in a bi-modal cavity for different optical inputs and initialization conditions as discussed in Chapter 2. We solve the relevant master equations using Python's QuTiP package to get the transient response of the system. That gives us the density matrix of the composite system $\Psi(t) = \psi_r(t) \otimes \psi_l(t) \otimes \psi_\Lambda(t)$ at any time t. The quantum state of the composite system Ψ is simply a tensor product ($\otimes$) of the quantum states of the r mode ψ_r, the l mode ψ_l and the Λ emitter ψ_Λ. We trace out the density matrices of the individual components, i.e., the r mode, the l mode and the Λ emitter to get the density matrices of the sub-systems $\rho_k(t)$, where $k \in \{r, l, \Lambda\}$. From the density matrix we directly calculate the Wigner function of the modes and the emitter as

$$W[\rho_k(t)](q,p) = \frac{1}{2\pi}\int_{-\infty}^{\infty} e^{ipx}\langle q - \frac{x}{2}|\rho_k(t)|q + \frac{x}{2}\rangle dx, \tag{4.16}$$

where the tuple (q, p) is the co-ordinate of the phase space. One can switch between the We investigate the Wigner function of the modes and the emitter to investigate if we can create quantum states with negative Wigner functions and non-Gaussian statistics using SPRINT-based deterministic single photon subtraction.

4.4.1 Continuous-wave coherent drive input

Once again, we start our investigation with the case where the r mode is being resonantly driven by a CW coherent source as discussed in Sec. 2.4. Initially, both the modes (mode r and mode l) are vacuum states, and the atom is in its ground state. Then, the mode r is driven with a CW coherent laser of power $P = 52$ pW. All the system parameters are the same from our previous discussion in Sec. 2.4: $\omega_d = \omega_r = \omega_1 = 2\pi \times 200$ THz, $\omega_2 = \omega_l$, $\omega_r - \omega_l = 2\pi \times 0.5$ GHz, $g_1 = g_2 = 2\pi \times 10$ GHz, $\kappa_r = \kappa_l = \gamma_{coh} = 2\pi \times 0.25$ GHz, $\gamma_1 = \gamma_2 = 0$.

In steady state condition, the r mode ends up in a coherent state with an average photon number of one, the l mode ends up in the vacuum state as all the photons eventually leak out of the cavity from that mode as observed in Fig. 4.2a. But more interestingly, the emitter is left in a highly non-Gaussian state with a negative Wigner function. We search for the instant we can observe the single photon in the l mode. In other words, we look for the time t, when $\rho_l(t)$ is closest to a single photon Fock state $|1\rangle$. But since the interaction time, i.e., the time for $\int_0^t dt\langle l_{out}^\dagger l_{out}\rangle$ to saturate to one is pretty long (see Fig. 2.8), it is

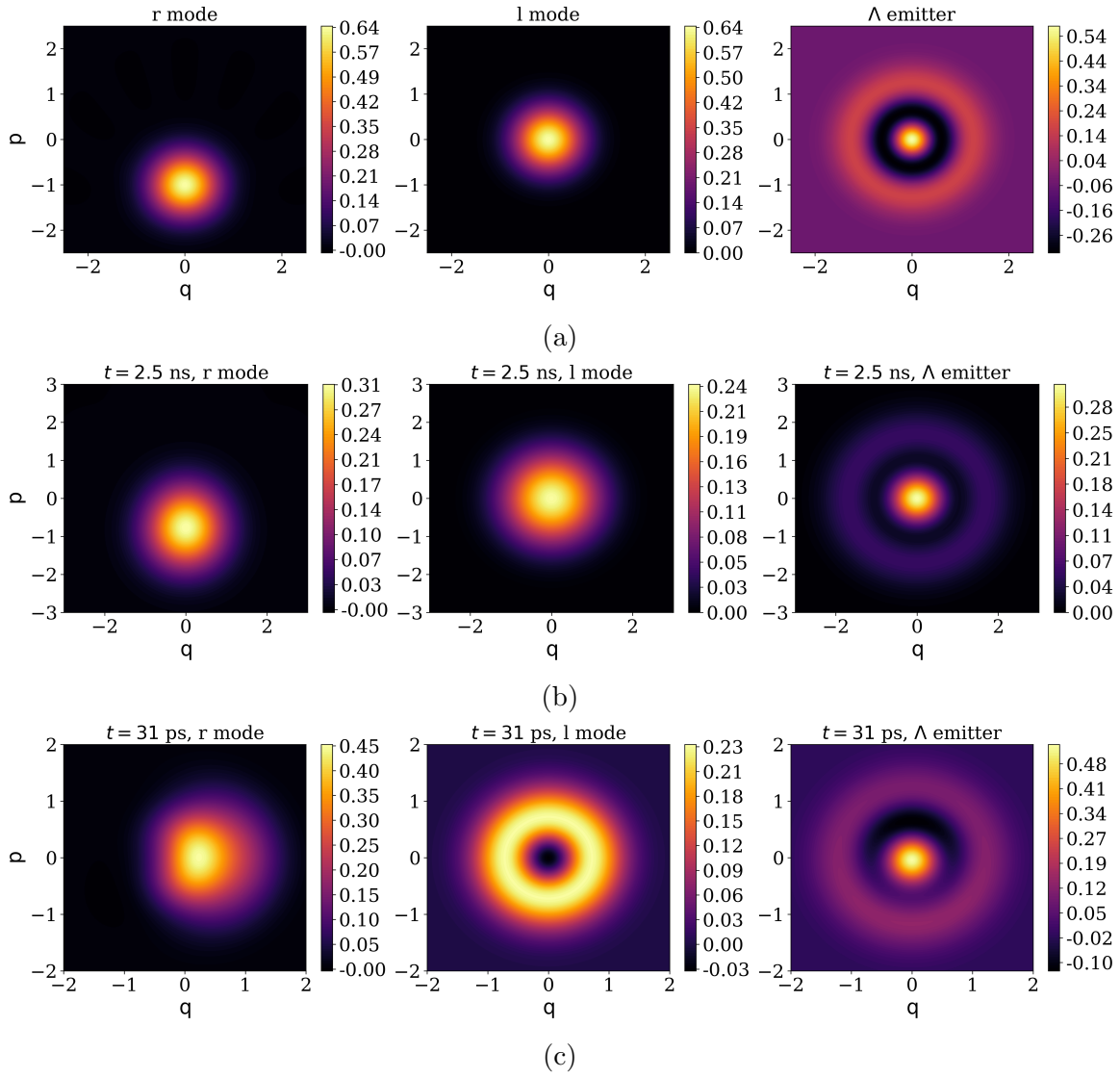

Figure 4.2: (a) The Wigner functions of the r mode, the l mode, and the quantum emitter in steady state when a CW coherent laser is used to drive the r mode. The r mode is a coherent state with mean photon number one, and the emitter is highly non-Gaussian. The single photon leaks out from mode l, leaving it in a vacuum state. (b) The Wigner functions for the system driven by a CW coherent laser when the instantaneous single photon fidelity of mode l is the highest (~ 0.35). (c) The Wigner functions when the instantaneous fidelity of the single photon in mode l is the highest (~ 0.72), for the case where mode r is initialized with a coherent state of mean photon number one. The quantum emitter is in a highly non-Gaussian state, and has negative Wigner function.

difficult to find the single photon state at any particular point in time. Looping over the entire interaction time, we find that the single photon Fock state created in the l mode has a maximum instantaneous fidelity[2] of only 0.35 at around 2.5 ns as shown in Fig. 4.2b.

To properly show the induced quantum correlations in the system, we also plot the conditional entropy $S(\rho|\rho_k)$ for ρ_k corresponding to density matrices of the r mode, l mode, and the three-level Λ emitter. Here ρ is the joint density matrix of the complete system. In Fig. 4.3a we can clearly see the conditional entropies $S(\rho|\rho_l)$ and $S(\rho|\rho_\Lambda)$ have negative values, which is a signature for entanglement between the l mode and the Λ emitter. Eventually, because of non-zero κ_l, the photon leaks out from the l mode. Thus one of the entangled sub-systems is lost, and thereby the conditional entropy saturates at zero with time. However, for $\kappa_l = 0$ (all other system parameters are the same), both $S(\rho|\rho_l)$ and $S(\rho|\rho_\Lambda)$ saturate to at -1 as shown in Fig. 4.3b. Also, we observe that $S(\rho|\rho_{l(\Lambda)}) = -S(\rho_{l(\Lambda)})$. This implies $S(\rho, \rho_{l(\Lambda)}) = 0$, i.e., ρ is a pure state, and the l mode and Λ emitter form an entangled Bell state.

4.4.2 Coherent state input

Next, we initialize our model with a coherent state with an average photon number of one in r mode as discussed in Sec. 2.5. As observed earlier, the interaction time is much shorter when we initialised the r mode with a coherent state compared to driving the r mode with a CW coherent drive input. In this case, we can clearly observe non-Gaussian characteristics in the l mode, as shown in Fig. 4.2c. In this simulation, $\kappa_r = \kappa_l = 2\pi \times 0.25$ GHz was considered, and all the other system parameters were kept unchanged. The single photon Fock state in the l mode has a maximum instantaneous fidelity of 0.72 at 31 ps. The emitter can also be seen to exist is a highly non-Gaussian state with a negative Wigner function.

The coherent state is a classical Gaussian state of light with a positive Gaussian Wigner function. In this section, we observed that even though we began with highly classical Gaussian states as inputs to the systems, we ended up creating non-Gaussian *resource* states with negative Wigner functions, and negative conditional entropies using SPRINT-based deterministic single photon subtraction. This type of entangled systems with quantum properties, and on-demand creation of non-classical single photon states can have applications in the fields of quantum communication, quantum networks, and quantum metrology.

[2]The fidelity of two density matrices ρ_1 and ρ_2 is given by $F(\rho_1, \rho_2) = \mathrm{Tr}\sqrt{\sqrt{\rho_1}\rho_2\sqrt{\rho_1}}$, and is a measure of similarity of ρ_1 and ρ_2. Thus, the single photon fidelity of the quantum state ρ_l is $F(\rho_l, |1\rangle\langle 1|)$.

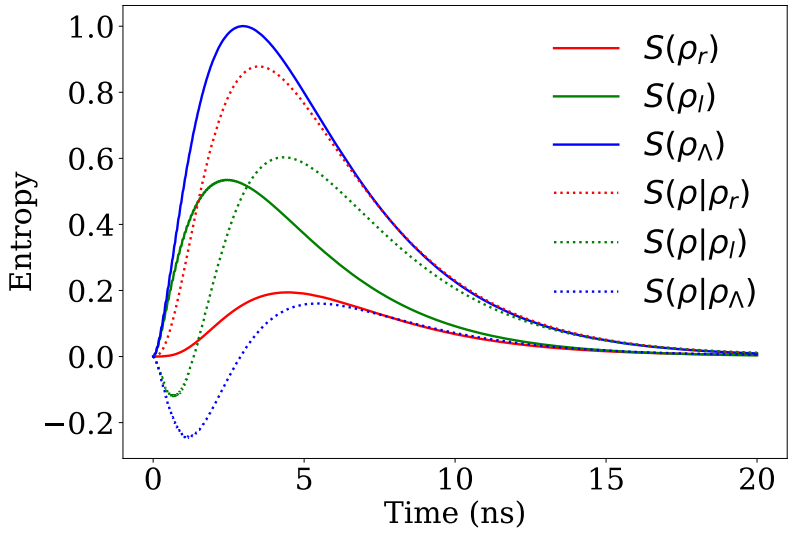

(a)

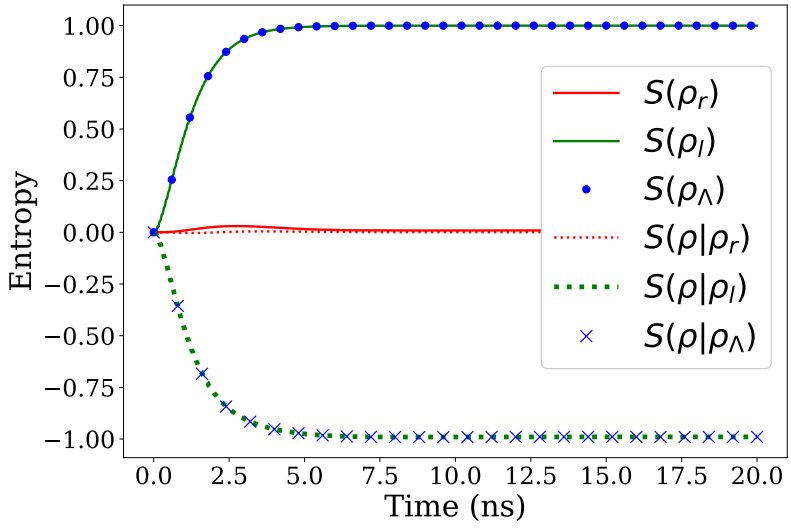

(b)

Figure 4.3: The time evolution of the entropy of the r mode, the l mode, and the three-level quantum emitter, along with their respective conditional entropies for a CW coherent laser drive when (a) $\kappa_r = \kappa_l = \gamma = 2\pi \times 0.25$ GHz, and (b) $\kappa_r = \gamma = 2\pi \times 0.25$ GHz, $\kappa_l = 0$. The conditional entropies $S(\rho|\rho_l)$ and $S(\rho|\rho_\Lambda)$ are negative, thereby showing the presence of entanglement in the system.

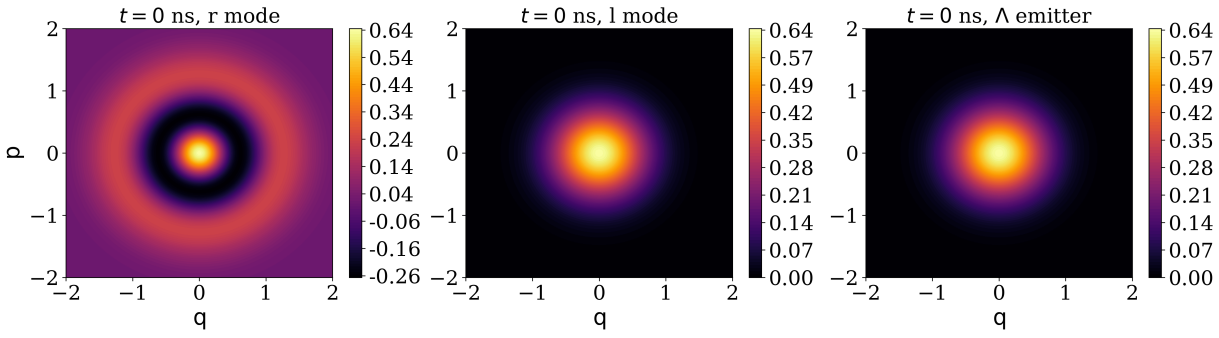

(a)

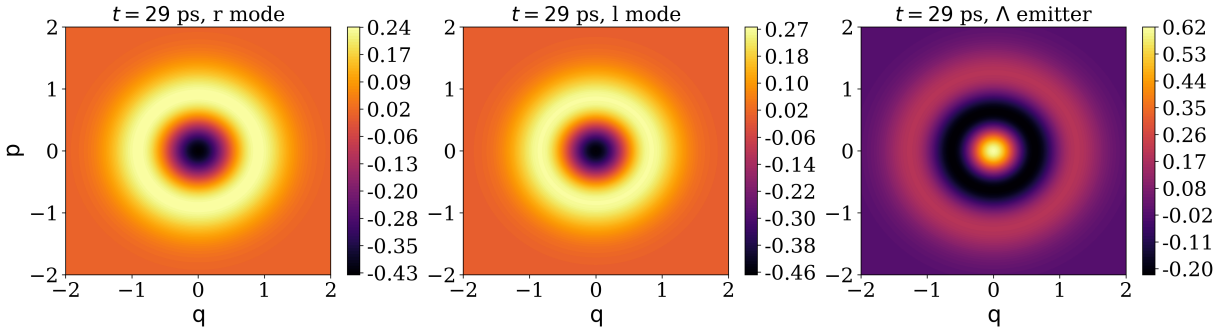

(b)

Figure 4.4: (a) The Wigner functions of the l mode, the r mode and the emitter at $t = 0$. The r mode is initialized with the two photon Fock state $|2\rangle$. (b) During the photon subtraction process, the maximum fidelity of the single photon Fock state in mode r is 0.93 at $t = 29$ ps. At the same time, the fidelity of the single photon state in mode r is 0.91. We can also see that the Wigner function of the emitter is highly non-Gaussian, and negative. For the simulations $\kappa_r = \kappa_l = 2\pi \times 0.25$ GHz was used. All other parameters are the same as used in Sec. 2.5.2.

4.5 Arithmetic with Fock states

In this section, once again we will be briefly visiting the situation from Sec. 2.5.2, where the r mode of the bi-modal cavity is initialized with the two photon Fock state $|2\rangle$, as shown in Fig. 4.4a. We then let the system evolve, and search for the timestamp when we can notice a single photon Fock state $|1\rangle$ in the l mode with highest instantaneous fidelity. The instantaneous fidelity of the state in mode l reaches a maximum of 0.93 at $t = 29$ ps as shown in Fig. 4.4b. At the same time, we observe that there is a single photon Fock state of fidelity 0.91 in mode r. One can also look at this operation as adding a single Fock

state photon to mode l, while subtracting a single Fock state photon from mode r.

Thus, such a SPRINT-based module can act as a deterministic "photon subtractor" for the r mode, and a deterministic "photon adder" for the l mode in the Fock basis. By cascading multiple three level emitters, or by switching the output modes once again into the input modes of the bi-modal cavity along with proper re-initialization of the emitter, it might be possible to create any higher order Fock state from smaller Fock states, and vice versa. However, having photons in the l mode can make the process not self-terminating unlike the SPRINT interaction we studied thus far, and might require fine-tuning of the system parameters along with some heralding/control processes to have an efficient single photon adder. It might be an interesting to explore the feasibility of such a stimulated Raman process for creating arbitrary Fock states on-demand in the next step of this project.

4.6 Future direction

In the first part of this thesis, we have seen that the SPRINT-based deterministic single photon subtraction can be used to subtract a single Fock state photon from any arbitrary source of light. However, it turns out that this operations is fundamentally different from simply the operation of the ideal deterministic photon subtraction operator $\hat{S} = |0\rangle\langle 0| + \sum_n |n-1\rangle\langle n|$. Even though the SPRINT-based process behaves similar to the $\hat{S}$ operator for a Fock state input, it has a very different effect on an input coherent state as shown in Fig. 4.5. Initially, from the Wigner distribution it might seem that the coherent state is getting squeezed. However, it is easily verified that it is not a squeezed state once the marginal Wigner distributions are plotted (see Fig. 4.5b), where the marginals of the Wigner function are defined by:

$$W_q(q,p) = \int W(q,p)dp = \langle q|\,\rho\,|q\rangle = \Pr(q,0), \tag{4.17a}$$

$$W_p(q,p) = \int W(q,p)dq = \langle p|\,\rho\,|p\rangle = \Pr\left(q,\frac{\pi}{2}\right). \tag{4.17b}$$

From Fig. 4.5 and 4.5b, we observe that the operator results in increased variance of q, but does not decrease the variance of p below the quantum limit. Going forward, it might be useful to develop a better understanding of what results in the difference between the SPRINT-based subtraction process, and the ideal subtraction operator by performing process tomography of SPRINT.

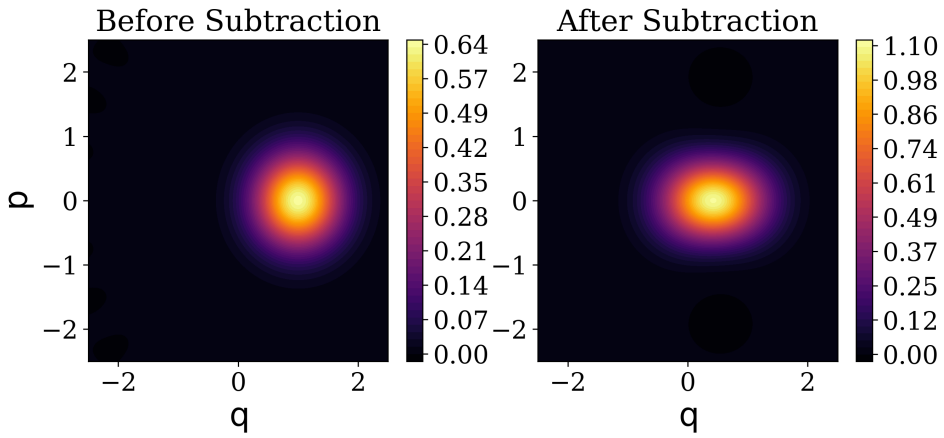

(a)

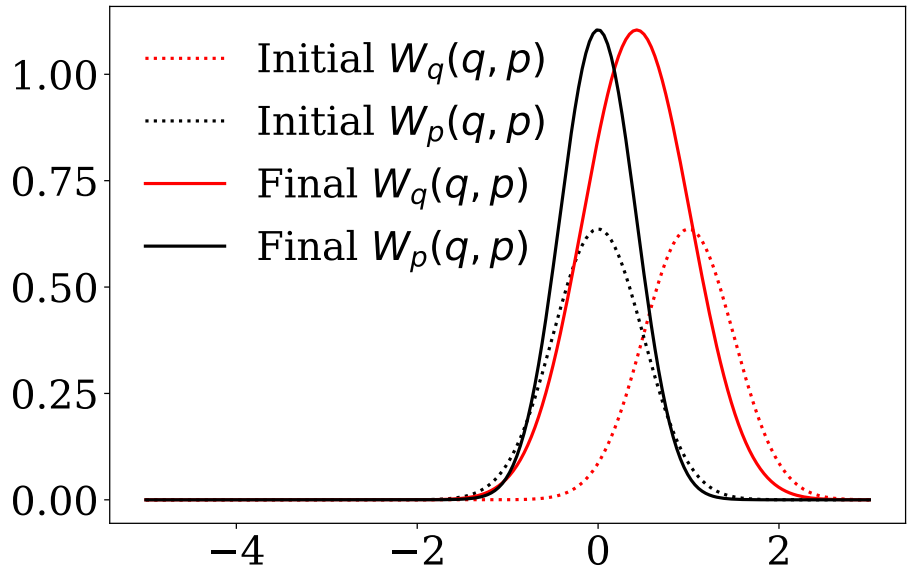

(b)

Figure 4.5: (a) The Wigner function of a coherent state with a mean photon number of 1 photon, before and after being operated on by the ideal deterministic subtraction operator $\hat{S}$. It stretches the Wigner function towards the vacuum. It makes the Wigner function look like an elongated squeezed state. (b) However, it can be easily verified that it is not a squeezed state once the marginal Wigner distributions are plotted. The operator results in increased variance of x, but does not decrease the variance of p below the quantum limit.

We have also shown that we can create non-Gaussian quantum states using the SPRINT-based photon subtraction mechanism. However, in our simulations we have not noticed any Wigner negativity in the mode from which the photon was subtracted. It might be useful to see if non-classical states can be observed in that mode by carefully optimizing over the simulation parameters like coupling strength of the emitter, strength of the cavity, and others.

Another avenue of future work would be to study if this kind of SPRINT-based photon subtraction/addition mechanism can be used for applications in quantum information processing like entanglement distillation. Heralded photon subtraction has been used for entanglement distillation from Gaussian states [6, 86]. It will be interesting to investigate if the SPRINT-based photon subtraction can be used for similar purposes.

Part II

Inverse design of nanophotonic structures for directional emission from NV centers

Chapter 5

Antenna formalism for quantum emitters

5.1 Motivation

In this chapter, we perform an *ab initio* study of the classical and quantum formulations of radiating dipoles. We try to understand why we can treat an emitter as a classical dipole in certain optics problems, and formulate the interaction between an emitter and a scattering nanoparticle using classical antenna theory. We shall also look at some of the important parameters of the emitter-nanoparticle system using definitions from antenna theory to develop an intuition of the problem. The goal is to give a background for Chapter 7, where we shall explore how we can control the emission pattern of a Nitrogen Vacancy (NV) center using sub-wavelength photonic structures, which essentially behave as optical antennas.

5.2 Classical formulation

5.2.1 Radiation reaction formalism

In the classical picture, we can model a dipole source of radiation as a harmonic oscillator. The oscillating charge experiences a back-action or radiation reaction because of its own emission. The motion of the undriven harmonic is described by the second order differential

equation

$$m\ddot{\mathbf{r}}(t) + \omega_0^2 m\mathbf{r}(t) = \mathbf{F}_r(t), \tag{5.1}$$

where m is the mass, ω_0 is the natural frequency of the oscillator, $\omega_0^2 m$ is the linear spring constant, and $\mathbf{F}_r$ is the radiation reaction force on the oscillating dipole. The radiation reaction force is given by the Abraham-Lorentz formula

$$\mathbf{F}_r(t) = \frac{q^2}{6\pi\epsilon_0 c^3}\dddot{\mathbf{r}}(t), \tag{5.2}$$

where q is the charge of the oscillating dipole, ϵ_0 is the permittivity of free space, and c is the speed of light. Considering a time harmonic solution to the equation of motion given by $\mathbf{r}(t) = \mathbf{r}_0 \exp(-i\omega_0 t)$, we get $\dddot{\mathbf{r}} = -\omega_0^2\dot{\mathbf{r}}$. Substituting this in the expression for the force $\mathbf{F}_r(t)$, we find that the force introduces damping in the system. Apart from attenuating the dipole oscillation strength, the damping also shifts the resonance frequency. If we assume a small damping $\gamma_0 \ll \omega_0$, then for a dipole with harmonic time dependence $\mathbf{p}(t) = p(t)\hat{\mathbf{p}}$ radiating in free space, the equation of motion is given by

$$\ddot{p}(t) + \gamma_0\dot{p}(t) + \omega_0^2 p(t) = 0, \tag{5.3}$$

where the damping constant γ_0 is the spontaneous emission rate in free space, and is given by

$$\gamma_0 = \frac{1}{4\pi\epsilon_0}\frac{2q^2\omega_0^2}{3mc^3}. \tag{5.4}$$

Now, if a scattering object object is present in the field of the dipole, Eq. 5.3 gets transformed to

$$\ddot{p}(t) + \gamma_0\dot{p}(t) + \omega_0^2 p(t) = \frac{q^2}{m}\hat{\mathbf{p}} \cdot \mathbf{E}_s(t), \tag{5.5}$$

where $\mathbf{E}_s(t)$ is the scattered electric field at the location of the dipole because of the presence of the scattering object. Under the assumption that we can express the time dependence of the dipole, and the reflected electric field as $\mathbf{p}(t) = \mathbf{p}_0 \exp(-i\Omega t)$, and

$\mathbf{E}_s(t) = \mathbf{E}_{s0}\exp(-i\Omega t)$ respectively, the complex frequency $\Omega = \omega - i\gamma/2$ can be expressed as [87]

$$\Omega = \pm\omega_0\left(1 - \frac{q^2}{2p_0 m\omega_0^2}\mathrm{Re}\left(\hat{\mathbf{p}}\cdot\mathbf{E}_{s0}\right) - \frac{\gamma_0}{8\omega_0^2}\right) - i\frac{\gamma_0}{2}\left(1 \pm \frac{q^2}{p_0 m\omega_0\gamma_0}\mathrm{Im}\left(\hat{\mathbf{p}}\cdot\mathbf{E}_{s0}\right)\right). \tag{5.6}$$

If we assume $\omega^2 \gg |q^2\hat{\mathbf{p}}\cdot\mathbf{E}_{s0}/(p_0 m)|$, γ_0^2, i.e., for small perturbations and small damping, the real part of Ω is $\sim \pm\omega_0$. Considering only the physically viable solution with + sign, at resonance we get:

$$\frac{\gamma}{\gamma_0} = 1 + \frac{q^2}{p_0 m\omega_0\gamma_0}\mathrm{Im}\left(\hat{\mathbf{p}}\cdot\mathbf{E}_{s0}\right) = 1 + \frac{6\pi\epsilon_0}{|\mathbf{p}_0|^2}\frac{c^3}{\omega_0^3}\mathrm{Im}\left(\mathbf{p}_0^*\cdot\mathbf{E}_{s0}\right). \tag{5.7}$$

5.2.2 Green's function formalism

From classical electromagnetic theory, the current density arising from a dipole moment located at $\mathbf{r}_0$ is given by

$$\mathbf{j}(\mathbf{r},t) = \dot{\mathbf{p}}(t)\delta\left(\mathbf{r} - \mathbf{r}_0\right). \tag{5.8}$$

Assuming harmonic time dependence of the current density and the dipole moment, we have

$$\mathbf{j}(\mathbf{r}) = -i\omega\mathbf{p}\delta\left(\mathbf{r} - \mathbf{r}_0\right). \tag{5.9}$$

From Poynting's theorem, the power radiated by a current source with harmonic time dependence is given by

$$P' = -\frac{1}{2}\int_V \mathrm{Re}\left(\mathbf{j}^*\cdot\mathbf{E}\right)dV = \frac{\omega}{2}\mathrm{Im}\left(\mathbf{p}^*\cdot\mathbf{E}(\mathbf{r}_0)\right) \tag{5.10}$$

For an arbitrarily oriented dipole $\mathbf{p}$ placed at $\mathbf{r}_0$, the induced electric field at point $\mathbf{r}$ can be determined by the dyadic Green's function of the medium as (see Fig. 5.1)

$$\mathbf{E}(\mathbf{r}) = \omega^2\mu_0\mu\overleftrightarrow{\mathbf{G}}\left(\mathbf{r},\mathbf{r}_0;\omega\right)\cdot\mathbf{p}(\mathbf{r}_0). \tag{5.11}$$

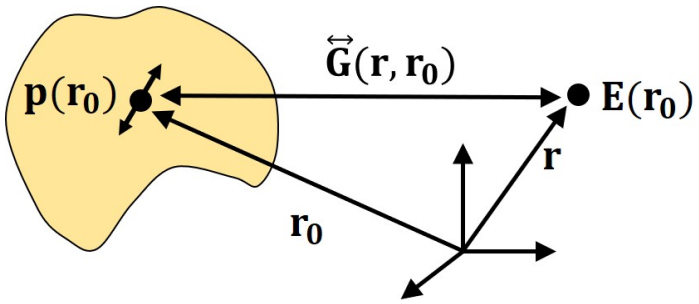

Figure 5.1: The dyadic Green's function $\overleftrightarrow{\mathbf{G}}(\mathbf{r}, \mathbf{r}_0)$ gives the electric field $\mathbf{E}$ at point $\mathbf{r}$ due to an arbitrarily oriented dipole $\mathbf{p}$ located at $\mathbf{r}_0$.

In Cartesian coordinate Green's dyadic is a 3×3 matrix given by

$$\overleftrightarrow{\mathbf{G}} = \begin{bmatrix} G_{xx} & G_{xy} & G_{xz} \\ G_{xy} & G_{yy} & G_{yz} \\ G_{xz} & G_{yz} & G_{zz} \end{bmatrix}, \tag{5.12}$$

where the first column specifies the electric field of a unit dipole oriented along one of the x-axis, the second column specifies the electric field of a unit dipole oriented along one of the y-axis, and the third column specifies the electric field of a unit dipole oriented along one of the z-axis. The elements of the matrix are the scalar Green's functions. In a homogenous environment, the electric field satisfies the wave equation

$$\nabla \times \nabla \times \mathbf{E}(\mathbf{r}) - k^2 \mathbf{E}(\mathbf{r}) = i\omega\mu_0\mu \mathbf{j}(\mathbf{r}). \tag{5.13}$$

Upon substituting $\mathbf{j}(\mathbf{r}) = -i\omega\mathbf{p}\delta(\mathbf{r} - \mathbf{r}_0)$, we get

$$\nabla \times \nabla \times \overleftrightarrow{\mathbf{G}}(\mathbf{r}, \mathbf{r}_0) - k^2 \overleftrightarrow{\mathbf{G}}(\mathbf{r}, \mathbf{r}_0) = \overleftrightarrow{\mathbf{I}}\,\delta(\mathbf{r} - \mathbf{r}_0), \tag{5.14}$$

where $\overleftrightarrow{\mathbf{I}}$ is the unit dyad. Upon solving the Green's dyadic under Lorentz gauge, it can be expressed in terms of the scalar Green's function $G(\mathbf{r}, \mathbf{r}_0)$ as [88]

$$\overleftrightarrow{\mathbf{G}}(\mathbf{r}, \mathbf{r}_0) = \left[\overleftrightarrow{\mathbf{I}} + \frac{1}{k^2}\nabla\nabla\right] G(\mathbf{r}, \mathbf{r}_0) = \left[\overleftrightarrow{\mathbf{I}} + \frac{1}{k^2}\nabla\nabla\right] \frac{\exp(\pm ik|\mathbf{r} - \mathbf{r}_0|)}{4\pi|\mathbf{r} - \mathbf{r}_0|}. \tag{5.15}$$

Here, $G(\mathbf{r}, \mathbf{r}_0) = \exp(\pm ik|\mathbf{r} - \mathbf{r}_0|)/4\pi|\mathbf{r} - \mathbf{r}_0|$ represents a spherical wave propagating from the origin for positive sign, and a spherical wave focusing at the origin for the negative sign in a homogenous environment.

After the small digression on dyadic Green's function, we substitute for the value of the electric field from Eq. 5.11 in Eq. 5.10, and we arrive at

$$P' = \frac{\omega^3 |\mathbf{p}|^2}{2c^2 \epsilon_0 \epsilon} \mathrm{Im}\left[\hat{\mathbf{p}} \cdot \overleftrightarrow{\mathbf{G}}(\mathbf{r}_0, \mathbf{r}_0; \omega) \cdot \hat{\mathbf{p}}\right]. \tag{5.16}$$

In free space, the real part of the Green's function $\overleftrightarrow{\mathbf{G}}_0(\mathbf{r}, \mathbf{r}_0; \omega)$ diverges as $\mathbf{r}$ approaches $\mathbf{r}_0$. However, the imaginary part still exists, and $\mathrm{Im}\left[\overleftrightarrow{\mathbf{G}}(\mathbf{r}_0, \mathbf{r}_0; \omega)\right] = (\omega/6\pi c)\overleftrightarrow{\mathbf{I}}$ [88]. Therefore, we get the expression for the power radiated in free space as

$$P_0 = \frac{|\mathbf{p}|^2 \omega^4}{12\pi \epsilon_0 \epsilon c^3}. \tag{5.17}$$

Considering that the electric field at $\mathbf{r}_0$ is composed of both direct, and scattered electric field components, i.e., $\mathbf{E}(\mathbf{r}_0) = \mathbf{E}_0(\mathbf{r}_0) + \mathbf{E}_s(\mathbf{r}_0)$, we get [88]

$$\frac{P}{P_0} = \frac{P_0 + P'}{P_0} = 1 + \frac{6\pi\epsilon_0\epsilon}{|\mathbf{p}|^2} \frac{c^3}{\omega^3} \mathrm{Im}\left(\mathbf{p}^* \cdot \mathbf{E}_s(\mathbf{r}_0)\right) = 1 + \frac{6\pi}{k} \mathrm{Im}\left[\hat{\mathbf{p}} \cdot \overleftrightarrow{\mathbf{G}}(\mathbf{r}_0, \mathbf{r}_0; \omega) \cdot \hat{\mathbf{p}}\right], \tag{5.18}$$

where $P = P_0 + P'$ is the total power radiated in the presence of a scattering medium. From Eqs. 5.7 and 5.18, we get the relationship [88]

$$\frac{P}{P_0} = \frac{\gamma}{\gamma_0}. \tag{5.19}$$

Hence, from Eq. 5.7 and Eq. 5.18, we notice that the modified decay rate in the presence of a scattering medium depends just upon the reflected electric field at point $\mathbf{r}_0$, i.e., at the position of the dipole itself. The problem is highly simplified, as the new decay rate can be calculated by calculating the field at a single point, without the need for modal analysis. Rather one can use real space wave propagation methods used in antenna theory to calculate the modified decay rate.

5.3 Quantum formulation

For a two level quantum emitter with ground state $|g\rangle$, and excited state $|e\rangle$ separated by transition frequency ω, coupled weakly with a scattering object, Fermi's golden rule gives the decay rate as [88]

$$\Gamma = \frac{\pi\omega}{3\hbar\epsilon_0}|\langle g|\mathbf{p}|e\rangle|^2\rho_{\mathbf{p}}(\mathbf{r}_0,\omega), \tag{5.20}$$

where $\rho_{\mathbf{p}}(\mathbf{r}_0,\omega)$ is the partial local density of states (PLDOS), and is given by

$$\text{PLDOS:}\quad \rho_{\mathbf{p}}(\mathbf{r}_0,\omega) = 3\sum_{\mathbf{k}_i}\left[\hat{\mathbf{p}}\cdot(\mathbf{f}_{\mathbf{k}_i}\mathbf{f}^*_{\mathbf{k}_i})\cdot\hat{\mathbf{p}}\right] = \frac{6\omega}{\pi c^2}\text{Im}\left[\hat{\mathbf{p}}\cdot\overleftrightarrow{\mathbf{G}}(\mathbf{r}_0,\mathbf{r}_0;\omega)\cdot\hat{\mathbf{p}}\right], \tag{5.21}$$

where $(\mathbf{f}_{\mathbf{k}_i}\mathbf{f}^*_{\mathbf{k}_i})$ denotes an outer product, and $\mathbf{f}_{\mathbf{k}_i}$ are the normal modes of the electric field. The normal modes are solutions of the wave equation

$$\nabla\times\nabla\times\mathbf{f}_{\mathbf{k}}(\mathbf{r},\omega_{\mathbf{k}}) - \frac{\omega_{\mathbf{k}}^2}{c^2}\mathbf{f}_{\mathbf{k}}(\mathbf{r},\omega_{\mathbf{k}}) = 0, \tag{5.22}$$

and satisfy the orthogonality condition

$$\iiint_V \mathbf{f}^*_{\mathbf{k}_i}(\mathbf{r},\omega_{\mathbf{k}_i})\mathbf{f}_{\mathbf{k}_j}(\mathbf{r},\omega_{\mathbf{k}_j})d^3r = \delta_{ij}, \tag{5.23}$$

The electric field operator is given by $\hat{\mathbf{E}} = \sum_{\mathbf{k}}\left[\mathbf{E}^{(+)}_{\mathbf{k}}\hat{a}_{\mathbf{k}}(t) + \mathbf{E}^{(-)}_{\mathbf{k}}\hat{a}^\dagger_{\mathbf{k}}(t)\right]$, where $\hat{a}_{\mathbf{k}}$ ($\hat{a}^\dagger_{\mathbf{k}}$) is the annihilation (creation) operator, and the complex electric field can be expressed in terms of the normal modes as

$$\mathbf{E}^{(+)}_{\mathbf{k}} = \sqrt{\frac{\hbar\omega_{\mathbf{k}}}{2\epsilon_0}}\mathbf{f}_{\mathbf{k}},\quad \mathbf{E}^{(-)}_{\mathbf{k}} = \sqrt{\frac{\hbar\omega_{\mathbf{k}}}{2\epsilon_0}}\mathbf{f}_{\mathbf{k}}. \tag{5.24}$$

The PLDOS at a point in space is a measure of the the number of electromagnetic modes available at that point, and directly governs the rate of radiation as shown by Fermi's golden rule. For an isotropic and homogeneous medium, if the transition has no

preferred fixed dipole axis $\hat{\mathbf{p}}$, we can calculate the total LDOS by averaging over all possible orientations as

$$\text{LDOS:} \quad \rho(\mathbf{r}_0, \omega) = \langle \rho_{\mathbf{p}}(\mathbf{r}_0, \omega) \rangle = \frac{2\omega}{\pi c^2} \text{Im} \left[\hat{\mathbf{p}} \cdot \text{Tr} \left\{ \overleftrightarrow{\mathbf{G}}(\mathbf{r}_0, \mathbf{r}_0; \omega) \right\} \cdot \hat{\mathbf{p}} \right]. \tag{5.25}$$

The volume integral of the LDOS gives the density of states (DOS), such that

$$\text{DOS:} \quad \rho(\omega) = \frac{1}{V} \iiint_V \rho(\mathbf{r}_0, \omega) d^3\mathbf{r}. \tag{5.26}$$

Using $\text{Im} \left[\overleftrightarrow{\mathbf{G}}(\mathbf{r}_0, \mathbf{r}_0; \omega) \right] = (\omega/6\pi c) \overleftrightarrow{\mathbf{I}}$ in free space, we get the relationship:

$$\text{Im} \left[\hat{\mathbf{p}} \cdot \text{Tr} \left\{ \overleftrightarrow{\mathbf{G}}(\mathbf{r}_0, \mathbf{r}_0; \omega) \right\} \cdot \hat{\mathbf{p}} \right] = 3 \times (\omega/6\pi c) = \omega/2\pi c \tag{5.27}$$

In free space, this gives

$$\rho_0 = (2\omega/\pi c^2) \times (\omega/2\pi c) = \omega^2/\pi^2 c^3, \quad \Gamma_0 = \omega^3 |\langle g|\mathbf{p}|e\rangle|^2 / 3\pi\epsilon_0 \hbar c^3 \tag{5.28}$$

This means that the lifetime of the emitter, which is inverse of the decay rate given by Fermi's golden rule is determined by the Green's function of the surrounding medium of the emitter. The modification of the spontaneous emission rate and the emission linewidth of the emitter due to the presence of the surrounding embedding material is known as Purcell effect. The ratio of the spontaneous emission rate of the emitter in the embedding material to its emission rate in vacuum, i.e., Γ/Γ_0 is the Purcell factor.

5.4 Bridging the classical and quantum formulations

The classical dipole radiation power P' in Eq. 5.16 can be expressed in terms of the PLDOS as

$$P' = \frac{\pi\omega^2}{12\epsilon_0} |\mathbf{p}|^2 \rho_{\mathbf{p}}(\mathbf{r}_0, \omega). \tag{5.29}$$

Comparing this to the spontaneous emission rate for the two-level quantum emitter, we find that [89]

$$\frac{P'}{\Gamma} = \frac{|\mathbf{p}|^2}{|\langle g|\mathbf{p}|e\rangle|^2} \frac{\hbar\omega}{4}. \tag{5.30}$$

This is an important relationship, and we can intuitively verify it from the fact that the classical dipole moment is twice the dipole moment of the optical transition because of the contribution of both $\langle g|\mathbf{p}|e\rangle$ and $\langle e|\mathbf{p}|g\rangle$ [90]. Also, the atomic transition rate from the excited state to the ground state, which is equal to the spontaneous emission rate can be expressed as $P'/(\hbar\omega)$.

Spontaneous decay of an emitter is a quantum effect, and one needs quantum electrodynamics to properly investigate it. But the simple relationship in Eq. 5.30 implies that we can treat the source of radiation as a classical dipole current source in suitable contexts in the weak interaction picture, as the Green's function formalism bridges the gap between the classical and quantum pictures through the LDOS. The classical and quantum descriptions give similar results as long as the radiation reaction is much greater than vacuum energy, and plays the predominant role in controlling the LDOS. Both classical and quantum electromagnetic theories agree upon the modes available to the emitter, even though the physics behind the decay is different. This is essentially because we can decompose the Green's function into a set of normal modes (see Eq. 5.21), which remain the same in both quantum and classical formalism [88]. Invoking the relationship in Eq. 5.30 thus allows us to treat the quantum emitter as a classical dipole in our simulations and calculations.

From the ongoing discussion, we also noticed that the decay rate of the classical dipole depends only upon the value of field at the position of the dipole. This makes antenna theory an useful tool to study the radiation properties of an emitter in the presence of a scattering object, where the scattering object can be modeled as an antenna. The physical properties of the scattering object, like geometry is captured by the dyadic Green's function, which in turn controls the LDOS, and the decay rate of the emitter.

5.5 Antenna formalism

Once we have established the fact that we can study effects on the spontaneous emission of an emitter in the vicinity of a scattering object in the form of antenna theory, we try to recast the phenomenon of Purcell effect into antenna theory jargon. The scattering object, which might be a nanoparticle, acts as an antenna for the quantum emitter. Due to the emitter, a dipole is induced in the nanoantenna. This induced dipole in turn radiates, thereby increasing the LDOS at the site of the emitter. This results in an enhanced decay rate of the emitter in the presence of the nanoparticle.

For a radiating dipole $\mathbf{p}(\mathbf{r}_0, t)$ with harmonic time dependence, the average radiated power is given by Eq. 5.10. We compare this with the power dissipated by a load Z_L in a circuit, given by $P = \mathrm{Re}(Z_L)|I|^2/2$, where I is the current flowing through the load. If

we consider the dipole is radiating along the z axis, the current I (in $\mathrm{A}\cdot\mathrm{m}$), voltage V (in $\mathrm{V}\cdot\mathrm{m}^{-1}$), and specific impedance Z (in $\Omega\cdot\mathrm{m}^{-2}$) maps to the dipole moment, the Green's function and the electric field as [91]

$$I \leftrightarrow -i\omega p_z(\mathbf{r}_0), \quad V \leftrightarrow -E_z(\mathbf{r}_0), \quad Z \leftrightarrow -i\omega\mu_0\mu G_{zz}(\mathbf{r}_0, \mathbf{r}_0; \omega). \tag{5.31}$$

From Eq. 5.10, we can express the antenna resistance is terms of LDOS as [89]

$$\mathrm{Re}(Z) = \frac{\pi}{12\epsilon_0}\rho_{\mathbf{p}}(\mathbf{r}_0, \omega). \tag{5.32}$$

Thus, a higher antenna resistance refers to higher LDOS, and subsequently a higher decay rate. Following suit, we can define the Purcell factor of any arbitrary nanoantenna for a low-loss emitter as [90]

$$F = \frac{\mathrm{Re}(Z_{in})}{\mathrm{Re}(Z_{0,in})} = \frac{\mathrm{Im}\left(G_{zz}(\mathbf{r}_0, \mathbf{r}_0; \omega)\right)}{\mathrm{Im}\left(G_{0,zz}(\mathbf{r}_0, \mathbf{r}_0; \omega)\right)}, \tag{5.33}$$

where Z_{in}, and $Z_{0,in}$ are the input impedances of the emitter in the presence, and absence of the nanoantenna.

5.5.1 Circuit model

In Ref. [91], Greffet *et al.* have presented a circuit model for explaining the interaction between the quantum emitter and the nanoantenna. They have shown, that we can successfully represent a quantum emitter, and nanoantenna as a collection of lumped circuit elements. A two level quantum emitter with a Lorentzian polarizability of the form $\alpha(\omega) = \alpha_0/(\omega_0^2 - \omega^2 - i\gamma\omega)$ has an internal impedance given by

$$Z_{in} = \frac{i}{\omega\alpha\epsilon_0} = \frac{\gamma}{\alpha_0\epsilon_0} + i\frac{\omega_0^2}{\alpha_0\epsilon_0\omega} - i\frac{\omega}{\alpha_0\epsilon_0}. \tag{5.34}$$

Thus, the quantum emitter can be modeled as a series connection of a resistor with resistance $R_{in} = \gamma/\alpha_0\epsilon_0$, an inductor with inductance $L_{in} = \omega_0^2/\alpha_0\epsilon_0\omega^2$, and a capacitor with capacitance $C_{in} = \alpha_0\epsilon_0/\omega^2$. Similarly they have shown, that the microcavity nanoantenna can be modeled as a parallel RLC circuit, where $R = Q\omega/\epsilon_0 V_{\mathrm{eff}}\omega_r^2$, $L = 1/\epsilon_0 V_{\mathrm{eff}}\omega_r^2$, and $C = \epsilon_0 V_{\mathrm{eff}}$, where Q is the quality factor, ω_r is the resonance frequency, and V_{eff} is the effective mode volume of the nanoantenna. The equivalent circuit of the emitter and the

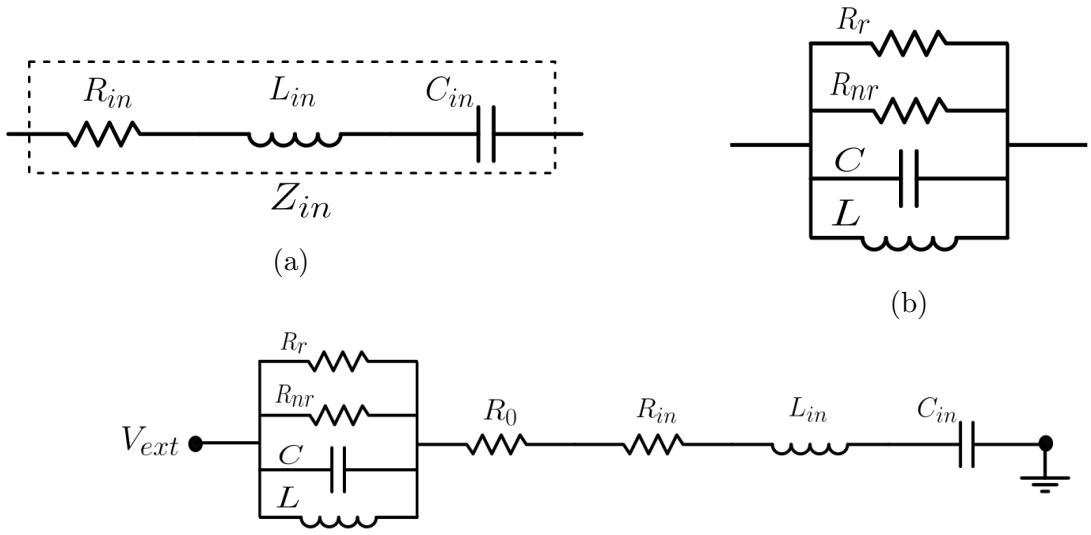

Figure 5.2: Equivalent circuit diagram for (a) a quantum emitter, (b) a nanoantenna, and (c) Purcell enhancement of emission from an emitter in the presence of a nanoantenna. V_{ext} represents the background field in the case of absorption. For the case of spontaneous emission, $V_{ext} = 0$.

nanoantenna is shown in Fig. 5.2. In the absence of a nanoantenna, the radiative efficiency of the emitter is defined by $\eta_{rad} = R_0/(R_{in} + R_0)$, where R_0 is the vacuum resistance, and is given by $R_0 = \omega\mu_0 \times \mathrm{Im}\left[G_0(\mathbf{r}_0, \mathbf{r}_0; \omega)\right] = \omega^2/6\pi\epsilon_0 c^3$. Similarly, the radiative yield of the nanoantenna is defined by $\eta_{na} = R_{nr}/(R_r + R_{nr})$, where R_r and R_{nr} are the radiative and non-radiative resistances. The Purcell factor (the enhancement in the spontaneous emission of the emitter in the presence of nanoantenna) of the nanoantenna is $F_{na} = (R_0 + R)/R_0$. From this, it is easy to see that the Purcell enhancement of the emitter in the presence of the nanoantenna is given by the ratio of the specific resistances if the emitter and the nanoantenna are on resonance. Thus,

$$F = \frac{R_0 + R\eta_{na}}{R_0 + R + R_{in}}. \tag{5.35}$$

By assuming $R \gg R_0$, the Purcell factor can be expressed as [91, 92]

$$F = \frac{1 + F_{na}\eta_{na}}{1 + F_{na}\eta_{rad}}. \tag{5.36}$$

5.5.2 Antenna parameters

i. Antenna radiation efficiency

The antenna radiation efficiency is defined as the ratio of the power radiated to the total dissipated power as

$$\eta_{rad} = \frac{P_{rad}}{P_{rad} + P_{loss}}. \tag{5.37}$$

P_{loss} is the power lost because of thermal effects and other loss channels. The intrinsic quantum yield of emitter is defined by the ratio of power radiated to the total power dissipated by the quantum emitter in the absence of nanoantenna

$$\eta_i = \frac{P_{0,rad}}{P_{0,rad} + P_{0,int}}, \tag{5.38}$$

where $P_{0,int}$ and $P_{0,int}$ represent the radiated power and intrinsic losses (arising from internal transitions) of the emitter in absence of the nanoantenna. Thus, taking the intrinsic loss into account, the effective antenna radiation efficiency can be reformulated as [89]

$$\eta_{rad} = \frac{P_{rad}/P_{0,rad}}{P_{rad}/P_{0,rad} + P_{loss}/P_{0,rad} + (1-\eta_i)/\eta_i}. \tag{5.39}$$

For $\eta_i \ll 1$, we can see that the overall efficiency of radiation is enhanced due to the presence of the nanoantenna, which helps in increasing the LDOS for more efficient emission.

ii. Antenna directivity and antenna gain

The directive gain or directivity of an antenna is given by the ratio of radiation intensity in a particular direction to the radiation intensity averaged over all directions. It can be expressed as

$$D(\theta, \phi) = \frac{4\pi}{P_{rad}} U(\theta, \phi), \tag{5.40}$$

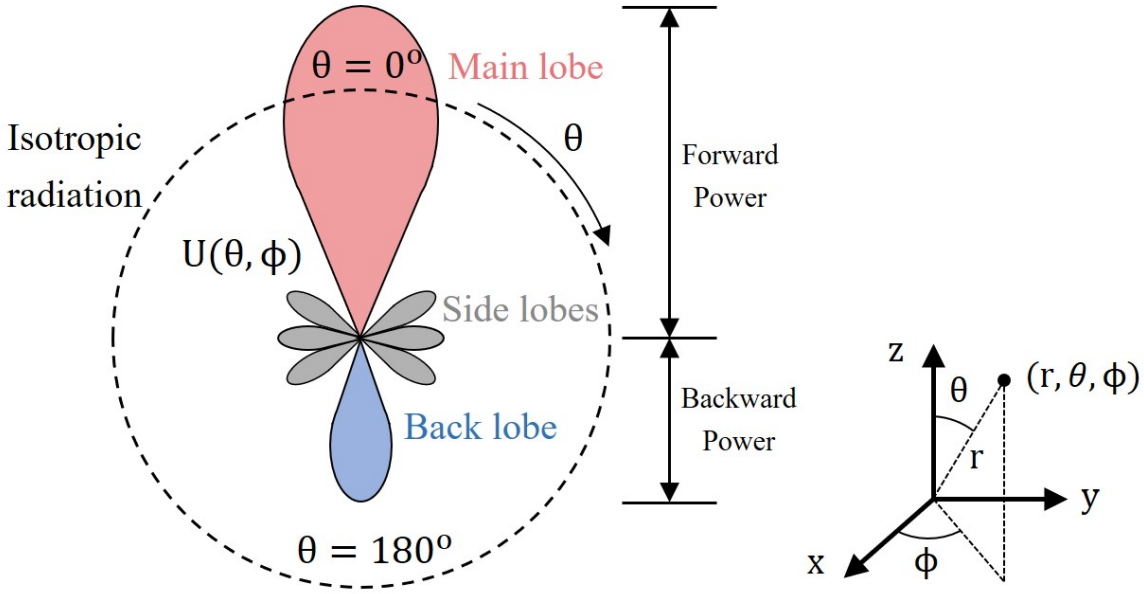

Figure 5.3: The radiation pattern $U(\theta, \phi)$ of an antenna, showing the main (front) lobe, the back lobe, and multiple side lobes. The dotted circle represents the radiation pattern of an isotropic antenna. The front to back ratio is given by the ratio of the forward, and the backward radiated powers.

where $U(\theta, \phi)$ is the radiation intensity along a particular direction defined by the zenith/ polar angle θ and azimuthal angle ϕ, such that,

$$\oiint_{\Omega} U(\theta, \phi) d\Omega = \int_{\phi=0}^{\phi=2\pi} \int_{\theta=0}^{\theta=\pi} U(\theta, \phi) \sin\theta d\phi d\theta = P_{rad}, \tag{5.41}$$

where $d\Omega$ is an infinitesimal element of the solid angle. The maximum directivity is the directivity in the direction of the maximum radiation intensity, given by $D_{max} = 4\pi U_{max}/P_{rad}$. Fig. 5.3 shows the radiation pattern of an antenna.

The antenna gain is defined as the ratio of radiation intensity in a direction to the radiation intensity that would be obtained if the power accepted by the antenna were radiated isotropically. Thus, it is given by

$$G = \frac{4\pi}{P_{rad} + P_{loss}} U(\theta, \phi) = \eta_{rad} D. \tag{5.42}$$

Another important measure of directional emission by an antenna that we shall be using in Chapter 7 is the front to back ratio (FBR). This is a ratio of the power in any specified direction of interest (forward direction), and the power radiated in the opposite direction (backward direction), i.e., 180° away from the angle of interest. Thus, it can be expressed as

$$\text{FBR (in dB)} = D|_{\text{forward,dB}} - D|_{\text{backward,dB}}. \tag{5.43}$$

Thus, we can increase the gain by including a nanoresonator antenna in the vicinity of an emitter to increase the radiation efficiency. We can also design nanoantennas (e.g. metasurfaces and different kinds of grating patterns) which allows us to have some degree of control over the directivity, and thus engineer the radiation pattern of an emitter. In Chapter 7 we shall investigate how we can design sub-wavelength photonic structures to control the radiation properties of an NV center.

Chapter 6

Adjoint optimization and inverse design

6.1 Motivation

In this chapter, we shall delve into the theoretical background necessary for understanding the inverse design approach based on adjoint optimization used in Chapter 7 for designing custom-made nanophotonic structures with desired properties.

6.2 Adjoint method for electromagnetic theory

The entire realm of electromagnetic (EM) theory is governed by the set of four Maxwell's equations. The interaction of EM fields with a scattering medium can be easily derived by solving the Maxwell's equations. However, often we come across the non-trivial scenario whereby we need to design a scattering medium, that gives a certain response to an incident field. In such a situation, one cannot guarantee that a physical solution for the problem exists. Even if the solution exists, one cannot guarantee that there would be a unique solution. What makes the process of design by specification even harder is that there exists too many degrees of freedom while designing even a nanoscale device. Thus, designing the device using a brute force approach by exhausting the rich parameter space as shown in Fig. 6.1 is not feasible. The adjoint optimization approach offers substantial speed-up compared to the brute force approach, and in this section we shall explore how it works.

The optimization problem of finding the best structure with the desired response to the incident field can be setup mathematically as:

$$\begin{aligned} &\underset{\text{through spatial variation of } \epsilon,\mu}{\text{Maximize}} && F(\mathbf{E},\mathbf{H},\epsilon,\mu,\omega) \\ &\text{Under constraints:} && \nabla\cdot\mathbf{E} = \frac{\rho}{\epsilon}, \\ & && \nabla\cdot\mathbf{H} = 0, \\ & && \nabla\times\mathbf{E} = -\mu\frac{\partial\mathbf{H}}{\partial t}, \\ & && \nabla\times\mathbf{H} = \mathbf{J} + \epsilon\frac{\partial\mathbf{E}}{\partial t}. \end{aligned} \tag{6.1}$$

Here, the permittivity $\epsilon(\mathbf{r})$, and the permeability $\mu(\mathbf{r})$ are the parameters that encompass the properties of the device that we can control, and $F(\mathbf{E},\mathbf{H},\epsilon,\mu,\omega)$ is the figure of merit (or cost function) that we want to maximize (or minimize - as dictated by the problem at hand). Thus, in simple words, we are interested in finding the vales of ϵ, and μ for our nano-structure, under the framework of Maxwell's equations. To make our life simpler, if we choose non-magnetic materials, $\mu = \mu_0$, we only need to optimize for the permittivity ϵ. One can also have harmonic time dependence of the fields, viz., $\mathbf{E}(t) = \mathbf{E}e^{-i\omega t}$ to further simplify the problem. The resultant optimization problem can be solved using gradient based techniques. We start by discretization of the device into small pixels, with each pixel being represented by its permittivity ϵ_i. But the device can consist of millions or billions of pixels. Thus, calculating the derivative of the cost function with respect to all the design parameters (i.e. finding the change in the figure of merit due to change in all the individual values of ϵ_i) is computationally expensive. But as we shall see, the adjoint method simplifies the problem substantially.

Now, to illustrate the principle of the adjoint optimization, we consider the following simple example. An electric field E_{in} is incident on the device characterized by its permittivity $\epsilon(r)$. The operation of the device can be visualized as a transformation $T(\epsilon)$ on the input field. As a result of the interaction with the device, the electric field at some specific point r_0 is $E(r_0)$ (for simplicity, and without loss of generality, we can consider that the field is scalar everywhere). Now, suppose we want to maximize the absolute value of the field at the point r_0. Thus, we can choose the figure of merit to be $F = \frac{1}{2}|E(r_0)|^2$. For simplicity, we consider material invariance in the out-of-plane direction, and the field is linearly polarized in the out-of-plane direction as well. This reduces the structure to a 2D lattice and we can consider that the fields are scalar. This is just for ease of understanding and notational convenience, and one can easily use the vectorial representations instead.

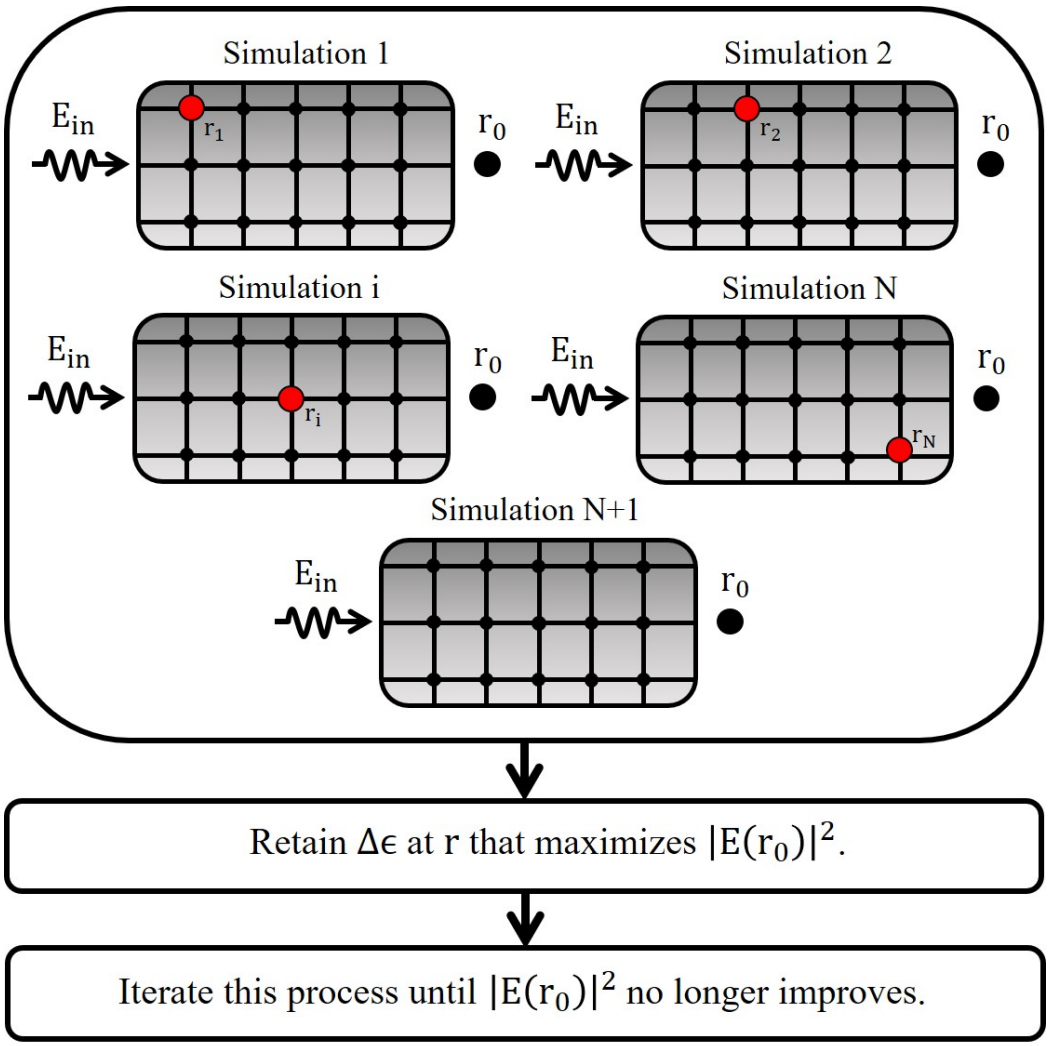

Figure 6.1: The brute force approach tries to find the best permittivity profile to maximize the square of the absolute value of the electric field at r_0 by iterating over all the possible dielectric inclusions. A dielectric change is made at every possible point, and the best inclusion is retained at every iteration. Each iteration contains $N + 1$ simulations. This process is repeated until $|E(r_0)|^2$ no longer improves.

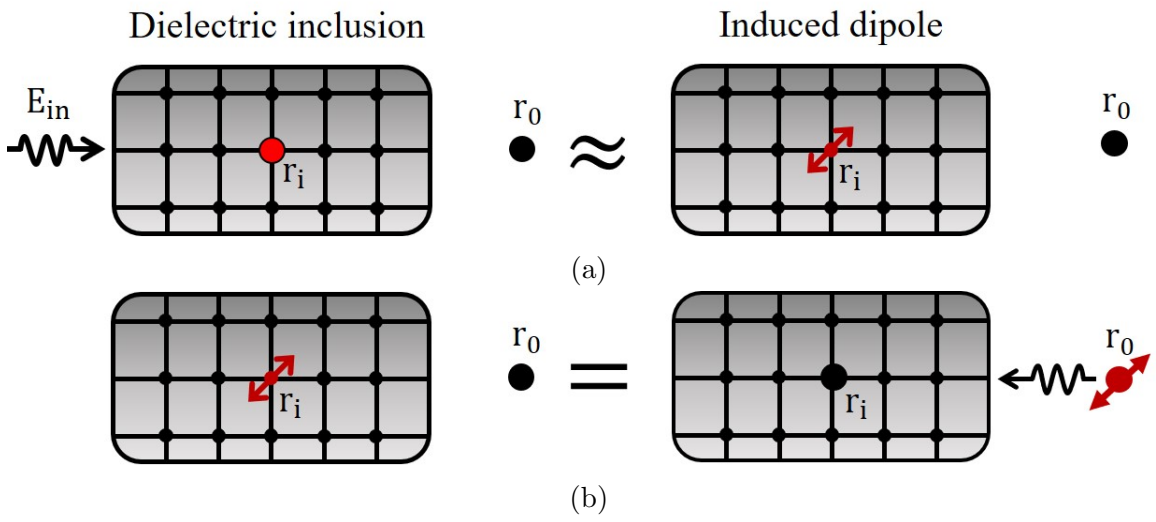

Figure 6.2: (a) Each dielectric inclusion can be approximated with an induced dipole moment $p_{\text{ind}}(r)$ at the point of inclusion r. (b) Because of Lorentz reciprocity theorem, the electric field at r_0 because of the presence of a dipole at r is equal to the electric field at r because of the presence of the same dipole at r_0. This makes the Green's function symmetric such that $G(r_0, r) = G(r, r_0)$.

Next, we introduce a small change of dielectric permittivity $\Delta\epsilon$ of volume ΔV at position r. That changes the figure of merit F by [93]

$$\begin{aligned}
\Delta F &= \frac{1}{2}|E_{\text{new}}(r_0)|^2 - \frac{1}{2}|E_{\text{old}}(r_0)|^2 \\
&= \frac{1}{2}\left[E_{\text{old}}(r_0) + \Delta E(r_0)\right]\left[E^*_{\text{old}}(r_0) + \Delta E^*(r_0)\right] - \frac{1}{2}E_{\text{old}}(r_0)\cdot E^*_{\text{old}}(r_0) \\
&= \frac{1}{2}\left[E_{\text{old}}(r_0)\cdot\Delta E^*(r_0) + E^*_{\text{old}}(r_0)\cdot\Delta E(r_0) + |\Delta E(r_0)|^2\right] \\
&\approx \text{Re}\left[E^*_{\text{old}}(r_0)\cdot\Delta E(r_0)\right] \quad \text{(Neglecting smaller terms for small inclusion)} \qquad (6.2)
\end{aligned}$$

where $E_{\text{old(new)}}(r_0)$ is the old (new) value of electric field at r_0 before (after) the introduction of $\Delta\epsilon$ at r, and $\Delta E(r_0)$ is the change in electric field at r_0 resulting from the change, i.e., $E_{\text{new}}(r_0) = E_{\text{old}}(r_0) + \Delta E(r_0)$. The small change in the dielectric at r results in an induced dipole moment $p_{\text{ind}}(r) = \alpha E_{\text{new}}(r) \approx \Delta\epsilon\Delta V E_{\text{new}}(r)$ at r as shown in Fig. 6.2a. Here, α is the polarizability of the dielectric inclusion, and is a function of the permittivity and the geometry of the inclusion. For a spherical inclusion of permittivity ϵ_2 in place of ϵ_1,

the polarizability is given by $\alpha_{sphere} = 3\epsilon_0 \Delta V \frac{\epsilon_2 - \epsilon_1}{\epsilon_2 + 2\epsilon_1}$ where ϵ_0 is the permittivity of free space. Thus, in the limit of small $\Delta\epsilon$, in free space we can express the polarizability as $\alpha_{sphere} = \Delta\epsilon\Delta V$. One can consider any shape for the dielectric inclusion, and choose the polarizability accordingly using the Clausius-Mossotti relationship. Thus, the change in electric field at r_0 can be expressed as:

$$\Delta E(r_0) = G(r_0, r) \cdot p_{\text{ind}}(r) = \Delta\epsilon\Delta V G(r_0, r) \cdot E_{\text{new}}(r), \tag{6.3}$$

where $G(r_0, r)$ is the scalar Green's function, and it is equal to the electric field at r_0 because of a unit dipole at r. Thus, one can rearrange Eq. 6.2, and Eq. 6.3 to get:

$$\frac{\Delta F}{\Delta \epsilon_r} = \epsilon_0 \Delta V \, \text{Re}\left[E^*_{\text{old}}(r_0) \cdot G(r_0, r) \cdot E_{\text{new}}(r)\right], \tag{6.4}$$

where ϵ_r is the relative permittivity of the inclusion and ϵ_0 is the permittivity of free space, such that $\Delta\epsilon_r = \Delta\epsilon/\epsilon_0$. For infinitesimal $\Delta\epsilon_r$, we can consider $E_{\text{new}}(r) \approx E_{\text{old}}(r)$. If $\Delta\epsilon_r$ is not small enough, we can compensate by making ΔV smaller. That gives us

$$\frac{\Delta F}{\Delta \epsilon_r} = \epsilon_0 \Delta V \, \text{Re}\left[E^*_{\text{old}}(r_0) \cdot G(r_0, r) \cdot E_{\text{old}}(r)\right] \tag{6.5}$$

According to Lorentz reciprocity theorem, the electric field at r_0 because of the presence of a unit dipole at r is equal to the electric field at r because of the presence of a similar unit dipole at r_0. This tells us that the Green's function is symmetric, and we get $G(r_0, r) = G(r, r_0)$ (see Fig. 6.2b). Using this relationship, we find that the derivative of the figure of merit can be expressed as

$$\begin{aligned} \frac{\Delta F}{\Delta \epsilon_r} &= \text{Re}\left[(\epsilon_0 \Delta V G(r, r_0) \cdot E^*_{\text{old}}(r_0)) \cdot E_{\text{old}}(r)\right] \\ &= \text{Re}\left[E^{\text{Ad}}(r) \cdot E_{\text{old}}(r)\right]. \end{aligned} \tag{6.6}$$

The adjoint electric field is given by $E^{\text{Ad}}(r) = \epsilon_0 \Delta V G(r, r_0) \cdot E^*_{\text{old}}(r_0)$ [94]. This represents the field at r due to a dipole at r_0 with amplitude $p_{\text{ind}}(r_0) = \epsilon_0 \Delta V E^*_{\text{old}}(r_0)$. It turns out that only two simulations are necessary to calculate the derivative of the figure of merit.

In the first (forward) simulation we find the strength of the electric field in our region of interest before any dielectric modifications. That gives us the values of $E_{\text{old}}(r)$ for all values of r including r_0. In the second (adjoint) simulation, we calculate the field produced

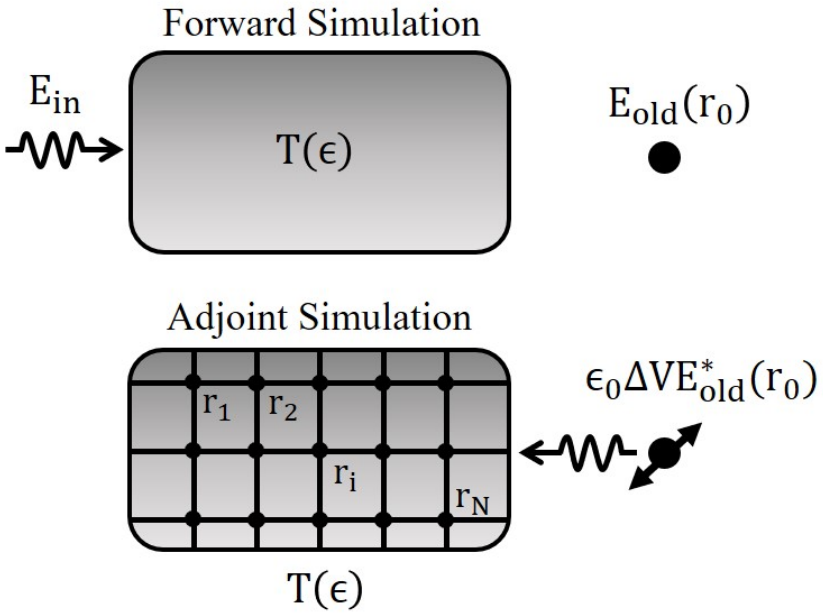

Figure 6.3: The adjoint optimization approach reduces the number of simulations at each iteration from $N+1$ to only two: (a) forward simulation, and (b) adjoint simulation. In forward simulation we calculate the electric field at r_0, and the region of interest as a result of the incident field E_{in}. In the adjoint simulation, a dipole is driven at r_0 to calculate the adjoint electric field. This greatly simplifies the process of calculating the derivative of the merit function $\Delta F/\Delta\epsilon_r$.

at all locations r in the region of interest by an oscillating dipole $p_{\text{ind}}(r_0) = \epsilon_0 \Delta V E^*_{\text{old}}(r_0)$ located at r_0. That gives us the values of $E^{\text{Ad}}(r)$ for all values of r. So the derivative of the figure of merit or cost function F with respect to the design parameter ϵ_i for every pixel r_i (and thus the effect of dielectric modification at any point r_i) can be calculated using only two simulations as shown in Fig. 6.3. That is a great reduction in computational resources compared to the $N+1$ simulations needed for a brute force approach.

Thus, we can now iteratively calculate the optimum values of the permittivity of our device for our task by using gradient descent/ascent technique, with the highly efficient adjoint approach of calculating the gradient of the merit function F as a subroutine. In each iteration, we calculate the derivative of F using the forward and adjoint simulations. Then, we move along the direction of the steepest descent/ascent in the parameter space of the merit function by making the relevant dielectric change, in pursuit of the global minima/maxima.

6.2.1 Shape and topology optimization

There are two ways we can optimize the geometry of the device by changing/perturbing the permittivity of the design domain at each iteration. The first type is a boundary (shape) perturbation at the surface of the two materials permittivity ϵ_1, and ϵ_2 as shown in Fig. 6.4a. It changes the outline of the device without changing its topology. The second type is a topological perturbation, which results from the addition of dielectric ϵ_2 in place of dielectric ϵ_1 (as shown in Fig. 6.4b), and vice-versa. This results in a change in the topology of the device. Thus, the topology perturbation method is more versatile compared to the boundary perturbation, and we shall be using it for the purpose of our optimization in Chapter 7. In this section, we shall briefly describe how these two different methods work [93, 95].

6.2.2 Topological perturbation

The relationship given in Eq. 6.6 can be generalised for 3D inverse design problems. The electric and magnetic fields are three-dimensional vectors, and the spatial variation of permittivity is given by the permittivity tensor. The merit function can be a function of the entire region of interest. In such a scenario, one might represent the merit function as

$$F(\mathbf{E},\mathbf{H}) = \iiint_V f(\mathbf{E}(\mathbf{r}),\mathbf{H}(\mathbf{r}))d^3\mathbf{r}, \tag{6.7}$$

such that the merit function is the result of calculating some function $f(\mathbf{E},\mathbf{H})$ over the entire region which has a volume of V. Since $\mathbf{E}$ and $\mathbf{H}$ are complex functions, we can write the change in the figure of merit dF as

$$\delta F = 2\,\mathrm{Re}\iiint_V \left[\frac{\partial f}{\partial \mathbf{E}}(\mathbf{r})\cdot d\mathbf{E}(\mathbf{r}) + \frac{\partial f}{\partial \mathbf{H}}(\mathbf{r})\cdot d\mathbf{H}(\mathbf{r})\right] d^3\mathbf{r}. \tag{6.8}$$

We can define Green's functions $\overleftrightarrow{\mathbf{G}}^{EP}(\mathbf{r},\mathbf{r}')$ and $\overleftrightarrow{\mathbf{G}}^{HP}(\mathbf{r},\mathbf{r}')$ which give the electric and magnetic field at $\mathbf{r}$ due to an unit electric dipole at $\mathbf{r}'$, such that the field variations is given by

$$d\mathbf{E}(\mathbf{r}) = \frac{1}{V_{\text{pert}}}\iiint_{V_{\text{pert}}} \overleftrightarrow{\mathbf{G}}^{EP}(\mathbf{r},\mathbf{r}')\mathbf{p}_{\text{ind}}(\mathbf{r}')d^3\mathbf{r}', \tag{6.9a}$$

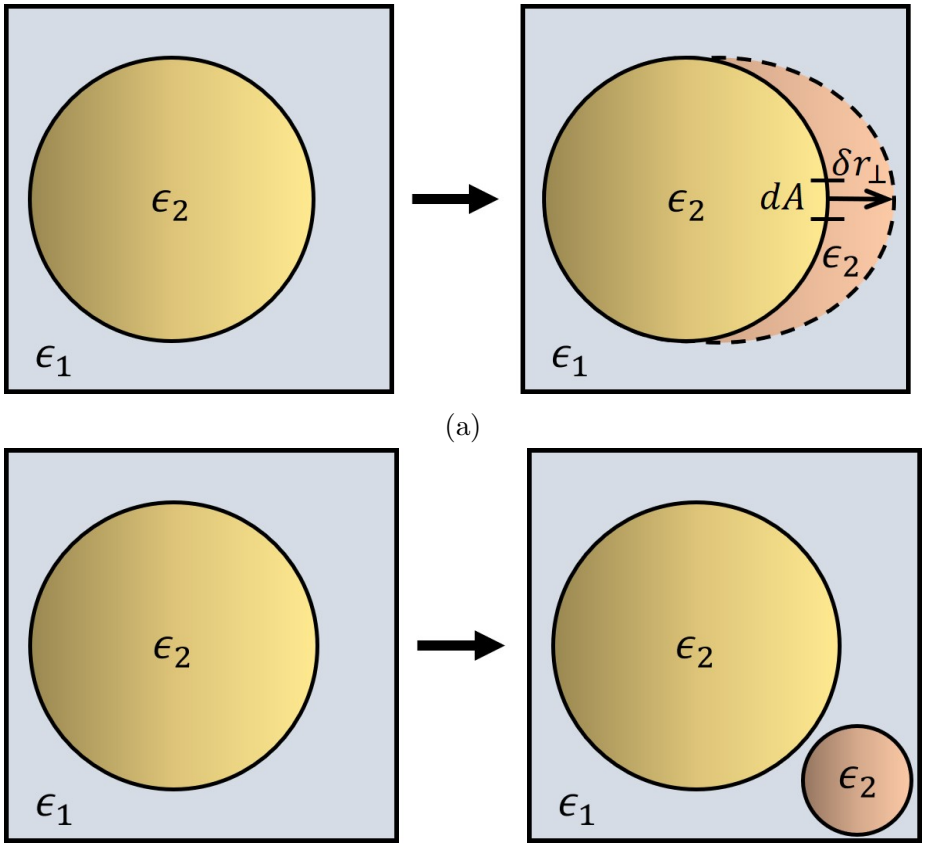

Figure 6.4: (a) A boundary perturbation changes the geometry of the surface between the two materials without changing the topology. (b) The topological perturbation changes the topology of the design domain by inclusion/removal of new material. For example, in this figure, addition of a material of permittivity ϵ_2 in the place of ϵ_1 changes the topology of the design. The volume of the dielectric addition (shown in pink) is V_{pert}.

$$d\mathbf{H}(\mathbf{r}) = \frac{1}{V_{\text{pert}}} \iiint_{V_{\text{pert}}} \overleftrightarrow{\mathbf{G}}^{HP}(\mathbf{r}, \mathbf{r}') \mathbf{p}_{\text{ind}}(\mathbf{r}') d^3\mathbf{r}', \tag{6.9b}$$

where V_{pert} is the volume over which the permittivity changes. We substitute these equations into the expression for δF, and use the symmetry of the Green's function, i.e., $G_{ij}^{EP}(\mathbf{r}, \mathbf{r}') = G_{ji}^{EP}(\mathbf{r}', \mathbf{r})$ and $G_{ij}^{HP}(\mathbf{r}, \mathbf{r}') = -G_{ji}^{EM}(\mathbf{r}', \mathbf{r})$ where $\overleftrightarrow{\mathbf{G}}^{EM}(\mathbf{r}', \mathbf{r})$ gives the electric field at $\mathbf{r}'$ due to a magnetic dipole at $\mathbf{r}$. That yields [93]:

$$\delta F = \frac{2}{V_{\text{pert}}} \text{Re} \left\{ \iiint_{V_{\text{pert}}} d^3\mathbf{r}' \mathbf{p}_{\text{ind}}(\mathbf{r}') \iiint_V d^3\mathbf{r} \left(\overleftrightarrow{\mathbf{G}}^{EP}(\mathbf{r}', \mathbf{r}) \frac{\partial f}{\partial \mathbf{E}}(\mathbf{r}) - \overleftrightarrow{\mathbf{G}}^{EM}(\mathbf{r}', \mathbf{r}) \frac{\partial f}{\partial \mathbf{H}}(\mathbf{r}) \right) \right\}$$
$$= \frac{2}{V_{\text{pert}}} \text{Re} \left\{ \iiint_{V_{\text{pert}}} d^3\mathbf{r}' \mathbf{p}_{\text{ind}}(\mathbf{r}') \cdot \mathbf{E}^{\text{Ad}}(\mathbf{r}') \right\}. \tag{6.10}$$

The induced dipole, the amplitude of the electric dipole $\frac{\partial f}{\partial \mathbf{E}}(\mathbf{r})$, and the amplitude of the magnetic dipole $\frac{\partial f}{\partial \mathbf{H}}(\mathbf{r})$ can be calculated in the forward simulation. The second part of the expression gives the adjoint field as a result of the oscillating electric and magnetic dipoles at $\mathbf{r}$.

Now, for topology a topological perturbation, we simply replace the induced dipole with the expression $\mathbf{p}_{\text{ind}}(\mathbf{r}') = 3\epsilon_0 V_{\text{pert}} \frac{\epsilon_2 - \epsilon_1}{\epsilon_2 + 2\epsilon_1} \mathbf{E}_{\text{old}}(\mathbf{r}')$ for a spherical inclusion under the assumption $\mathbf{E}_{\text{new}}(\mathbf{r}') = \mathbf{E}_{\text{old}}(\mathbf{r}')$. This gives us the change in the merit function to be

$$\delta F = 2 \,\text{Re} \left\{ 3\epsilon_0 \frac{\epsilon_2 - \epsilon_1}{\epsilon_2 + 2\epsilon_1} \mathbf{E}_{\text{old}}(\mathbf{r}') \cdot \mathbf{E}^{\text{Ad}}(\mathbf{r}') \right\}. \tag{6.11}$$

For any other geometry of dielectric inclusion with polarizability tensor $\overleftrightarrow{\alpha}$, we have $\delta F = \frac{2}{V_{\text{pert}}} \text{Re} \left\{ \overleftrightarrow{\alpha} \mathbf{E}_{\text{old}}(\mathbf{r}') \cdot \mathbf{E}^{\text{Ad}}(\mathbf{r}') \right\}$. As we observed, this method creates an inclusion of ϵ_2 in a material of ϵ_1, and thus changes the topology of the structure. In the forward simulation we calculate $\mathbf{E}_{\text{old}}(\mathbf{r}')$, and in the adjoint simulation we find the adjoint field $\mathbf{E}^{\text{Ad}}(\mathbf{r}')$ at every point $\mathbf{r}'$. Then we add a dielectric inclusion $\Delta\epsilon$ such that δF is maximized. We repeat this process until the merit function saturates.

6.2.3 Boundary perturbation

For shape optimization via boundary perturbation, let us consider that there is a material of permittivity ϵ_2 in a region of permittivity ϵ_1. We shall be morphing the boundary of the two materials via small boundary perturbations. Let us consider a differential surface area dA where the boundary changes perpendicular to the surface by $dr_\perp$ as shown in Fig. 6.4a. Then, we can re-write Eq. 6.10 as

$$\begin{aligned}\delta F &= \frac{2}{V_{\text{pert}}}\,\text{Re}\left\{\iiint_{V_{\text{pert}}} \mathbf{p}_{\text{ind}}(\mathbf{r}')\cdot\mathbf{E}^{\text{Ad}}(\mathbf{r}')dr_\perp dA\right\}\\ &= \frac{2}{V_{\text{pert}}}\,\text{Re}\left\{\iint_{A} \mathbf{p}_{\text{ind}}(\mathbf{r}')\cdot\mathbf{E}^{\text{Ad}}(\mathbf{r}')\delta r_\perp(\mathbf{r}')dA\right\}\\ &\quad\left(\text{For infinitesimal perturbation, we can consider } \int dr_\perp \to \delta r_\perp(\mathbf{r}').\right)\end{aligned} \tag{6.12}$$

Next, we decompose the field into components parallel ($\|$) and perpendicular ($\perp$) to the surface. Then, by using the boundary conditions, for small perturbations, the new electric field is given by

$$\mathbf{E}_{\text{new}}(\mathbf{r}') \approx \mathbf{E}^{\|}_{\text{old}}(\mathbf{r}') + \frac{\mathbf{D}^{\perp}_{\text{old}}(\mathbf{r}')}{\epsilon_2} = \mathbf{E}^{\|}_{\text{old}}(\mathbf{r}') + \frac{\epsilon_1}{\epsilon_2}\mathbf{E}^{\perp}_{\text{old}}(\mathbf{r}'). \tag{6.13}$$

Using this relationship, for a small spherical inclusion we get

$$\delta F = 2\,\text{Re}\left\{(\epsilon_2-\epsilon_1)\left(\mathbf{E}^{\|}_{\text{old}}(\mathbf{r}') + \frac{\epsilon_1}{\epsilon_2}\mathbf{E}^{\perp}_{\text{old}}(\mathbf{r}')\right)\cdot\mathbf{E}^{\text{Ad}}(\mathbf{r}')\right\}. \tag{6.14}$$

If we also decompose the adjoint field as $\mathbf{E}^{\text{Ad}}(\mathbf{r}') = \mathbf{E}^{\text{Ad},\|}(\mathbf{r}') + \dfrac{\mathbf{D}^{\text{Ad},\perp}(\mathbf{r}')}{\epsilon_1} = \mathbf{E}^{\text{Ad},\|}(\mathbf{r}') + \frac{\epsilon_1}{\epsilon_2}\mathbf{E}^{\text{Ad},\perp}(\mathbf{r}')$, we get

$$\delta F = \frac{2}{V_{\text{pert}}}\,\text{Re}\iint_A\left[(\epsilon_2-\epsilon_1)\mathbf{E}^{\|}_{\text{old}}(\mathbf{r}')\cdot\mathbf{E}^{\text{Ad},\|}(\mathbf{r}') + (\epsilon_2-\epsilon_1)\frac{\mathbf{D}^{\perp}_{\text{old}}(\mathbf{r}')}{\epsilon_2}\cdot\frac{\mathbf{D}^{\text{Ad},\perp}(\mathbf{r}')}{\epsilon_1}\right]\delta r_\perp(\mathbf{r}')dA. \tag{6.15}$$

To move along the gradient in the parameter space, we can simply assign [93]

$$\delta r_\perp(\mathbf{r}') \sim \text{Re}\left[(\epsilon_2-\epsilon_1)\mathbf{E}^{\|}_{\text{old}}(\mathbf{r}')\cdot\mathbf{E}^{\text{Ad},\|}(\mathbf{r}') + (\epsilon_2-\epsilon_1)\frac{\mathbf{D}^{\perp}_{\text{old}}(\mathbf{r}')}{\epsilon_2}\cdot\frac{\mathbf{D}^{\text{Ad},\perp}(\mathbf{r}')}{\epsilon_1}\right], \tag{6.16}$$

upto some factor (a hyperparameter) for all points $\mathbf{r}'$ on the surface. As observed, this only leads to changing the boundary of the surface. In the forward simulation we calculate $\mathbf{E}_{\text{old}}(\mathbf{r}')$ and the amplitude of the adjoint dipoles. In the adjoint simulation, we calculate the adjoint field. Finally, we change the boundary of the object using the update rule given in Eq. 6.16.

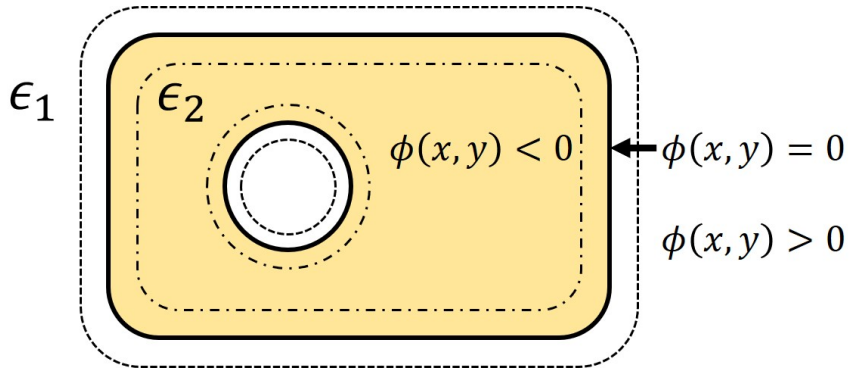

Figure 6.5: The signed level set function $\phi(x, y)$ is negative inside the material with permittivity ϵ_2, and positive in the region with permittivity ϵ_1. And the zeros of the level set function $\phi(x, y) = 0$ define the boundary between the two materials.

6.3 Fabrication dependent optimization constraints

In order to be able to converge at any arbitrary geometry, we can treat each pixel on the boundary of the object as a particle evolving semi-autonomously. However, this gives rise to two important issues. First, this method of optimization is computationally inefficient as it requires a lot of processing capacity. Second, we might converge at a geometry which might have sharp edges/ narrow bridges/ tiny islands making it very difficult to accurately produce using standard fabrication techniques.

By using level set methods (for more in-depth exploration please check Ref. [96, 97]) one can significantly reduce the amount of computational resources required, and set constraints that ensure that we converge at a structure that can be accurately made in a cleanroom. For example, for a geometry with only two types of materials, the essential information is carried by the boundary between the two regions. Thus, we construct a signed level set function $\phi(x, y) : \mathbb{R}^2 \to \mathbb{R}$ which encodes the information of the boundary between the materials. The boundary lies on the curve $\phi(x, y) = 0$. Also, the value of the function is positive for one material, and negative for another (see Fig. 6.5), i.e.,

$$\epsilon(x, y) = \begin{cases} \epsilon_1 & \text{for } \phi(x, y) > 0 \\ \epsilon_2 & \text{for } \phi(x, y) < 0. \end{cases} \tag{6.17}$$

Another interesting feature of the the level set function is that it is a distance function, i.e., the magnitude of the function at any point is its distance from the closest boundary.

For example, for a circle, $\phi(x, y) = \sqrt{x^2 + y^2} - R$. This results in the interesting property $|\nabla\phi(x, y)| = 1$, $\forall x, y$, where $\nabla\phi = \nabla_x\phi + \nabla_y\phi$.

Now, this level set function can be evolved by making it a time-dependent function, and using the following Hamilton-Jacobi partial differential equation (PDE):

$$\frac{\partial\phi}{\partial t} + v(x, y)|\nabla\phi| = 0, \tag{6.18}$$

where $v(x, y) : \mathbb{R}^2 \to \mathbb{R}$ is a scalar velocity field. One simple choice of the velocity field can be $v = \frac{\mathrm{d}F}{\mathrm{d}\phi}$. We start the simulation at $t = 0$, and continue evolving the structure until we converge.

However, to avoid designs with sharp corners and edges, we can select a better velocity field. Thereby, we change our evolution PDE to [98]:

$$\frac{\partial\phi}{\partial t} - w(\varrho)\varrho|\nabla\phi| = 0, \tag{6.19}$$

where, ϱ is the local curvature (in two dimensions) as given by:

$$\varrho = \nabla \cdot \left(\frac{\nabla\phi}{|\nabla\phi|}\right), \tag{6.20}$$

and $w(\varrho)$ is a function that restricts the local curvature to go above a threshold ϱ_{thres}. In the most simple case, $w(\varrho)$ can be a function that has a value of 1 for curvature greater than ϱ_{thres}, and a value of 0 otherwise. However, other kinds of smoother weighing function w can be chosen for better performance [98]. Evolving the level set function this way instead of evolving each and every point and keeping track of the entire design region proves to be a significantly simpler task computationally.

Even after selecting the aforementioned parameters carefully, there might still exist narrow bridges and small islands with low curvatures. Morphological dilation can be used to fill up small holes, or thicken/dilate narrow/small features. Morphological erosion can also be used to remove small islands, and remove small, narrow features. Some curvature filters can also we used to smoothen any remaining rough nooks and crannies [98]. Finally, we can arrive at a design that can be accurately fabricated in a cleanroom with standard techniques.

Chapter 7

Inverse design of optical antennas for engineering directional emission from NV centers

7.1 Motivation

NV centers are solid state color centers found in diamonds, which are formed when a nitrogen atom replaces a carbon atom in the diamond lattice. These point defects have now been quite extensively studied for half a century, and have emerged as a promising platform for quantum sensing [10, 99–104], quantum memories [105–107], and quantum information processing [8, 108, 109]. They are a promising candidate among other solid state emitters because of a myriad of favourable properties like high integrability [110, 111], stable room temperature operations [9, 112], easy electronic spin state initialization and readout using microwave and optical pulses [113–115], long electron spin coherence time [100, 116, 117], and precise geometrical control using ion implantation [118, 119]. But for efficient readout of NV centers for any application, it is essential to control its emission pattern. In this chapter, we propose a device for efficient extraction of light from NV centers, by achieving control over its radiation pattern using adjoint optimization.

First, in Sec. 7.2, we provide a brief introduction to the properties (crystal structure and electronic level structure) of NV centers essential for subsequent discussions. Then, in Sec. 7.3, we shall study the performance of some nanophotonic structures previously used by other research groups to efficiently extract light from various quantum emitters. In Sec. 7.4 we propose our structure designed with the help of adjoint optimization technique, and

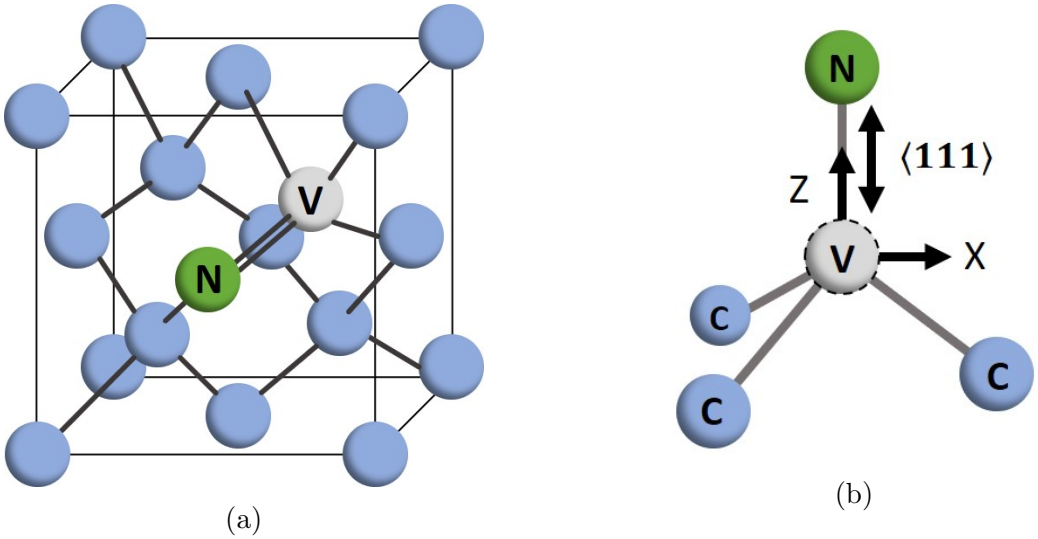

(a) (b)

Figure 7.1: (a) An NV center in the fcc diamond lattice formed by a lattice vacancy (grey) along with a nitrogen atom (green). (b) Schematic of the defect structure of an NV center with the vacancy (grey), the substitutional nitrogen atom (green), and the nearest neighbour carbon atoms (blue). The dipole axis lies along the major symmetry axis in the Z-direction. The NV center radiates perpendicular to the [111] surface of the diamond unit cell.

predict its performance. Finally, in Sec. 7.5, we discuss the confocal microscope we have built for imaging the NV centers, and for characterization of the proposed device. We conclude with a brief discussion about the future direction of the project.

The work in this chapter has been done together with Vinodh Raj Rajagopal Muthu. Both of us have contributed to the simulations, as well as the experimental work reported in this chapter. Dr. Rubayet Al Maruf helped us setup the confocal microscope. I would also like to thank Dr. Behrooz Semnani and Prof. Michal Bajcsy for helpful discussions, and guidance throughout the project.

7.2 NV center structure

7.2.1 Crystalline structure

The NV center is a point defect in diamond formed by a lattice vacancy along with a substitute nitrogen atom. Unlike an emitter in free space, the geometry of the fcc diamond

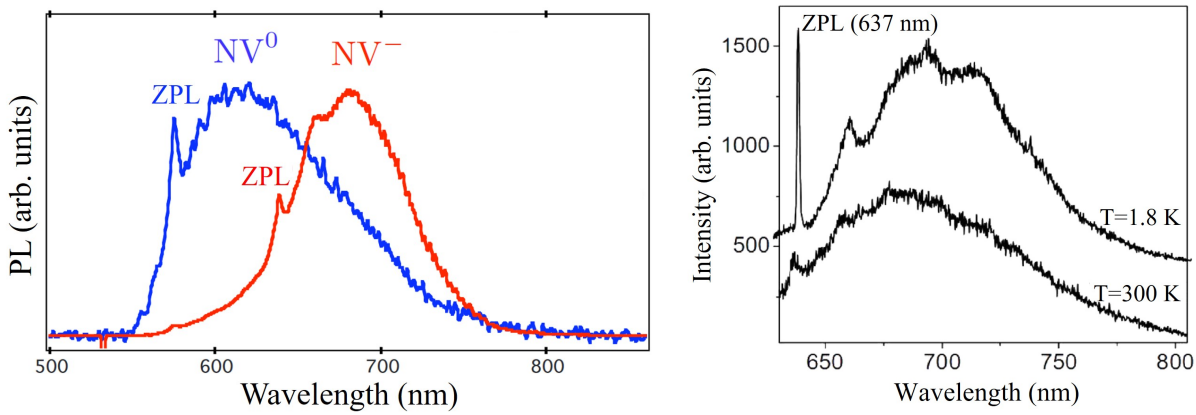

(a) (b)

Figure 7.2: (a) Normalized photoluminiscence (PL) spectrum of single NV^0 (in blue) and NV^- (in red) centers with their ZPLs at 575 nm and 637 nm respectively when excited with off-resonant green light at 532 nm at room temperature ($T = 300$K). Figure adapted from Ref. [122]. (b) The PL spectrum of NV^- at room temperature ($T = 300$K) and at low temperatures ($T = 1.8$K). Figure adapted from Ref. [123].

crystal define the symmetries, and physical properties of the defect center. It is oriented along the [111] crystalline direction [120]. The NV center is known to have C_{3v} symmetry, which determines the dipole transitions in its electronic level structure. It means that the NV center is structurally invariant under C_{3v} symmetry operations – two rotations by 120° rotations about the NV axis (C_3, and C_3^{-1}), three reflections on vertical planes containing the NV axis and a carbon atom (R_1, R_2, and R_3), and the identity (I) operation. For further details about the C_{3v} symmetry, and the transformations the different electronic levels (A_1, A_2, E) undergo under the different symmetry operations, the reader can refer to L.I. Childress' PhD thesis [121]. Fig. 7.1 shows a model of the crystalline structure of the NV center.

7.2.2 Electronic level structure

The NV center is known to exist in two different charge states: the negatively charged NV^-, and the neutral NV^0 state. NV^0 has five electrons (one each from the three neighboring carbon atoms, and two from nitrogen's valence band), whereas NV^- has six electrons, thus making it negatively charged. They can be distinguished by their distinct zero phonon line (ZPL). The ZPL is a sharp peak in the fluorescence spectrum arising from photons

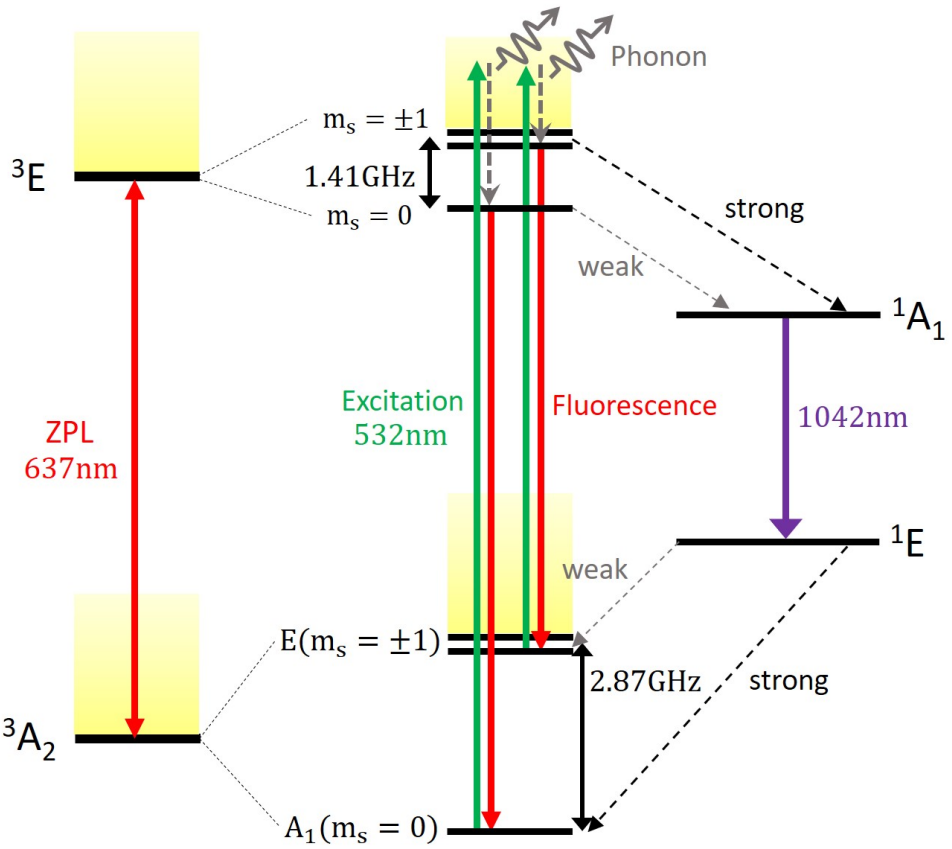

Figure 7.3: The electronic level structure of an NV center, showing the triplet ground state $^3A_2$, the excited state ^3E, and the metastable $^1A_1$, and ^1E states. The vibronic levels associated with the phonon sideband transitions have been shaded yellow.

emitted when the NV center decays from the excited state directly to ground state without interaction with the phonons (vibrations) of the diamond lattice. NV^- exhibits a ZPL at 637 nm (1.945 eV), whereas NV^0 exhibits a ZPL at 575 nm (2.156 eV) (see Fig. 7.2a). NV^- have been widely studied, and is the commonly used form of NV center. For the purpose of our study, we will only be considering NV^- centers only.

Fig. 7.3 shows the schematic of the NV center level structure. The NV center has an optical ZPL transition between the ground state triplet $^3A_2$, and the excited ^3E levels. The ground state triplet splits due to spin-spin, and spin-orbit interactions into the A_1 level corresponding to $m_s = 0$, and two E levels corresponding to $m_s = \pm 1$, where m_s is the magnetic quantum number. The $m_s = 0$, and $m_s = \pm 1$ levels have a separation

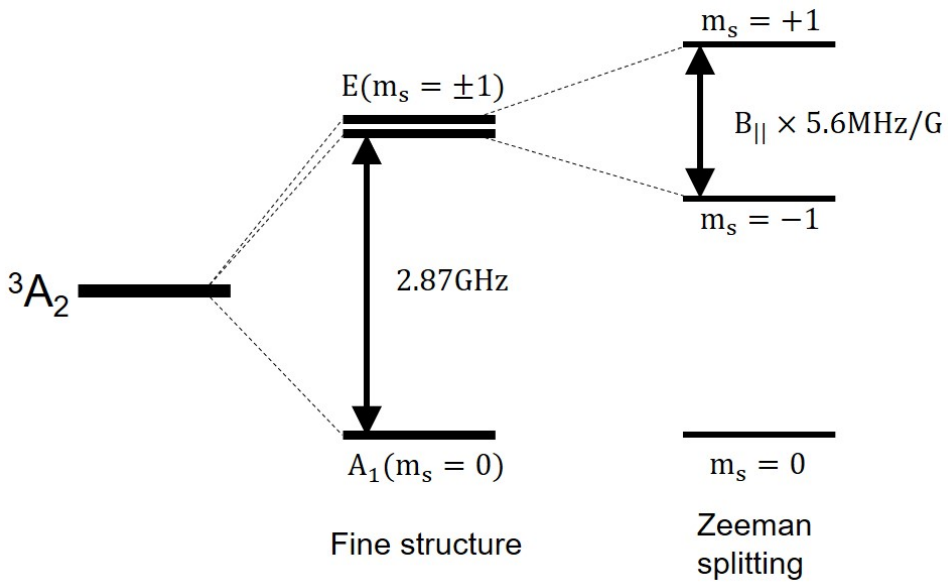

Figure 7.4: The electronic ground state $^3A_2$ of the NV center, showing the zero field magnetic splitting of 2.87 GHz, and the Zeeman splitting of the $m_s = \pm 1$ states under the effect of a magnetic field $B_{||}$, parallel to the z-axis.

of $\sim$ 2.87 GHz. The 637 nm ZPL transition, along with the detection of 2.87 GHz zero field magnetic splitting of the ground state using hole burning [124], electron paramagnetic resonance (EPR) [125], or optically detected magnetic resonance (ODMR) [116] act as the experimental signatures of detecting an NV center. Apart from the fine-structure splitting, the application of a magnetic field $B_{||}$ parallel to the NV z-axis causes a Zeeman split of $B_{||} \times 5.6$ MHz/G in the $m_s = \pm 1$ level (see Fig. 7.4) [115, 126]. Similarly, the excited state ^3E also shows spin degeneracy, and there is a splitting of $\sim$ 1.41 GHz among the $m_s = 0$, and $m_s = \pm 1$ states [127].

The electronic states also have a continuum of vibronic states associated with them. When a green laser at 532 nm is used to excite the NV center in its ground state, it is excited to one of the excited vibronic states. Now, the NV center might decay to the ground state through multiple pathways. The vibronic levels of the NV center decay readily to the excited state ^3E via emission of phonons. Primarily, the excited state decays through the phononic sideband (PSB) which extends approximately from 650 nm to 800 nm. The excited state can also decay through a metastable $^1A_1$ level (see Fig. 7.3) through inter system crossing (ISC). However, occasionally the excited state also decays directly from the ^3E level to the $^3A_2$, without the help of any phononic sidebands. That gives rise to the red

ZPL fluorescence at 637 nm. The ZPL is more prominent at lower temperatures, but can still be resolved at room temperature (see Fig. 7.2b). However, unfortunately, irrespective of the large range of temperature, only a very small amount ($\sim 3-4\%$) of the total emission goes into the ZPL [128, 129]. Still, the ZPL is an important part of the spectrum, and is useful for quantum information processing because the sideband radiation, which makes up the bulk of the spectrum unfortunately loses its coherence and dephases very quickly.

Spin initialization and readout

The NV center's spin can be polarized using an off-resonant green excitation at room temperature. Though there are various debates and some open questions about the exact mechanism of the optically induced spin polarization, the following model gives us an intuitive picture, and matches experimental observations. At thermal equilibrium, the ground state of the NV center is in an approximately equal mixture of the different spin states. Upon illumination with green light, the NV center is excited to the ^3E level. The transitions between the ^3E to $^3A_2$ level follow the spin selection rule $\Delta m_s = 0$, i.e., they are spin-preserving. So, decay from the $m_s = 0$ excited state results in the NV center ending up in the $m_s = 0$ ground state. However, if the excited state is in $m_s = \pm 1$ spin state, it can undergo inter system crossing with probability 1/3, and decay via the $^1A_1 \rightarrow ^1 E$ transition. As shown in Fig. 7.3, this makes the NV center end up in the $m_s = 0$ ground state. Thus, in a few optical cycles the ground state of the NV center can be almost completely spin-polarised to the $m_s = 0$ level. Once in the $m_s = 0$ ground state, we can successfully go to $m_s = \pm 1$ spin states using resonant microwave $\pi-$pulses. One can also create a superposition of the spin states of the form $1/\sqrt{2}\left(|0\rangle + i\,|1\rangle\right)$ by using a microwave $\pi/2-$pulse. If this state to precess for a time t, the spin $|1\rangle$ component picks up a phase of ϕ, thereby giving the state $1/\sqrt{2}\left(|0\rangle + ie^{i\phi}\,|1\rangle\right)$. Thus, using the proper pulse sequence one can create any arbitrary superposition of the spin states.

Readout of the spin state of the NV center at room temperature is possible by using an off-resonant green laser just like spin initialization. Upon illumination by the green light, the $m_s = \pm 1$ state fluoresces less than the $m_s = 0$ state. This happens due to the higher probability of inter system crossing from the $m_s = \pm 1$ excited state. Over the course of a few optical excitation cycles, the initial $m_s = \pm 1$ state results in fewer optical transitions from the excited state to the ground state. Thus, one can readout the state by integrating over the fluorescence spectrum. Usually, the fluorescence from the $m_s = \pm 1$ state is about $20-40\%$ lower compared to the $m_s = 0$ state [121, 130]. However, if we illuminate the NV center for too many cycles, it will eventually end up being spin polarized to the $m_s = 0$ level. Thus, careful consideration of the detection window is necessary. However, at low

temperature, the spin decay rate is very small, and the fluorescence is visible. So, a laser resonant with the $m_s = 0$ transition is used. The NV center fluoresces only if the emitter was in the $m_s = 0$ state. Ref. [109] reported a readout fidelity of 95% using this method.

7.3 Engineering emission pattern of NV centers with nanophotonic structures

Over the years, multiple nanophotonic structures have been explored for efficient extraction of light from quantum emitters. Some of the prominent ones include solid immersion lenses (SILs) [33, 131–134], nanopillars [135–139], and bull's eye gratings [140–142]. Here, we shall provide a quantitative comparison of these structures' ability to successfully direct the extracted light out of an NV center embedded in a diamond in a particular direction. In particular, for our application, we want the radiation to be confined in a primary radiation lobe pointed perpendicular to the surface of the diamond with a small half angle, and thus have low numerical aperture (NA). These structures can be effectively considered to be optical antennas that direct the emission from the emitter.

A rectangular slab

The simplest case we can consider is that of an NV center embedded in a rectangular slab of diamond. The NV center radiates along the $\langle 111 \rangle$ axis. Thus, to maximize collection efficiency, we consider a diamond sample cut along the (111) surface throughout our study. Hence, the NV center can be modeled as a radiating dipole with its axis parallel to the surface. However, the large refractive index mismatch at the diamond-air interface results in Fresnel reflection. For normal incidence, the Fresnel reflection coefficient is

$$r = \frac{n_{\text{diamond}} - n_{\text{air}}}{n_{\text{diamond}} + n_{\text{air}}} \approx 0.4. \tag{7.1}$$

The amount of reflection is higher for greater angles of incidence, and total internal reflection occurs once the angle of incidence exceeds the critical angle ($\theta_c = 23.6°$). In fact, most of the radiation is reflected back into the diamond sample, as can be seen from the field, and directivity plots in Fig. 7.5. The photons that make it out of the slab successfully aren't highly directional either, but are scattered across a rather wide angle. This makes the rectangular slab highly non-ideal for extracting emission from the NV center, and specialized nanophotonic structures are needed to guide the emission out of the diamond.

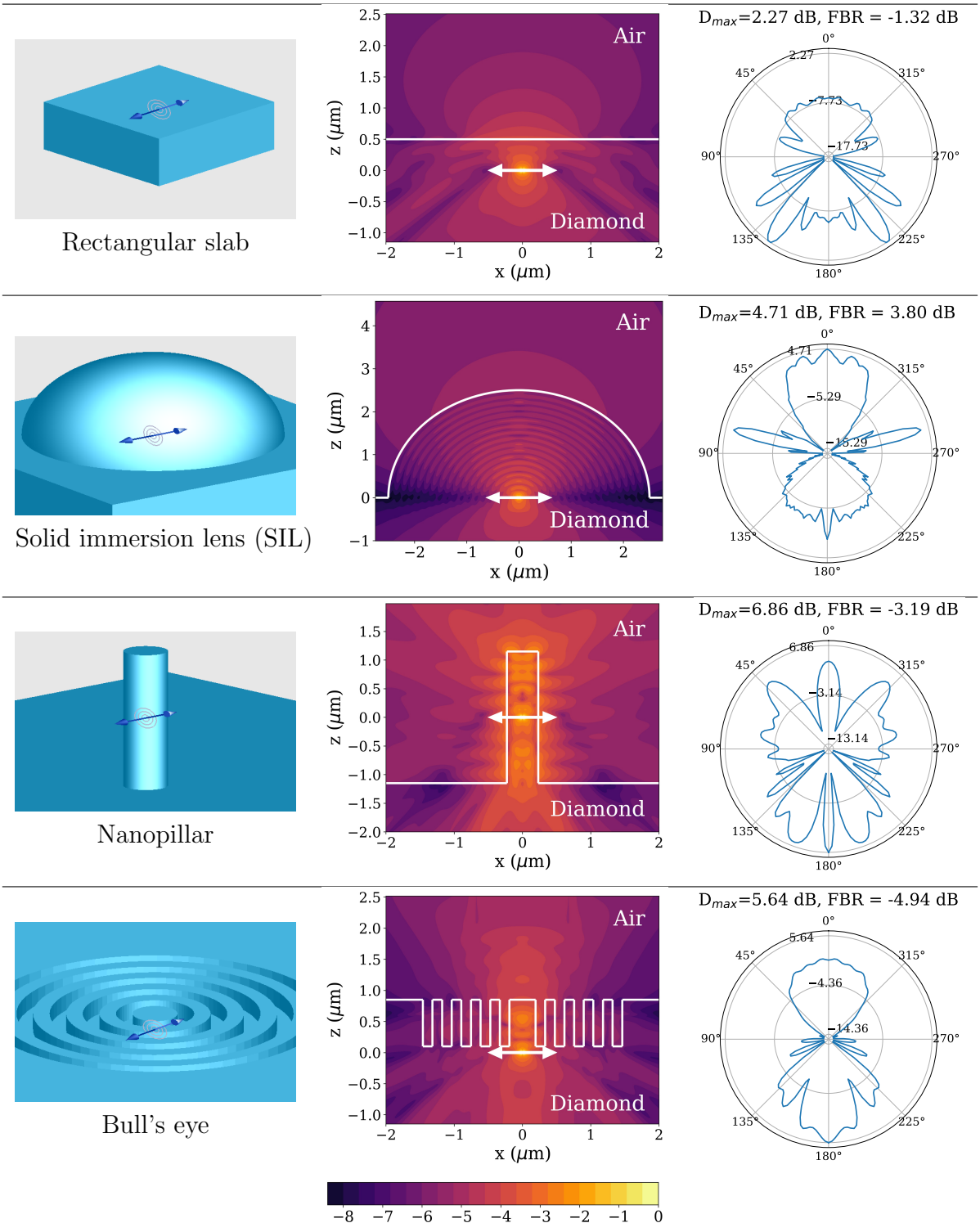

Figure 7.5: The simulation geometry, the observed electric field profile along the $X - Z$ plane at $y = 0$, and the radiation pattern (with directivity and FBR) for a rectangular slab, a solid immersion lens (SIL), a nanopillar, and a bull's eye structure.

Solid immersion lenses (SILs)

SILs try to overcome the problem of total internal reflection at higher angles of incidence. The NV center is located at the focus of a hemisphere with radius 2.5µm (see Fig. 7.5), so that the emitted rays are perpendicular to the diamond-air interface. This reduces the amount of reflection at the surface, and improves the amount of light extracted from the NV center in the upward direction. Fig. 7.5 shows the finite difference time domain (FDTD) simulations of the field pattern, and the directivity for a SIL with radius 2.5µm. The maximum directivity ($D_{\max}$) is 4.71dB, with a front-to-back ratio (FBR) of 3.80dB. However, the SIL does not show high selectivity in its upward propagating field. The main radiation lobe in the upward direction is spread across a half angle of nearly 90°, and thus has a high numerical aperture (NA$\sim$ 1). Our goal is to have a geometry that can confine the radiation to a narrow cone, and provide a highly directional pattern of radiation. Thus, the SIL isn't an ideal candidate for our purpose. However, the performance of this basic version of SIL can be improved by putting a layer of reflecting material (for example Au as in Ref. [134]) below the emitter to enhance the upward radiation.

Nanopillars

The nanopillar is a cylindrical structure with the NV center embedded in it. The photons emitted by the NV center are coupled to the guided fundamental mode HE_{11} of the nanopillar/nanowire. At the top of the nanopillar, the guided mode couples with the modes in the free space, and thus propagates forward. In our simulations, we used nanopillar of height 2.3µm, and radius 230nm corresponding to dimensions reported in Ref. [139]. The field distribution and the directivity of the emission obtained from FDTD simulations is shown in Fig. 7.5. Our FDTD simulations show a maximum directivity of 6.86dB, and an FBR of −3.19. More, importantly the upward directivity is only 3.66dB. The mode mismatch between the guided modes in the nanopillar with the free space propagation mode can be decreased for more efficient free space propagation of the radiation by tapering the top of the pillar.

Bull's eye gratings

The bull's eye geometry is a high contrast distributed Bragg reflector (DBR) etched in a circular 2-dimensional pattern, with the NV center at its center [140–142]. We simulated a bull's eye with a periodicity $a = \lambda/n_{\text{diamond}}$, corresponding to a second-order Bragg grating at $\lambda = 680$nm. The planar 2D Bragg grating reflects back the emitted light, that might

propagate radially in-plane out from the emitter. This provides a tight horizontal confinement along the $X-Y$ plane. On the other hand, the effective refractive index near the interface is lowered because of the grating structure. Hence, the light that travels vertically, along the Z direction, faces a lower refractive index mismatch at the interface. This helps more photons to successfully couple from the NV center embedded in the diamond to free space. Hence, the bull's eye geometry selectively enhances emission in the vertical direction, while providing a tight horizontal confinement. Fig. 7.5 shows the simulated field pattern,

and the directivity achieved with a bull's eye pattern. From the radiation pattern, we can clearly observe the superior horizontal field confinement in the bull's eye compared to the other structures, as the upward propagating field is confined within a half angle of $\sim 45°$. The maximum directivity achieved is 5.64dB, with an FBR of -4.94dB.

7.4 Adjoint optimization based approach

None of the previously discussed nanophotonic structures provide the flexibility to arbitrarily control the emission properties of the NV center. However, adjoint optimization method provides the flexibility to design a geometry suited for a specific application. We aim to design a 2D grating on the surface of a (111)−oriented diamond sample, such that most of the radiation from an NV center embedded in the diamond can couple with free space. We want the structure to provide high directivity in the upward direction. In other words, the radiation pattern should have the main lobe with a small half angle in the upward direction with a large positive value of FBR. In most applications, we will need to couple the radiation from an emitter into a waveguide. Thus, additionally we want to maximize the coupling of the NV center's radiation with a waveguide (a nanofiber in particular) by suitably shaping the mode's spatial profile. That would eliminate the need for bulky optics elements like lenses for efficiently coupling the radiation into the nanofiber. With this goal in mind, let us formally define the problem statement that we have tried to provide a solution for.

Problem statement:

Suppose there is an NV center 0.5µm below the surface of a (111)−oriented diamond sample. Also, there is a single mode nanofiber of radius $r = 0.7$µm sitting 2µm above the diamond sample. What pattern can we etch on the surface of the diamond to maximize the mode overlap between the guided mode in the fiber, and the radiation from the NV center?

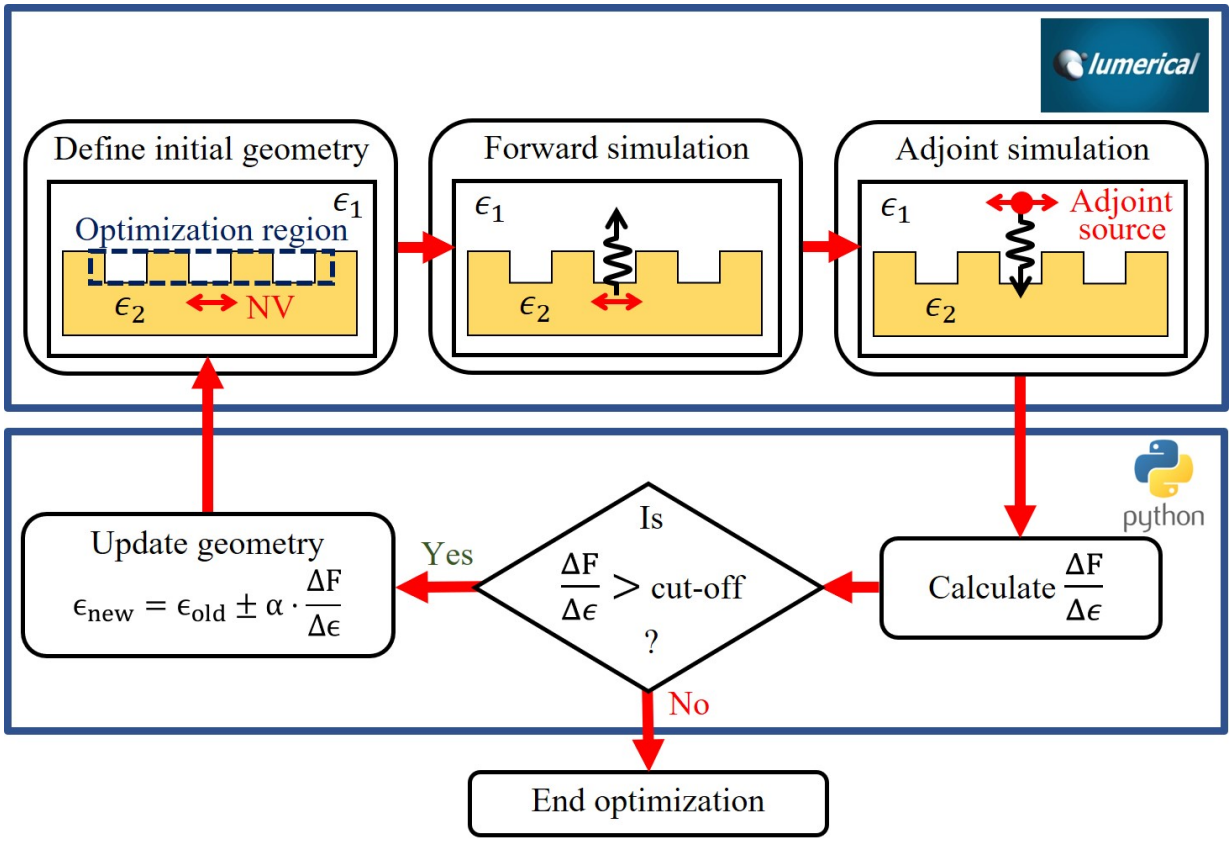

Figure 7.6: A schematic representation of implementation of the adjoint optimization algorithm using lumopt API. Here, we have shown the simplest update relationship for a gradient ascent/descent process with learning rate α for simplicity. However, the actual update relationships used are usually much more complicated.

7.4.1 Simulation process overview

We use Lumerical's inverse design suite to solve our adjoint optimization problem. The optimization process is performed in Python by the LumOpt, whereas the electromagnetic FDTD simulations are performed by Lumerical [94][1]. The Lumerical Automation API coordinates the simultaneous processes by interfacing the calculations done in Python and on Lumerical. A simplified version of the simulation process is shown in Fig. 7.6. First, the initial geometry of the problem is defined in Lumerical. We want to optimize the parameters inside the *optimization region* of the geometry. Next, we run the forward, and the adjoint

[1]The source code for the LumOpt wrapper is available in Ref. [143].

simulations in Lumerical to calculate the derivative of the figure of merit with respect to the design parameter. The gradient descent/ascent (or any other gradient based optimization methods like the L-BFGS-B[2], which is the default method used by Lumerical) optimization subroutine to update the geometry in each iteration runs in Python. In each iteration, the geometry in the *optimization region* is updated accordingly to maximize the merit function. We keep on iterating, and updating the geometry until the merit function saturates. We use the more generalized and versatile topology optimization method, instead of shape optimization to update the geometry of the *optimization region* in our problem.

Initial geometry

We initialize our optimization region with a bull's eye pattern etched onto the diamond surface, with the NV center being at the center of the bull's eye as shown in Fig. 7.7a. The depth of etching is 0.3µm, and the periodicity is $\lambda/n_{\text{diamond}} \approx 282$nm corresponding to the second order Bragg grating for wavelength $\lambda = 680$nm. We selected the particular central wavelength as we wanted to optimize collection for the entire spectrum, and the NV center's spectra has as maximum at ~ 680nm. We chose to initialize our simulation with the bull's eye because we are interested in a 2-dimensional etch pattern unlike the nanopillar or the SIL. The advantages of the bull's eye pattern over its counterparts are manyfold – it is easier to fabricate, is better suited for integrated development, and provides better mechanically stability on account of being a 2D structure. But most importantly, it also provides a tighter confinement of the field propagating in the upward direction compared to structures like the nanopillar and the SIL. Thus, we think it provides a good starting point for the optimization algorithm to start looking at the feature space.

Optimization region

We choose a 3µm $\times$ 3µm square with the emitter at its center as the optimization region. In other words, we are aiming for a pattern with a footprint $\leq$ 3µm $\times$ 3µm.

Figure of merit

For our problem, we choose the figure of merit to be the transmission of the NV center emission into the fundamental TE mode of the nanofiber. Mathematically, we can define it

[2]L-BFGS-B is a form of limited memory Broyden-Fletcher-Goldfarb-Shanno algorithm with bounded variables serving as the only constraints of optimization.

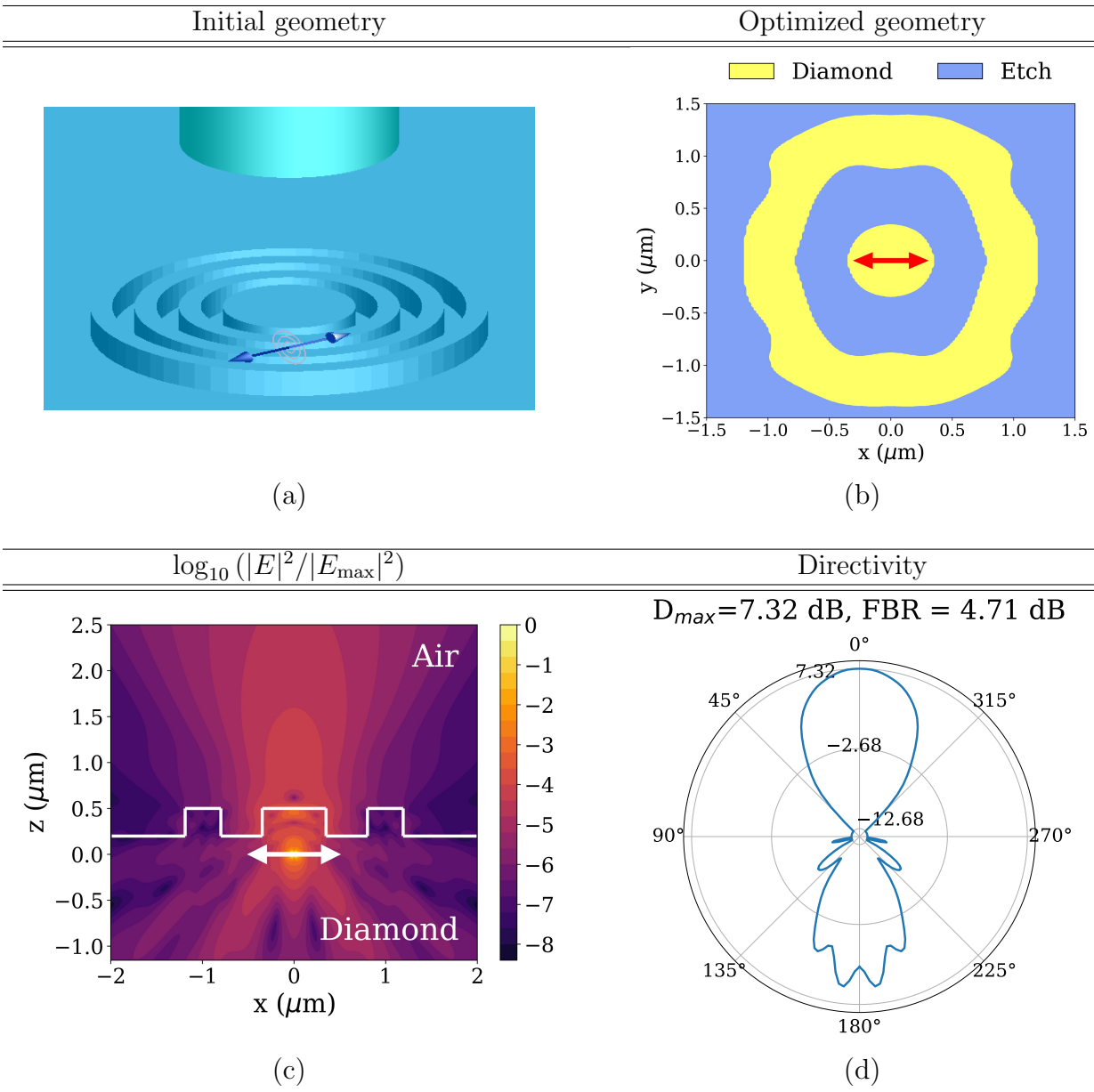

Figure 7.7: (a) The initial geometry used for the optimization. (b) The optimized etching pattern the algorithm converged at. (c) The electric field profile in the $X-Z$ plane at $y=0$ with the optimized pattern. (d) The radiation pattern (with directivity and FBR) achieved with the optimized structure.

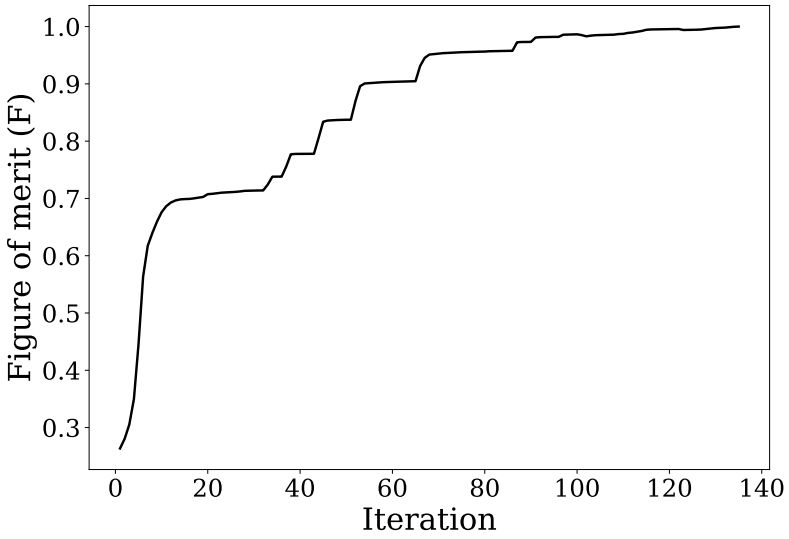

Figure 7.8: The normalized learning curve, i.e., the evolution of the figure of merit (F) with iterations during the optimization process.

as the overlap integral between the emission of the NV center and the fundamental mode of the waveguide at the surface of the fiber. Explicitly, this is given by

$$F = \frac{|\iint \mathbf{E} \times \mathbf{H}_m^* \cdot d\mathbf{S} + \iint \mathbf{E}_m^* \times \mathbf{H} \cdot d\mathbf{S}|^2}{\iint \mathrm{Re}\{\mathbf{E}_m \times \mathbf{H}_m^*\} \cdot d\mathbf{S}}, \tag{7.2}$$

where $\mathbf{E}$ and $\mathbf{H}$ are the electric and magnetic fields at the input of the nanofiber calculated from the forward simulation, and $\mathbf{E}_m$ and $\mathbf{H}_m$ are the electric and magnetic field profiles of the fundamental mode of the fiber [94]. The integration is performed over the spectral range of the dipole with its peak at 680nm. As opposed to only maximizing the free space extraction of light from the NV centers as reported in Ref. [144, 145], our design also performs mode shaping for efficient coupling with the waveguide mode. We shall discuss more about the work reported in these publications later in Sec. 7.6.

Optimized geometry

After running the simulation, we get the optimized geometry as shown in Fig. 7.7b. The field distribution achieved with the optimized geometry, and the directivity of the emission are also shown in Fig. 7.7. We notice that the optimized geometry provides

an improvement in the directivity of the radiation pattern by minimizing side lobes, and constricting the main radiation lobe within a half angle of $\sim 45°$. The maximum directivity achieved is 7.32dB with an FBR of 4.71dB. This turns out to be significantly superior to the performance of the previously proposed structures we studied in Sec. 7.3.

7.4.2 Sensitivity analysis

Now, even though we optimized our geometry for an NV center 0.5µm below the air-diamond interface, and at the center of the optimization region, it is practically very difficult to exactly satisfy those conditions. Thus, we perform sensitivity analysis to test the sensitivity of the optimized structure to the location of the emitter.

Analysis I: Emission sensitivity

To test the positional sensitivity of the NV center on the light extraction efficiency, we exploit the reciprocity condition from antenna theory, that allows us to interchange the transmitter, and the receiver. Thus, this time we excite the diamond sample with the fundamental mode of the nanofiber. This fundamental mode source with a central wavelength of $\lambda = 680$nm is positioned 2µm above the diamond's surface (exactly where the nanofiber collecting the radiation from the NV center would be) as shown in the top row of Fig. 7.9. As expected, we notice that the strength of the electric field is maximum at the ideal location of the NV center, i.e., exactly 0.5µm below the surface, and at the origin of the FDTD simulation region (at $x = y = z = 0$ as shown in the middle row of Fig. 7.9). The third row of Fig. 7.9 shows how quickly the strength of the field decays around the maxima. That signifies the amount of permissible error/flexibility in the position of the NV center with respect to its ideal location, without causing major loss in the collection efficiency. We observe that the sensitivity along the x and y axis has a full width half maximum (FWHM) of 200nm and 160nm respectively. The performance of the optimized structure is even more resilient to changes in the z direction, and has an FWHM of almost a micrometer.

Analysis II: Excitation sensitivity

However, it is also important to confirm if all the NV centers falling within the hotspots shown in Fig. 7.9 are being excited in the first place. To check that, we test the positional sensitivity of the NV center to the green excitation laser at 532nm. In other words, we investigate what is the volume of the diamond sample where the excitation beam is focused,

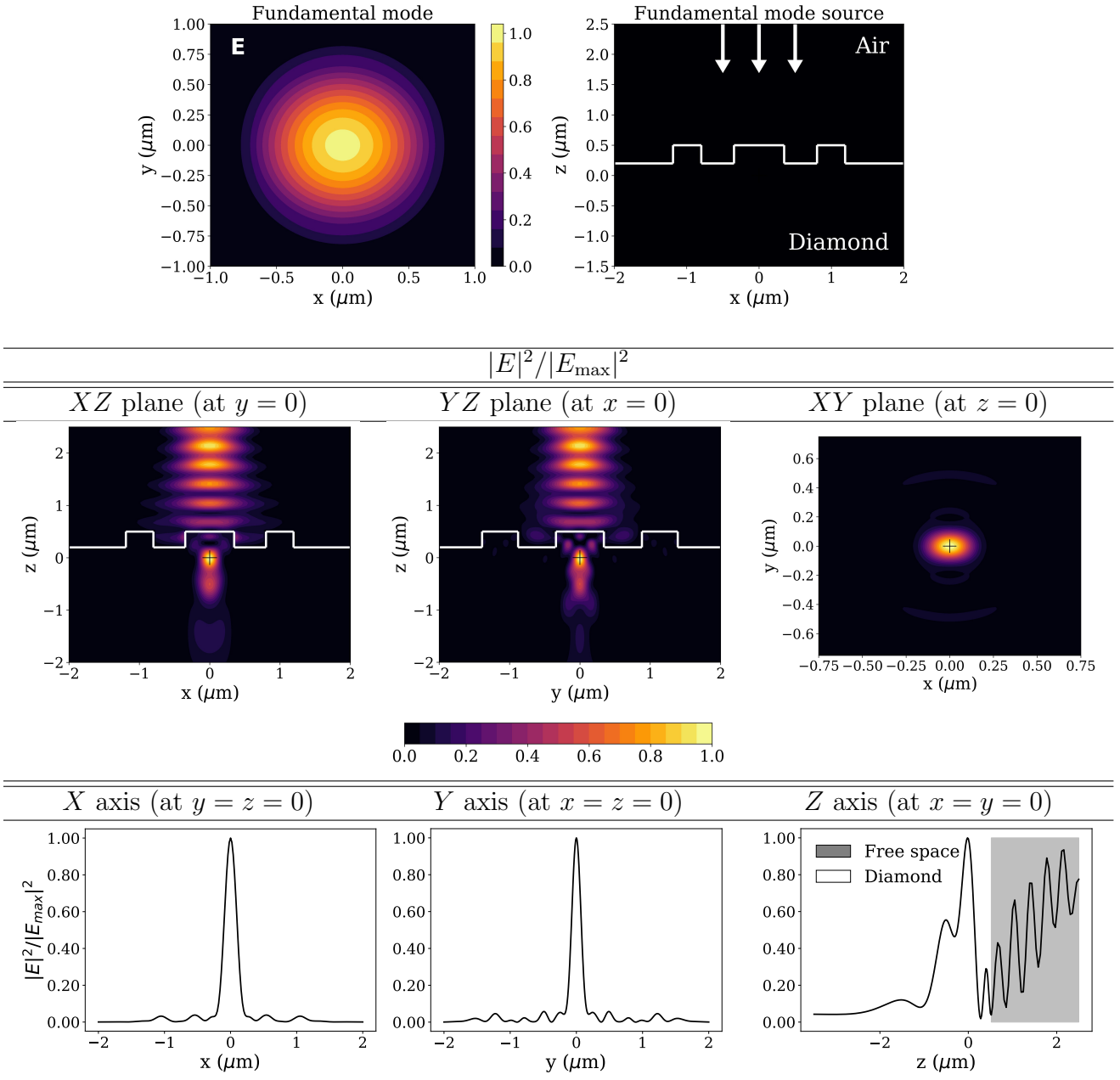

Figure 7.9: The field pattern (second row), and the sensitivity of the location of the NV center (third row) when the optimized structure is illuminated with a fundamental mode source (first row) centered at $\lambda = 680$nm positioned 2μm above the diamond surface.

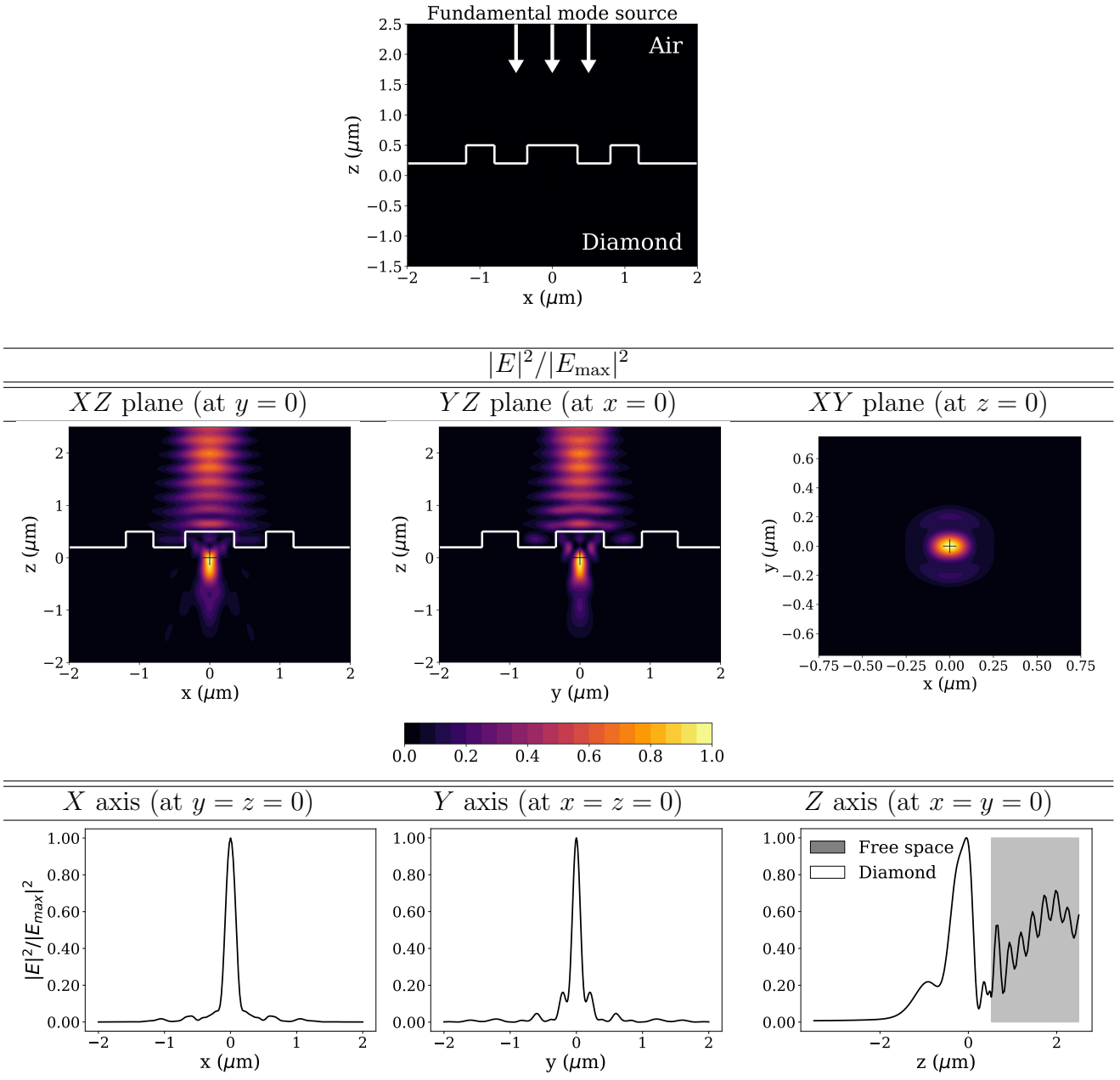

Figure 7.10: The field pattern (second row), and the sensitivity of the location of the NV center (third row) when the optimized structure is illuminated with a fundamental wave source (first row) at $\lambda = 532$nm.

and the NV centers are successfully excited. Thus, we excite the structure from above using a fundamental mode source at 532nm positioned at the tip of the fiber. From the results of our simulations as shown in Fig. 7.10, we observe that the structure is successful in focusing the excitation beam at the location of the NV center pretty well. The field concentration is maximum at $x = y = 0$ along the horizontal plane, and the FWHM is $\sim 140-160$nm across both the axis. However, we see that the field intensity maxima does not lie exactly at $z = 0$ (since the design is optimized for a different wavelength). Still, the field intensity is strong enough to excite the an NV center at $z = 0$. From this simulation, we can conclude that the same fiber can be successfully used to excite the NV centers, and collect the emission simultaneously. That is a significant advantage provided by our proposed structure.

Moreover, the NV centers in a $<$ 5ppb diamond are approximately $\sim$ 100nm away from each other. So, the probability of exciting more than one NV in the $z = 0$ plane is low. However, one might excite NV centers at a different depth, due to the broad peak along the $z-$ axis. But as we shall see in the next section, we can minimize the fluorescence from background NV centers using a confocal setup.

7.5 Confocal microscopy

To observe the fluorescence from the individual NV centers, we use a confocal scanning microscopy setup. Unlike a simple fluorescence microscopy setup, the confocal microscope helps in getting high contrast images of the NV centers, by filtering out off-focus radiation from surrounding NV centers in the sample. First, we shall briefly look at the basic working principle of a confocal microscopy setup in Sec. 7.5.1 before discussing our experimental setup in greater details.

7.5.1 Theory

In a standard fluorescence microscopy, the fluorescence from the entire illuminated part of the sample is imaged in one shot. This results in a low resolution image of the fluorescing sample, because the light coming from the off-focus regions of the sample are imaged along with the part of the sample on focus. Confocal microscopy helps us avoid that problem through spatial filtering, and also provides control over the depth of field. It collects the emission only from the part of the sample under focus, and blocks secondary emissions from off-focus regions of the sample. The basic principles of operation of a confocal microscope is explained with Fig. 7.11.

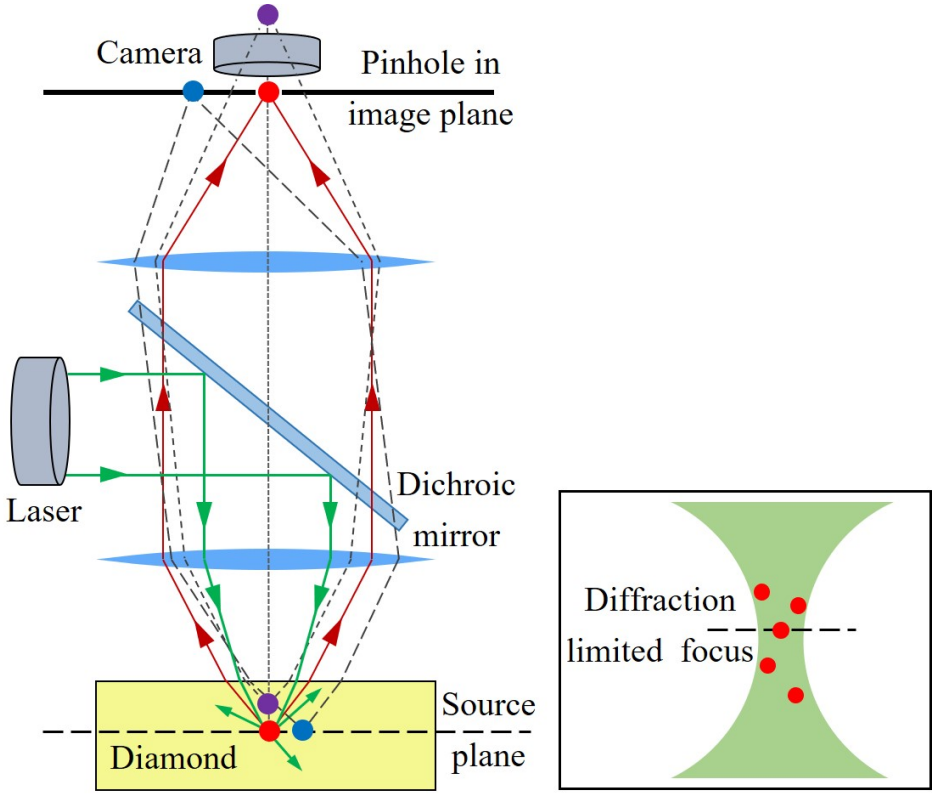

Figure 7.11: Figure showing the principles of confocal microscopy of NV centers in a piece of diamond. As shown in the inset, the diffraction limited focus might have multiple NV centers. However, the confocal setup helps us to reject the light coming from unwanted NV centrs in the background, and create a high resolution image of the NV centers we want to image (ones that lie on the source plane and the optical axis).

When the NV centers in the diamond are excited with a green laser at 532nm, they emit red light (PSB at $\sim 650 - 800$nm, with ZPL at 637nm) upon decay. There is a dichromatic (or simply dichroic) mirror that reflects the green light, but allows red light to pass through. When the green light hits the diamond, there might be multiple NV centers inside the diffraction limited focus of the laser beam (as shown in the inset of Fig. 7.11). Again, the light is scattered inside the diamond, and might excite other NV centers not in focus. The confocal microscope setup blocks the light from surrounding NV centers – either off-focus on the source plane containing the NV-center of interest (blue dot in Fig. 7.11), or at a different depth inside the diamond sample (purple dot in Fig. 7.11). The off-focus NV centers on the source plane but away from optical axis are imaged away from

the optical axis on the image plane, and is blocked by the pinhole. On the other hand, the NV centers on the optical axis at a different depth are imaged away from the image plane, and the pinhole blocks most of its light, thereby creating a sharp image of the NV centers on the source plane only, with very little background scattering.

The image of points on the source plane of the objective is formed on the plane of the pinhole (image plane), and thus they are known as conjugate planes. Also, the pinhole is a *con*jugate point of the *focal* point of the objective lens, hence giving this setup its name – *confocal* microscopy. Now, the image of the entire source plane can be created by using a pair of mechanically rotating mirrors to raster scan the green laser across the entire diamond sample. We achieve this using a galvanometer mirror (or simply galvo) in our experimental setup.

7.5.2 Experimental design

Modeling wave propagation through optical setup

For designing the confocal microscope setup, and to determine essential experimental parameters, we follow the Gaussian wave propagation model used in Ref. [146]. We use the complex-ray description of a Gaussian beam, and propagate it using the ABCD matrices from ray optics [147, 148].

The propagating beams are considered to be Gaussian or TEM_{00}, and can be expressed as (in polar coordinates) [149]:

$$\Psi(\mathbf{r}) = \underbrace{\Psi_0 \frac{w_0}{w(z)} \exp\left[-\frac{r^2}{w^2(z)}\right]}_{\text{Amplitude}} \underbrace{\exp\left[ikz - i\tan^{-1}\left(\frac{z}{z_0}\right)\right]}_{\text{Longitudinal phase}} \underbrace{\exp\left[ik\frac{r^2}{2R(z)}\right]}_{\text{Radial phase}}, \tag{7.3}$$

where $r = \sqrt{x^2 + y^2}$, z_0 is the Rayleigh length, $w_0 = \sqrt{\lambda z_0/\pi}$ is the beam radius/waist, $R(z) = z\left[1 + (z_0/z)^2\right]$ is the radius of curvature at z, and $z-$axis is the optical axis. The beam radius is considered to be the distance from the optical axis where the intensity of the Gaussian beam is $1/e^2$. The beam radius can be expressed as

$$w(z) = w_0\sqrt{1 + \left(\frac{z}{z_0}\right)^2} = w_0\sqrt{1 + \left(\frac{\lambda z}{\pi w_0^2}\right)^2}. \tag{7.4}$$

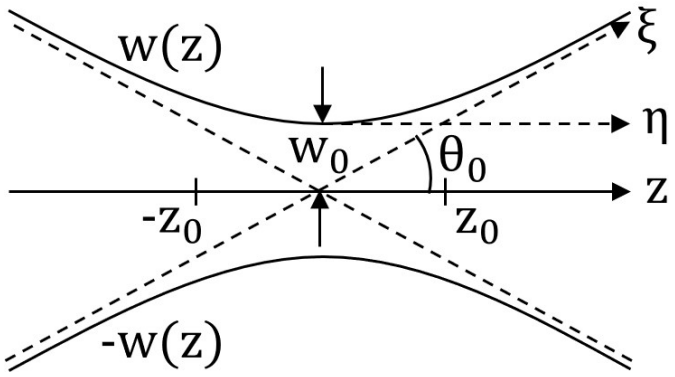

Figure 7.12: The hyperbolic Gaussian beam profile with the two rays: ξ along the asymptote, and η parallel to $z-$axis which is also the optical axis.

The beam profile is hyperbolic in nature, and asymptotic to the line passing through the origin at an angle $\theta_0 \approx w_0/z_0 = \lambda/\pi w_0$ (in paraxial regime) as shown in Fig. 7.12. Thus, we can define a complex ray $X = \xi + i\eta$, where ξ and η are two rays that completely define the Gaussian beam. For simplicity, we consider ξ to be a ray diverging from the focus at the asymptotic angle θ_0, and η is a beam parallel to the optical axis at ray waist (see Fig. 7.12). Thus, these rays can be expressed as the following ray vectors:

$$\xi = \begin{pmatrix} 0 \\ \theta_0 \end{pmatrix}, \quad \eta = \begin{pmatrix} w_0 \\ 0 \end{pmatrix}. \tag{7.5}$$

The beam profile is given as $w(z) = \sqrt{\xi_x(z)^2 + \eta_x(z)^2}$, where $\xi_x(z) \approx z\theta_0 = w_0 z/z_0$ and $\eta_x(z) = w_0$ are the beam waists (the x components) of the respective rays at z. One can check that at $z = 0$, the diverging ray ξ passes through the optical axis, and that implies $\xi_x(0) = 0$. Also, the waist ray is at a distance of w_0 away from the optical axis, and that implies $\eta_x(0) = w_0$. That gives $w(0) = w_0$.

Once we are provided with the initial Gaussian beam input, we can write down the diverging and waist rays in terms of the ray vectors. Next, we can propagate the rays ξ and η using the ABCD matrices for propagation through air, and through a thin lens (of focal length f), as given by:

$$M_{\text{air}} = \begin{pmatrix} 1 & z \\ 0 & 1 \end{pmatrix}, \quad M_{\text{lens}} = \begin{pmatrix} 1 & 0 \\ -\frac{1}{f} & 1 \end{pmatrix}, \tag{7.6}$$

to find the beam radius at any point along the optical path. The Mathematica code (inspired from Ref. [146]) used to calculate the beam, along with the plot of the the red

beam width as it passes through the lenses is given in Appendix E. It helps is visualizing the beams as they pass through different optical components, and measure the beam waist at any point of the setup.

Diamond sample

We will be using highly pure type IIa diamonds purchased from Applied Diamond Inc. for fabricating our proposed device. We got two different grades of diamond samples – with $<$ 1ppm, and $<$ 5ppb nitrogen concentrations (1ppm refers to a density of 1.76×10^{17} NVs/cc). The diamond samples are cut along the (111) orientation, so that the emission from the NV centers are perpendicular to the surface of the diamond for greater extraction efficiency.

Objective

We are using the Mitutoyo MY 100X-806 objective which provides a 100$\times$ magnification, and has a numerical aperture (NA) of 0.7. The objective provides a magnification of 100 for a tube lens of focal length 200mm and working distance 6mm. For a tube lens of focal length f_{tube}, the magnification will be $m = 100 \times f_{\text{tube}}(\text{mm})/200(\text{mm})$. Thus, the effective focal length (EFL) is the design focal length divided by the design magnification, i.e., $f = f_{\text{design tube lens}}/m_{\text{design}} = 200(\text{mm})/100 = 2\text{mm}$. Also, we can calculate the back aperture diameter/ entrance pupil diameter (EP) to be $D = 2 \times f \times \text{N.A} = 2 \times 2 \times 0.7 = 2.8\text{mm}$. The spot diameter for the green laser (532nm) is $\phi = 4\lambda f/\pi D \approx 0.48\mu\text{m}$. The objective also has a field number (FN) of 24. That means, the field of view (FOV) diameter is FN/magnification $= 24/100 = 0.24\text{mm}$.

The objective is also infinity corrected. It means that the input of the objective needs to be collimated to be focused on the focal plane. If the collimated beam is not parallel to the optical axis, the image will still be formed on the focal plane, but away from the optical axis. This type of objective is advantageous as the beam of light is parallel/collimated between the objective and the tube lens. That makes the magnification independent of the distance between the objective and the tube lens. Also, addition of filters/mirrors/beamsplitters on the path between the objective and the tube lens does not change the location of image formation.

Table 7.1: The magnification settings available in the confocal microscope setup.

f_{L1} (mm)	f_{L2} (mm)	f_{L3} (mm)	Magnification
100	100	100	50
200	100	100	100
100	35	100	∼143
200	35	100	∼286

Galvanometer (galvo) mirrors

We are using a two axis galvo (GVSM002-US) from Thorlabs to scan over the diamond sample. To scan over the sample, we are using a manual controller circuit (see Appendix F) for now. In the future, the process of raster scan might need to be automated using a data acquisition (DAQ) board for better control. The galvo also allows us to choose between the following resolution modes - 0.5, 0.8, and 1 V/deg. With GPS011 linear power supply unit it provides an angular resolution of 0.0008° (15 µrad).

Dichroic mirror

The 552nm single-edge laser dichroic beamsplitter from Semrock transmits ($> 94 - 95\%$) light above 552nm, and reflects ($> 96 - 99\%$) the light for lower wavelengths. Thus, it transmits the red light emitted by the NV centers, while reflecting the green laser used for excitation. It works as a filter to separate the excitation field from the emission field.

Magnification settings

The effective magnification provided by the objective is $m_{obj} = 100 \times f_{L1}(\text{mm})/200(\text{mm})$, where L1 is the tube lens focal length (see Fig. 7.13). The net magnification by the microscope is given by $m_{total} = m_{obj} \times f_{L3}/f_{L2} = 0.5 \times f_{L1}f_{L3}/f_{L2}$. For the images in Figs. 7.14c, 7.14d, 7.14e, we used $f_{L1} = 100\text{mm}$, $f_{L2} = f_{L3} = 200\text{mm}$. Thus, the total magnification is 50×. In the final microscope, the magnification options available are shown in Table 7.1. The lenses are mounted on flip mounts to help us easily switch between different magnifications.

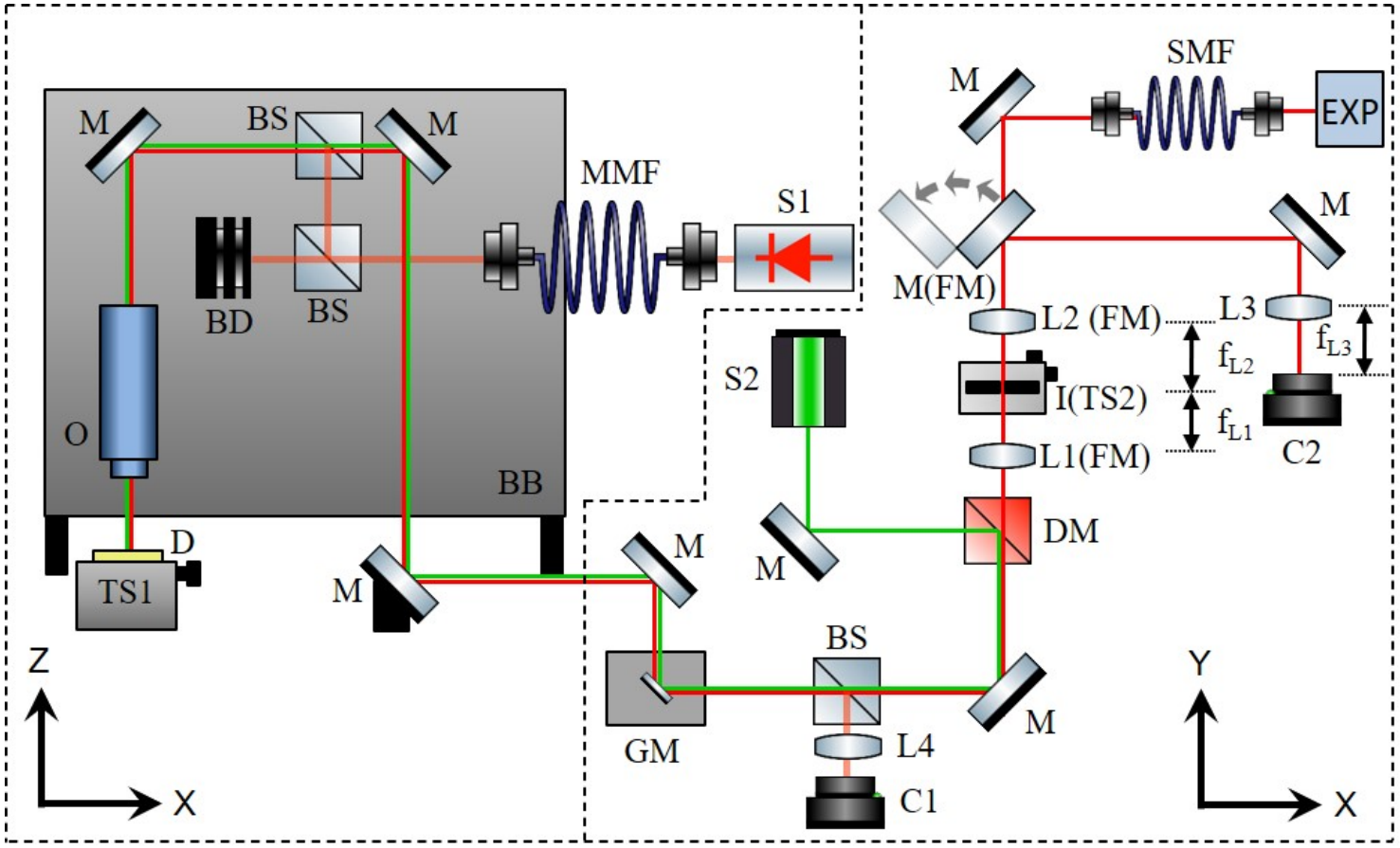

Figure 7.13: The confocal microscopy setup for imaging NV centers. The part numbers of the different components are available in Table 7.2. f_{Li} = Focal length of lens Li; BD = Beam dump; EXP = Experimental setup for spectroscopy, and $g^{(2)}$ measurement.

Table 7.2: Experimental components for confocal microscopy of NV centers.

Component	**Manufacturer**	**Part number/ Specifications**	**Diagram[1]**
Laser	Lighthouse Photonics	Sprout-G	S2
Fiber-coupled red LED	Thorlabs	M625F2	S1
Diamond sample (type IIa)	Applied Diamond Inc.	$<$ 1ppm, $<$ 5ppb, (111) orientation	D
Translation stage	Thorlabs	MBT616D	TS1
	Machifit	LD60-LM	TS2
Galvo mirror	Thorlabs	GVSM002-US	GM
Objective	Mitutoyo	MY 100X-806	O
CMOS camera	FLIR	BFS-PGE-31S4M-C	C2
	Edmund Optics	EO-5012M	C1
Dichroic mirror	Semrock	LM01-552-25	DM
Mirrors	Newport	10D620ER.2	M
Lens	Thorlabs	AC254-035-A-ML	L2
	Thorlabs	AC254-100-A-ML	L1,L2,L3
	Thorlabs	AC254-200-A-ML	L1
90-10 Beamsplitter	Thorlabs	BSN10	BS
Fiber 50-50 beamsplitter	Thorlabs	TM50R5F2A	EXP[2]
Iris	Thorlabs	IDA25Z	I
Single mode fiber optic patch cable	Thorlabs	SM600	SMF
Multimode fiber optic patch cable	Thorlabs	M76L02	MMF
Breadboard	Thorlabs	MB12	BB
Flip mount	Thorlabs	TRF90	FM

[1] See Fig. 7.13
[2] For $g^{(2)}$ measurement

7.5.3 First operations with the microscope

In Fig. 7.14 we can see the first images taken with our microscope. Initially, we use a 5× microscope objective to verify the alignment of the optics. Fig. 7.14a shows the first image taken with the microscope with the 5× objective. We observe the image of a microscope calibration slide using only the red LED as illumination. In the figure, each division of the scale is 10µm apart. Next, we switch to the 100× objective we got from Mitutoyo to

take images, and verify our achieved magnification. With the 100× objective we took the image of an e-beam lithography dose test wafer shown in Fig. 7.14b. Each square in the pattern has a dimension of 2.5 × 2.5µm. The total magnification of the image is 50×.

Next, we try to image a type Ib (100)-oriented diamond sample from Element Six with an NV concentration < 200ppm [150]. The images of the diamond sample can be seen in Fig. 7.14. In Fig. 7.14c, we used only the red LED (S1 in Fig. 7.13) as the illumination source. Then, we turned on our green laser (S2 in Fig. 7.13) at 532nm, and a power of 7µW. On doing that, we observed the emergence of a bright spot, which has been circled in Fig. 7.14d. Next, we turned off the red LED, and only the bright spot remained (see Fig. 7.14e). The bright spot has a diameter of ∼ 0.8µm, and we suspect it might be an NV center since it fluoresces at a wavelength above 552nm (cut-off wavelength of the dichroic mirror) upon excitation with green laser at 532nm. However, more tests like detection of ZPL, and hyperfine splitting of the electronic ground state can be performed to objectively verify that it is indeed an NV center.

7.6 Recently reported photon extractors designed using adjoint optimization

Recently we learnt about the efforts of two other groups in designing light extractors for NV centers embedded in diamond using adjoint optimization [144, 145]. Unlike us, both of them used (100)−oriented diamond as their substrate where the NV center axis is at an angle of 35.3° with respect to the diamond's surface. Choosing a (111)−oriented diamond is advantageous by default, since the NV center radiates perpendicular to the surface of the substrate in this orientation.

In Ref. [144], Wambold *et al.* proposed a silicon based light extractor designed using topology optimization as shown in Fig. 7.15a for use in applications related to quantum sensing. They used the spectrum-averaged extraction efficiency of light from the NV center as a broadband figure of merit given by [144]:

$$F = \frac{\int I_{NV}(\lambda) \times \eta(\lambda) d\lambda}{\int I_{NV}(\lambda) d\lambda}, \tag{7.7}$$

where $I_{NV}(\lambda)$ is the normalized spectrum of an NV center, and $\eta(\lambda)$ is the extraction efficiency at a particular wavelength λ given by the ratio of the number of photons emitted into free space in the presence of the extractor to the number of photons emitted into free space in the absence of the extractor. The structure consists of a layer of Si on the

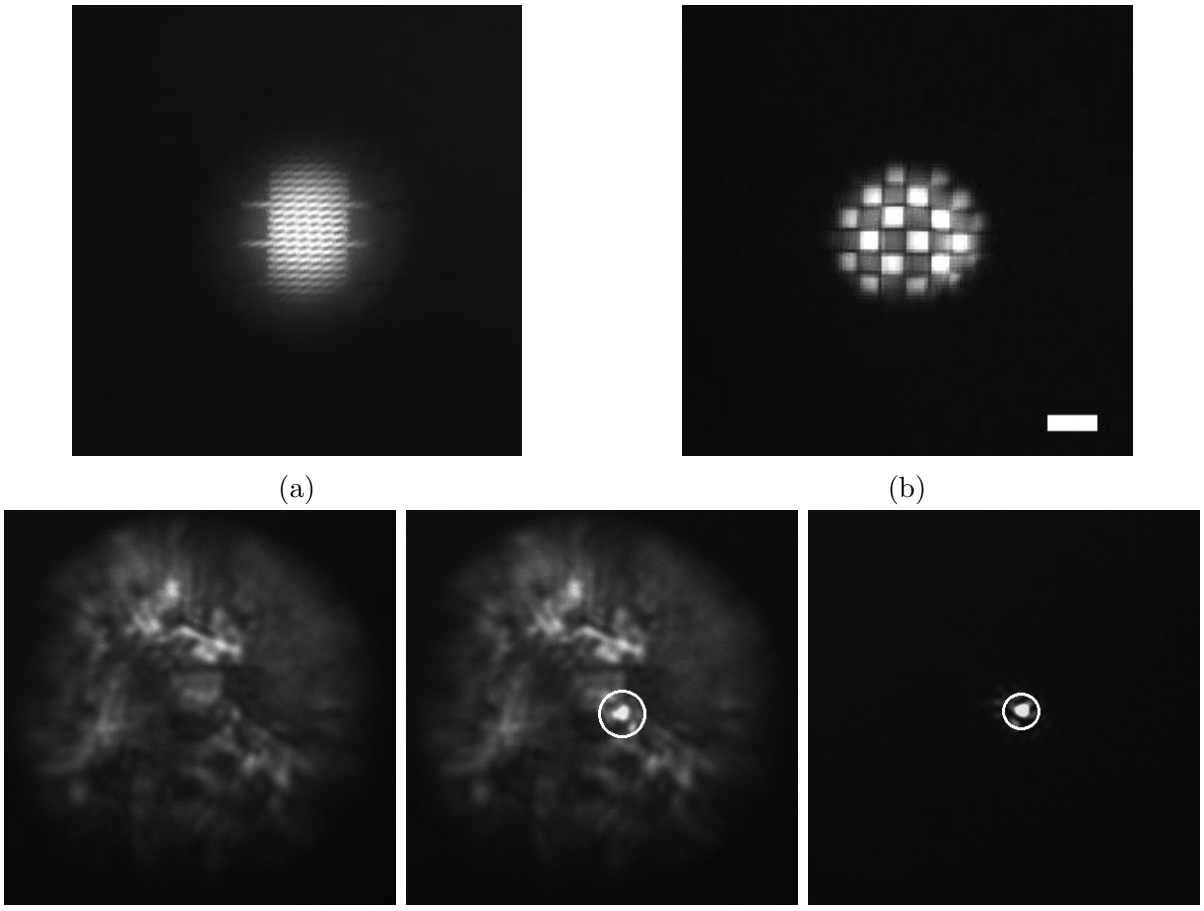

Figure 7.14: (a) The first image of a calibration slide taken with our microscope using a 5× objective. Each division on the scale is 10µm. (b) The first image taken with our microscope using the 100× objective and a red LED illumination. Each square has a dimension of 2.5 × 2.5µm. The reference scale bar is 5µm long. (c,d,e) One of the first images taken of a diamond sample. In (c) we used only red LED illumination. In (d), when we turned on the excitation green laser at 532nm along with the red LED, we noticed a bright spot appear (circled). In (e) we switched off the red LED, and use only the green laser. But the bright spot ($\sim$ 0.8µm in diameter) is still visible, leading us to believe it might be an NV center.

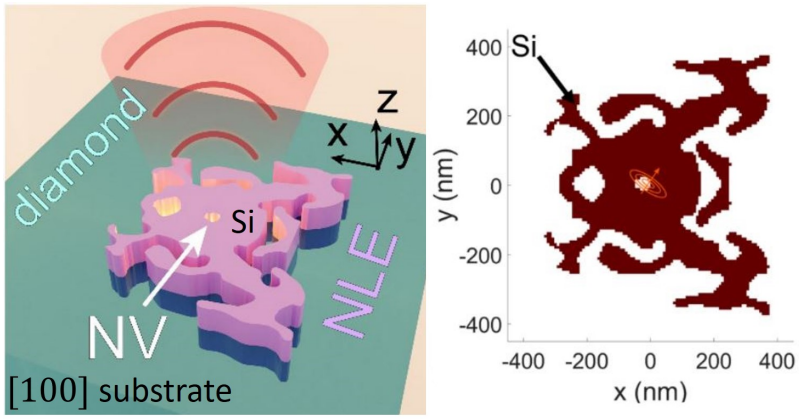

(a)

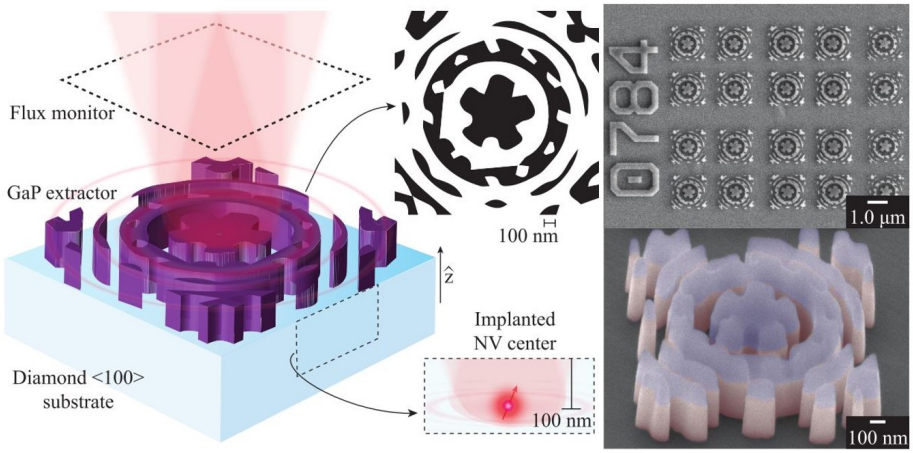

(b)

Figure 7.15: Recently reported photon extractors designed using adjoint optimization. (a) A Si based photon extractor proposed by Wambold *et al.*. Figure adapted from Ref. [144]. (b) A GaP based photon extractor proposed by Chakravarthi *et al.*. Figure adapted from Ref. [145].

(100) surface of the diamond substrate. They optimized the thickness of the extractor, and selected a 300nm thick Si layer for their design. The footprint of their design is 800nm × 800nm. They predict that their design is able to guide the upward radiation from an NV center placed 10nm below the surface into a cone of half angle 30°. They also predicted a Purcell enhancement of ~ 3, and a $35\times$ enhancement in the about of fluorescence extracted into free space at the surface of the structure. Though the structure

does not involve etching into the diamond sample, the close proximity of the NV center to the diamond-silicon might have undesirable effects which need to be studied experimentally.

In Ref. [145], Chakravarthi *et al.* reported the realization of a gallium phosphide (GaP) based photon extractor as shown in Fig. 7.15b for use in applications related to quantum information processing. They used topology optimization to design the photon extractor for an NV center implanted at a depth of 100nm from the surface of the (100)−oriented diamond sample. The GaP layer is 250nm thick, and the device has a footprint of 1.5µm × 1.5µm. In their optimization problem, they tried to maximize the flux passing through a square monitor of size 1.5µm × 1.5µm, and located 400nm above the device as shown in Fig. 7.15b. They reported an average flux enhancement of $\sim 6\times$ and a maximum $14\times$ enhancement of the photon extraction efficiency at ZPL. To make the device, they transferred a 250nm thick GaP membrane on the diamond surface via wet lift-off, followed by electron beam lithography (EBL) and reactive ion etching (RIE) of the GaP layer. In the paper, the authors also noted a significant deterioration in the quality of the NV center marked by linewidth broadening, spectral diffusion and ionization after the etching process. Oxygen annealing at a high temperature was used to somewhat improve the state of the emitter post-fabrication.

Both the devices reported in Ref. [144, 145] maximize the photon collection efficiency in the near field of the device. On the contrary, we try to maximize the photon collection efficiency into a nanofiber located 2µm away from the device. Moreover, our structure also performs mode shaping to couple the emission into the waveguide. However, one significant drawback for our device is that it involves the etching of the diamond substrate. More importantly, from our work, and the work reported in Ref. [144, 145], we can see how adjoint optimization can be used to design photonic devices for efficient extraction and coupling of light from defect centers in a variety of solid state hosts for various applications related to quantum sensing and information processing alike. This approach allows us to easily tweak our design based on our need, and proves to be a powerful tool to solve non-trivial problems in photonics.

7.7 Future directions

Due to unforeseen hurdles thrown by COVID-19, in this thesis we could not accomplish as much as we would have liked to. The following constitute the main future landmarks in the project going forward.

7.7.1 Further design improvements

In our work, for simplicity we maximized the figure of merit function F for a dipole source with a Gaussian spectrum, such that the center frequency of the spectrum matches the center frequency of the NV spectrum. However, one can extend this formalism to optimize the broadband performance of the structure by optimizing the device over a different range of the spectrum. Or one could also design a device for maximizing the collection at the ZPL frequency only.

The performance of the proposed device could also be be improved by introducing a reflective metallic layer (for example gold) below the diamond sample to minimize loss of radiation from emission in the backward direction. The introduction of the metallic structure might also result in Purcell enhancement of the emission rate.

Furthermore, algorithmic/ automatic differentiation might be used going forward instead of adjoint optimization as recently proposed in Ref. [151], to design multilayered structures of optimized thickness. Moreover, this method using RCWA promises to be faster that the adjoint optimization technique as well.

7.7.2 Confocal microscope setup

At the moment, we can scan small areas of the diamond sample by controlling the galvo mirrors. However, to improve the range and control of the galvo movement, extra lenses can be used to ensure that the back aperture of the objective and the galvo are conjugate to each other. Also, to automate the raster scan of the diamond sample, a DAQ board interface can be employed in the future.

7.7.3 Device fabrication

A major next step would be to fabricate our proposed device on the type IIb (111)-oriented diamond samples acquired from Applied Diamond Inc. Multiple devices can be fabricated on the sample, so that we have a higher chance of getting a device with a NV center near its center, and at approximately the depth the device has been optimized for. Ref. [135–137, 139, 152–155] provide a good guidance for choosing fabrication steps, and recipes for etching the desired pattern on the diamond substrate.

The diamond samples we will be using are too small to be properly spin coated with a resist without the formation of edge beads. One way to bypass that problem is to create a recess of correct depth on a larger piece of silicon wafer, and sticking the diamond sample

in it using some kind of adhesive or resist like vacuum grease/ crystal bond/ hydrogen silsesquioxane (HSQ). However, further study is required to decide which works the best. It is followed by cleaning the diamond surface, spin coating the resist, and developing it. HSQ (FOx and/or XR e-beam resist) is the usual resists of choice while working with diamond [135–137, 153, 155]. Another issue that needs to be studied is if we need to use any hard mask masks for the fabrication process, and if so, what would be a good choice for a mask. After the resist is patterned by lithography, we would need to etch the pattern on the diamond sample. There are multiple etching recipes available in the aforementioned references, starting from oxygen plasma etching, to etching with SF_6 and Cl_2. Proper care needs to be taken while choosing the correct recipe for our purpose to avoid over-heating or surface charge accumulation on the sample during the etching process.

Unfortunately, there is one drawback of etching the pattern directly on the diamond substrate. The etching process can highly degrade the quality of the NV center emitters in the diamond. Thus, the sample might require annealing after the etching process is complete to rejuvenate the NV centers [156]. Another possible option is precisely ion-implanting NVs at the center of the etched structure to avoid damaging the NVs during the etching process.

I would like to acknowledge helpful discussions with personnel at Quantum-Nano Fabrication and Characterization Facility (QNFCF) for guidance regarding possible fabrication methods.

7.7.4 Device characterization

Once many devices have been fabricated, one needs to look for 'ideal' cases where the NV center is near the center of the fabricated device, and at proper depth from the surface. The etched structure should significantly enhance the number of counts recorded at the photodetector even with a low NA objective, compared to a simple rectangular diamond slab because of the highly directive properties of the structure. Thereafter, the collection efficiency of the NV center's radiation might be measured into a single mode fiber 2µm away from the air-diamond interface for exact characterization of the device. However, that would require additional experimental efforts. Another additional benchmark that might be used for the device characterization is comparing the collection efficiencies at different numerical apertures to show the highly directional properties of the device.

Chapter 8

Conclusion

8.1 Deterministic single photon subtraction

In the first half of this thesis, we studied how we can perform deterministic single photon subtraction using single photon Raman interaction (SPRINT), which can provide significantly higher success rates compared to heralded photon subtraction processes relying upon beamsplitter like operations.

In Chapter 2, we studied the process of deterministic single photon subtraction in a bi-modal cavity. We studied the performance, and temporal dynamics of such a system for different types of input light. We find that we can achieve perfect single photon subtraction with a CW coherent drive and Fock states, even with low input intensities for correct cavity parameters. Whereas, for coherent pulses, that is not true. The input coherent pulse must have sufficient mean photon number for a photon to be subtracted with unit probability. We investigated the cavity parameters like the coupling strength (a measure of the mode volume and thus spatial confinement provided by the cavity) and cavity decay rate (a measure of the Q-factor and thus temporal confinement provided by the cavity) needed for successful single photon subtraction from the single photon Fock state. We also studied the second order auto-correlation function of the cavity modes. Interestingly, we observed $g^{(2)}$ values below unity, followed by super-bunching even for an input CW coherent laser drive.

In Chapter 3, we theoretically studied the feasibility of photon subtraction using a single three-level emitter coupled with a chiral waveguide, for continuous-wave (CW) coherent drive, coherent Gaussian pulses, and Fock states as input. We noticed that in ideal limits, with perfect chirality and coupling efficiencies, one can achieve perfect single photon

subtraction with a CW coherent or a Fock state input of arbitrary intensity. However, for Gaussian pulses of coherent light, we need the average photon number needs to be above a threshold for a single photon subtraction with unit probability, even if the pulsewidth is arbitrarily long. Also, the probability of success depends on the pulsewidth, i.e., the time scale of the interaction, and increases with increasing pulsewidth. Later, we discussed the influence of parameters like chirality, coupling efficiency, mode area, and group velocity while choosing an emitter-waveguide pair for the purpose of photon subtraction. It seems solid state emitters are preferable because of their larger coupling efficiencies, high integrability (which also leads to smaller mode areas). On the other hand, photonic crystal waveguides (PCW) have high chirality, and can provide high group index, leading to small group velocity, and higher probability of subtraction. We concluded that quantum dots (QD) coupled with high group index PCWs would be a great choice for SPRINT-based photon subtraction in a waveguide system.

Finally, in Chapter 4, we explored the creation of non-classical states using photon subtraction process. We discussed how SPRINT can be used to create highly non-Gaussian states, like Fock states with negative Wigner functions. We also observed negative conditional entropies, suggesting the creation of entanglement in the system. As an interesting example, we propose how such a SPRINT-based system could be potentially used to make Fock states of arbitrary photon number. We conclude with a brief discussion on potential future topics of investigation.

8.2 Inverse design of nanophotonic structures for directional emission from NV centers

In the second half of the thesis, we studied how to control the emission properties of an emitter, particularly NV centers, using adjoint optimization technique. First, in Chapter 5, we looked at the *ab initio* derivations of the formalism of radiation in the classical, and quantum pictures. We observed, how the local density of states (LDOS) bridges the gap between the two domains, thereby allowing us to treat quantum emitters as classical dipoles in suitable contexts for weak interactions. This simplifies many problems, and allows us to study interaction of quantum emitters with a scattering medium using the tools available in the arsenal of classical antenna theory. Finally, we provided the classical circuit/ antenna theoretic description of the interaction between an emitter, and a scattering object/ nanoparticle.

In Chapter 6, we studied how we can use adjoint optimization to design devices that have desired electromagnetic response. We showed how the optimization algorithm dras-

tically reduces computational resources needed for simulations by making clever use of the concept of reciprocity in Maxwell's electromagnetic theory. Finally, we briefly try to introduce the concepts of shape and topology optimization using fabrication dependent constraints for designing devices that be successfully manufactured by a foundry.

In Chapter 7, we propose a device to enhance directional emission of NV centers, and efficient coupling with a nanofiber situated 2µm away from the diamond-air interface. First, we provide a brief introduction to NV centers, and their crucial geometric and electronic properties. Next, we compare the performance of nanophotonic structure reported in the literature to enhance the emission properties of solid state emitters. Then, we explain our design philosophy and the underlying process, and propose a device designed with the help of adjoint optimization. Our device has a maximum directivity of 7.32dB, which is higher that the previously discussed structures, like the solid immersion lens (SIL), the nanopillar, or the bull's eye pattern. The novelty of the device is that, it does not require extra focusing elements to properly couple the light into the waveguide. Later, we discuss in detail how we set up a confocal microscopy setup in our laboratory to image the NV centers, and characterize our proposed device in the future. We conclude with a brief discussion of the future steps to bring the project to fruition.

References

[1] M. Planck, *Original Papers in quantum physics*, vol. 1. Taylor & Francis Group, 1972.

[2] A. Einstein, "Über einen die Erzeugung und Verwandlung des Lichtes betreffenden heuristischen Gesichtspunkt," *Annalen der Physik*, vol. 322, no. 6, pp. 132–148, 1905.

[3] P. A. M. Dirac, "The quantum theory of the emission and absorption of radiation," in *Special Relativity and Quantum Theory*, pp. 157–179, Springer Netherlands, 1988.

[4] R. J. Glauber, "Coherent and incoherent states of the radiation field," *Physical Review*, vol. 131, pp. 2766–2788, sep 1963.

[5] V. Parigi, A. Zavatta, M. Kim, and M. Bellini, "Probing quantum commutation rules by addition and subtraction of single photons to/from a light field," *Science*, vol. 317, pp. 1890–1893, Sep 2007.

[6] A. Ourjoumtsev, A. Dantan, R. Tualle-Brouri, and P. Grangier, "Increasing entanglement between gaussian states by coherent photon subtraction," *Physical Review Letters*, vol. 98, Jan 2007.

[7] M. Walschaers, S. Sarkar, V. Parigi, and N. Treps, "Tailoring non-gaussian continuous-variable graph states," *Physical Review Letters*, vol. 121, Nov 2018.

[8] L. Childress, J. M. Taylor, A. S. Sørensen, and M. D. Lukin, "Fault-tolerant quantum communication based on solid-state photon emitters," *Physical Review Letters*, vol. 96, Feb 2006.

[9] I. Aharonovich, S. Castelletto, D. A. Simpson, C.-H. Su, A. D. Greentree, and S. Prawer, "Diamond-based single-photon emitters," *Reports on Progress in Physics*, vol. 74, p. 076501, Jun 2011.

[10] F. Casola, T. van der Sar, and A. Yacoby, "Probing condensed matter physics with magnetometry based on nitrogen-vacancy centres in diamond," *Nature Reviews Materials*, vol. 3, Jan 2018.

[11] A. Zavatta, V. Parigi, M. S. Kim, and M. Bellini, "Subtracting photons from arbitrary light fields: experimental test of coherent state invariance by single-photon annihilation," *New Journal of Physics*, vol. 10, p. 123006, Dec 2008.

[12] M. Walschaers, C. Fabre, V. Parigi, and N. Treps, "Statistical signatures of multimode single-photon-added and -subtracted states of light," *Physical Review A*, vol. 96, Nov 2017.

[13] M. He, R. Malaney, and J. Green, "Quantum communications via satellite with photon subtraction," in *2018 IEEE Globecom Workshops (GC Wkshps)*, IEEE, Dec 2018.

[14] C. Navarrete-Benlloch, R. García-Patrón, J. H. Shapiro, and N. J. Cerf, "Enhancing quantum entanglement by photon addition and subtraction," *Physical Review A*, vol. 86, Jul 2012.

[15] S. Zhang, Y. Dong, X. Zou, B. Shi, and G. Guo, "Continuous-variable-entanglement distillation with photon addition," *Physical Review A*, vol. 88, Sep 2013.

[16] K. Huang, H. L. Jeannic, O. Morin, T. Darras, G. Guccione, A. Cavaillès, and J. Laurat, "Engineering optical hybrid entanglement between discrete- and continuous-variable states," *New Journal of Physics*, vol. 21, p. 083033, Aug 2019.

[17] S. Olivares and M. G. A. Paris, "Squeezed fock state by inconclusive photon subtraction," *Journal of Optics B: Quantum and Semiclassical Optics*, vol. 7, pp. S616–S621, Nov 2005.

[18] A. Ourjoumtsev, H. Jeong, R. Tualle-Brouri, and P. Grangier, "Generation of optical 'schrdinger cats' from photon number states," *Nature*, vol. 448, pp. 784–786, Aug 2007.

[19] H. Takahashi, K. Wakui, S. Suzuki, M. Takeoka, K. Hayasaka, A. Furusawa, and M. Sasaki, "Generation of large-amplitude coherent-state superposition via ancilla-assisted photon subtraction," *Physical Review Letters*, vol. 101, Dec 2008.

[20] T. Gerrits, S. Glancy, T. S. Clement, B. Calkins, A. E. Lita, A. J. Miller, A. L. Migdall, S. W. Nam, R. P. Mirin, and E. Knill, "Generation of optical coherent-state

superpositions by number-resolved photon subtraction from the squeezed vacuum," *Physical Review A*, vol. 82, Sep 2010.

[21] M. S. Kim, E. Park, P. L. Knight, and H. Jeong, "Nonclassicality of a photon-subtracted gaussian field," *Physical Review A*, vol. 71, Apr 2005.

[22] J. Wenger, R. Tualle-Brouri, and P. Grangier, "Non-gaussian statistics from individual pulses of squeezed light," *Physical Review Letters*, vol. 92, Apr 2004.

[23] Y.-S. Ra, C. Jacquard, A. Dufour, C. Fabre, and N. Treps, "Tomography of a mode-tunable coherent single-photon subtractor," *Physical Review X*, vol. 7, Jul 2017.

[24] V. Averchenko, C. Jacquard, V. Thiel, C. Fabre, and N. Treps, "Multimode theory of single-photon subtraction," *New Journal of Physics*, vol. 18, p. 083042, Aug 2016.

[25] A. I. Lvovsky, H. Hansen, T. Aichele, O. Benson, J. Mlynek, and S. Schiller, "Quantum state reconstruction of the single-photon fock state," *Physical Review Letters*, vol. 87, Jul 2001.

[26] J. Honer, R. Löw, H. Weimer, T. Pfau, and H. P. Büchler, "Artificial atoms can do more than atoms: Deterministic single photon subtraction from arbitrary light fields," *Phys. Rev. Lett.*, vol. 107, p. 093601, Aug 2011.

[27] S. Rosenblum, O. Bechler, I. Shomroni, Y. Lovsky, G. Guendelman, and B. Dayan, "Extraction of a single photon from an optical pulse," *Nature Photonics*, vol. 10, pp. 19–22, Nov 2015.

[28] C. Tresp, C. Zimmer, I. Mirgorodskiy, H. Gorniaczyk, A. Paris-Mandoki, and S. Hofferbeth, "Single-photon absorber based on strongly interacting rydberg atoms," *Phys. Rev. Lett.*, vol. 117, p. 223001, 2016.

[29] D. Pinotsi and A. Imamoglu, "Single photon absorption by a single quantum emitter," *Physical Review Letters*, vol. 100, Mar 2008.

[30] S. Rosenblum, S. Parkins, and B. Dayan, "Photon routing in cavity QED: Beyond the fundamental limit of photon blockade," *Physical Review A*, vol. 84, Sep 2011.

[31] S. Rosenblum, A. Borne, and B. Dayan, "Analysis of deterministic swapping of photonic and atomic states through single-photon raman interaction," *Physical Review A*, vol. 95, Mar 2017.

[32] I. Aharonovich, D. Englund, and M. Toth, "Solid-state single-photon emitters," *Nature Photonics*, vol. 10, pp. 631–641, Sep 2016.

[33] T. Schröder, F. Gädeke, M. J. Banholzer, and O. Benson, "Ultrabright and efficient single-photon generation based on nitrogen-vacancy centres in nanodiamonds on a solid immersion lens," *New Journal of Physics*, vol. 13, p. 055017, May 2011.

[34] E. Neu, D. Steinmetz, J. Riedrich-Möller, S. Gsell, M. Fischer, M. Schreck, and C. Becher, "Single photon emission from silicon-vacancy colour centres in chemical vapour deposition nano-diamonds on iridium," *New Journal of Physics*, vol. 13, p. 025012, Feb 2011.

[35] S. Castelletto, B. C. Johnson, V. Ivády, N. Stavrias, T. Umeda, A. Gali, and T. Ohshima, "A silicon carbide room-temperature single-photon source," *Nature Materials*, vol. 13, pp. 151–156, Nov 2013.

[36] A. J. Morfa, B. C. Gibson, M. Karg, T. J. Karle, A. D. Greentree, P. Mulvaney, and S. Tomljenovic-Hanic, "Single-photon emission and quantum characterization of zinc oxide defects," *Nano Letters*, vol. 12, pp. 949–954, Jan 2012.

[37] P. Siyushev, K. Xia, R. Reuter, M. Jamali, N. Zhao, N. Yang, C. Duan, N. Kukharchyk, A. D. Wieck, R. Kolesov, and J. Wrachtrup, "Coherent properties of single rare-earth spin qubits," *Nature Communications*, vol. 5, May 2014.

[38] T. T. Tran, K. Bray, M. J. Ford, M. Toth, and I. Aharonovich, "Quantum emission from hexagonal boron nitride monolayers," *Nature Nanotechnology*, vol. 11, pp. 37–41, Oct 2015.

[39] X. Ma, N. F. Hartmann, J. K. S. Baldwin, S. K. Doorn, and H. Htoon, "Room-temperature single-photon generation from solitary dopants of carbon nanotubes," *Nature Nanotechnology*, vol. 10, pp. 671–675, Jul 2015.

[40] P. Senellart, G. Solomon, and A. White, "High-performance semiconductor quantum-dot single-photon sources," *Nature Nanotechnology*, vol. 12, pp. 1026–1039, Nov 2017.

[41] J. Du, W. Li, and M. Bajcsy, "Deterministic single-photon subtraction based on a coupled single quantum dot-cavity system," *Optics Express*, vol. 28, p. 6835, Feb 2020.

[42] C. Fabre and N. Treps, "Modes and states in quantum optics," *Reviews of Modern Physics*, vol. 92, Sep 2020.

[43] H. Carmichael, *An Open Systems Approach to Quantum Optics*. Springer Berlin Heidelberg, 1993.

[44] J. Johansson, P. Nation, and F. Nori, "QuTiP: An open-source python framework for the dynamics of open quantum systems," *Computer Physics Communications*, vol. 183, pp. 1760–1772, aug 2012.

[45] J. Johansson, P. Nation, and F. Nori, "QuTiP 2: A python framework for the dynamics of open quantum systems," *Computer Physics Communications*, vol. 184, pp. 1234–1240, apr 2013.

[46] K. Mølmer, Y. Castin, and J. Dalibard, "Monte carlo wave-function method in quantum optics," *Journal of the Optical Society of America B*, vol. 10, p. 524, Mar 1993.

[47] A. Majumdar, M. Bajcsy, A. Rundquist, and J. Vučković, "Loss-enabled sub-poissonian light generation in a bimodal nanocavity," *Physical Review Letters*, vol. 108, May 2012.

[48] A. Rundquist, M. Bajcsy, A. Majumdar, T. Sarmiento, K. Fischer, K. G. Lagoudakis, S. Buckley, A. Y. Piggott, and J. Vučković, "Nonclassical higher-order photon correlations with a quantum dot strongly coupled to a photonic-crystal nanocavity," *Physical Review A*, vol. 90, Aug 2014.

[49] C. W. Gardiner and M. J. Collett, "Input and output in damped quantum systems: Quantum stochastic differential equations and the master equation," *Phys. Rev. A*, vol. 31, pp. 3761–3774, Jun 1985.

[50] G. R. Bappi, "Design and applications of single-photon devices based on waveguides coupled to quantum emitters," 2016.

[51] H. Zheng, "Interacting photons in waveguide-qed and applications in quantum information processing," *PhD Thesis*, 2013.

[52] S. Fan, Ş. E. Kocabaş, and J.-T. Shen, "Input-output formalism for few-photon transport in one-dimensional nanophotonic waveguides coupled to a qubit," *Phys. Rev. A*, vol. 82, p. 063821, Dec 2010.

[53] R. Trivedi, K. Fischer, S. Xu, S. Fan, and J. Vuckovic, "Few-photon scattering and emission from low-dimensional quantum systems," *Physical Review B*, vol. 98, Oct 2018.

[54] K. A. Fischer, R. Trivedi, V. Ramasesh, I. Siddiqi, and J. Vučković, "Scattering into one-dimensional waveguides from a coherently-driven quantum-optical system," *Quantum*, vol. 2, p. 69, May 2018.

[55] E. Rephaeli and S. Fan, "Dissipation in few-photon waveguide transport [invited]," *Photonics Research*, vol. 1, p. 110, Aug 2013.

[56] R. Mitsch, C. Sayrin, B. Albrecht, P. Schneeweiss, and A. Rauschenbeutel, "Quantum state-controlled directional spontaneous emission of photons into a nanophotonic waveguide," *Nature Communications*, vol. 5, p. 5713, 2014.

[57] Ş. E. Kocabaş, E. Rephaeli, and S. Fan, "Resonance fluorescence in a waveguide geometry," *Phys. Rev. A*, vol. 85, p. 023817, Feb 2012.

[58] A. Goban, C.-L. Hung, S.-P. Yu, J. Hood, J. Muniz, J. Lee, M. Martin, A. McClung, K. Choi, D. Chang, O. Painter, and H. Kimble, "Atom–light interactions in photonic crystals," *Nature Communications*, vol. 5, May 2014.

[59] M. Arcari, I. Söllner, A. Javadi, S. L. Hansen, S. Mahmoodian, J. Liu, H. Thyrrestrup, E. Lee, J. Song, S. Stobbe, and P. Lodahl, "Near-unity coupling efficiency of a quantum emitter to a photonic crystal waveguide," *Phys. Rev. Lett.*, vol. 113, p. 093603, Aug 2014.

[60] P. Lodahl, S. Mahmoodian, S. Stobbe, A. Rauschenbeutel, P. Schneeweiss, J. Volz, H. Pichler, and P. Zoller, "Chiral quantum optics," *Nature*, vol. 541, p. 473, 2017.

[61] C. Ciuti and I. Carusotto, "Input-output theory of cavities in the ultrastrong coupling regime: The case of time-independent cavity parameters," *Physical Review A*, vol. 74, Sep 2006.

[62] R. Loudon, *The quantum theory of light / Rodney Loudon.* Clarendon Press Oxford, 1973.

[63] F. L. Kien, S. D. Gupta, V. I. Balykin, and K. Hakuta, "Spontaneous emission of a cesium atom near a nanofiber: Efficient coupling of light to guided modes," *Phys. Rev. A*, vol. 72, p. 032509, Sep 2005.

[64] E. Vetsch, D. Reitz, G. Sague, R. Schmidt, S. T. Dawkins, and A. Rauschenbeutel, "Optical interface created by laser-cooled atoms trapped in the evanescent field surrounding an optical nanofiber," *Phys. Rev. Lett.*, vol. 104, p. 203603, 2010.

[65] F. L. Kien, S. S. S. Hejazi, T. Busch, V. G. Truong, and S. N. Chormaic, "Channeling of spontaneous emission from an atom into the fundamental and higher-order modes of a vacuum-clad ultrathin optical fiber," *Phys. Rev. A*, vol. 96, p. 043859, Oct 2017.

[66] A. Goban, K. S. Choi, D. J. Alton, D. Ding, C. Lacroûte, M. Pototschnig, T. Thiele, N. P. Stern, and H. J. Kimble, "Demonstration of a state-insensitive, compensated nanofiber trap," *Physical Review Letters*, vol. 109, Jul 2012.

[67] T. G. Tiecke, J. D. Thompson, N. P. de Leon, L. R. Liu, V. Vuletić, and M. D. Lukin, "Nanophotonic quantum phase switch with a single atom," *Nature*, vol. 508, pp. 241–244, Apr 2014.

[68] I. Söllner, S. Mahmoodian, S. L. Hansen, L. Midolo, A. Javadi, G. Kirsanske, T. Pregnolato, H. El-Ella, E. H. Lee, J. D. Song, S. Stobbe, and P. Lodahl, "Deterministic photon–emitter coupling in chiral photonic circuits," *Nature Nanotechnology*, vol. 10, p. 775, 2015.

[69] H. Thyrrestrup, L. Sapienza, and P. Lodahl, "Extraction of the β-factor for single quantum dots coupled to a photonic crystal waveguide," *Applied Physics Letters*, vol. 96, p. 231106, Jun 2010.

[70] T. Reichert, S. Lichtmannecker, G. Reithmaier, M. Zeitlmair, J. Wembacher, A. Rauscher, M. Bichler, K. Müller, M. Kaniber, and J. J. Finley, "Highly directed emission from self-assembled quantum dots into guided modes in disordered photonic-crystal waveguides," *Phys. Rev. B*, vol. 90, p. 115310, Sep 2014.

[71] G. Lecamp, P. Lalanne, and J. P. Hugonin, "Very large spontaneous-emission β factors in photonic-crystal waveguides," *Phys. Rev. Lett.*, vol. 99, p. 023902, Jul 2007.

[72] H. P. Robertson, "The uncertainty principle," *Physical Review*, vol. 34, pp. 163–164, Jul 1929.

[73] A. I. Lvovsky and M. G. Raymer, "Continuous-variable optical quantum-state tomography," *Reviews of Modern Physics*, vol. 81, pp. 299–332, Mar 2009.

[74] R. Simon, N. Mukunda, and B. Dutta, "Quantum-noise matrix for multimode systems: U(n) invariance, squeezing, and normal forms," *Physical Review A*, vol. 49, pp. 1567–1583, Mar 1994.

[75] S. Olivares, "Quantum optics in the phase space," *The European Physical Journal Special Topics*, vol. 203, pp. 3–24, Apr 2012.

[76] C. Weedbrook, S. Pirandola, R. García-Patrón, N. J. Cerf, T. C. Ralph, J. H. Shapiro, and S. Lloyd, "Gaussian quantum information," *Reviews of Modern Physics*, vol. 84, pp. 621–669, May 2012.

[77] D. Gottesman, "The Heisenberg Representation of Quantum Computers," *Proc. XXII International Colloquium on Group Theoretical Methods in Physics*, pp. 32–43, 1999.

[78] J. Eisert, S. Scheel, and M. B. Plenio, "Distilling gaussian states with gaussian operations is impossible," *Physical Review Letters*, vol. 89, Sep 2002.

[79] T. Opatrný, G. Kurizki, and D.-G. Welsch, "Improvement on teleportation of continuous variables by photon subtraction via conditional measurement," *Physical Review A*, vol. 61, Feb 2000.

[80] T. C. Ralph, A. P. Lund, and A. Lvovsky, "Nondeterministic noiseless linear amplification of quantum systems," in *AIP Conference Proceedings*, AIP, 2009.

[81] G. Y. Xiang, T. C. Ralph, A. P. Lund, N. Walk, and G. J. Pryde, "Heralded noiseless linear amplification and distillation of entanglement," *Nature Photonics*, vol. 4, pp. 316–319, Mar 2010.

[82] A. Zavatta, J. Fiurášek, and M. Bellini, "A high-fidelity noiseless amplifier for quantum light states," *Nature Photonics*, vol. 5, pp. 52–56, Nov 2010.

[83] B. Schumacher, "Quantum coding," *Physical Review A*, vol. 51, pp. 2738–2747, Apr. 1995.

[84] J. von Neumann, *Mathematische Grundlagen der Quantenmechanik*. Springer Verlag, Berlin, 1932.

[85] N. J. Cerf and C. Adami, "Entropic bell inequalities," *Physical Review A*, vol. 55, pp. 3371–3374, May 1997.

[86] Y. Kurochkin, A. S. Prasad, and A. I. Lvovsky, "Distillation of the two-mode squeezed state," *Physical Review Letters*, vol. 112, Feb 2014.

[87] G. Harel and I. Abram, "Spontaneous emission in a cavity: Quantum and classical radiation-reaction viewpoint," 2000.

[88] L. Novotny and B. Hecht, *Principles of Nano-Optics*. Cambridge University Press, 2012.

[89] P. Bharadwaj, B. Deutsch, and L. Novotny, "Optical antennas," *Advances in Optics and Photonics*, vol. 1, p. 438, Aug 2009.

[90] A. E. Krasnok, A. P. Slobozhanyuk, C. R. Simovski, S. A. Tretyakov, A. N. Poddubny, A. E. Miroshnichenko, Y. S. Kivshar, and P. A. Belov, "An antenna model for the purcell effect," *Scientific Reports*, vol. 5, Aug 2015.

[91] J.-J. Greffet, M. Laroche, and F. Marquier, "Impedance of a nanoantenna and a single quantum emitter," *Physical Review Letters*, vol. 105, Sep 2010.

[92] J. B. Khurgin, G. Sun, and R. A. Soref, "Electroluminescence efficiency enhancement using metal nanoparticles," *Applied Physics Letters*, vol. 93, p. 021120, Jul 2008.

[93] O. D. Miller, "Photonic design: From fundamental solar cell physics to computational inverse design," *PhD Thesis*, 2012.

[94] C. M. Lalau-Keraly, S. Bhargava, O. D. Miller, and E. Yablonovitch, "Adjoint shape optimization applied to electromagnetic design," *Optics Express*, vol. 21, p. 21693, Sep 2013.

[95] S. Bhargava, *Heat-Assisted Magnetic Recording: Fundamental Limits to Inverse Electromagnetic Design*. PhD thesis, EECS Department, University of California, Berkeley, May 2015.

[96] S. Osher and J. A. Sethian, "Fronts propagating with curvature-dependent speed: Algorithms based on hamilton-jacobi formulations," *Journal of Computational Physics*, vol. 79, pp. 12–49, Nov 1988.

[97] S. Osher and R. Fedkiw, "Particle level set method," in *Applied Mathematical Sciences*, pp. 79–86, Springer New York, 2003.

[98] A. Y. Piggott, "Automated Design of Photonic Devices," *PhD Thesis*, no. Jun, p. 112, 2018.

[99] G. Balasubramanian, I. Y. Chan, R. Kolesov, M. Al-Hmoud, J. Tisler, C. Shin, C. Kim, A. Wojcik, P. R. Hemmer, A. Krueger, T. Hanke, A. Leitenstorfer, R. Bratschitsch, F. Jelezko, and J. Wrachtrup, "Nanoscale imaging magnetometry with diamond spins under ambient conditions," *Nature*, vol. 455, pp. 648–651, Oct 2008.

[100] J. M. Taylor, P. Cappellaro, L. Childress, L. Jiang, D. Budker, P. R. Hemmer, A. Yacoby, R. Walsworth, and M. D. Lukin, "High-sensitivity diamond magnetometer with nanoscale resolution," *Nature Physics*, vol. 4, pp. 810–816, Sep 2008.

[101] G. Kucsko, P. C. Maurer, N. Y. Yao, M. Kubo, H. J. Noh, P. K. Lo, H. Park, and M. D. Lukin, "Nanometre-scale thermometry in a living cell," *Nature*, vol. 500, pp. 54–58, Jul 2013.

[102] F. Dolde, H. Fedder, M. W. Doherty, T. Nbauer, F. Rempp, G. Balasubramanian, T. Wolf, F. Reinhard, L. C. L. Hollenberg, F. Jelezko, and J. Wrachtrup, "Electric-field sensing using single diamond spins," *Nature Physics*, vol. 7, pp. 459–463, Apr 2011.

[103] M. W. Doherty, V. V. Struzhkin, D. A. Simpson, L. P. McGuinness, Y. Meng, A. Stacey, T. J. Karle, R. J. Hemley, N. B. Manson, L. C. Hollenberg, and S. Prawer, "Electronic properties and metrology applications of the DiamondNV-center under pressure," *Physical Review Letters*, vol. 112, Jan 2014.

[104] M. P. Ledbetter, K. Jensen, R. Fischer, A. Jarmola, and D. Budker, "Gyroscopes based on nitrogen-vacancy centers in diamond," *Physical Review A*, vol. 86, Nov 2012.

[105] M. V. G. Dutt, L. Childress, L. Jiang, E. Togan, J. Maze, F. Jelezko, A. S. Zibrov, P. R. Hemmer, and M. D. Lukin, "Quantum register based on individual electronic and nuclear spin qubits in diamond," *Science*, vol. 316, pp. 1312–1316, Jun 2007.

[106] P. Neumann, R. Kolesov, B. Naydenov, J. Beck, F. Rempp, M. Steiner, V. Jacques, G. Balasubramanian, M. L. Markham, D. J. Twitchen, S. Pezzagna, J. Meijer, J. Twamley, F. Jelezko, and J. Wrachtrup, "Quantum register based on coupled electron spins in a room-temperature solid," *Nature Physics*, vol. 6, pp. 249–253, Feb 2010.

[107] P. C. Maurer, G. Kucsko, C. Latta, L. Jiang, N. Y. Yao, S. D. Bennett, F. Pastawski, D. Hunger, N. Chisholm, M. Markham, D. J. Twitchen, J. I. Cirac, and M. D. Lukin, "Room-temperature quantum bit memory exceeding one second," *Science*, vol. 336, pp. 1283–1286, Jun 2012.

[108] A. Beveratos, R. Brouri, T. Gacoin, A. Villing, J.-P. Poizat, and P. Grangier, "Single photon quantum cryptography," *Physical Review Letters*, vol. 89, Oct 2002.

[109] J. Wrachtrup and F. Jelezko, "Processing quantum information in diamond," *Journal of Physics: Condensed Matter*, vol. 18, pp. S807–S824, May 2006.

[110] M. Gould, S. Chakravarthi, I. R. Christen, N. Thomas, S. Dadgostar, Y. Song, M. L. Lee, F. Hatami, and K.-M. C. Fu, "Large-scale GaP-on-diamond integrated photonics platform for NV center-based quantum information," *Journal of the Optical Society of America B*, vol. 33, p. B35, Jan 2016.

[111] D. Kim, M. I. Ibrahim, C. Foy, M. E. Trusheim, R. Han, and D. R. Englund, "A CMOS-integrated quantum sensor based on nitrogen–vacancy centres," *Nature Electronics*, vol. 2, pp. 284–289, Jul 2019.

[112] C. Kurtsiefer, S. Mayer, P. Zarda, and H. Weinfurter, "Stable solid-state source of single photons," *Physical Review Letters*, vol. 85, pp. 290–293, Jul 2000.

[113] F. Jelezko, T. Gaebel, I. Popa, A. Gruber, and J. Wrachtrup, "Observation of coherent oscillations in a single electron spin," *Physical Review Letters*, vol. 92, Feb 2004.

[114] F. Jelezko, T. Gaebel, I. Popa, M. Domhan, A. Gruber, and J. Wrachtrup, "Observation of coherent oscillation of a single nuclear spin and realization of a two-qubit conditional quantum gate," *Physical Review Letters*, vol. 93, Sep 2004.

[115] D. B. Bucher, D. P. L. A. Craik, M. P. Backlund, M. J. Turner, O. B. Dor, D. R. Glenn, and R. L. Walsworth, "Quantum diamond spectrometer for nanoscale NMR and ESR spectroscopy," *Nature Protocols*, vol. 14, pp. 2707–2747, Aug 2019.

[116] E. van Oort, N. B. Manson, and M. Glasbeek, "Optically detected spin coherence of the diamond n-v centre in its triplet ground state," *Journal of Physics C: Solid State Physics*, vol. 21, pp. 4385–4391, Aug 1988.

[117] D. Farfurnik, A. Jarmola, L. M. Pham, Z. H. Wang, V. V. Dobrovitski, R. L. Walsworth, D. Budker, and N. Bar-Gill, "Optimizing a dynamical decoupling protocol for solid-state electronic spin ensembles in diamond," *Physical Review B*, vol. 92, Aug 2015.

[118] S. Sangtawesin, T. O. Brundage, Z. J. Atkins, and J. R. Petta, "Highly tunable formation of nitrogen-vacancy centers via ion implantation," *Applied Physics Letters*, vol. 105, p. 063107, Aug 2014.

[119] J. Meijer, B. Burchard, M. Domhan, C. Wittmann, T. Gaebel, I. Popa, F. Jelezko, and J. Wrachtrup, "Generation of single color centers by focused nitrogen implantation," *Applied Physics Letters*, vol. 87, p. 261909, Dec 2005.

[120] G. Davies and M. F. Hamer, "Optical studies of the 1.945 eV vibronic band in diamond," *Proceedings of the Royal Society of London. A. Mathematical and Physical Sciences*, vol. 348, pp. 285–298, Feb 1976.

[121] L. I. Childress, "Coherent manipulation of single quantum systems in the solid state," *PhD Thesis*, p. 188, Mar 2007.

[122] L. Rondin, G. Dantelle, A. Slablab, F. Grosshans, F. Treussart, P. Bergonzo, S. Perruchas, T. Gacoin, M. Chaigneau, H.-C. Chang, V. Jacques, and J.-F. Roch, "Surface-induced charge state conversion of nitrogen-vacancy defects in nanodiamonds," *Physical Review B*, vol. 82, Sep 2010.

[123] K. Beha, H. Fedder, M. Wolfer, M. C. Becker, P. Siyushev, M. Jamali, A. Batalov, C. Hinz, J. Hees, L. Kirste, H. Obloh, E. Gheeraert, B. Naydenov, I. Jakobi, F. Dolde, S. Pezzagna, D. Twittchen, M. Markham, D. Dregely, H. Giessen, J. Meijer, F. Jelezko, C. E. Nebel, R. Bratschitsch, A. Leitenstorfer, and J. Wrachtrup, "Diamond nanophotonics," *Beilstein Journal of Nanotechnology*, vol. 3, pp. 895–908, Dec 2012.

[124] N. Reddy, N. Manson, and E. Krausz, "Two-laser spectral hole burning in a colour centre in diamond," *Journal of Luminescence*, vol. 38, pp. 46–47, Dec 1987.

[125] J. H. N. Loubser and J. A. van Wyk, "Electron spin resonance in the study of diamond," *Reports on Progress in Physics*, vol. 41, pp. 1201–1248, Aug 1978.

[126] P. M. Kehayias, "Exploring Basic Properties and Applications of Nitrogen-Vacancy Color Centers in Diamond," *PhD Thesis*, 2015.

[127] M. Auzinsh, A. Berzins, D. Budker, L. Busaite, R. Ferber, F. Gahbauer, R. Lazda, A. Wickenbrock, and H. Zheng, "Hyperfine level structure in nitrogen-vacancy centers near the ground-state level anticrossing," *Physical Review B*, vol. 100, Aug 2019.

[128] H. Kaupp, C. Deutsch, H.-C. Chang, J. Reichel, T. W. Hänsch, and D. Hunger, "Scaling laws of the cavity enhancement for nitrogen-vacancy centers in diamond," *Physical Review A*, vol. 88, Nov 2013.

[129] P. E. Barclay, K.-M. C. Fu, C. Santori, A. Faraon, and R. G. Beausoleil, "Hybrid nanocavity resonant enhancement of color center emission in diamond," *Physical Review X*, vol. 1, Sep 2011.

[130] A. Gruber, "Scanning confocal optical microscopy and magnetic resonance on single defect centers," *Science*, vol. 276, pp. 2012–2014, Jun 1997.

[131] J. P. Hadden, J. P. Harrison, A. C. Stanley-Clarke, L. Marseglia, Y.-L. D. Ho, B. R. Patton, J. L. O'Brien, and J. G. Rarity, "Strongly enhanced photon collection from diamond defect centers under microfabricated integrated solid immersion lenses," *Applied Physics Letters*, vol. 97, p. 241901, Dec 2010.

[132] L. Marseglia, J. P. Hadden, A. C. Stanley-Clarke, J. P. Harrison, B. Patton, Y.-L. D. Ho, B. Naydenov, F. Jelezko, J. Meijer, P. R. Dolan, J. M. Smith, J. G. Rarity, and J. L. O'Brien, "Nanofabricated solid immersion lenses registered to single emitters in diamond," *Applied Physics Letters*, vol. 98, p. 133107, Mar 2011.

[133] D. Riedel, D. Rohner, M. Ganzhorn, T. Kaldewey, P. Appel, E. Neu, R. Warburton, and P. Maletinsky, "Low-loss broadband antenna for efficient photon collection from a coherent spin in diamond," *Physical Review Applied*, vol. 2, Dec 2014.

[134] Y. Ma, G. Ballesteros, J. M. Zajac, J. Sun, and B. D. Gerardot, "Highly directional emission from a quantum emitter embedded in a hemispherical cavity," *Optics Letters*, vol. 40, p. 2373, May 2015.

[135] B. J. Hausmann, M. Khan, Y. Zhang, T. M. Babinec, K. Martinick, M. McCutcheon, P. R. Hemmer, and M. Lončar, "Fabrication of diamond nanowires for quantum information processing applications," *Diamond and Related Materials*, vol. 19, pp. 621–629, May 2010.

[136] T. M. Babinec, B. J. M. Hausmann, M. Khan, Y. Zhang, J. R. Maze, P. R. Hemmer, and M. Lončar, "A diamond nanowire single-photon source," *Nature Nanotechnology*, vol. 5, pp. 195–199, Feb 2010.

[137] J. T. Choy, B. J. M. Hausmann, T. M. Babinec, I. Bulu, M. Khan, P. Maletinsky, A. Yacoby, and M. Lončar, "Enhanced single-photon emission from a diamond–silver aperture," *Nature Photonics*, vol. 5, pp. 738–743, Oct 2011.

[138] S. A. Momenzadeh, R. J. Stöhr, F. F. de Oliveira, A. Brunner, A. Denisenko, S. Yang, F. Reinhard, and J. Wrachtrup, "Nanoengineered diamond waveguide as a robust bright platform for nanomagnetometry using shallow nitrogen vacancy centers," *Nano Letters*, vol. 15, pp. 165–169, Dec 2014.

[139] E. Neu, P. Appel, M. Ganzhorn, J. Miguel-Sánchez, M. Lesik, V. Mille, V. Jacques, A. Tallaire, J. Achard, and P. Maletinsky, "Photonic nano-structures on (111)-oriented diamond," *Applied Physics Letters*, vol. 104, p. 153108, Apr 2014.

[140] M. Y. Su and R. P. Mirin, "Enhanced light extraction from circular bragg grating coupled microcavities," *Applied Physics Letters*, vol. 89, p. 033105, Jul 2006.

[141] M. Davanço, M. T. Rakher, D. Schuh, A. Badolato, and K. Srinivasan, "A circular dielectric grating for vertical extraction of single quantum dot emission," *Applied Physics Letters*, vol. 99, p. 041102, Jul 2011.

[142] L. Li, E. H. Chen, J. Zheng, S. L. Mouradian, F. Dolde, T. Schröder, S. Karaveli, M. L. Markham, D. J. Twitchen, and D. Englund, "Efficient photon collection from a nitrogen vacancy center in a circular bullseye grating," *Nano Letters*, vol. 15, pp. 1493–1497, Mar 2015.

[143] C. M. Lalau-Keraly, "Lumopt: Python based continuous adjoint optimization wrapper for lumerical." https://github.com/chriskeraly/lumopt.

[144] R. A. Wambold, Z. Yu, Y. Xiao, B. Bachman, G. Jaffe, S. Kolkowitz, J. T. Choy, M. A. Eriksson, R. J. Hamers, and M. A. Kats, "Adjoint-optimized nanoscale light extractor for nitrogen-vacancy centers in diamond," *Nanophotonics*, vol. 10, pp. 393–401, Nov 2020.

[145] S. Chakravarthi, P. Chao, C. Pederson, S. Molesky, A. Ivanov, K. Hestroffer, F. Hatami, A. W. Rodriguez, and K.-M. C. Fu, "Inverse-designed photon extractors for optically addressable defect qubits," *Optica*, vol. 7, p. 1805, Dec 2020.

[146] Patange, Om, "On an instrument for the coherent investigation of nitrogen-vacancy centres in diamond," *Masters Thesis*, 2013.

[147] H. Kogelnik and T. Li, "Laser beams and resonators," *Proceedings of the IEEE*, vol. 54, no. 10, pp. 1312–1329, 1966.

[148] J. Arnaud, "Representation of gaussian beams by complex rays," *Applied Optics*, vol. 24, p. 538, Feb 1985.

[149] D. A. Steck, *Classical and modern optics*. 2006.

[150] Element Six, "Cvd diamond handbook." https://e6cvd.com/media/wysiwyg/pdf/CVD_Diamond_Handbook_digital_01.07.20.pdf.

[151] S. Colburn and A. Majumdar, "Inverse design and flexible parameterization of meta-optics using algorithmic differentiation," *Communications Physics*, vol. 4, Mar 2021.

[152] L. Li, T. Schrder, E. H. Chen, M. Walsh, I. Bayn, J. Goldstein, O. Gaathon, M. E. Trusheim, M. Lu, J. Mower, M. Cotlet, M. L. Markham, D. J. Twitchen, and D. Englund, "Coherent spin control of a nanocavity-enhanced qubit in diamond," *Nature Communications*, vol. 6, Jan 2015.

[153] B. J. M. Hausmann, "Nanophotonics in diamond," *PhD Thesis*, 2013.

[154] M. Challier, S. Sonusen, A. Barfuss, D. Rohner, D. Riedel, J. Koelbl, M. Ganzhorn, P. Appel, P. Maletinsky, and E. Neu, "Advanced fabrication of single-crystal diamond membranes for quantum technologies," *Micromachines*, vol. 9, p. 148, Mar 2018.

[155] M. Radtke, R. Nelz, A. Slablab, and E. Neu, "Reliable nanofabrication of single-crystal diamond photonic nanostructures for nanoscale sensing," *Micromachines*, vol. 10, p. 718, Oct 2019.

[156] S. Cui, "Near-surface nitrogen vacancy centers in diamond," *PhD Thesis*, 2014.

[157] K. Schönhammer, "Luttinger liquids: the basic concepts," in *Physics and Chemistry of Materials with Low-Dimens*, pp. 93–136, Springer Netherlands.

[158] T. Stauber, "Tomonaga-luttinger model with an impurity for a weak two-body interaction," *Physical Review B*, vol. 67, May 2003.

[159] T. Giamarchi, *Quantum Physics in One Dimension*. Oxford University Press, Dec 2003.

[160] J. Flannery, "Optical resonators integrated into a hollow core photonic crystal fiber for enhanced light-matter interactions," *PhD Thesis*, 2019.

APPENDICES

Appendix A

Deterministic single photon subtraction with a three-level to a chiral waveguide

A.1 Derivation of real space Hamiltonian

In the continuous mode limit we have the Hamiltonian

$$H/\hbar = \omega_{eg}\sigma_{ee} + \int_{-\infty}^{\infty} a_k^\dagger a_k \omega_k dk + \int_{-\infty}^{\infty} V(k)\sqrt{\frac{L}{2\pi}}\left(a_k\sigma_+ + a_k^\dagger\sigma_-\right)dk. \tag{A.1}$$

Here, we shall derive the real space Hamiltonian following the approach in Ref. [51]. We assume that we can linearize the dispersion relationship around the atomic transition frequency as $\omega_k \approx \omega_{eg} + v_g(k - k_{eg})$ (see Fig. A.1). Moreover, we want to extend this Hamiltonian to consider the case where there are two counter propagating modes: the right-propagating mode with operator $r(x)$, and the left-propagating mode with operator $l(x)$. Thus, we can have both positive and negative wavevectors. The linearized dispersion relationships for the two counter-propagating modes are given by: $\omega_r \approx \omega_{eg} + v_g(k - k_{eg})$ for the right-propagating mode, and $\omega_l \approx \omega_{eg} - v_g(k + k_{eg})$ for the left-propagating mode. Then we shall use the substitution $\omega_k = v_g|k|$ to consider both positive and negative wavevectors, and introduce the independent left and right modes in Eq. A.1. We also consider that the coupling constant is frequency independent, i.e., $V(k) = \mathcal{V}$. Doing so, we get:

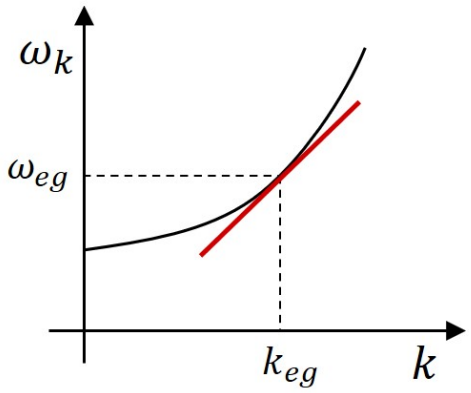

Figure A.1: The waveguide dispersion relationship is considered to be linear around ω_{eg} for near resonant interactions.

$$H/\hbar = \omega_{eg}\sigma_{ee} + \int_0^\infty \left[r_k^\dagger r_k + l_{-k}^\dagger l_{-k}\right] v_g k dk + \int_0^\infty \mathcal{V}\sqrt{\frac{L}{2\pi}} \left[(r_k + l_{-k})\,\sigma_+ + \left(r_k^\dagger + l_{-k}^\dagger\right)\sigma_-\right] dk. \tag{A.2}$$

This mathematical treatment for a 1D quantum system is very similar to the Tomonaga-Luttinger model [157–159]. For near-resonant interactions, contributions of far-detuned interactions can be ignored. That allows us to set the lower limit of the integration to $-\infty$ for simplicity. So, we get

$$H/\hbar = \omega_{eg}\sigma_{ee} + \int_{-\infty}^\infty \left[r_k^\dagger r_k - l_k^\dagger l_k\right] v_g k dk + \int_{-\infty}^\infty V\frac{1}{\sqrt{2\pi}} \left[(r_k + l_k)\,\sigma_+ + \left(r_k^\dagger + l_k^\dagger\right)\sigma_-\right] dk, \tag{A.3}$$

where $V = \sqrt{L}\mathcal{V}$. Now, we can move from k- space to real space using the Fourier transform relationships:

$$l(x) = \frac{1}{\sqrt{2\pi}}\int_{-\infty}^\infty l_k e^{ikx} dk, \quad r(x) = \frac{1}{\sqrt{2\pi}}\int_{-\infty}^\infty r_k e^{ikx} dk. \tag{A.4}$$

Using this relationship, we get the real space Hamiltonian:

$$H/\hbar = \omega_{eg}\sigma_{ee} - iv_g \int_{-\infty}^{\infty} dx \left[r^\dagger(x) \frac{\partial}{\partial x} r(x) - l^\dagger(x) \frac{\partial}{\partial x} l(x) \right] + \int_{-\infty}^{\infty} dx V \delta(x) \left(r^\dagger(x)\sigma_- + r(x)\sigma_+ + l^\dagger(x)\sigma_- + l(x)\sigma_+ \right), \quad \text{(A.5)}$$

Appendix B

Fabrication of photonic crystals for making cavities inside hollow core fibers

This work was done together with Vinodh Raj Rajagopal Muthu, and Dr. Rubayet Al Maruf, with advice and assistance from Dr. Jeremy Flannery. We used the fabrication recipe developed by Dr. Jeremy Flannery for fabricating the photonic crystals reported in Ref. [160]. We started with a Si chip with a layer of SiN, and a protective PMMA coating on top. The steps followed were (see Fig. B.1):

I. Remove PMMA

The PMMA was removed by sonicating the chip in Remover PG at 80°C for 15mins.

II. Etch SiN to correct thickness

The SiN layer was etched down to 430nm thickness by reactive ion etching (RIE) (Oxford Instruments ICP380). Standard reflectometry (Filmetrics F40) was used to measure the thickness of the SiN layer before, and after etching process, and for measuring the etch rate. We used a mixture of C_4F_8 at 130 SCCM, and SF_6 at 60 SCCM, at 10mTorr pressure, 1000W ICP RF power, and 30W platen RF power. The platen temperature was 15°C. Before etching, the chamber was *conditioned* by running the recipe for 45mins with a dummy sample to remove any impurities from the chamber.

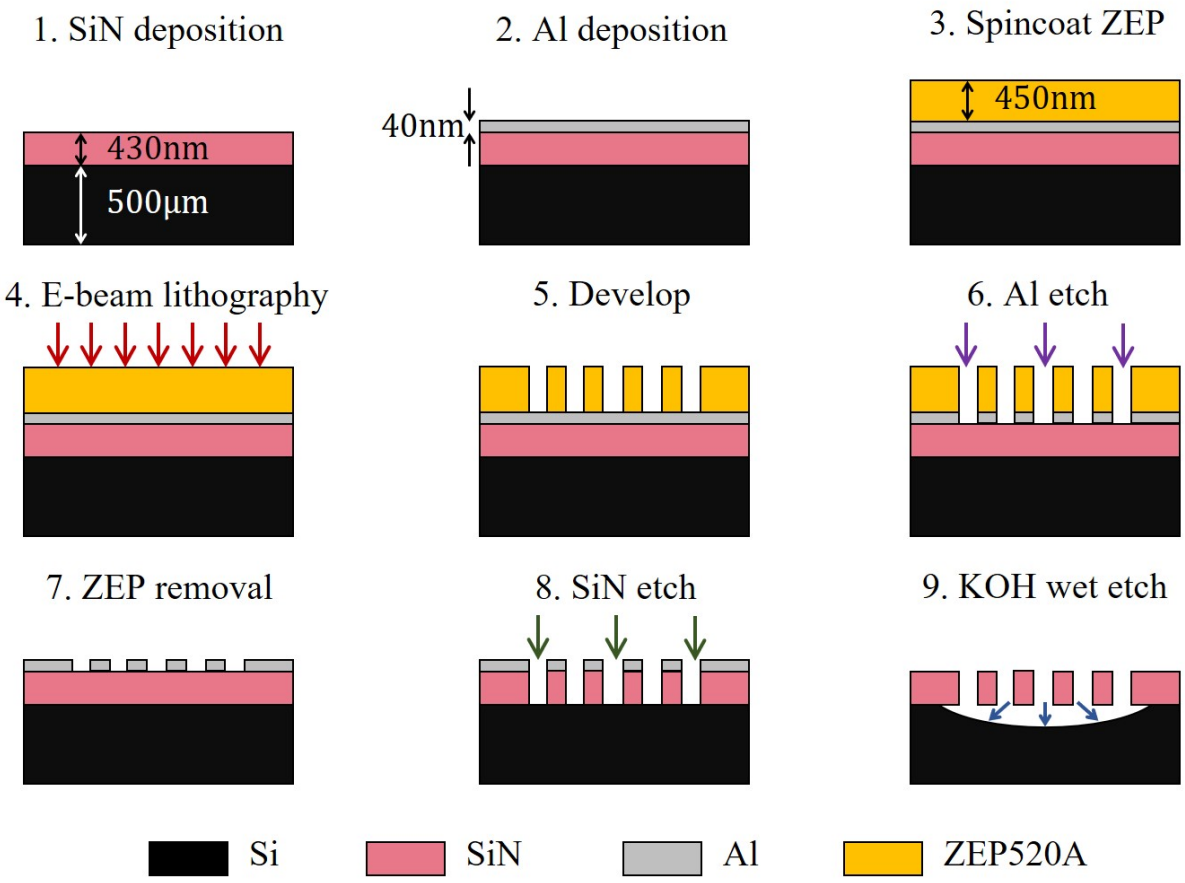

Figure B.1: The fabrication process for the photonic crystal membrane.

III. Deposit Aluminum

A 40nm layer of Al was deposited on the SiN film using e-beam physical vapour deposition (Intlvac Nanochrome II) as a hard mask for step VIII.

IV. Spincoat ZEP

A 450nm thick layer of the positive resist ZEP520A (Zeon Chemicals) on the layer of Al. A speed of 3000rpm was used for 60s, with a ramp of 3000rpm/s. The resist was developed by baking it on a hot-plate for 2mins at 180°C.

V. E-beam lithography (EBL)

The hexagonal hole pattern was written on ZEP using EBL (JEOL JBX-6300FS) at 100keV. The pattern was developed by treating the chips with amyl-acetate for 90s.

VI. Etch Aluminum

First, any oxide layer on the chip is removed by etching with a mixture of Cl_2 at 10 SCCM, BCl_3 at 40 SCCM, and 50 SCCM N_2 at 5mTorr pressure, 800W ICP power, and 150W HF power for 8s. Next, the Al is etched with a mixture of Cl_2 at 40 SCCM, BCl_3 at 10 SCCM, and 50 SCCM N_2 at 5mTorr pressure, 800W ICP power, and 120W HF power for 10s.

VII. Remove ZEP

ZEP was removed by sonicating the chip in Remover PG at 80°C for 15mins.

VIII. Etch SiN

The SiN layer is etched using the same recipe as in step II. The sample is over-etched to etch a SiN layer 1.5 times thicker than the original layer to ensure that the holes properly go through the SiN layer.

VIII. KOH wet etch

The Si substrate, and the Al hard mask is etched using KOH wet etch. The sample is put in 45% conc. KOH solution at 80°C for 1 hour, followed by two separate 5min long baths in deionized water also at 80°C. After that, the samples are immersed for 5min each into two separate beakers with IPA. This step of the fabrication process was performed by Rubayet al Maruf for us.

Appendix C

Deterministic single photon subtraction codes

C.1 Temporal dynamics of SPRINT with coherent continuous input in waveguide

```
import numpy as np
import scipy.linalg as lin
import matplotlib.pyplot as plt
import matplotlib as mpl

mpl.rcParams.update({'font.size': 20})
mpl.rcParams['font.family'] = 'serif'
mpl.rcParams['text.latex.preamble'] = [r'\boldmath']

beta = 1                        # Coupling efficiency
F = 1.4                         # Purcell factor
gamma0 = 2*np.pi*5.22           # Spontaneous emission rate in free space
gamma_tot = F*gamma0
gamma_g = gamma_tot*beta        # Guided gamma
gamma_r = gamma_tot*(1-beta)    # Radiated gamma
gamma = gamma_r                 # Gamma in OBE

V1 = V2 = np.sqrt(gamma_g/np.pi)  # Coupling strengths
xi = 1                            # Directivity
VR1 = np.sqrt(xi)*V1
VL2 = np.sqrt(xi)*V2
VL1 = np.sqrt(1-xi)*V1
```

```
VR2 = np.sqrt(1-xi)*V2
n = 1                                   # Input average photon number
alpha = np.sqrt(2*np.pi*n)

# [[sigma_13], [sigma_31], [sigma_33], [sigma_11], [sigma_22]]
x = np.matrix([[0], [0], [0], [1], [0]])

# Matrix of co-efficients of Master's Equation set
M = np.matrix([[-(np.pi*(VR1**2+VL1**2+VR2**2+VL2**2)+gamma), 0, 1j*VR1*alpha, -1j*VR1*alpha, 0],
               [0, -(np.pi*(VR1**2+VL1**2+VR2**2+VL2**2)+gamma), -1j*VR1*alpha, 1j*VR1*alpha, 0],
               [1j*VR1*alpha, -1j*VR1*alpha, -2*(np.pi*(VR1**2+VL1**2+VR2**2+VL2**2)+gamma), 0, 0],
               [-1j*VR1*alpha, 1j*VR1*alpha, 2*np.pi*(VR1**2+VL1**2), 0, 0],
               [0, 0, 2*np.pi*(VR2**2+VL2**2), 0, 0]])

t = np.linspace(0, 0.1, 1001)
sigma11 = np.zeros(len(t))
sigma22 = np.zeros(len(t))

lout1 = np.zeros(len(t))
lout2 = np.zeros(len(t))
rout1 = np.zeros(len(t))
rout2 = np.zeros(len(t))
routint2 = np.zeros(len(t))
routint1 = np.zeros(len(t))
routint = np.zeros(len(t))
sigma13 = np.zeros(len(t))
sigma31 = np.zeros(len(t))

# Initial condition
sigma11[0] = 1
sigma13[0] = 0
sigma31[0] = 0
rout1[0] = alpha**2/(2*np.pi)
routint2[0] = 0
routint1[0] = 0
routint[0] = 0

for i in range(1, len(t)):
    x = lin.expm(M*t[i])*x
    sigma13[i] = abs(x.item(0))
    sigma31[i] = abs(x.item(1))
    sigma11[i] = abs(x.item(3))
```

```
    sigma22[i] = abs(x.item(4))
    lout1[i] = 2*np.pi*(VL1**2)*abs(x.item(2))
    lout2[i] = 2*np.pi*(VL2**2)*abs(x.item(2))
    rout1[i] = abs(alpha**2/(2*np.pi)+1j*VR1*(alpha*x.item(1)-alpha*x.
   item(0))+2*np.pi*VR1**2*x.item(2))
    rout2[i] = 2*np.pi*(VR2**2)*abs(x.item(2))
    routint2[i] = routint2[i - 1] + (rout2[i] * 1 / 1001)
    routint1[i] = routint1[i - 1] + (rout1[i] * 1 / 1001)
    routint[i] = routint1[i] + routint2[i]

plt.plot(t, sigma22*xi, linewidth=1.5, label=r'$\int_{0}^{t} \langle l^{\
   dag}_{2,out} l_{2,out} \rangle dt^{\prime}$')
## Uncomment the following lines to plot them
#plt.plot(t, lout2, linewidth=1.5, label=r'$\langle l^{\dag}_{2,out} l_
   {2,out} \rangle$')
#plt.plot(t, rout1, linewidth=1.5, label=r'$\langle r^{\dag}_{1,out} r_
   {1,out} \rangle$')
#plt.plot(t, routint, linewidth=1.5, label=r'$\int_{0}^{t} \langle r^{\
   dag}_{out} r_{out} \rangle dt^{\prime}$')
#plt.plot(t, sigma22*VL1**2/(VR2**2+VL2**2), linewidth=1.5, label=r'$\
   int_{0}^{t} \langle l^{\dag}_{1,out} l_{1,out} \rangle dt^{\prime}$')
#plt.plot(t, sigma22*(1-xi), linewidth=1.5, label=r'$\int_{0}^{t} \langle
    r^{\dag}_{2,out} r_{2,out} \rangle dt^{\prime}$')
#plt.plot(t, sigma11, linewidth=1.5, label=r'$\langle \sigma_{11} \
   rangle$')
#plt.plot(t, sigma22, linewidth=1.5, label=r'$\langle \sigma_{22} \
   rangle$')
plt.xlabel(r'$\rm{ \tau }$', fontsize=25)
plt.ylabel(r'$\rm{ \int_0^{\tau} \langle l_{out}^{(2)\dagger} l_{out
   }^{(2)} \rangle dt }$', fontsize=25)
plt.title(r'$\xi = %g, \beta = %g, |\alpha|^{2} = %g$' % (xi, beta, alpha
   **2/(2*np.pi)), fontsize=25)
plt.legend(loc=0)
plt.grid()
plt.show()
```

C.2 Dependence of deterministic single photon subtraction probability on pulsewidth with coherent pulsed input in waveguide

```
def f(t, tau):
    return np.sqrt(2)*np.exp(-2*(t/tau)**2)/np.power(np.pi*tau**2, 1/4)

```

```
beta = 1                        # Coupling efficiency
F = 1.4                         # Purcell factor
gamma0 = 2*np.pi*5.22           # Spontaneous emission rate in free space
gamma_tot = F*gamma0
gamma_g = gamma_tot*beta        # Guided gamma
gamma_r = gamma_tot*(1-beta) # Radiated gamma
gamma = gamma_r                 # Gamma in OBE

V1 = V2 = np.sqrt(gamma_g/np.pi)  # Coupling strengths
xi = 1                            # Directivity
VR1 = np.sqrt(xi)*V1
VL2 = np.sqrt(xi)*V2
VL1 = np.sqrt(1-xi)*V1
VR2 = np.sqrt(1-xi)*V2
n = 1                             # Input average photon number
alpha = np.sqrt(n)

# Initial condition of [[sigma_13], [sigma_31], [sigma_33], [sigma_11], [
    sigma_22]]
x0 = np.matrix([[0], [0], [0], [1], [0]])

# List of pulsewidth
tau = np.linspace(0, 15, 40)

prob = []

for j in range(0, len(tau)):
    t = np.linspace(-5 * tau[j], 5 * tau[j], 50001)
    sigma22 = np.zeros(len(t))
    x = x0

    for i in range(0, len(t)):
        # Matrix of co-efficients of Master's Equation set
        M = np.matrix([[-(np.pi * (VR1 ** 2 + VL1 ** 2 + VR2 ** 2 + VL2
    ** 2) + gamma), 0, 1j * np.sqrt(2 * np.pi) * VR1 * alpha * f(t[i],
    tau[j]), -1j * np.sqrt(2 * np.pi) * VR1 * alpha * f(t[i], tau[j]),
    0],
                       [0, -(np.pi * (VR1 ** 2 + VL1 ** 2 + VR2 ** 2 +
    VL2 ** 2) + gamma), -1j * np.sqrt(2 * np.pi) * VR1 * alpha * f(t[i],
    tau[j]), 1j * np.sqrt(2 * np.pi) * VR1 * alpha * f(t[i], tau[j]), 0],
                       [1j * np.sqrt(2 * np.pi) * VR1 * alpha * f(t[i],
    tau[j]), -1j * np.sqrt(2 * np.pi) * VR1 * alpha * f(t[i], tau[j]), -2
     * (np.pi * (VR1 ** 2 + VL1 ** 2 + VR2 ** 2 + VL2 ** 2) + gamma), 0,
    0],
                       [-1j * np.sqrt(2 * np.pi) * VR1 * alpha * f(t[i],
    tau[j]), 1j * np.sqrt(2 * np.pi) * VR1 * alpha * f(t[i], tau[j]), 2 *
```

```
    np.pi * (VR1 ** 2 + VL1 ** 2), 0, 0],
                    [0, 0, 2 * np.pi * (VR2 ** 2 + VL2 ** 2), 0, 0]])
        x = x + (t[i] - t[i - 1]) * M * x

        sigma22[i] = abs(x.item(4))

    prob.append(sigma22[50000]*beta)

plt.plot(tau, prob, 'ro', linewidth=1.5)
plt.plot(tau, prob, 'k', linewidth=1.5)
plt.xlabel(r'$\tau$', fontsize=25)
plt.ylabel(r'$P = \int_0^{\tau} \langle l_{out}^{\dagger} l_{out} \rangle
    dt$', fontsize=25)
plt.title(r'$\overline{n}_{in} = %g ,\xi = %g, \beta = %g$' % (n, xi,
   beta), fontsize=25)
plt.grid()
plt.show()
```

C.3 Dependence of deterministic single photon subtraction probability on input photon number for Fock state input in waveguide

```
import numpy as np
import numpy.matlib as matlib
import matplotlib
import matplotlib.pyplot as plt

matplotlib.rcParams.update({'font.size': 30})

def f(t, tau):
    return np.sqrt(2)*np.exp(-2*(t/tau)**2)/np.power(np.pi*tau**2, 1/4)

beta = 1                        # Coupling efficiency
F = 1.4                         # Purcell factor
gamma0 = 2*np.pi*5.22           # Spontaneous emission rate in free space
gamma_tot = F*gamma0
gamma_g = gamma_tot*beta        # Guided gamma
gamma_r = gamma_tot*(1-beta)    # Radiated gamma
gamma = gamma_r                 # Gamma in OBE

V1 = V2 = np.sqrt(gamma_g/np.pi)  # Coupling strengths
xi = 1                            # Directivity
VR1 = np.sqrt(beta)*V1
```

```
VL2 = np.sqrt(beta)*V2
VL1 = np.sqrt(1-beta)*V1
VR2 = np.sqrt(1-beta)*V2

N = 5                                   # Input photon number
tau = 1                                 # Pulsewidth

t = np.linspace(-5*tau, 5*tau, 50001)
sigma11 = np.zeros((N+1, len(t)))
lout2 = np.zeros((N+1, len(t)))
lout2int = np.zeros((N+1, len(t)))

M = matlib.zeros((4*(N+1)**2, 4*(N+1)**2), dtype=np.complex)
x = matlib.zeros((4*(N+1)**2, 1))

for i in range(N+1):
    x[4*((N+1)*i+i)+3] = 1

    for j in range(N+1):
        M[4*((N+1)*i+j), 4*((N+1)*i+j)] = -(np.pi*(VR1**2+VL1**2+VR2**2+
    VL2**2)+gamma)
        M[4*((N+1)*i+j)+1, 4*((N+1)*i+j)+1] = -(np.pi*(VR1**2+VL1**2+VR2
    **2+VL2**2)+gamma)
        M[4*((N+1)*i+j)+2, 4*((N+1)*i+j)+2] = -2*(np.pi*(VR1**2+VL1**2+
    VR2**2+VL2**2)+gamma)
        M[4*((N+1)*i+j)+3, 4*((N+1)*i+j)+2] = 2*np.pi*(VR1**2+VL1**2)

for i in range(1, len(t)):
    for j in range(N+1):
        for k in range(N+1):
            if k >= 1:
                M[4*((N+1)*j+k), 4*((N+1)*j+k-1)+2] = 1j*np.sqrt(2*np.pi)
    *VR1*np.sqrt(k)*f(t[i], tau)
                M[4*((N+1)*j+k), 4*((N+1)*j+k-1)+3] = -1j*np.sqrt(2*np.pi
    )*VR1*np.sqrt(k)*f(t[i], tau)
                M[4*((N+1)*j+k)+2, 4*((N+1)*j+k-1)+1] = -1j*np.sqrt(2*np.
    pi)*VR1*np.sqrt(k)*f(t[i], tau)
                M[4*((N+1)*j+k)+3, 4*((N+1)*j+k-1)+1] = 1j*np.sqrt(2*np.
    pi)*VR1*np.sqrt(k)*f(t[i], tau)
            if j >= 1:
                M[4*((N+1)*j+k)+1, 4*((N+1)*(j-1)+k)+2] = -1j*np.sqrt(2*
    np.pi)*VR1*np.sqrt(j)*f(t[i], tau)
                M[4*((N+1)*j+k)+1, 4*((N+1)*(j-1)+k)+3] = 1j*np.sqrt(2*np
    .pi)*VR1*np.sqrt(j)*f(t[i], tau)
                M[4*((N+1)*j+k)+2, 4*((N+1)*(j-1)+k)] = 1j*np.sqrt(2*np.
    pi)*VR1*np.sqrt(j)*f(t[i], tau)
```

```
                M[4*((N+1)*j+k)+3, 4*((N+1)*(j-1)+k)] = -1j*np.sqrt(2*np.
    pi)*VR1*np.sqrt(j)*f(t[i], tau)

     x = x+(t[i]-t[i-1])*M*x

     for j in range(N+1):
         lout2[j][i] = 2*np.pi*VL2**2*abs(x.item(4*((N+1)*j+j)+2))
         lout2int[j][i] = lout2int[j][i-1]+lout2[j][i]*(t[i]-t[i-1])

plt.plot(range(1, N+1), np.linspace(1, N, N) - lout2int[1:, -1], 'bo--',
    linewidth=1.5, label='After subtraction')
plt.plot(range(1, N+1), range(1, N+1), 'k--', linewidth=1.5, label='
    Before subtraction')
plt.plot(range(1, N+1), lout2int[1:, -1], 'mo--', linewidth=1.5, label='
    Subtracted photons')
plt.xlabel(r'$n_{in}$', fontsize=25)
plt.ylabel(r'$n_{out}$', fontsize=25)
plt.xticks(range(1, N+1))
plt.legend(loc=0, fontsize=25)
plt.yticks(np.linspace(0, N, N+1))
plt.title(r'$\xi = %g, \beta = %g, \tau = %g$' % (xi, beta, tau),
    fontsize=30)
plt.grid()
plt.show()
```

C.4 Temporal dynamics of SPRINT in a cavity with no drive and with a coherent state ($\bar{n} = 1$) in r mode initially

```
#Unit GHz
# Coupling strength
g_1 = g_2 = 2 * np.pi * 10

# Energy level frequencies
wr = 2*2*np.pi*10**5
wl = wa - 0.5*2*np.pi
w13 = 2*2*np.pi*10**5
w12 = 0.5*2*np.pi

# Frequencies in rotating frame if resonant drive is present
#del_wr = wr - wr
#del_wl = wl - wr
#del_w13 = w13 - wr
```

```
15
16 # Loss terms
17 gamma = 2 * np.pi * 0.25
18 gamma31 = gamma32 = gamma
19 kappa = gamma
20 kappa_r = kappa
21 kappa_l = kappa
22
23 N = M = 5       # Size of Hilbert space
24 samples = 10001
25 t = 5
26 tlist = np.linspace(0,t,samples)
27
28 # Three atomic states
29 one = basis(3,0)
30 three = basis(3,1)
31 two = basis(3,2)
32
33 # Atom density matrix elements
34 sig11 = one*one.dag()
35 sig22 = two*two.dag()
36 sig33 = three*three.dag()
37 sig12 = one*two.dag()
38 sig13 = one*three.dag()
39 sig23 = two*three.dag()
40
41 # Tensor space will be in the form mode_r * mode_l * atom
42 r = tensor(destroy(N),qeye(M),qeye(3))
43 l = tensor(qeye(N),destroy(M),qeye(3))
44
45 sigma11 = tensor(qeye(N),qeye(M),sig11)
46 sigma22 = tensor(qeye(N),qeye(M),sig22)
47 sigma33 = tensor(qeye(N),qeye(M),sig33)
48 sigma12 = tensor(qeye(N),qeye(M),sig12)
49 sigma13 = tensor(qeye(N),qeye(M),sig13)
50 sigma23 = tensor(qeye(N),qeye(M),sig23)
51
52 # Initial condition
53 psi0 = tensor(coherent(N,1),basis(M,0),basis(3,0))
54 rho_i = psi0 * psi0.dag()
55
56 # Hamiltonian
57 H_int = g_1 * (r * sigma13.dag() + r.dag() * sigma13) + g_2 * (l *
      sigma23.dag() + l.dag() * sigma23)
58 H_0 = wr * r.dag() * r + wl * l.dag() * l + w13 * sigma33 + w12 * sigma22
59 H = H_0 + H_int
```

```
60
61 # Hamiltonian if resonant drive is present
62 #d = kappa/2
63 #Hd = d * (r + r.dag())
64 #H_int = g_1 * (r * sigma13.dag() + r.dag() * sigma13) + g_2 * (l *
       sigma23.dag() + l.dag() * sigma23)
65 #H_0 = del_wr * r.dag() * r + del_wl * l.dag() * l + del_w13 * sigma33 +
       w12 * sigma22
66 #H = H_0 + H_int + Hd
67
68 # Collapse operators
69 C_1 = np.sqrt(kappa_r) * r
70 C_2 = np.sqrt(kappa_l) * l
71 C_3 = np.sqrt(gamma) * sigma33
72 C_4 = np.sqrt(gamma31) * sigma13
73 C_4 = np.sqrt(gamma32) * sigma23
74 c_ops = [C_1,C_2,C_3,C_4,C_5]
75
76 options = Options()
77 options.nsteps = 10000
78
79 # Uncomment the next 2 lines for Monte Carlo simulations
80 #ntraj = 100
81 #result = mcsolve(H,psi0,tlist,c_ops,[sigma11,sigma22,sigma33,r.dag()*r,l
       .dag()*l,C_1.dag()*C_1,C_2.dag()*C_2],options=options,ntraj=ntraj,
       progress_bar=HTMLProgressBar())
82
83 # Master equation solver
84 result = mesolve(H,psi0,tlist,c_ops,[sigma11,sigma22,sigma33,r.dag()*r,l.
       dag()*l,C_1.dag()*C_1,C_2.dag()*C_2],options=options,progress_bar=
       HTMLProgressBar())
85
86 # Plot
87 fig, axes = plt.subplots(2, 2, figsize=(16, 8), sharex=True)
88
89 axes[0,0].plot(tlist,result.expect[0], label=r'${\langle \sigma_{11} \
       rangle}$', lw=2)
90 axes[0,0].plot(tlist,result.expect[1], label=r'${\langle \sigma_{22} \
       rangle}$', lw=2)
91 axes[0,0].plot(tlist,result.expect[2], label=r'${\langle \sigma_{33} \
       rangle}$', lw=2)
92 axes[0,0].legend(loc=1)
93
94 axes[0,1].plot(tlist, result.expect[3], label=r'${\langle r^{\dag}r \
       rangle}$',lw=2)
95 axes[0,1].plot(tlist, result.expect[4], label=r'${\langle l^{\dag}l \
```

```
    range}$', lw=2)
axes[0,1].legend(frameon=False, framealpha=1)

axes[1,0].plot(tlist, result.expect[5], label=r'${\langle r_{out}^{\dag}
    r_{out} \rangle}$', lw=2)
axes[1,0].plot(tlist, result.expect[6], label=r'${\langle l_{out}^{\dag}
    l_{out} \rangle}$', lw=2)
axes[1,0].legend(frameon=False, framealpha=1)
axes[1,0].set_xlabel('Time (ns)')

routint = np.zeros(len(tlist))
loutint = np.zeros(len(tlist))
rout = result.expect[5]
lout = result.expect[6]

for i in range(1,len(tlist)):
    routint[i] = (rout[i]*((t)/samples) + routint[i-1])
    loutint[i] = (lout[i]*((t)/samples) + loutint[i-1])

axes[1,1].plot(tlist, routint, label=r'${\int_{0}^{t} dt \langle r_{out
    }^{\dag}r_{out} \rangle}$', lw=2)
axes[1,1].plot(tlist, loutint, label=r'${\int_{0}^{t} dt \langle l_{out
    }^{\dag}l_{out} \rangle}$',lw=2)
axes[1,1].legend(frameon=False, framealpha=1,loc='upper right',
    bbox_to_anchor=(1, 0.58))
axes[1,1].set_xlabel('Time (ns)')

np.savez('Transient_initial_n_1_kappa_equal_N_5.npz',sigma11=result.
    expect[0],sigma22=result.expect[1],sigma33=result.expect[2],r_dag_r=
    result.expect[3],l_dag_l=result.expect[4],r_out=result.expect[5],
    l_out=result.expect[6],int_r_out=routint,int_l_out=loutint,kappa_r=
    kappa_r,kappa_l=kappa_l,N=N,tlist=tlist)
```

C.5 Calculating second-order correlation function

```
samples = 10001
t = 20
tlist = np.linspace(0,t,samples)

# Master equation solver
result = mesolve(H,psi0,tlist,c_ops,[r.dag()*r.dag()*r*r,r.dag()*r,l.dag
    ()*l.dag()*l*l,l.dag()*l],progress_bar=True)

# Calculate g(2) of modes r and l
g2_r = result.expect[0]/(result.expect[1])**2
```

```
g2_l = result.expect[2]/(result.expect[3])**2
```

C.6 Calculating Wigner function $W(x,p)$ when instantaneous fidelity of single photon in l mode is maximum

```
# Master equation solver
result=mesolve(H,psi0,tlist,c_ops,[],progress_bar=HTMLProgressBar())

# Find time with maximum fidelity by looping through the density matrices
    at different times
fid_list = []

for i in range(samples):
    rho_l = (result.states[i]).ptrace(1)
    fid_list.append(fidelity(rho_l,fock_dm(N,1)))

t_id = np.argmax(fid_list)
rho_id = result.states[t_id]

# Reduced density matrices of modes r (0) and l (1), and the emitter (2)
rho0 = rho_id.ptrace(0)
rho1 = rho_id.ptrace(1)
rho2 = rho_id.ptrace(2)

xvec = np.linspace(-3,3,200)
W0 = wigner(rho0,xvec,xvec,'iterative',2)
W1 = wigner(rho1,xvec,xvec,'iterative',2)
W2 = wigner(rho2,xvec,xvec,'iterative',2)

# Plot
fig, axes = plt.subplots(1, 3, figsize=(20,4.5))
cont0 = axes[0].contourf(xvec, xvec, W0, 100, cmap='inferno')
lbl0 = axes[0].set_title(r"$t=%.1f$ ns, r mode" %(t*t_id/samples),
   fontsize=20)
v1 = np.linspace(W0.min(), W0.max(), 10, endpoint=True)
cbar=fig.colorbar(cont0, ax=axes[0], ticks=v1)
cbar.ax.set_yticklabels(["{:4.2f}".format(i) for i in v1])

cont1 = axes[1].contourf(xvec, xvec, W1, 100, cmap='inferno')
lbl1 = axes[1].set_title(r"$t=%.1f$ ns, l mode" %(t*t_id/samples),
   fontsize=20)
v1 = np.linspace(W1.min(), W1.max(), 10, endpoint=True)
```

```
cbar=fig.colorbar(cont1, ax=axes[1], ticks=v1)
cbar.ax.set_yticklabels(["{:4.2f}".format(i) for i in v1])

cont2 = axes[2].contourf(xvec, xvec, W2, 100, cmap='inferno')
lbl2 = axes[2].set_title(r"$t=%.1f$ ns, $\Lambda$ emitter" %(t*t_id/
    samples), fontsize=20)
v1 = np.linspace(W2.min(), W2.max(), 10, endpoint=True)
cbar=fig.colorbar(cont2, ax=axes[2])
cbar.ax.set_yticklabels(["{:4.2f}".format(i) for i in v1])
```

C.7 Calculating the entropies

```
# Master equation solver
result=mesolve(H,psi0,tlist,c_ops,[],progress_bar=HTMLProgressBar())

S_r=[]
S_l=[]
S_atom=[]
S_rho_r = []
S_rho_l = []
S_rho_atom = []

# Calculate the entropies
for i in range(0,len(tlist)):
    rho = result.states[i]
    rho1 = rho.ptrace(0)
    rho2 = rho.ptrace(1)
    rho3 = rho.ptrace(2)
    S_rho_r.append(entropy_conditional(rho,0,base=2))
    S_rho_l.append(entropy_conditional(rho,1,base=2))
    S_rho_atom.append(entropy_conditional(rho,2,base=2))
    S_r.append(entropy_vn(rho1,base=2))
    S_l.append(entropy_vn(rho2,base=2))
    S_atom.append(entropy_vn(rho3,base=2))

# Plot
fig = plt.figure(figsize=(10,7))
plt.plot(tlist, S_r, 'r', label=r'$S(\rho_r)$', lw=2)
plt.plot(tlist, S_l, 'g', label=r'$S(\rho_l)$', lw=2)
plt.plot(tlist, S_atom, 'b', label=r'$S(\rho_{\Lambda})$', lw=2)
plt.plot(tlist, S_rho_r, 'r:', label=r'$S(\rho|\rho_r)$', lw=2)
plt.plot(tlist, S_rho_l, 'g:', label=r'$S(\rho|\rho_l)$', lw=2)
plt.plot(tlist, S_rho_atom, 'b:', label=r'$S(\rho|\rho_{\Lambda})$', lw
    =2)
plt.legend(frameon=False, framealpha=1, fontsize=27, loc='upper right',
```

```
    bbox_to_anchor=(1, 1))
plt.xlabel('Time (ns)', fontsize=25)
plt.ylabel('Entropy', fontsize=25)
```

C.8 Ideal deterministic single photon subtraction operator

```
# N = Size of Hilbert space
def subtract(N, offset=0):
    matrix = np.zeros([N, N], dtype=complex)
    matrix[0,0] = 1
    for i in range(0, N-1):
        matrix[i,i+1] = 1
    return Qobj(matrix, isherm=False)
```

Appendix D

Inverse design codes

This work was done together with Vinodh Raj Rajagopal Muthu.

D.1 Lumerical code (.lsf)

```
switchtolayout;
selectall;
delete;

## SIM PARAMS
opt_size_x = 3.0e-6;
opt_size_y = 3.0e-6;
opt_size_z = 300e-9;

fiber_rad = 700e-9;

dist_to_source = 200e-9;
dist_to_fiber = 2e-6;

grating_thickness = 300e-9;

size_x = opt_size_x + 1.5e-6;
size_y = opt_size_y + 1.5e-6;
size_z_min = - (grating_thickness/2 + dist_to_source + 50e-9);
size_z_max = grating_thickness/2 + dist_to_fiber + 50e-9;

wavelength = 680e-9;

```

```
diamond_index = 2.41;
fiber_index = 1.44;
air_index = 1;

dx = 20e-9;

# DIAMOND SAMPLE
addrect;
set('name','diamond sample');
set('x',0);
set('x span',2*opt_size_x);
set('y',0);
set('y span',2*opt_size_y);
set('z max',-grating_thickness/2);
set('z min',-grating_thickness/2 - 1e-6);
set('index',diamond_index);

# OUTPUT FIBER
addcircle;
set('name','output fiber top');
set('x',0);
set('y',0);
set('radius',fiber_rad);
set('z min',grating_thickness/2 + dist_to_fiber);
set('z max',grating_thickness/2 + dist_to_fiber + 5e-6);
set('index',fiber_index);

# NV CENTER SOURCE
adddipole;
set('x',0);
set('y',0);
set('z',-grating_thickness/2 - dist_to_source);
set('amplitude',1);
set('center wavelength',wavelength);
set('wavelength span',0);
set('theta',90);

# FDTD
addfdtd;
set('dimension','3D');
set('background index',air_index);
set('mesh accuracy',3); #< To increase this, we also need to refine the
    optimization mesh below 20nm
set('x min',-size_x/2);
set('x max',size_x/2);
set('y min',-size_y/2);
```

```
set('y max',size_y/2);
set('z min',size_z_min - 0.5e-6);
set('z max',size_z_max);
set('auto shutoff min',1e-7);

# OPTIMIZATION FIELDS MONITOR IN OPTIMIZABLE REGION
addpower;
set('name','opt_fields');
set('monitor type','3D');
set('x',0);
set('x span',opt_size_x);
set('y',0);
set('y span',opt_size_y);
set('z',0);
set('z span',opt_size_z);

# FOM
addpower;
set('name','fom');
set('monitor type','2D Z-normal');
set('x',0);
set('x span',fiber_rad * 2.5);
set('y',0);
set('y span',fiber_rad * 2.5);
set('z',grating_thickness/2 + dist_to_fiber);

# FOR LATER VISUALIZATION
addindex;
set('name','global_index');
set('monitor type','3D');
set('x min',-size_x/2);
set('x max',size_x/2);
set('y min',-size_y/2);
set('y max',size_y/2);
set('z min',-opt_size_z/2);
set('z max',opt_size_z/2);
set('enabled',true);

# INITIAL BULLSEYE GEOMETRY
addstructuregroup;
set('name','initial_guess');
mesh_order = 2;
period = wavelength/diamond_index; #< Second order Bragg grating
    criterion
radius = 2 * period;
ridge_width = period/2;
```

```
114
115 addcircle;
116 set('name','center_circle');
117 set('x',0);
118 set('y',0);
119 set('radius',radius - ridge_width);
120 set('z max',grating_thickness/2);
121 set('z min',-grating_thickness/2);
122 set('index',diamond_index);
123 addtogroup("initial_guess");
124
125 for (0; 2*(radius + ridge_width) < opt_size_x; 0) {
126     addring;
127     set('name','ring');
128     set("x",0);
129     set("y",0);
130     set("inner radius",radius);
131     set("outer radius",radius + ridge_width);
132     set("z",0);
133     set("z span",grating_thickness);
134     set('index',diamond_index);
135     addtogroup("initial_guess");
136     radius = radius + period;
137 }
```

D.2 Python code (.py)

```
1  # General purpose imports
2  import numpy as np
3  import os
4  import sys
5  import scipy as sp
6
7  # Uncomment the next two lines if using Linux
8  #import imp
9  #lumapi = imp.load_source("lumapi", "/opt/lumerical/2019b/api/python/
       lumapi.py")
10
11 # Optimization specific imports
12 from lumopt import CONFIG
13 from lumopt.geometries.topology import TopologyOptimization2D,
       TopologyOptimization3DLayered
14 from lumopt.utilities.load_lumerical_scripts import load_from_lsf
15 from lumopt.figures_of_merit.modematch import ModeMatch
16 from lumopt.optimization import Optimization
```

```
from lumopt.optimizers.generic_optimizers import ScipyOptimizers
from lumopt.utilities.wavelengths import Wavelengths

# DEFINE BASE SIMULATION #
def runSim(params, eps_air, eps_diamond, x_pos, y_pos, z_pos, size_x, filter_R):

    # DEFINE A 3D TOPOLOGY OPTIMIZATION REGION #
    geometry = TopologyOptimization3DLayered(params=params, eps_min=eps_air, eps_max=eps_diamond, x=x_pos, y=y_pos, z=z_pos, filter_R=filter_R)

    # DEFINE FIGURE OF MERIT #
    # The base simulation script defines a field monitor named 'fom' at the point where we want to modematch to the fundamental TE mode
    fom = ModeMatch(monitor_name = 'fom', mode_number = 'Fundamental TE mode', direction = 'Forward', norm_p = 2)

    # DEFINE OPTIMIZATION ALGORITHM #
    optimizer = ScipyOptimizers(max_iter=40, method='L-BFGS-B', scaling_factor=1, pgtol=1e-6, ftol=1e-4, scale_initial_gradient_to=0.25)

    # LOAD TEMPLATE SCRIPT AND SUBSTITUTE PARAMETERS #
    script = load_from_lsf(os.path.join(CONFIG['root'], 'examples/NV_grating/dipole_source.lsf'))

    wavelengths = Wavelengths(start = 680e-9, stop = 680e-9, points = 1)
    opt = Optimization(base_script=script, wavelengths = wavelengths, fom=fom, geometry=geometry, optimizer=optimizer, use_deps=False, hide_fdtd_cad=True, plot_history=False, store_all_simulations=False)

    # RUN THE OPTIMIZER #
    opt.run()

if __name__ == '__main__':
    size_x = 3000
    size_y = 3000
    size_z = 300

    filter_R = 400e-9

    # Permittivity of diamond and air
    eps_diamond = 2.41**2
    eps_air = 1**2

```

```
53      if len(sys.argv) > 2 :
54          size_x = int(sys.argv[1])
55          filter_R = int(sys.argv[2])*1e-9
56          print(size_x,filter_R)
57
58      x_points = int(size_x/20) + 1
59      y_points = int(size_y/20) + 1
60      z_points = int(size_z/20) + 1
61
62      x_pos = np.linspace(-size_x/2*1e-9,size_x/2*1e-9,x_points)
63      y_pos = np.linspace(-size_y/2*1e-9,size_y/2*1e-9,y_points)
64      z_pos = np.linspace(-size_z/2*1e-9,size_z/2*1e-9,z_points)
65
66      ## And then also a few systematic tests
67      paramList=[None,                                #< Use the structure
    defined in the project file as initial condition
68                 np.ones((x_points,y_points)),        #< Start with the
    domain filled with eps_diamond
69                 0.5*np.ones((x_points,y_points)),    #< Start with the
    domain filled with (eps_diamond+eps_air)/2
70                 np.zeros((x_points,y_points)),       #< Start with the
    domain filled with eps_air
71                 ]
72
73      for curParams in paramList:
74          runSim(curParams, eps_air, eps_diamond, x_pos, y_pos, z_pos,
    size_x*1e-9, filter_R)
```

Appendix E

Gaussian beam waist calculation code

This work was done together with Vinodh Raj Rajagopal Muthu.

E.1 Mathematica code

```
(*ABCD Matrices*)
Lens[f_] := {{1, 0}, {-1/f, 1}};
Air[d_] := {{1, d}, {0, 1}};

(*The ray vectors at z=0*)
Xi[wavelength_, w0_] := {{0}, {wavelength/(Pi*w0)}};
Eta[w0_] := {{w0}, {0}};

WInit = 1.4*2;(*The back aperture diameter of the objective is 2.8mm*)
Lambda = 532*(10^-9);
f1 = 100; f2 = 200; f3 = 200;
d1 = ((f1^2)/f2) + f1 - (d3*((f1/f2)^2));
(*This relationship will be useful when putting lenses between the \
galvo and the objective,so that the back aperture of the objective \
and the galvo are conjugate.However,in this simulation the value of \
d1 does not matter.*)
d2 = f1 + f2; d3 = 150; d4 = f3;

(*Propagation through air*)
M1 = Air[z];
Eta1 = M1.Eta[WInit]; Xi1 = M1.Xi[Lambda, WInit];
R1 = Sqrt[Eta1[[1]]^2 + Xi1[[1]]^2];

```

```
(*Propagation through lens L1*)
M2 = Air[z - d1].Lens[f1].Air[d1];
Eta2 = M2.Eta[WInit]; Xi2 = M2.Xi[Lambda, WInit];
R2 = Sqrt[Eta2[[1]]^2 + Xi2[[1]]^2];

(*Propagation through lens L2*)
M3 = Air[z - d1 - d2].Lens[f2].Air[d2].Lens[f1].Air[d1];
Eta3 = M3.Eta[WInit]; Xi3 = M3.Xi[Lambda, WInit];
R3 = Sqrt[Eta3[[1]]^2 + Xi3[[1]]^2];

(*Propagation through lens L3*)
M4 = Air[z - d1 - d2 - d3].Lens[f3].Air[d3].Lens[f2].Air[d2].Lens[
    f1].Air[d1];
Eta4 = M4.Eta[WInit]; Xi4 = M4.Xi[Lambda, WInit];
R4 = Sqrt[Eta4[[1]]^2 + Xi4[[1]]^2];

Plot[Piecewise[{{R1, z < d1}, {R2,
    d1 < z < (d2 + d1)}, {R3, (d1 + d2 + d3) > z > (d2 + d1)}, {R4,
    z > (d1 + d2 + d3)}}], {z, 0, d1 + d2 + d3 + d4},
 AxesLabel -> {"z (mm)", "Beam radius (mm)"}, ImageSize -> Large,
 LabelStyle -> {24, GrayLevel[0]}]
```

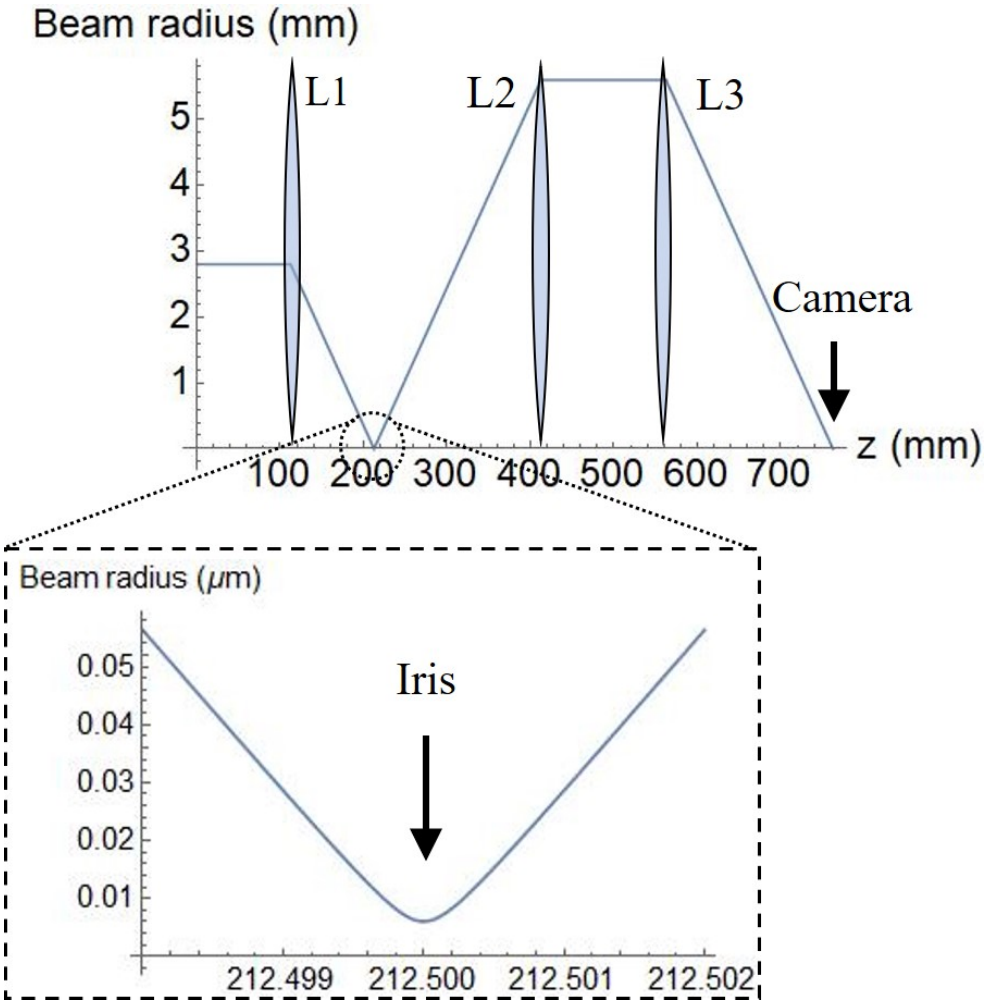

Figure E.1: Beam radius of the red light while moving though the optical setup for $f_{L1} =$ 100mm, $f_{L2} = 200$mm, and $f_{L3} = 200$mm.

Appendix F

Galvo controller circuit

This work was done together with Vinodh Raj Rajagopal Muthu.

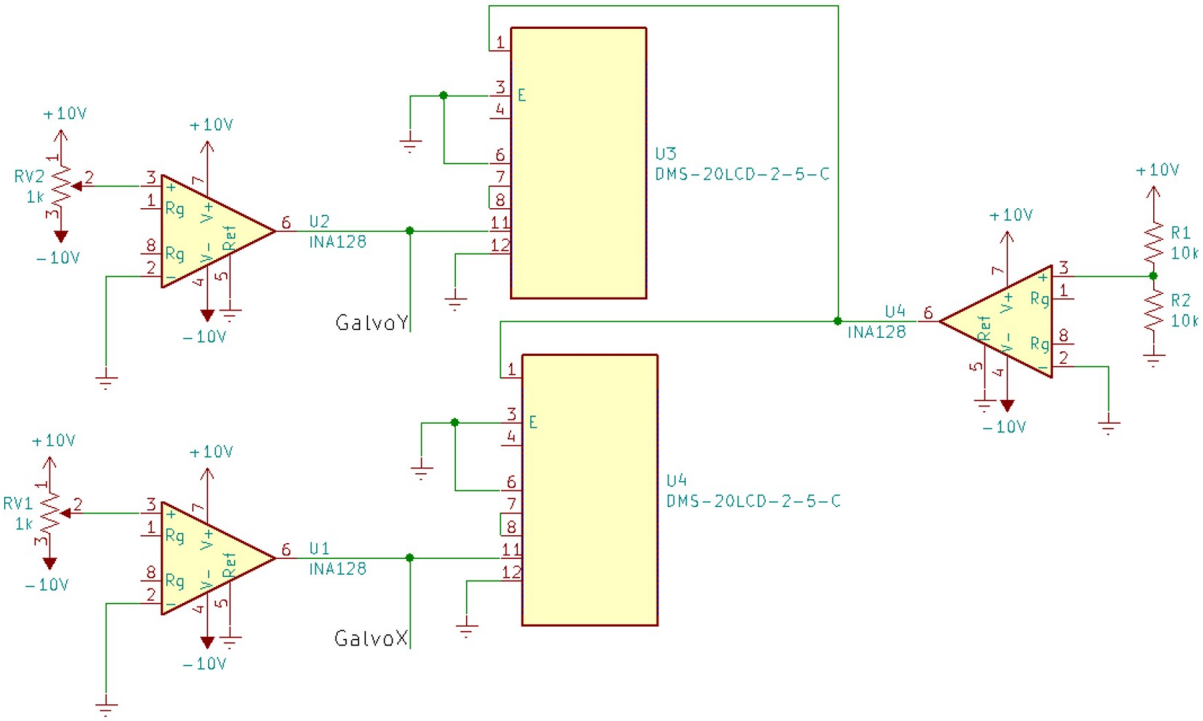

Figure F.1: The manual galvo controller circuit schematic.